Volume : 2 Issue : 1 eISSN: 3059-9504
Dec. 2025

Api Journal of Science

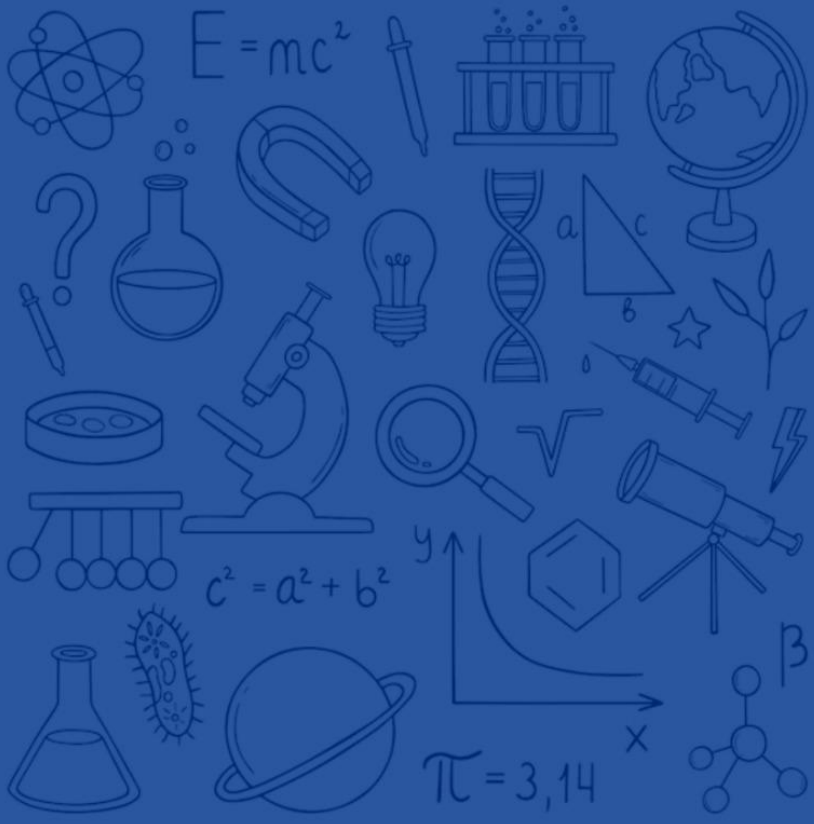

Published by:
Research Management Cell
Siddhanath Science Campus
Tribhuvan University, Nepal

Editorial Board

EDITORIAL

Research Management Cell, Siddhanath Science Campus, Tribhuvan University, is delighted to present second issue of scientific Journal "Api Journal of Science (AJS)". AJS is a peer reviewed journal and aims to publish original research articles of all the science disciplines. We are very grateful to all the authors who have chosen to submit their manuscripts to AJS for publication. We are indebted to all the potential researchers and reviewers for their valuable time and effort for their rigorous evaluation process. Hard work of our editors, contributors, and esteemed supporters made it possible to reach at the publication stage.

Special thanks go to the contributors for providing their innovative research works to the readers via this regular issue of AJS. The AJS editorial team appreciates any feedback for its improvement. Finally, I appreciate your constructive feedback and further correspondence.

Editor-in-Chief

Dr. Bhawani Datt Joshi

Api Journal of Science

Structure, Electronic, and Vibrational properties of Salbutamol using Quantum Chemical and Molecular Docking Approaches

Dipak Joshi, Bhawani Datt Joshi*

Department of Physics, Siddhanath Science Campus, Tribhuvan University Mahendranagar, 10400

Research Article

ISSN: 3059-9504 (online)
DOI: https://doi.org/10.3126/ajs.v2i1.87744

Article History

Received: August 12, 2025; Revised: October 05, 2025; Accepted: October 10, 2025; Published: December 25, 2025

Keywords

Salbutamol, Density Functional Theory, β_2-Adrenergic Receptor, Molecular Docking, Vibrational Analysis, HOMO–LUMO, Drug Binding

***Corresponding author**

Email: bhawani.joshi@snsc.tu.edu.np (BD Joshi)
Orcid: https://orcid.org/0000-0003-3276-9319

ABSTRACT

Molecular structure, vibrational spectra, electronic properties, and receptor binding mechanism Salbutamol, a short-acting β_2-adrenergic agonist used in asthma therapy, were studied using density functional theory (DFT) and molecular docking methods. The molecular geometry was optimized at the DFT/B3LYP/3-21G level of theory. The calculated rotational constants are A = 0.917 GHz, B = 0.209 GHz, and C = 0.182 GHz provide insights into the molecular moments of inertia. The HOMO-LUMO energy gap was found to be 5.14 eV in the gas phase, decreasing in polar solvents, which indicated enhanced electronic polarization. Time-dependent DFT (TD-DFT) simulations revealed strong $\pi \rightarrow \pi^*$ electronic transitions in the near-ultraviolet region. Molecular docking of Salbutamol into the binding site of the human β_2-adrenergic receptor (PDB ID: 3NY8) yielded a binding affinity of -7.545 kcal/mol. The docking pose shows that Salbutamol forms hydrogen bonds with ASP113 and ASN312, and engages in hydrophobic contacts with VAL114, VAL117, and PHE290. These structural and electronic insights rationalize the known biological activity of Salbutamol and may guide the future design of improved β_2-agonist drugs.

1. INTRODUCTION

Salbutamol, also known as Albuterol and chemically as 4-[2-(tert-butylamino)-1-hydroxyethyl]-2-(hydroxymethyl)phenol, is a selective β_2-adrenergic receptor agonist widely used to manage acute bronchospasm in asthma and chronic broncho-pulmonary conditions [1]. Its white crystalline powder structure includes a benzene ring inclined at 74.5° and a *tert*-butyl group positioned opposite amino and hydroxy groups, contributing to its high receptor selectivity and potent smooth muscle relaxation in the lungs [2,3]. It is administered primarily by inhalation for rapid onset within 5 minutes, with effects lasting up to 14 hours if taken orally [4,5]. Besides bronchodilation, Salbutamol influences cardiovascular, uterine, metabolic, and neurological systems [6,7,8]. High systemic doses may cause side effects such as tachycardia, but therapeutic inhalation doses have minimal impact on physical performance, leading to its regulation by WADA since 2004 [9]. The molecular structure of title molecule is shown in Fig. 1.

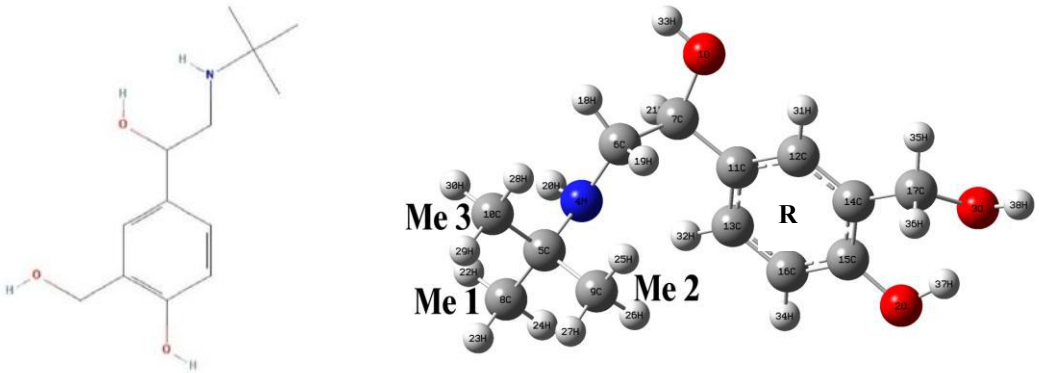

Fig. 1: (a) Molecular Structure of Salbutamol (source: PubChem) (b) Optimized structure of Salbutamol molecule using symbol and labelling of atom.

Apart from asthma and COPD, Salbutamol is also prescribed to prevent exercise-induced bronchospasm and explored for its potential benefit in acute respiratory distress syndrome by enhancing alveolar fluid clearance and reducing inflammation.

Literature reveals that Ali et al. (2009) studied Salbutamol hemisulphate using FT-Raman, IR, and DFT to identify vibrational modes linked to hydrogen bonding [10]. Zhao et al. (2020) analyzed Salbutamol binding to human serum albumin using spectroscopy and docking, revealing binding-induced conformational changes [14While previous studies have focused on specific aspects of Salbutamol, such as its crystallographic disorder or binding to serum albumin, a comprehensive theoretical study integrating its detailed structural, vibrational, and electronic properties with its binding mechanism to the β_2-adrenergic receptor is lacking. Therefore, this study aims to bridge this gap by providing a unified computational characterization of Salbutamol using DFT and molecular docking to bridge this gap and establish a solid structure activity relation.

2. MATERIALS AND METHODS

In this work, the initial molecular geometry of Salbutamol was retrieved from the PubChem database [15]. Geometry optimization was performed using Density Functional Theory (DFT) at the B3LYP/3-21G level of theory without any geometric constraints, employing the Gaussian 09 software package [16].
Following optimization, vibrational frequency calculations were conducted at the same level of theory to confirm the optimized structure corresponds to a minimum on the potential energy surface (no imaginary frequencies), yielding 108 vibrational modes as predicted by the formula 3N-6, where N is the number of atoms [17]. Potential energy distribution (PED) was analyzed using GAR2PED software, which utilizes internal coordinates and localized symmetry following Pulay's recommendations [18,19]. Visualization of the calculated IR and Raman vibrational spectra was conducted using GaussView, and the intensities were plotted using OriginPro 7 software [20]. To correct the systematic overestimation of vibrational wavenumbers common in DFT methods, scaling was applied using the wavenumber linear (WLS) approach as follows: $\ddot{\upsilon}_{obs} = (1.0087 - 0.0000163 \times \ddot{\upsilon}_{cal}) \times \ddot{\upsilon}_{cal}$ [21]. Electronic excitation spectra were predicted with time-dependent DFT (TD-DFT) calculations to evaluate excited states, electronic transitions, and oscillator strengths [22].

Molecular docking studies were carried out using SwissDock, which applies EADock DSS algorithms, with AutoDock Vina parameters for ligand and receptor preparation [23,24,25]. The three-dimensional structure of the target protein, the human β_2-adrenergic receptor (PDB ID: 3NY8), was selected as it is a high-resolution structure co-crystallized with a bound ligand, providing a reliable model for studying agonist binding. This structure was obtained from the RCSB Protein Data Bank and used without modification for docking studies. Salbutamol's ligand structure was provided in SMILES format and automatically converted to a 3D energy-minimized form prior to docking.

All computational and docking visualizations were systematically processed using GaussView, GAR2PED, Discovery Studio, and OriginPro 7 to support detailed structural and interaction analyses.

3. RESULTS AND DISCUSSION

3.1 Geometry Optimization

The optimized molecular geometry of Salbutamol consists of a substituted phenylethanolamine backbone, including a benzene ring, an aliphatic side chain, and polar functional groups such as hydroxyl and secondary amine. The geometry was optimized using the DFT/B3LYP/3-21G level of theory, and the structural parameters such as bond lengths, bond angles, and dihedral angles are summarized in Table 1.

Table 1: Optimized geometric parameters of Salbutamol at B3LYP/3-21G level

Bond Length		Bond Angle		Dihedral Angle	
Optimized Parameters	Value (Å)	Optimized Parameters	Value (º)	Optimized Parameters	Value (º)
O1-C7	1.466	C7-O1-H33	107.4	H33-O1-C7-C6	-66.6
O1-H33	0.993	C5-C4-C6	117.9	H33-O1-C7-C11	171.3
O2-C15	1.375	C5-C4-H20	109.3	C6-N4-C5-C8	175.8
O2-H37	1.018	C6-N4-H20	109.9	C6-N4-C5-C9	-66.8
O3-C17	1.490	N4-C5-C9	109.1	C5-N4-C6-C7	167.9
O3-H38	0.993	C7-C6-H18	107.6	C9-C5-C8-H22	179.4

N4-C5	1.499	O1-C7-C6	108.2	C9-C5-C8-H23	59.6
N4-C6	1.477	C6-C7-C11	113.2	C9-C5-C8-H24	-60.9
N4-H20	1.028	C5-C8-H23	110.4	O1-C7-C11-C12	-5.7
C5-C8	1.544	C5-C8-H24	109.5	O1-C7-C11-C13	175.6
C6-H18	1.107	H22-C8-H23	108.3	C6-C7-C11-C12	-124.7
C7-C11	1.520	C7-C11-C13	121.5	C6-C7-C11-C13	56.6
C7-H21	1.103	C12-C14-C15	120.0	C7-C11-C12-C14	-179.4
C11-C12	1.396	C15-C14-C17	119.9	C12-C14-C15-O2	178.4
C11-C13	1.403	O2-C15-C14	122.3	C12-C14-C15-C16	-1.4
C12-C14	1.396	O2-C15-C16	119.1	C17-C14-C15-O2	-6.0
C13-C16	1.390	C14-C15-C16	118.6	C17-C14-C15-C16	174.2
C13-H32	1.082	C13-C16-C15	121.1	C12-C14-C17-O3	-146.7
C14-C15	1.409	C13-C16-H34	121.3	C12-C14-C17-H35	-25.9
C14-C17	1.511	C15-C16-H34	117.7	C12-C14-C17-H36	93.8
C15-C16	1.401	O3-C17-C14	108.9	O2-C15-C16-C13	-179.4

The aromatic ring comprises carbon atoms C11 to C16. The bond lengths within this ring are nearly uniform, with values such as C11-C12 = 1.396 Å, C11-C13 = 1.403 Å, C12-C14 = 1.396 Å, and C13-C16 = 1.390 Å. These values are consistent with the expected range for delocalized C-C bonds in a benzene ring. The bond angles between the ring carbons, such as C11-C12-C14 = 121.2° and C12-C14-C15 = 120.0°, further support the sp^2 hybridization and planarity of the ring system. At the para position of the aromatic ring, a hydroxyl group is attached through the C15-O2 bond, with a length of 1.375 Å. The O1-C7 bond is 1.466 Å in length, consistent with a typical C-O single bond.

The secondary amine nitrogen N4 is bonded to C5 and C6 with lengths of 1.499 Å and 1.477 Å, respectively. The N-H bond (N4-H20) is calculated to be 1.028 Å. These values are in agreement with standard C-N and N-H bond lengths found in similar molecular frameworks. The three methyl groups: Me1(C8), Me2(C9), and Me3(C10) are attached to the central carbon C5. Each C-C bond between C5 and the methyl groups lies in the range of 1.542-1.550 Å, which is characteristic of single bonds between sp^3 hybridized carbons. Dihedral angles across the aromatic-substituted region also indicate slight deviations from complete planarity. For example, the dihedral angle O1-C7-C11-C12 is -5.6°, while C7-C11-C12-C14 is -179.4°, showing the ring system and side chain are almost coplanar. On the other end, the tail of the molecule containing C17 and O3 has a twisted arrangement, as observed in C14-C17-O3-H38 = -166.1°.

3.2 **Mulliken Atomic Charges**

Among all atoms, the oxygen atoms exhibit the most negative Mulliken charges, consistent with their strong electronegativity. Specifically, atom O2 has the most negative charge of -0.64282, followed by atom N4 (-0.56011) and atom O1 (-0.55171). The carbon atoms in Salbutamol display a wide range of charge distributions. Atom C15 stands out with the highest positive Mulliken charge of +0.291077, indicating a significantly electron-deficient site likely to undergo nucleophilic attack or serve as a binding interface for electron-rich partners. The hydrogen atoms in Salbutamol show predominantly positive Mulliken charges, as expected due to their bonding to more electronegative atoms. Notably, H37 and H38 possess the highest positive values of +0.363623 and +0.35796, respectively, indicating strong polarization and their potential to act as hydrogen bond donors in biological interactions. Mullikan atomic charges are listed in Table 2 and plotted in Fig. 2.

Table 2: Mulliken Atomic charge of Salbutamol

Atoms	Mulliken Atomic Charge	Atoms	Mulliken Atomic Charge	Atoms	Mulliken Atomic Charge
O1	-0.55171	C14	-0.02906	H27	0.179326
O2	-0.64282	C15	0.291077	H28	0.187725
O3	-0.54628	C16	-0.18482	H29	0.184907
N4	-0.56011	C17	-0.1999	H30	0.174804
C5	0.025053	H18	0.149599	H31	0.198251
C6	-0.21105	H19	0.228297	H32	0.202864
C7	-0.01237	H20	0.263248	H33	0.33596
C8	-0.5076	H21	0.182942	H34	0.188266
C9	-0.50684	H22	0.173372	H35	0.208931
C10	-0.52317	H23	0.184967	H36	0.205416
C11	-0.00883	H24	0.202907	H37	0.363623
C12	-0.19306	H25	0.185208	H38	0.35796
C13	-0.2063	H26	0.209205		

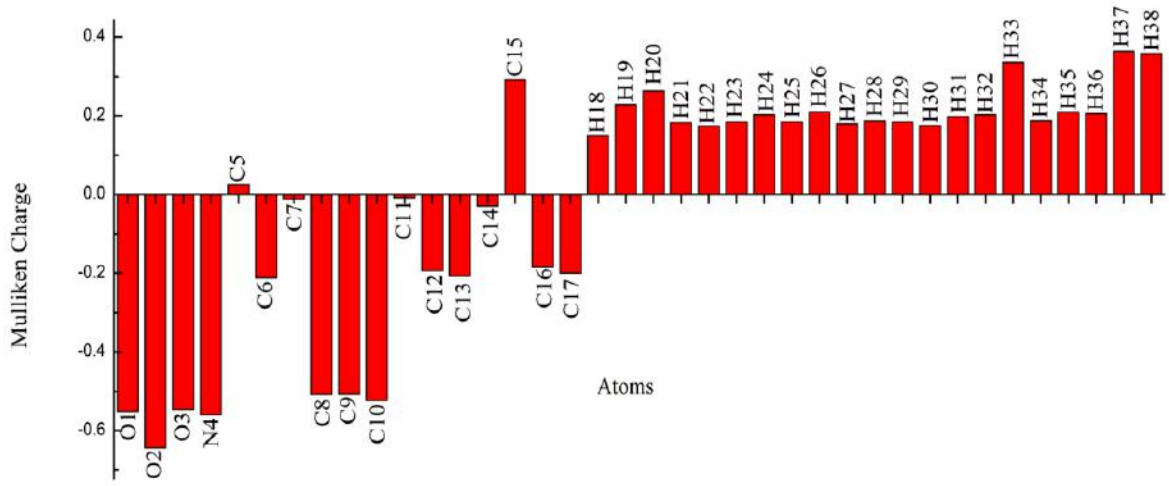

Fig. 2: Mulliken atomic charge vs atoms.

3.3 Vibrational Assignment

The vibrational spectra of Salbutamol were analyzed using Density Functional Theory (DFT) and Hartree-Fock (HF) calculations, providing insights into the nature of molecular bonding and intramolecular interactions. The calculated vibrational wavenumers are listed in Table 3. The IR and Raman spectra are given in Figs. 3 and 4, respectively.

Table 3: Vibrational wavenumbers (cm^{-1}), Raman Activity ($Å^4$/amu), IR intensity (km/mol), and their potential energy distribution.

Wavenumber			Raman Activity	IR Intensity	Potential Energy Distribution (PED) (≥ 5%)
Unscaled	Scaled				
DFT	DFT	HF			
3505	3336	3683	378.6	1.79	υ(O3H)(100)

3496	3327	3676	193.4	2.15	υ(O1H)(100)
3385	3227	3521	66.2	2.51	υ(NH)(100)
3237	3094	3489	142.4	7.78	R[υ(C13H)(80)+υ(C16H)(18)]
3231	3089	3257	42.7	1.40	R[υ(C12H)](98)
3219	3078	3246	69.3	5.12	R[υ(C16H)(81)+υ(C13H)(18)]
3142	3008	3233	67.6	21.87	Me2[$\upsilon(CH_3)$](48)+$\upsilon(C6H_2)$(40)+Me1[$\upsilon(CH_3)$](5)
3139	3005	3164	41.7	30.91	$\upsilon(C6H_2)$(50)+Me2[$\upsilon(CH_3)$](29)+Me1[$\upsilon(CH_3)$](19)
3133	3000	3143	25.8	8.32	Me1[$\upsilon(CH_3)$](70)+Me2[$\upsilon(CH_3)$](20)
3120	2988	3130	91.9	54.17	Me2[$\upsilon(CH_3)$](51)+Me3[$\upsilon(CH_3)$](38)
3113	2983	3117	10.8	4.09	Me3[$\upsilon(CH_3)$](58)+Me2[$\upsilon(CH_3)$](37)
3110	2979	3110	95.4	34.59	Me1[$\upsilon(CH_3)$](61)+Me3[$\upsilon(CH_3)$](29)
3103	2973	3108	11.2	4.33	Me3[$\upsilon(CH_3)$](65)+Me1[$\upsilon(CH_3)$](34)
3092	2963	3102	147.6	496.92	υ(O2H) (93)+$\upsilon(C17H_2)$(6)
3072	2945	3101	52.0	89.81	$\upsilon(C17H_2)$ (94) +υ(O2H)(6)
3059	2933	3069	145.6	6.87	Me2[$\upsilon(CH_3)$](94)
3046	2921	3055	120.9	31.35	Me1[$\upsilon(CH_3)$](56) +Me3[$\upsilon(CH_3)$](38)
3041	2916	3052	3.2	15.60	Me3[$\upsilon(CH_3)$](59)+Me1[$\upsilon(CH_3)$](40)
3003	2882	3049	125.4	58.30	$\upsilon(C17H_2)$(99)
2969	2851	3047	112.3	59.00	υ(C7H)(98)
2923	2809	2989	104.9	99.71	$\upsilon(C6H_2)$(98)
1669	1638	1764	9.8	44.41	R[υ(CC)(43)+δ(CHO)(23)+δ_a(5)+δ_{in}(CO)(5)+δ_{in}(C12H)(5)]
1633	1604	1724	42.9	52.10	R[υ(CC)(49)+δ(CHO)(16)+δ_{in}(C13H)(11)+δ_a(7)]
1583	1556	1660	1.7	13.93	Me2[(δ_a(34)+δ_a'(5)+ρ'(5))(CH_3)]+Me1[(δ_a(15)+δ_a'(14))(CH_3)]+Me3[(δ_a'(10)+δ_a(6))(CH_3)]
1573	1546	1656	12.7	5.87	Me3[$\delta_a(CH_3)$](43)+Me1[(δ_a(19)+δ_a'(14))(CH_3)+ρ(NH)(8)
1566	1540	1651	20.2	7.48	Me2[$\delta_a'(CH_3)$](49)+Me3[(δ_a'(23)+δ_a(6))(CH_3)]+Me1[$\delta_a'(CH_3)$](9)
1564	1538	1647	15.8	13.54	$\delta_{sc}(C17H_2)$(79)+$\delta_{sc}'(C17H_2)$(6)
1560	1533	1645	19.8	2.82	$\delta_{sc}(C6H_2)$(56)+Me1[$\delta_a(CH_3)$](18)+$\delta_{sc}(C17H_2)$(6)+Me1[$\delta_a'(CH_3)$](5)+Me2[δ_a(CH$_3$)](5)
1551	1525	1640	11.2	3.79	Me2[$\delta_a(CH_3)$](29)+$\delta_{sc}(C6H_2)$(28)+Me1[$\delta_a'(CH_3)$](18)+Me1[$\delta_a(CH_3)$](13)
1549	1523	1629	31.9	1.75	Me3[(δ_a'(32)+δ_a(21))(CH_3)+Me1[$\delta_a'(CH_3)$](22)+Me2[$\delta_a(CH_3)$](13)
1547	1521	1626	5.0	59.18	R[υ(CC)(41)+δ_{in}(C12H)(9)+δ_{in}(C17C)(9)+υ(CO2)(6)+δ(CHO)(5)]+ω($C17H_2$)(6)
1542	1517	1621	9.8	0.73	Me2[(δ_a'(35)+δ_a(5))(CH_3)]+Me3[(δ_a'(21)+δ_a(11))(CH_3)]+Me1[(δ_a(11)+δ_a'(6))(CH_3)]
1529	1504	1611	5.2	117.05	R[υ(CC)(24)+δ(CHO)(22)+δ_{in}(C16H)(19)+δ_{in}(C13H)(8)]+$\delta_{sc}(C17H_2)$(5)
1516	1492	1590	7.7	12.61	ρ(NH)(71)+Me1[$\delta_a(CH_3)$](7)
1468	1446	1560	1.7	14.25	Me2[$\delta_s(CH_3)$](38)+Me1[$\delta_s(CH_3)$](29)+Me3[$\delta_s(CH_3)$](24)
1447	1426	1537	6.3	31.85	R[υ(CC)(24)+δ_{in}(C13H)(18)+υ(CC)(11)+δ_{in}(C12H)(10)+δ(CHO)(6)+υ(CC17)(6)]
1444	1423	1536	4.8	25.91	Me2[$\delta_s(CH_3)$](52)+Me3[$\delta_s(CH_3)$](29)+Me1[$\delta_s(CH_3)$](10)

1443	1422	1533	2.3	18.09	Me1[$\delta_s(CH_3)$](50)+Me3[$\delta_s(CH_3)$](28)
1437	1416	1524	18.7	31.08	δ(CHO)(16)+ρ(CH)(15)+Me3[$\delta_s(CH_3)$](13)+(ω(10)+γ(6))($C6H_2$)+ρ'(CH)(10)+R[υ(C11C)](8)
1423	1402	1509	23.5	10.04	ω($C17H_2$) (60) +δ(CHO3) (15) +R[υ(CC17)](8)
1388	1369	1487	21.1	9.98	ω($C6H_2$)(53)+ρ'(CH)(22)+υ(CC)(5)
1354	1336	1443	16.7	0.31	ρ(CH)(36)+(ω(18)+γ(6))($C6H_2$)+ρ'(CH)(17)+δ(CHO)(7)
1345	1327	1407	12.1	22.81	R[υ(CC)](51)+δ_{in}(C16H)(9)+δ_{in}(C12H)(5)+δ_{in}(C17C)(5)]+ρ(CH)(6)
1315	1298	1396	6.3	1.13	R[υ(CC)(24)+δ_{in}(C12H)(16)+υ(CC17)(8)+δ_{in}(C13H)(5)]+ρ'(CH)(5)
1309	1293	1375	5.5	11.20	γ($C6H_2$)(16)+υ(C9C)(9)+υ(C5N)(7)+Me3[ρ'(CH_3)](6)+δ_{oop}(NC5C)(6)+Me1[ρ(CH_3)](5)+δ_{sc}(NH)(5)+R[δ_{in}(C12H)](5)
1298	1282	1363	3.1	112.87	R[υ(CO2(39)+δ_{trig}(13)+υ(CC)(13)+δ(CHO)(9)+δ_{in}(C13H)(6)]
1271	1256	1356	0.9	33.99	Me2[ρ(CH_3)](20)+υ(C8C)(19)+δ_{oop}(NC5C)(11)+Me3[ρ(CH_3)](10)+υ(C10C)(5)+ρ(NC5C)(5)
1263	1248	1350	4.5	46.31	δ(CHO3)(20)+R[υ(CC)(27)+δ_{trig}(7)+δ_{in}(C16H)(6)+υ(CC17)(5)]+ω($C17H_2$)(12)
1253	1238	1336	3.1	58.02	Me1[ρ'(CH_3)](17)+Me2[ρ'(CH_3)](16)+υ(C10C)(14)+δ_{oop}(NC5C)(15)+υ(C5N)(9)+γ($C6H_2$)(6)
1244	1230	1320	23.1	28.62	γ($C17H_2$)(57)+R[υ(CC)(7)+δ_{in}(C12H)(5)]+δ(CHO3)(6)
1240	1226	1303	6.4	8.88	ρ'(CH)(19)+γ($C17H_2$)(11)+γ($C6H_2$)(9)+ρ(CH)(7)+δ(CHO)(5)+R[υ(CC)](5)
1230	1216	1273	12.6	4.12	γ($C6H_2$)(26)+ρ(CH)(14)+δ(CHO)(10)+ρ(NH)(5)
1202	1188	1253	19.4	37.34	δ(CHO3)(18)+δ(CHO)(18)+R[δ_{in}(C16H)(8)+υ(CC)(8)+δ_{in}(C13H)(6)+υ(CC17)(6)]+ρ(CH)(8)
1178	1165	1240	5.8	23.32	R[υ(CC)(14)+δ_{in}(C16H)(14)+δ_{trig}(11)+υ(C11C)(10)+δ_{in}(C13H)(10)+δ_{in}(C12H)(7)]+δ(CHO)(7)
1139	1128	1205	4.6	58.92	R[υ(CC)(22)+δ_{trig}(12)+υ(CC17)(11)+δ_{in}(C12H)(11)+υ(C11C)(6)]+δ(CHO3)(7)+ρ($C17H_2$)(6)
1119	1108	1194	5.2	22.78	υ(C6N)(19)+Me2[ρ'(CH_3)](11)+ρ($C6H_2$)(9)+Me1[ρ'(CH_3)](9)+δ_{sc}(NH)(7)+Me3[ρ(CH_3)](7)+υ(CC)(5)+δ_{oop}(CH)(5)
1092	1082	1182	8.1	9.88	υ(C6N)(40)+υ(CC)(15)+ρ($C6H_2$)(11)+υ(C5N)(9)+δ_{oop}(CH)(5)
1074	1065	1151	8.3	3.01	Me3[(ρ'(34)+ρ(7))(CH_3)]+Me1[ρ(17)+ρ'(6))(CH_3)]+Me2[ρ(CH_3)](11)+υ(C6N)(5)
1058	1049	1150	6.2	31.53	Me2[ρ'(CH_3)](21)+Me1[ρ'(CH_3)](13)+υ(CC)(10)+υ(CO1)(9)+ρ($C6H_2$)(7)+υ(C6N)(6)+δ_{oop}(CH)(5)
1042	1033	1142	2.3	1.75	R[δ_{oop}(C13H)(23)+δ_{oop}(C16H)(11)+δ_{oop}(C12H)(5)+τ'$_a$(5)]+ρ($C17H_2$)(27)+υ(CO1)(5)
1039	1030	1132	1.4	5.82	R[δ_{oop}(C13H)(30)+δ_{oop}(C16H)(14)+Puck(14)]+ρ($C17H_2$)(9)+υ(CO1)(9)
1030	1022	1117	1.6	43.25	υ(CO1)(40)+ρ($C17H_2$)(16)+δ_{oop}(CH)(10)+δ_{sc}'($C6H_2$)(5)
1009	1001	1100	6.6	16.68	ρ($C6H_2$)(14)+υ(CC)(14)+υ(CO3)(9)+ρ($C17H_2$)(8)+R[υ(CC)](7)
998	991	1074	0.0	0.06	Me2[ρ(CH_3)](28)+Me1[ρ(CH_3)](25)+Me3[ρ(CH_3)](23)+Me1[ρ'(CH_3)](7)+Me3[ρ'(CH_3)](6)+Me2[ρ'(CH_3)](6)
983	976	1065	14.5	31.81	υ(CO3)(47)+R[δ_{oop}(C12H)](14)+υ(CC)(8)
955	949	1056	5.5	17.15	R[δ_{oop}(C12H)](43)+R[Puck](6)+υ(C9C)(6)
947	941	1005	8.9	9.18	R[δ_{oop}(C12H)](22)+υ(C9C)(17)+υ(C8C)(9)+ρ($C6H_2$)(7)+Me1[ρ(CH_3)](5)+Me3[ρ(CH_3)](5)
925	919	989	10.3	0.28	υ(C8C)(27)+υ(C10C)(20)+Me3[ρ'(CH_3)](10)+Me3[ρ(CH_3)](9)+Me2[ρ(CH_3)](8)+Me1[ρ'(CH_3)](5)
923	917	982	6.9	9.48	R[τ(CO)(11)+δ_{trig}(10)+δ_a(9)+υ(CC17)(9)+δ_{oop}(C12H)(8)]+υ(CO_3)(5)+υ(CC)(5)
912	906	977	5.9	2.97	υ(C5N)(25)+υ(C10C)(16)+Me2[ρ'(CH_3)](7)+Me1[ρ'(CH_3)](6)+υ(C8C)(6)+R[δ_{oop}(C16H)](6)

896	891	967	1.7	102.40	R[δ_{oop}(C16H)(36)+δ_{oop}(C13H)(17)+δ_{oop}(CO)(16)+τ_a(8)+Puck(6)]
889	884	877	5.2	95.97	R[τ(CO)](61)+υ(CO3)(12)
790	787	835	1.5	2.92	R[Puck(56)+δ_{oop}(CO)(18)+δ_{oop}(C17C)(9)+δ_{oop}(C11C)(6)]
784	781	795	11.9	17.80	R[υ(CC)(16)+υ(CO2)(15)+Puck(10)+δ_{trig}(6)+δ'_a(6)+υ(C11C)(6)+υ(CC17)(5)]
749	747	780	8.3	8.65	υ(C9C)(26)+υ(C10C)(22)+(δ(12)+δ_{sc}(9))(NH)+υ(C8C)(11)
743	741	776	7.4	11.24	R[δ'_a(12)+υ(C11C)(10)+δ_{trig}(7)+υ(CC)(6)+υ(CC17)(6)]+δ_{oop}(CH)(17)+δ_{sc}'($C17H_2$)(6)+δ(NH)(5)
700	699	725	5.9	91.68	δ(NH)(45)+υ(C5N)(12)+υ(C6N)(9)+δ_{sc}(NH)(7)+δ_{sc}'($C6H_2$)(5)
661	660	714	4.6	14.48	R[δ'_a(24)+δ_{oop}(C11C)(7)+τ_a(7)+δ_{in}(CO)(7)+δ_{oop}(C17C)(5)]+δ_{sc}'($C17H_2$)(18)
620	619	673	0.8	12.35	R[τ_a(19)+δ_{oop}(CO)(16)+δ_{oop}(C11C)(13)]+δ_{oop}(CH)(10)+δ_{sc}'($C17H_2$)(5)
562	562	611	2.1	18.23	δ_{oop}(CH)(28)+R[δ_a(14)+τ_a(7)+Puck(5)]
523	523	559	1.0	16.54	δ_{oop}(CH)(17)+ρ(NC5C)(16)+R[Puck(6)+τ_a(5)+δ_{oop}(CO)(5)]+δ_{sc}(NH)(14)
512	512	541	4.3	5.21	R[δ_{in}(CO)(10)+δ'_a(8)+δ_{oop}(CO)(8)+δ_{in}(C11C)(7)+Puck(7)+τ_a(7)+δ_{in}(C17C)(5)]+δ_{oop}(CH)(9)
482	482	531	2.3	9.13	R[τ'_a(45)+δ_{oop}(C17C)(22)+(δ_{in}(8)+δ_{oop}(5))(CO)]
468	468	498	2.2	4.58	δ_{oop}(NC5C)(40)+R[δ_{in}(CO)(11)+τ'_a(9)+δ'_a(6)]
448	448	476	0.9	7.24	(ρ'(49)+δ_{oop}(18))(NC5C)
438	439	473	1.8	2.92	R[δ_{in}(CO)(11)+Puck(7)+δ_{oop}(CO)(7)+δ_{oop}(C17C)(6)]+δ_{oop}(CH)(10)+(δ_{oop}(17)+ρ(5))(NC5C)
418	418	425	4.2	22.24	R[τ'_a(18)+δ_{in}(C17C)(7)+δ(CHO)(5)]+τ(CO3)(16)+δ_{sc}'($C17H_2$)(15)
401	402	418	1.3	3.35	δ_{oop}(NC5C)(26)+R[δ_a(14)+δ_{in}(CO)(6)+δ_{in}(C11C)(5)]+δ_{oop}(CH)(8)
366	367	392	2.5	3.40	δ_{oop}(NC5C)(34)+R[δ_{oop}(C11C)(6)+δ_a(6)]+δ_{oop}(CH)(6)
352	353	377	0.6	0.30	(δ_{oop}(50)+ρ'(26))(NC5C)
346	347	342	0.7	30.82	R[δ_{in}(C17C)](40)+δ_{sc}'($C17H_2$)(14)+τ(CO3)(9)+δ_{oop}(CH)(7)
337	338	332	7.7	46.07	(τ(49)+υ(5))(CO3)+δ_{sc}'($C17H_2$)(12)+R[τ(CO)](6)
308	309	314	1.1	11.43	(ρ(21)+δ_{oop}(11))(NC5C)+δ_{oop}(CH)(21) +R[τ_a](6)+υ(C6N)(5)
289	291	313	0.3	4.63	τ(C8C)(53)+R[τ_a(5)+δ_{oop}(C17C)(5)]+τ(C10C)(6)
288	289	297	1.4	7.91	R[δ_{oop}(C17C)(10)+τ_a(10)+δ_{oop}(C11C)(6)+δ_{in}(C17C)(5)]+τ(C8C)(11)+τ(C10C)(6)+δ_{oop}(CH)(6)+δ_{sc}'($C6H_2$)(5)
261	262	291	0.1	0.76	τ(C10C)(57)+τ(C9C)(28)
251	253	278	1.6	14.54	τ(C7C6)(16)+τ(C9C)(15)+τ(C10C)(13)+τ(CO1)(12)+τ(C8C)(11)+τ(C5N)(8)
235	236	240	6.7	120.90	τ(CO1)(71)+τ(C9C)(8)
211	213	218	1.2	8.30	τ(C9C)(21)+δ_{oop}(CH)(10)+τ(C7C6)(10)+δ_{sc}(NH)(8)+R[τ_a](5)
187	188	197	3.7	7.86	R[(τ(36)+δ_{oop}(16)+δ_{in}(9)(C17C))+τ_a(7)+δ_{oop}(C11C)(5)+τ'_a(5)]
173	174	187	0.8	4.31	R[δ_{in}(C11C)(33)+δ_{in}(C17C)(12)]+τ(C7C6)(10)+δ_{sc}'($C6H_2$)(8)
147	148	169	0.3	1.77	R[δ_{in}(C11C)(12)+τ_a(7)]+τ(C5N)(18)+τ(C9C)(15)+δ_{oop}(CH)(11)+τ(C7C6)(6)+τ(C10C)(5)
121	121	118	0.9	0.78	R[(τ(19)+δ_{in}(7))(C17C)+τ(CO)(19)+τ_a(12)+δ_{oop}(C11C)(5)]+δ_{oop}(CH)(13)+δ_{sc}'($C6H_2$)(5)+τ(C7C6)(5)
110	111	112	0.2	3.03	τ(C7C6)(21)+R[τ(C17C)(10)+τ(CO)(7)]+δ_{sc}'($C6H_2$)(15)+τ(C11C7)(7)+δ_{sc}(N)(6)
83	84	68	0.5	1.81	R[(τ (57)+δ_{in}(9))(C17C)+τ(CO)(14)]

53	54	52	1.5	1.97	τ(C11C7)(22)+τ(C6N)(21)+τ(C7C6)(14)+R[τ(CO)(6)+τ_a(5)]+δ(NH)(6)+τ(C5N)(6)
36	36	38	1.5	0.97	τ(C5N)(49)+τ(C9C)(16)+τ(C7C6)(11)+τ(C11C7)(8)
19	18	17	2.1	1.30	τ(C11C7)(47)+τ(C6N)(27)+δ_{oop}(CH)(7)+τ(C5N)(6)

Types of Vibration: υ: stretching, δ: deformation (bending), δ_{in}: in-plane bending, δ_{oop}: out-of-plane bending, ρ: rocking, τ: torsion, γ: scissoring, δ_a: deformation (asymmetric).

Aromatic Ring Vibrations

Salbutamol contains a substituted benzene ring, which shows characteristic vibrational bands. The C-H stretching vibrations were observed in the high-frequency region between 3078 cm^{-1} and 3094 cm^{-1}. The C-C ring stretching vibrations were identified in the mid-IR region, with prominent bands at 1604 cm^{-1} and 1504 cm^{-1}, in good agreement with experimental FT-IR data [10].

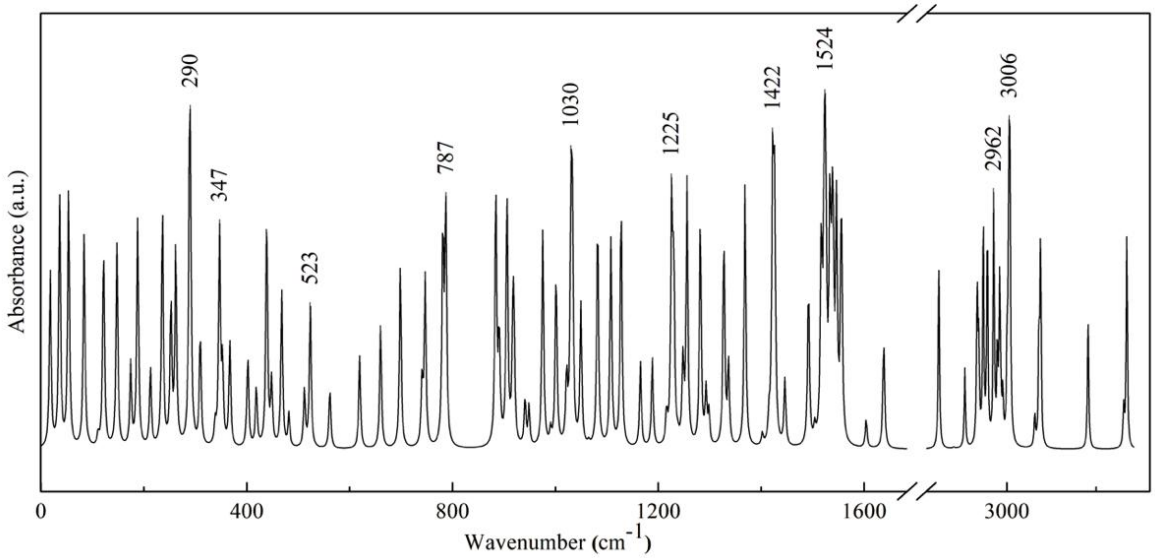

Fig. 3: FTIR Spectra of Salbutamol between 0-3400 cm^{-1} ranges at B3LYP/3-21G level.

Hydroxyl (-OH) Group Vibrations

The computed O-H stretching vibrations at 3336 cm^{-1} and 3327 cm^{-1} are in good agreement with the experimental FT-IR data reported by Ali et al. [10], who observed broad bands in the 3200-3600 cm^{-1} region indicative of hydrogen-bonded hydroxyl groups. The N-H stretch calculated at 3227 cm^{-1} also falls within the typical range for secondary amines and aligns with previous computational studies [12].

Methyl (-CH_3) Group Vibrations

The asymmetric and symmetric C-H stretching vibrations of the methyl groups were observed in the regions 2973-3008 cm^{-1} and 2916-2933 cm^{-1}, respectively. The corresponding deformation modes were found between 1523-1556 cm^{-1} (asymmetric) and 1422-1446 cm^{-1} (symmetric). These values are consistent with reported vibrations for aliphatic systems [17].

The low-frequency region (<500 cm^{-1}) is dominated by torsional motions and out-of-plane deformations, reflecting the molecular flexibility of the aliphatic side chain and ring substituents.

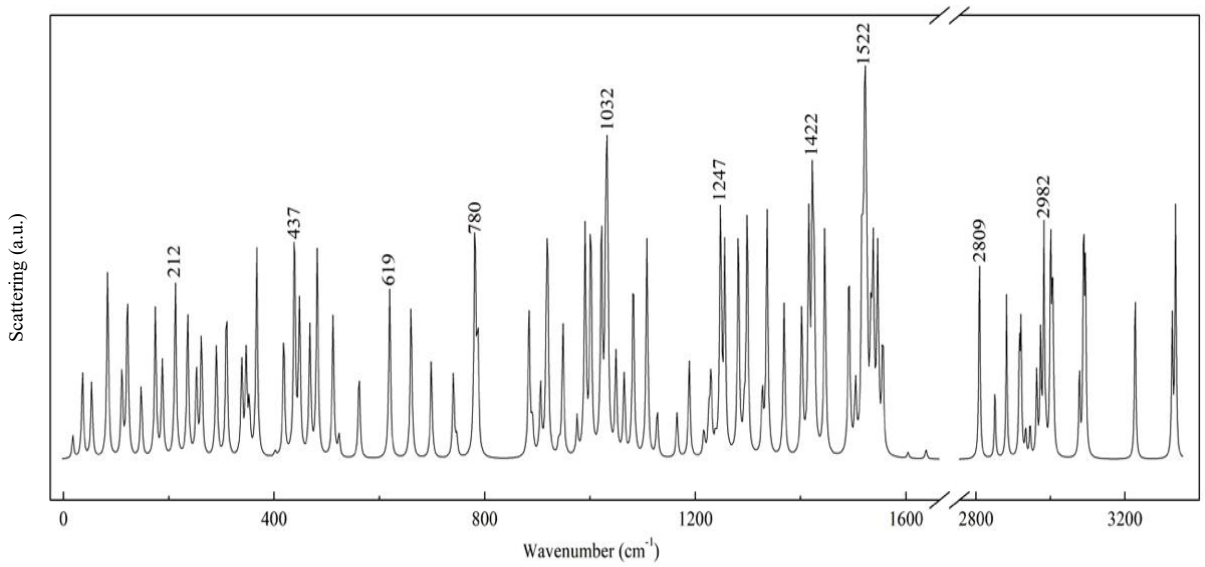

Fig. 4: Raman spectra plot of Salbutamol between the ranges 0-3400 cm^{-1} at B3LYP/3-21 G.

3.4 UV-Vis Spectral Analysis

From the table, it is clear that the main dipole transition occurs at 256 nm (H→L) with oscillator strength 0.040 and vertical excitation energy of 4.8 eV in the gas phase, whereas those values in water were 254 nm (H→L) with oscillator strength 0.044 and vertical excitation energy of 4.9 eV, and those values in ethanol occur at 254 nm (H→L) with oscillator strength 0.046 and vertical excitation energy of 4.9 eV as listed in Table 4.

Table 4: Calculated electronic properties (energy gap, absorption wavelengths, oscillatory strength and Dipole moments) of Salbutamol.

Phase	Transition states	Wavelength(nm)	Energy (eV)	Oscillator strength	Type of transition	Dipole moment
Gas	H→L	256	4.8	0.040	$\pi \rightarrow \pi^*$	3.882
	H-1→L	228	5.4	0.015		
	H→L+1	223	5.6	0.038		
Water	H→L	254	4.9	0.044		4.231
	H-1→L	240	5.2	0.003		
	H→L+1	225	5.5	0.074		
Ethanol	H→L	254	4.9	0.046		4.176
	H-1→L	239	5.2	0.025		
	H→L+1	224	5.5	0.081		

The HOMO-LUMO plots corresponding to H→L in gaseous, water, and ethanol phases are represented in Fig. 5. The energy difference ($\Delta E_g = E_{LUMO} - E_{HOMO}$) between the two molecular orbitals was 5.53 eV, 5.59 eV, and 5.59 eV, respectively, in the gas, water, and ethanol phases. The main electronic transition in the title molecule was found to be form π→ π*. The optimized (gas-phase) Salbutamol molecule has a computed dipole moment of 3.2035 D, indicating moderate molecular polarity. In contrast, the dipole moments calculated in solvent are larger (Table 4 shows 3.882 D in gas, 4.231 D in water, and 4.176 D in ethanol). This increase in the dipole moment in water and ethanol reflects enhanced polarization of the molecule in a polar environment - the solvent stabilizes charge separation, increasing the overall dipole moment in solution suggests stronger interactions with polar media or receptors. The difference between the optimized-structure value (3.2035 D) and the gas-phase value (3.8816 D) arises from calculation conditions and demonstrates consistency in the trend of polarity. polarity of Salbutamol. In practical terms, a higher The UV absorption plot of Salbutamol in the gas phase shows one distinct peak, indicating specific electronic transitions within the molecule.

The most significant peak at 191 nm, represents the primary electronic transition with the highest probability and energy absorption. The UV absorption plot of Salbutamol in a water solvent displays one key absorption peak at 190.4 nm, indicating electronic transitions within the Salbutamol molecule. The UV plot of Salbutamol in ethanol also shows one distinct absorbance peak. The most prominent peak is at 191 nm.

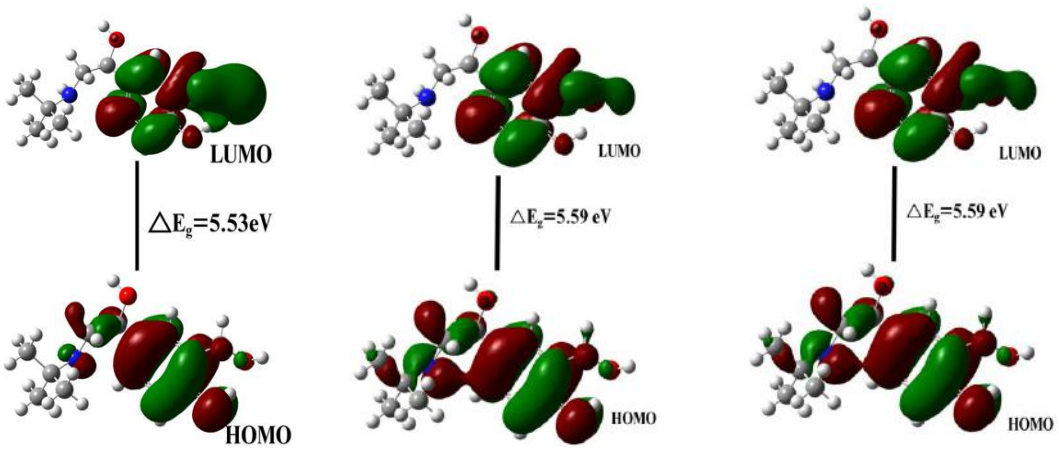

Fig. 5: HOMO-LUMO plot of Salbutamol in gas, water and ethanol respectively.

3.5 Molecular Electrostatic potential (MEP) Surface

The Molecular Electrostatic Potential (MEP) provides a visual representation of the charge distribution within a molecule, which is essential for understanding electrophilic and nucleophilic reactivity. Mathematically, the MEP at a point r in the space around a molecule (in atomic units) can be expressed as [26]:

$$V(r) = \sum_A \frac{z_A}{|\vec{R}_A - \vec{r}|} - \int \frac{\rho(\vec{r_1}')dr'}{|r' - r|}$$

In the present study, the MEP surface of Salbutamol was generated using the optimized geometry obtained at the DFT/B3LYP level with the 3-21 basis set. The MEP is color-mapped onto the molecular van der Waals surface, where red indicates regions of most negative electrostatic potential (attractive to electrophiles), and blue represents most positive potential (attractive to nucleophiles), with green showing regions of neutral potential. The visualized MEP surface of Salbutamol (Fig. 6 left) shows that, red regions are concentrated around the hydroxyl (-OH) groups and oxygen atoms, indicating electron rich sites that are prone to electrophilic attack. Blue regions are primarily located near hydrogen atoms attached to the aromatic ring and amine group, suggesting electron deficient sites favorable for nucleophilic interactions. Green zones, representing areas of zero potential, are generally seen over the non-polar regions such as methyl groups and hydrocarbon chains. The contour plot in Fig. 6(right) offers a detailed two-dimensional perspective on the molecular electrostatic potential (MEP) distribution of Salbutamol. Contour lines, each representing a constant value of electrostatic potential, allow for precise identification of regions with similar electronic character across the molecular surface. Closely spaced contour lines indicate rapid changes in potential, often found adjacent to highly electronegative atoms such as oxygen, while wider spacing suggests more gradually varying regions, typical of non-polar groups like methyl or hydrocarbon chains.

3.6 ADMET Property Analysis

In this section, we present the ADMET (Absorption, Distribution, Metabolism, Excretion, and Toxicity) profile of Salbutamol, predicted using the SwissADME and pkCSM web tools. These in silico assessments are essential for early-stage evaluation of pharmacokinetic behavior and safety.

Salbutamol's drug-likeness was first evaluated against Lipinski's "Rule of Five", which stipulates that, for good oral bioavailability. As shown in Table 5, Salbutamol (MW = 239.31 g/mol; H-bond donors = 4; acceptors = 4; rotatable bonds = 5; WLogP = 0.83) violates none of these criteria, confirming its compliance with Lipinski's guidelines. Salbutamol's LD_{50} was predicted as 2.395 mol/kg (~573 g/kg), placing it well above 5000 mg/kg; thus, it falls into Class VI (non-toxic) upon oral administration [27]. Passive gastrointestinal absorption (HIA) and blood-brain barrier (BBB) permeation were assessed using the BOILED-Egg model on SwissADME. Salbutamol (TPSA = 72.72 Å²; WLogP = 0.83) lies squarely within the white region (high HIA) but outside the yolk (limited BBB permeation), and is colored red (non-P-gp substrate), indicating favorable oral absorption and negligible brain entry (Fig. 7).

The bioavailability radar further highlights Salbutamol's pharmacokinetic fitness by overlaying six physicochemical descriptors (lipophilicity, size, polarity, solubility, flexibility, saturation) against optimal ranges. All parameters fall within the "pink" optimal polygon, and its bioavailability score of 0.55 confirms good overall oral bioavailability.

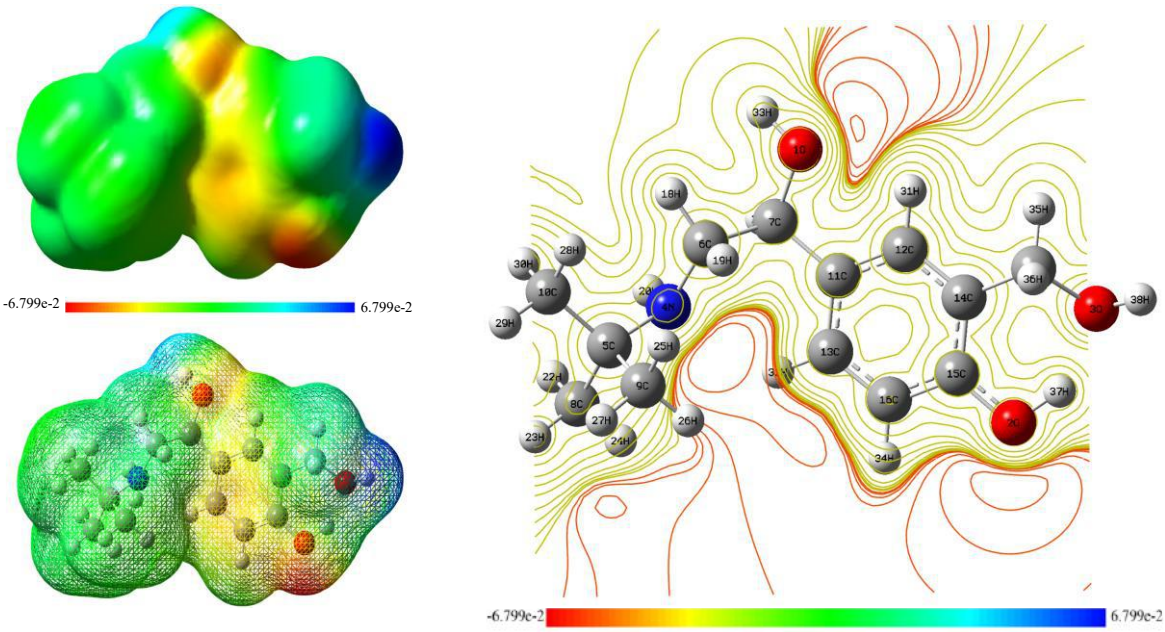

Fig. 6: (a) Molecular electrostatic potential map, and (b) Contour plot of molecular electrostatic potential surface of Salbutamol.

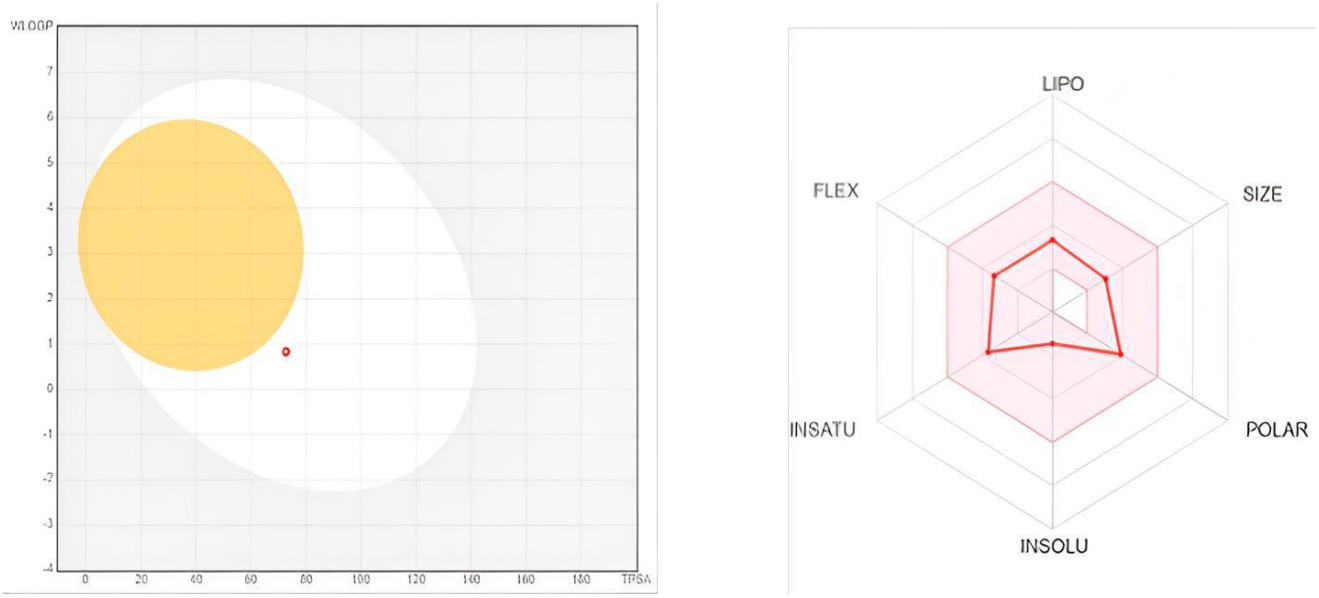

Fig. 7: Swiss ADME boiled egg model and bioavailability radar chart for Salbutamol.

Table 5: The different ADMET parameters for Salbutamol.

Parameters	Value	Parameters	Value
Molecular weight(g/mol)	239.31	Lipophilicity (WlogP)	0.83
Rotatable bond	5	Water solubility (logS)	-1.45
Hydrogen bond acceptor	4	Permeability coefficients (log Kp cm/s)	-7.54
Hydrogen bond donor	4	Lipinski violations	0
Topological polar surface area ($Å^2$)	72.72	GI absorption	High
Molar refractivity	67.60	Synthetic accessibility	2.30

Blood brain-barrier permeate	No	Bioavailability score	0.55
P-glycoprotein substrate	No	Lethal Dose (LD 50)	2.395l/kg

3.7 Molecular Docking

Molecular docking studies were performed to predict the binding mode and affinity of Salbutamol with the human β_2-adrenergic receptor (PDB ID: 3NY8). Blind docking using SwissDock generated 20 potential binding modes. The top-ranked pose, with a calculated binding affinity of -7.545 kcal/mol, indicated the most favorable interaction. The full list of binding affinities for all clusters is provided in Table 6.

Table 6: Calculated Binding Affinities (kcal/mol) of Salbutamol β_2 Adrenergic Receptor Complex Obtained from SwissDock.

Model	Calculated affinity (kcal/mol)	Model	Calculated affinity (kcal/mol)	Model	Calculated affinity (kcal/mol)
1	-7.545	8	-6.519	15	-6.186
2	-7.058	9	-6.411	16	-6.137
3	-6.730	10	-6.407	17	-5.989
4	-6.599	11	-6.393	18	-5.862
5	-6.552	12	-6.310	19	-5.823
6	-6.541	13	-6.293	20	-5.729
7	-6.519	14	-6.223		

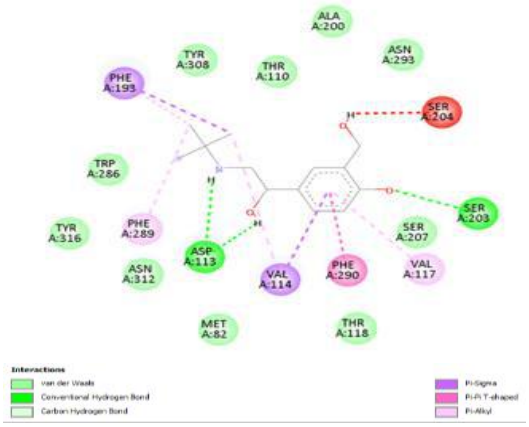

Fig. 8: 2D- ligand interaction diagram of Salbutamol with 3NY8.

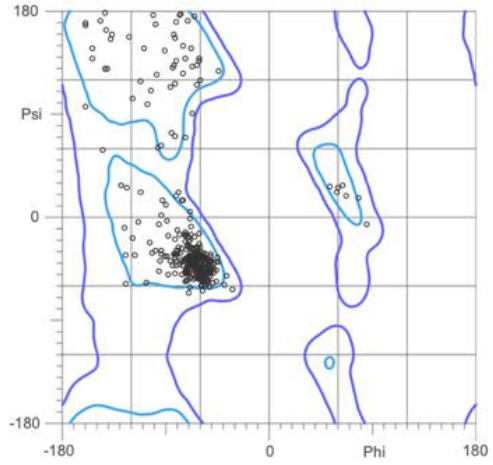

Fig. 9: Ramachandran plot of protein 3NY8.

The visualization of the ligand-receptor complex was performed using BIOVIA Discovery Studio Visualizer, which revealed significant hydrogen bonding and hydrophobic contacts within the binding cavity. The 2D interaction diagram (Fig. 8) shows that Salbutamol forms multiple hydrogen bonds with key residues in the receptor, which are crucial for stability and activity. The 3D docked structures (Fig. 10) illustrate how Salbutamol is situated within the hydrophobic pocket of the protein, aligned along the active site groove and stabilized by non-covalent interactions.

To assess the conformational quality of the protein structure, a Ramachandran plot was generated using MolProbity, which demonstrated that most residues lie within the allowed and favored regions, suggesting the receptor is sterically stable and suitable for docking. The plot is shown in Fig. 9.

The observed binding mode is consistent with the electronic properties revealed by the MEP and Mulliken charge analyses. The hydrogen bond formation with ASP113 and ASN312 involves the positively charged hydrogen atoms of the protonated amine and hydroxyl groups, which were identified as strong hydrogen bond donors (high positive Mulliken charges on H20, H37, H38). Furthermore, the electron-

rich oxygen atoms (O1, O2, O3), which showed highly negative MEP regions, are positioned to act as hydrogen bond acceptors with surrounding water molecules or protein residues not visible in the docking pose.

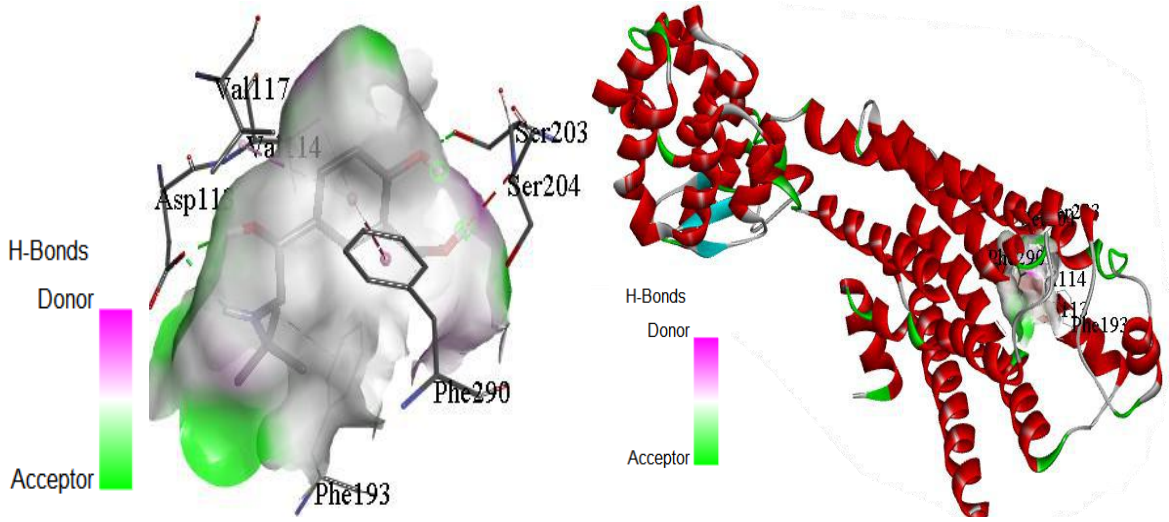

Fig. 10: Docked 3D structure showing binding pocket and with receptor binding pocket in terms of H-bond.

4. CONCLUSION

This study provides a comprehensive computational profile of Salbutamol by integrating DFT and molecular docking analyses. The optimized molecular geometry confirms the expected structural features, while the vibrational assignments, including key O-H, N-H, and C-H stretches, are consistent with literature and confirm the reliability of the computational model. Electronic property analysis revealed a HOMO-LUMO gap of 5.53 eV, indicating moderate chemical stability, and a significant increase in dipole moment in polar solvents, highlighting its solvation behavior. Crucially, molecular docking with the β_2-adrenergic receptor (3NY8) yielded a strong binding affinity (-7.545 kcal/mol), rationalizing its pharmacological activity. The binding pose shows critical interactions: hydrogen bonds with ASP113 and ASN312, and hydrophobic contacts with VAL114, VAL117, and PHE290. A clear structure-activity relationship for salbutamol is established by integrating these data from molecular structure and electronic distribution to receptor binding. This provides important insights for the logical design of new and more potent β_2-agonist medications.

AUTHOR CONTRIBUTION

D. Joshi: Writing-original draft, Investigation, and Formal analysis; B.D. Joshi: Methodology, Writing-review and Editing, Conceptualization, and Supervision.

CONFLICTS OF INTEREST

There are no conflicts to declare.

ACKNOWLEDGEMENTS

Authors acknowledge to Siddhanath Science Campus for providing lab facility and Prof. Poonam Tandon, Deen Dayal Gorakhpur University, Gorakhpur, India for providing Gaussian software.

REFERENCES

[1] L. Marques, N. Vale, Salbutamol in the management of asthma: A review, *International Journal of Molecular Sciences*, **23** (2022) 14207. https://doi.org/10.3390/ijms232214207

[2] J.P. Beale, N.C. Stephenson, A structural study of a pyridine inclusion compound of bis (dimethyl-o-thiolophenylarsine) palladium (II), *Structural Science*, **28** (1972) 557-60. https://doi.org/10.1107/S0567740872002742

[3] I.P. Hall, Bronchohdilators, Beta Agonists, Encyclopedia of Respiratory Medicine, Academic Press, (2022), 288-292, ISBN 9780123708793

[4] L.E. Martin, J.C. Hobson, J.A. Page, C. Harrison, Metabolic studies of salbutamol-3H: A new bronchodilator, in rat, rabbit, dog and man. *European Journal of Pharmacology*, **14** (1971) 183-99, 183-199. https://doi.org/10.1016/0014-2999(71)90211-1

[5] A.E. Tribe, R.M. Wong, J.S. Robinson, A controlled trial of intravenous salbutamol and aminophylline in acute asthma, *Medical Journal of Australia*, **2** (1976) 749-52. https://doi.org/10.5694/j.1326-5377.1976.tb128275.x

[6] W. MacNee, N.J. Douglas, M.F. Sudlow, Effects of inhalation of beta-sympathomimetic and atropine-like drugs on airway calibre in normal subjects, *Clinical Science*, **63** (1982) 137-43. https://doi.org/10.1042/cs0630137

[7] F. Riedel, H. von der Hart, Variable response to inhaled salbutamol of different lung function parameters in healthy children, *Lung*, **164** (1986) 333-8. https://doi.org/10.1007/BF02713658

[8] C.A. Sorbini, V. Grassi, C. Tantucci, L. Corea, M. Bentivoglio, P. Verdecchia, M. Motolese, Ventilatory effects of selective beta 1-(prenalterol) or beta 2-(salbutamol) adrenoceptor agonism in man, *International Journal of Clinical Pharmacology, Therapy, and Toxicology*, **22** (1984) 570-5 .https://pubmed.ncbi.nlm.nih.gov/6150902

[9] H. Allen, S.H. Backhouse, J.H. Hull, O.J. Price, Anti-Doping policy, therapeutic use exemption and medication use in athletes with asthma: a narrative review and critical appraisal of current regulations, Sports *Medicine*, **49** (2019) 659-68. https://doi.org/10.1007/s40279-019-01075-z

[10] H.R. Ali, H.G. Edwards, J. Kendrick, I.J. Scowen, Vibrational spectroscopic study of salbutamol hemisulphate, *Drug testing and analysis*, **1**(2009) 51-6. https://doi.org/10.1002/dta.8

[11] S. Bandaru, G. Tiwari, J. Akka, V. Kumar Marri, M. Alvala, Ravi V. Gutlapalli, A. Nayarisseri, H. Prasad Mundluru, Identification of high affinity bioactive Salbutamol conformer directed against mutated (Thr164Ile) beta 2 adrenergic receptor, *Current topics in medicinal chemistry,* **15** (2015) 50-6. https://doi.org/10.2174/1568026615666150112113040

[12] R. Omer, P. Koparır, L. Ahmed, M. Koparır, Computational determination the reactivity of salbutamol and propranolol drugs, *Turkish Computational and Theoretical Chemistry,* **4** (2020) 67-75. https://doi.org/10.33435/tcandtc.768758

[13] A.J. Al-Ani, P.M. Szell, Z. Rehman, H. Blade, H.P. Wheatcroft, L.P. Hughes, S.P. Brown, C.C. Wilson, Combining X-ray and NMR Crystallography to Explore the Crystallographic Disorder in Salbutamol Oxalate, *Crystal Growth & Design*, **22** (2022) 4696-707. https://doi.org/10.1021/acs.cgd.1c01093

[14] T. Zhao, Z. Liu, J. Niu, B. Lv, Y. Xiao, Y. Li, Investigation of the interaction mechanism between salbutamol a human serum albumin by multispectroscopic and molecular docking, *BioMed Research International*, **1** (2020) 1693602. https://doi.org/10.1155/2020/1693602

[15] H.E. Pence, A. Williams, ChemSpider: an online chemical information resource, Journal of Chemical Education, 87(2010) 1123-1124. https://doi.org/10.1021/ed100697w

[16] C. Lee, W. Yang, R.G. Parr, Development of the Colle-Salvetti correlation-energy formula into a functional of the electron density, *Physical Review B*, **37** (1988) 785. https://doi.org/10.1103/PhysRevB.37.785R

[17] B.D. Joshi, J.B. Khadka, A. Bhatt, Structure, electronic and vibrational study of 7-methyl-2, 3-dihydro-(1, 3) thiazolo (3, 2-a) pyrimidin-5-one by using density functional theory. *Journal of Institute of Science and Technology*, 22(2018) 1-11. https://doi.org/10.3126/jist.v22i2.19589\

[18] P. Pulay, G. Fogarasi, F. Pang, J.E. Boggs, Systematic ab initio gradient calculation of molecular geometries, force constants, and dipole moment derivatives, *Journal of the American Chemical Society*, **101** (1979) 2550-60. https://doi.org/10.1021/ja00504a009

[19] G. Fogarasi, X. Zhou, P.W. Taylor, P. Pulay, The calculation of ab initio molecular geometries: efficient optimization by natural internal coordinates and empirical correction by offset forces, *Journal of the American Chemical Society*, **114** (1992) 8191-201. https://doi.org/10.1021/ja00047a032

[20] A.J. Frisch, A.B. Nielson, A.J. Holder, GaussView user manual, Gaussian Inc., Pittsburgh, PA, (2000) 556.

[21] H. Yoshida, K. Takeda, J. Okamura, A. Ehara, H. Matsuura, A new approach to vibrational analysis of large molecules by density functional theory: wavenumber-linear scaling method, *The Journal of Physical Chemistry A*, **106** (2002) 3580-6. https://doi.org/10.1021/jp013084m

[22] M.E. Casida, K.C Casida, D.R. Salahub, Excited-state potential energy curves from time-dependent density-functional theory: A cross section of formaldehyde's 1A1 manifold, *International Journal of Quantum Chemistry*, **70** (1998) 933-41. https://doi.org/10.1002/(SICI)1097-461X(1998)70:4/5<933::AID-QUA39>3.0.CO;2-Z

[23] O. Trott, A.J. Olson, AutoDock Vina: improving the speed and accuracy of docking with a new scoring function, efficient optimization, and multithreading. *Journal of computational chemistry,* **31** (2010) 455-61. https://doi.org/10.1002/jcc.21334

[24] G.M. Morris, R. Huey, W. Lindstrom, M.F. Sanner, R.K. Belew, D.S. Goodsell, A.J. Olson, AutoDock4 and AutoDockTools4: Automated docking with selective receptor flexibility, Journal of computational chemistry, **30** (2009) 2785-91. https://doi.org/10.1002/jcc.21256

[25] M. Bugnon, U.F. Röhrig, M. Goullieux, M.A. Perez, A. Daina, O. Michielin, V. Zoete, SwissDock 2024: major enhancements for small-molecule docking with AttractingCavities and AutoDock Vina, *Nucleic acids research,* **52** (2024) 324-32. https://doi.org/10.1093/nar/gkae300

[26] R. Parthasarathi, V. Subramanian, P.K. Chattaraj, Effect of electric field on the global and local reactivity indices, *Chemical Physics Letters*, **382** (2003) 48-56. https://doi.org/10.1016/j.cplett.2003.09.160

[27] A. Daina, O. Michielin, V. Zoete, SwissADME: a free web tool to evaluate pharmacokinetics, drug-likeness and medicinal chemistry friendliness of small molecules, *Scientific Reports*, **7** (2017) 42717. https://doi.org/10.1038/srep42717

Ethnobotanical Study of Wild Plant Species Used by Local People of Bhageshwor Rural Municipality, Dadeldhura, Nepal

Gajendra Prasad Chataut

Nepalese Army Institute of Health Sciences, Sanobharyang, Kathmandu, Nepal

Research Article

ISSN: 3059-9504 (online)
DOI: https://doi.org/10.3136/ajs.v2i1.87745

Article History

Received: September 22, 2025; Revised: October 25, 2025; Accepted: October 28, 2025 Published: December 25, 2025

Keywords

Conservation, Dadeldhura, Ethnobotany, Interview, Semi-structured

Corresponding Author

Email: gagendrachataut73@gmail.com (GP Chataut)

ABSTRACT

Ethnobotany is a science that integrates society and plants, contributing to biodiversity conservation strategy of a country. The study aims to document the ethnobotanical knowledge of wild plant species in Bhageshwor Rural Municipality, Dadeldhura. This study was conducted from October 2023 to October 2024 for data collection through interviews, group discussions with key informants or local knowledgeable individuals (N=200), and semi-structured and open-ended questionnaires, as well as field visits to adjoining villages, using participatory observations. A total of 70 wild plant species with 65 genera and 40 families are recorded, among them 65 species are native while remaining five are invasive alien species. Local people use 28 species (40%) for food and fodder and only two species were used as timber. The ethnobotanical study of wild plant species shows the cultural, heritage and social values of respective plants. So, large number of research works may be helpful for the exploration and conservation of wild plant species; therefore, local governments should manage and document the local wild plant species through ethnobotany.

1. INTRODUCTION

The term ethnobotany was coined by American botanist John William Harshberger at the University of Pennsylvania in 1895. Ethnobotany refers to the study of the interrelationship between plants and people, transmitted many generations through cultural practices and traditional knowledge. Since ancient times communities has utilized plants for various purposes including food, fodder, furniture, medicine, clothing, fabrics, crafts, soaps, detergents, dyes, chemicals, and building materials [1, 2]. Traditional medical knowledge held by the elder members of the community is primarily transmitted orally across generations. This valuable knowledge must be [systematically recorded, explored, and preserved for the benefit of human health [3]. In terms of medicine and treatment, the local older adults have a great experience and knowledge about their surrounding local plants used to cure ailments that were once prevalent in a particular area [4] but are currently decreasing in ethnobotanical uses due to the modernization and the loss of local knowledge [5]. The practice of use of ethnobotanical knowledge is widespread; a total of 136 medicinal plant species [6]. Similarly, in Tripura, India, documented that 113 medicinal plants from 56 families are used in the healthcare systems of human beings [7].

Nepal occupies about 0.1% of the Earth's land surface, which consists of approximately 1762 medicinal and aromatic plants among these medicinal plants *Centella asiatica* was used dominantly. However, their use was found to be high in the mid-hills and mountain regions of Nepal [8]. The species richness of medicinal plants decreased with increasing altitude, but use intensity increased with altitude in Nepal [9]. Medicinal plants are a subset of plants that have a significant role in the healthcare system, such as the treatment of various diseases of human beings, such as gastrointestinal, parasitic, and hepatobiliary ailments, followed by those involving the blood and lymphatic systems [6, 10]. Non-timber forest products (NTFPs) of the Parche community of the Madi rural Municipality, presented within the Annapurna Conservation Area of Kaski, Nepal, were primarily utilized for medicinal purposes, accounting for 67.64% followed by vegetables of 11.67%, commercialization of 5.88%, and fruits of 8.82%, while insecticides accounted for 5.88% [11]. The Far-Western region of Nepal is rich in plant diversity; some of these plants have medicinal properties for human beings [12, 13]. According to Joshi et al., total 76 plants were used by the local people of the Api Nampa conservation area in Darchula, far-western Nepal, for healthcare services and cosmetic purposes among women [14]. Medicinal and aromatic plants have various roles in the improvement of the livelihood of local people, so

developing the knowledge about the sustainable use of their properties is essential for the conservation of biodiversity [15]. Plants have various uses, but overexploitation and unsustainable use, as well as the destruction of natural resources, have been contributing to the decline of biodiversity [16]. Hence, ethnobotanical knowledge is essential for the primary healthcare of local people and a source of economic improvement. Therefore, conservation and management of traditional knowledge should be integrated with scientific processing. This study seeks to document the ethnobotanical knowledge of wild plant species in Bhageshwor Rural Municipality, Dadeldhura, Nepal, contributing to the preservation of both cultural heritage and biodiversity.

2. MATERIALS AND METHODS

2.1 Study area

Dadeldhura District is a beautiful hill station of Sudurpashim Province, Nepal, covering an area of 1,538 km² and geographically ranging from tropical to temperate regions, consisting of seven local levels. The geographic coordination of the district lies between 28.59° to 29.26°, latitude 80.12° to 80.47°, and elevation ranges from 462 to 2639 m. The study was conducted in Bhageshwor Rural Municipality, Dadeldhura, Sudurpashim Province, Nepal [Fig. 1]. The Rural Municipality is one of the local levels of Dadeldhura District, consisting of five wards and situated 14 km away West from headquarter Khalanga, Dadeldhura. The Rural Municipality covers 233.38 Km^2 areas and consists of 13132 human populations (Population census survey, 2078 B.S.). The major ethnic groups are Brahmin, Chhetri, Sarki, Kami, Damai, Tamata, and the major religions are Hinduism and Buddhism; however, the languages of communication are Doteli and Nepali. The study area is located in the subtropical region of Nepal, characterized by a moderate climate, with hot summers and cold winters. The vegetation dominantly consists of *Pinus roxburghii* forest with associated species *Alnus nepalensis*, *Rhododendron arborium, Terminalia alata, Indigofera heterantha, Syzygium cumini, Rubus elepticus, Berberis aristata,* and *Myrica esculenta.*

2.2 Data collection and data analysis

The study was carried out during October 2023 to October 2024. Ethnobotanical knowledge on plants and plant parts used by local people was collected by interviewing key informants using frequent field visits in the adjoining five villages (Kurnayal, Bagarkot, Adungra, Chulla, Bogata) by participatory observations, group discussion, and interviews with local knowledgeable people (total 200) through semi-structured and open-ended questionnaires about the uses of wild plants. Plant specimens of the study area were collected, and all information about the plants, such as distribution, habitats, and plant status, was noted. Identification of plant species is facilitated through the use of relevant literatures [17-21]. Data entry and calculation were done by using Microsoft Excel 2016.

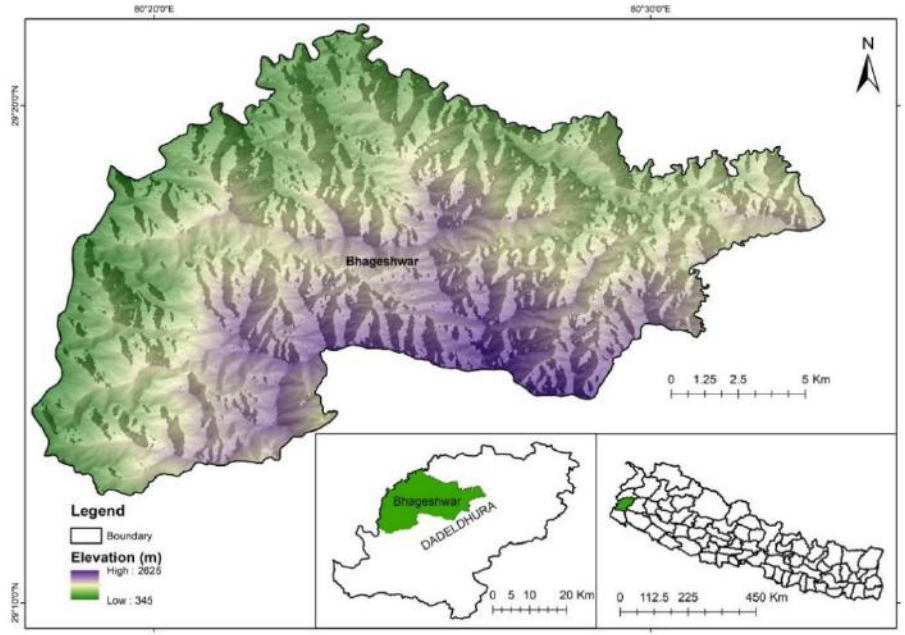

Fig. 1. Map of the study area showing the sampling locations in Bhageshwor Rural Municipality, Dadeldhura, Nepal.

3. RESULT AND DISCUSSION

In this study, a total of 70 wild vascular plant species were documented, representing 65 genera and 40 families. Of these species, 68 (97%) were angiosperms comprising 60 dicots and 7 monocots while one (1.5%) was a gymnosperm (*Pinus roxburghii*), and another one species (1.5%) was a pteridophyte (*Dryopteris cochleata*). These findings are consistent with [22], who recorded the 54 ethno-medicinal wild plant species belonging to 29 families and 44 genera in the Tharu community of Parsa District, Nepal. In terms of growth habit trees species were the most prevalent, accounting for 27 species (38%) followed by shrubs 18 species (26%), herbs each with 18 species (26%) and climbers with 7 species (10%) (Fig.2a). This pattern is consistent with findings from a previous study [23]; herbaceous plants were the most abundant with 179 (57%) species. These were followed by shrubs with 64 species (21%), trees with 44 species (14%), and climbers with 25 species (8%). Among the recorded families, Asteraceae was the most dominant, comprising six species, followed by Moraceae with five species. Rosaceae and Poaceae each contributed four species, while Fabaceae and Phyllanthaceae included three species

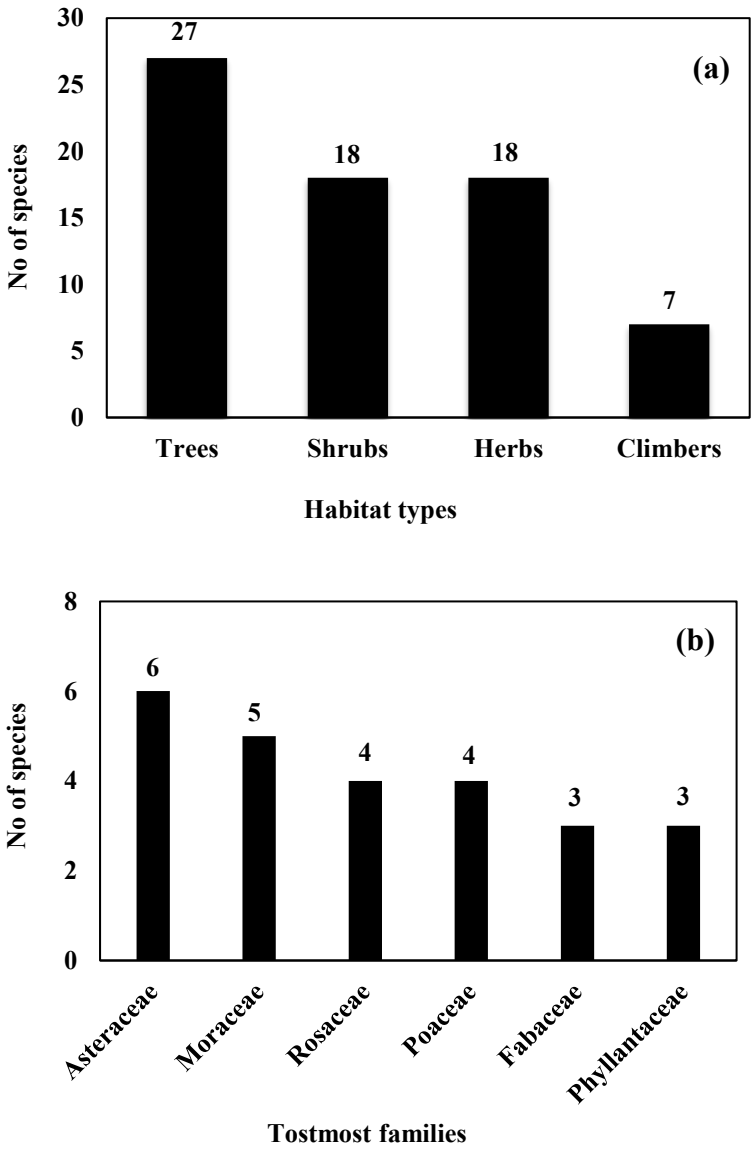

Fig. 2: (a) Different habitat forms; herbs, shrubs, trees, and climbers present in the study area, (b) topmost families present in the study area.

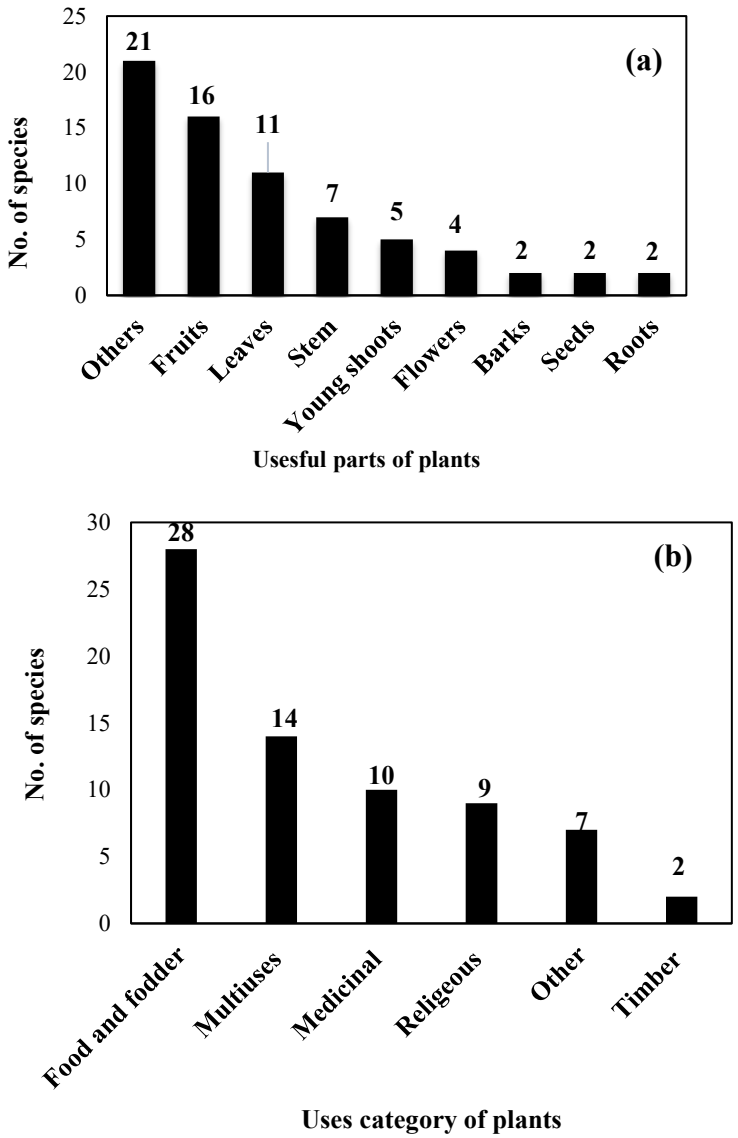

Fig. 3: (a) Number of species in reference to the used parts of plants and, (b) the uses category of the plants.

each (Fig. 2b), consistent with findings from [5]. Of the total species, five species (8%) were identified as invasive. Despite their invasive nature, local communities utilized these plants for medicinal and fodder purposes. For instance, *Ageratina adenophora*, *Ageratum conyzoides*, and *Ageratum houstonianum* were commonly applied to treat cut wounds, while *Bidens pilosa* and *Oxalis latifolia* served as fodder, similar to native species. Likewise, 108 weed species were used medicinally by local people in the Kanchanpur district of Nepal [13].

Regarding ethnobotanical uses, local communities in the study area utilized plant species for various purposes. The most common use was for food and fodder, accounting for 28 species (40%), followed by multi-purpose use with 14 species (20%), medicinal use with 10 species (14%), religious purposes with 9 species (13%), and timber with 2 species (3%) (Fig. 3a). Additionally, 7 species (10%) were used for other purposes such as making rope, using leaves as bedding for domestic animals, and using stems to prepare mats. These uses were grouped under the "other" category. These findings align with Anwar et al. [24], who recorded that leaves were used as medicine for the treatment of human being.

Medicinal plants exhibited a wide range of useful parts. Indigenous people of the Bhageshwor area primarily used fruits from 16 species (23%), leaves from 11 species (16%), stems from 7 species (10%), young shoots from 5 species (7%), flowers from 4 species (6%), bark, seeds, and roots from 2 species each (3%). The remaining 21 species (31%) had multiple useful parts, including combinations such as whole plant, stem and leaves, flowers and young roots, or leaves and bark, which were categorized under "other" (Fig. 3b). Similarly, in the Wana District of Pakistan, leaves were reported as the most commonly used plant part for medicinal purposes by local communities [25].

4. CONCLUSIONS

This study documents a total of 70 wild vascular plant species, with the highest number (28 species) used for food and fodder purposes. This was followed by 14 multi-use species, 10 medicinal species, nine species used for religious purposes, seven categorized under other uses, and two timber species. While plants offer a variety of useful parts, the findings indicate that fruits are the most commonly utilized, whereas bark, seeds, and roots are among the least used. The Dadeldhura district is notably rich in plant diversity and holds extensive ethnobotanical knowledge within its local communities. However, research in this region remains limited. Therefore, further studies should be conducted across other local administrative levels to support the exploration and conservation of indigenous plant species, contributing to both ecological preservation and the sustainable development of the nation.

AUTHOR CONTRIBUTINS

All the works were carried by G, Chataut.

CONFLICT OF INTEREST

There no conflicts to declare.

ACKNOWLEDGMENTS

The author acknowledges Mrs. Sarita Paneru help during data collection from the field, and thanks Mr. Rosan Babu Adhikari for grant support during the writing of the manuscript, and Basu Dev Poudel for the preparation of the map of the study area.

REFERENCES

[1] M. Anwar, N. Akhtar, Quantitative ethnobotanical assessment of plant resources of District Swabi, Khyber Pakhtunkhwa, Pakistan, Ethnobotany Research and Applications, **31**(28) (2025) 1-22. https://doi.org/10.32859/era.31.28.1-22.

[2] S.K. Singhariya, An introduction to ethnobotany, concept, history, importance, and scope, International Journal of Novel Research and Development, **8** (10) (2023) 391 397.

[3] N. Chavda, R. Rathore, N. Solanki, An overview of the historical background of ethnobotany and the indigenous culture of India, International Journal of Creative Research Thoughts, **10** (2022) 738-751.

[4] Sushila, A brief overview of the origins of ethnobotany and India's indigenous culture, International Journal of Multidisciplinary Research and Development, **9** (7) (2022) 127-132.

[5] C. Dhar, M. Bhagawati, B. Debnath, B.K. Datta, Documentation of ethnomedicinal knowledge of native flora utilized by Bishnupriya Manipuri people of Tripura, India, Ethnobotany Research and Applications, **31** (59) (2025) 1-29. https://doi.org/10.32859/era.31.59.1-29.

[6] S. Asiimwe, J. Namu Kobe, R. Byamukama, B. Imalingat, Ethnobotanical survey of medicinal plant species used by communities around Mabira and Mpanga Central Forest Reserves, Uganda, Tropical Medicine and Health, **49** (52) (2021) 1-10. https://doi.org/10.1186/s41182-021-00341-z.

[7] S. Sen, R. Chakraborty, B. De, N. Devanna, An ethnobotanical survey of medicinal plants used by ethnic people in the West and South districts of Tripura, India, Journal of Forestry and Research, **22**(3) (2011) 417–426. https://doi.org/10.1007/s11676-011-0184-6.

[8] R.M. Kunwar, B. Baral, S. Luintel, et al. Ethnomedicinal landscape: distribution of used medicinal plant species in Nepal, Journal of Ethnobiology Ethnomedicine, **18** (34) (2022) 1-11. https://doi.org/10.1186/s13002-022-00531-x.

[9] R.M. Kunwar, R.W. Bussmann, Ethnobotany in the Nepal Himalaya. Journal of Ethnobiology and Ethnomedicine, **4** (24) (2008) 1-8. https://doi.org/10.1186/1746 4269-4-24.

[10] K. Dulal, S. Chaudhary, Y. Uprety, N. Shrestha, S. Shakya, N.N. Munankarmi, Ethnomedicinal plants used by the local people of Changunarayan Municipality,

Bhaktapur, Nepal, A Journal of Plants, People and Applied Research, **23** (2022) 1-27. https://doi.org/10.32859/era.23.37.1-27.

[11] C. Sherpa, Non- Timber Forest products and their role in rural livelihoods: A case study from the Annapurna Conservation Area, Nepal, Ethnobotany Research and Applications, **30** (2025) 1–15. htts://doi.org/10.32859/era.30.20.1-15.

[12] R.M. Kunwar, L. Mahat, A.P. Acharya, R.W. Bussmann, Medicinal plants, traditional medicine, markets, and management in far-west Nepal, Journal of Ethnobiology and Ethnomedicine, **12** (2013) 9-24. https://doi.org/10.1186/1746-4269-9-24.

[13] M.D. Bhatt, Y.P. Adhikari, R.M. Kunwar, Ethnomedicinal Values of Weeds in Kanchanpur District, Far-Western Nepal, Ethnobotany Research and Applications, **21** (19) (2021) 1-19. https://doi.org/10.32859/era.21.19.1-19.

[14] D. Joshi, R.M. Kunwar, Y.R. Pokharel, M.D. Bhatt, Ecology and ethnobotany in and around Api Nampa conservation area (ANCA), Darchula, Nepal, Ethnobotany Research & Applications, **22** (49) (2021) 1-13. https://doi.org/10.32859/era.22.49.1-13.

[15] S.K. Ghimire, Medicinal plants in the Nepal Himalaya: current issues, sustainable harvesting, knowledge gaps and research priorities. In medicinal plants in Nepal: an anthology of contemporary Research (P.K. Jha, S. B. Karmacharya, M.K. Chettri, C.B. Thapa and B.B. Shrestha, eds.), Ecological society, (2008) 25–42.

[16] B. Malla, D. P. Gauchan, R. B. Chhetri, An ethnobotanical study of medicinal plants used by ethnic people in the Parbat district of western Nepal, Journal of Ethnopharmacology, **165** (2015) 103-11. https://doi.org/10.1016/j.jep.2014.12.057

[17] O. Polunin, A. Stainton, Flowers of the Himalaya, Oxford University Press, New Delhi, India, (1984).

[18] S.B. Malla, S. B. Rajbhandari, T. B. Shrestha, P. M. Adhikari, S. R. Adhikari, P. R. Shakya, Flora of Kathmandu Valley, Department of Medicinal Plants, Kathmandu, Nepal, Bulletin of the Department of Medical Plants, Nepal, 11 (1986).

[19] M.F. Watson, H. Ikeda, K.R. Rajbhandari, S. Akiyama, C.A. Pendry, K.K. Shrestha, eds. Flora of Nepal Volume 3: Magnoliaceae to Rosaceae, Royal Botanical Garden, Edinburgh, UK, (2011).

[20] K.K. Shrestha, P. Bhandari, S. Bhattarai, Plants of Nepal: Gymnosperms and Angiosperms, Heritage Publishers & Distributors, Kathmandu, Nepal, (2022).

[21] POWO, Plants of the world online. Facilitated by the Royal Botanical Gardens, Kew. Available online: https://powo.science.kew.org (accessed on 25 Nov. 2024).

[22] S. Singh, Ethnobotanical study of indigenous knowledge of some wild plants in Parsa district, Nepal, Journal of Natural History Museum, **29** (2018) 103-121. https://doi.org/10.3126/jnhm.v29i0.19042.

[23] G.P. Chataut, K.P. Sharma, B.B. Shrestha, M. Siwakoti, Native and alien plant species diversity across forest types in the mid-hills of central Nepal, Botanica Orientalis Journal of Plant Science, **16** (2025) 34-42. https://doi:10.3126/botor.v16i1.79986.

[24] T. Anwar, H. Qureshi, G. Sarwar, E.H. Siddiqui, N. Shakir, H.S. Almoallim, M.J Ansari, Ethnobotanical evaluation and Traditional uses of medicinal flora used to treat various ailments by local inhabitants, Advances in Integrative Medicine, **11**(2) (2024) 93–106. https://doil.org/10.1016/j.aimed.2024.05.002.

[25] M. Ullah, M.U. Khan, A.Mahmood, et al., An ethnobotanical survey of indigenous medicinal plants in Wana district, South Waziristan agency, Pakistan Journal of Ethnopharmacology, **150** (3) (2013) 918–924. https://doi.org/10.1016/j.jep.2013.09.032.

Annex: 1. Ethnobotanically useful plant species of Bhageshwor Rural Municipality, Dadeldhura.

Name of species	Plant group	Local name	Family	Habitat	Useful parts	Uses category	Uses
Achyranthes bidentata Bl.	Dicots	Datiwan	Amaranthaceae	H	Stem	Religious	Stems are used for religious purposes during the Teej puja.
Aegle marmelos (L.) Corrêa	Dicots	Beal	Rutaceae	T	Fruits, leaves	Religious	Leaves are used for religious purposes during worship of the deity Mahadev, and Fruits are used as food.
Agave vera-cruz Mill.	Monocots	Rambas	Asparagaceae	S	Leaves	Other	Leaves retting; used to make rope.
Ageratina adenophora (Spreng) King & H.Rob.*	Dicots	Banmara	Asteraceae	H	Leaves	Medicine	Leaves paste is used to stop the bleeding of a cut wound.
Ageratum conyzoides Sieber ex Steud.*	Dicots	Gandhae	Asteraceae	H	Stem, Leaves	Multiuse	Leaves paste is used to stop the bleeding of a cut wound, and stems with leaves are used as fodder.
Ageratum houstonianum Mill. *	Dicots	Gandhae	Asteraceae	H	Stem, Leaves	Multiuse	Leaves paste is used to stop the bleeding of a cut wound, and stems with leaves are used as fodder.
Antidesma acidum Retz.	Dicots	Emelchi	Phyllanthaceae	S	Fruits	Food	Fruits are used as food
Artemisia indica Willd.	Dicots	Kurjo	Asteraceae	H	Leaves	Medicine	Leaf paste is used to repel the insects of crops.
Asparagus filicinus Buch.-Ham. ex D. Don	Monocots	Jhejarine	Asparagaceae	H	Young shoot	Food	Young shoots are used as food.
Bambusa jaintiana R.B. Majumdar.	Dicots	Bans	Poaceae	S	Stem	Religious	Stem is used for religious purposes, such as the ownership of a new house and a funeral ceremony.
Bauhinia variegata L.	Dicots	Koiral	Fabaceae	T	Flower	Food	Floral buds are used to make a pickle.
Berberis aristata DC.	Dicots	Kirmada	Berberidaceae	S	Fruits	Food	Fruits are used as food
Bergenia ciliata (Haw.) Sternb.	Dicots	Syalpode	Saxifragaceae	H	Rhizome	Medicine	Rhizome is used as medicine to treat intestinal pain and digestive problems.
Bidens pilosa L.*	Dicots	Kalo kuro	Asteraceae	H	Stem, Leaves	Multiuse	Leaf paste is used as medicine for cut wounds, and the young shoot is used as fodder.
Bridelia retusa (L.) A.Juss.	Dicots	Gayo	Phyllanthaceae	S	Bark	Medicine	Bark paste is used during the swelling of the muscles of the body parts.

Bombax ceiba L.	Dicots	Simal	Malvaceae	T	Flower, young root	Food	Flowers are used as food, and the paste of young roots is used as an ingredient in wet bread of rice.
Cannabis sativa L.	Dicots	Aattar	Cannabaceae	H	leaves, seed	Multiuse	Leaves are used in religious purposes during worship of the deity Mahadev, and seeds help make pickles.
Celtis australis L.	Dicots	Khadka	Cannabaceae	T	Leaves	Fodder	Leaves are used as fodder
Chenopodium album L.	Dicots	Bethe	Chenopodiaceae	H	Young shoot	Food	Young shoot is used as vegetables.
Cinnamomum tamala (Buch.-Ham.) T. Nees & Nees	Dicots	Dalchini	Lauraceae	T	Leaves, Bark	Food	Leaves and barks are used as spices.
Cissampelos pareira L.	Dicots	Musebeli	Menispermaceae	C	Leaves	Medicine	Paste of leaves is used to cover wounds.
Colebrookea oppositifolia Sm.	Dicots	Barmeula	Lamiaceae	S	Leaves	Other	Leaves are used as bedding for domestic animals.
Colocasia fallax Schott	Dicots	Gaaba	Araceae	H	Stem, Leaves	Food	Stems with leaves are used as vegetables.
Coriaria nepalensis Wall.	Dicots	Machaline	Coriariaceae	S	Fruits	Food	Fruits are used as food materials.
Cuscuta reflexa Roxb.	Dicots	Akasebeli	Convolvulaceae	C	Stem	Medicine	Used as medicine for the cough, pain, urination.
Cynodon dactylon (L.) Pers.	Monocots	Dubo	Poaceae	H	Stem with leaves	Multiuse	Stem uses during religious purposes: puja, make a bed for the bride and groom during the marriage ceremony, and paste is used on the swollen part of the body.
Cyperus pangorei Rottb.	Monocots	Mutho	Cyperaceae	H	Stem	Other	Stems are helpful to prepare the mat.
Datura metel L.	Dicots	Dathuro	Solanaceae	S	Flowers, Fruits	Religious	Flowers and fruits are used for religious purposes during worship of the deity Mahadev.
Dioscorea bulbifera L.	Monocots	Gheta	Dioscoriaceae	C	Root	Food	Roots are used as food materials
Dioscorea deltoidea Wall. Ex. Griseb.	Monocots	Bhykur	Dioscoriaceae	C	Root	Food	Roots are used as food materials
Diploknema butyracea (Roxb.) H.J.Lam	Dicots	Cheuri	Sapotaceae	T	Flower, Fruits, Seed	Multiuse	Flowers containing honey; useful for the collection of honey, Fruits are used as food, seeds are helpful to prepare the oil, and leaves are used to make a leaf plate.
Dryopteris cochleata (D. Don) C. Chr.	Pteridophyta	Aakudi	Polypodiaceae	H	Young shoot	Food	Young shoots are used as vegetables
Elaeagnus umbellata var. *umbellata*	Dicots	Maleda	Elaeagnaceae	C	Fruits	Food	Fruits are used as food

Engelhardia spicata Lechen ex Blume	Dicots	Mauwa	Juglamdaceae	T	Leaves	Other	Paste of leaves is helpful to kill fish in rivers
Eulaliopsis binata (Retz.) C.E.Hubb	Dicots	Babeyo	Poaceae	H	Leaves	Other	Leaves are helpful to prepare the sweeper
Euphorbia royleana Boiss.	Dicots	Seudi	Euphorbiaceae	S	Latex, stem	Religious	Latex is used in swollen parts of the body. Stems are placed at the center of roof of the house of newly constructed.
Ficus auriculata Lour.	Dicots	Timalo	Moraceae	T	Fruits, Leaves	Multiuse	Young fruits are used as vegetables, and mature fruits are used as food. Leaves are helpful to make a leaf plate in a religious ceremony.
Ficus benghalensis L.	Dicots	Bar	Moraceae	T	Leaves	Religious	Leaves are used for religious purposes
Ficus semicordata Buch. - Ham. ex Sm.	Dicots	Khenayo	Moraceae	T	Fruits, Leaves	Multiuse	Matured fruits are used as food materials, and leaves are used as fodder.
Ficus religiosa L.	Dicots	Pepal	Moraceae	T	Leaves	Religious	Leaves are used for religious purposes
Galinsoga quadriradiata Ruiz & Pav.*	Dicots	Khursanyae	Asteraceae	H	Stem with leaves	Medicine	Paste of the stem with leaves is used as medicine for skin allergies.
Grewia optiva J.R.Drumm. ex Burret	Dicots	Bhaewal	Malvaceae	T	Stem, Leaves, Fruits	Multiuse	Stem fiber is used to make roap, leaves are used as fodder, and fruits are used as food.
Indigofera heterantha Wall. ex Brandis	Dicots	Sakena	Fabaceae	S	Flower	Food	Flowers are used as a vegetable
Justicia adhatoda L.	Dicots	Basinga	Acanthaceae	S	Flowers	Medicine	Leaves are used as manure and medicine for asthma, cough, and fever.
Mallotus nepalensis (Lam.) Mull. Arg.	Dicots	Rueno	Euphorbiaceae	T	Stem, Seeds	Timber	Mature stems help make agricultural tools.
Mentha arvensis L.	Dicots	Podhana	Lamiaceae	H	Young shoot	Food	Young shoots are used as a pickle.
Morus alba L.	Dicots	Kimbu	Moraceae	T	Fruits	Food	Fruits are used as food
Myrica esculenta Buch.-Ham. ex D.Don	Dicots	Kaphal	Myrtaceae	T	Fruits	Food	Fruits are used as food
Persea gamblei (King ex Hook. f.) Kosterm.	Dicots	Kaulo	Lauraceae	T	Bark	Food	Fruits are used as food
Persicaria hydropiper (L.) Delarbe	Dicots	Gaeradae	Polygonaceae	H	Whole body	Other	Paste is used as a soft fish poison to kill fish in the river.
Phanera vahlii (Wight & Arn.) Benth.	Dicots	Damada	Fabaceae	C	Seeds	Multiuse	Seeds are used as food, and leaves are helpful to make a leaf plate.

Phyllanthus emblica L.	Dicots	Oala	Phyllanthaceae	T	Fruits	Food	Fruits help prepare the pickle
Pinus roxburghii Sarg.	Gymnosperms	Sallo	Pinaceae	T	Seeds	Multiuse	Seeds are used as food, and fallen leaves are used as mulch in horticulture.
Prunus cerasoides D. Don	Dicots	Panyue	Rosaceae	T	Stem with leaves	Religious	Stems with leaves are used in religious ceremonies to make gates and mandaps.
Pyracantha crenulata (D.Don) M.Roem.	Dicots	Gangaru	Rosaceae	S	Fruits	Multiuses	Stems are helpful in agricultural tools, and fruits are used as food.
Pyrus pashia Buch.-Ham. ex D.Don	Dicots	Maile	Rosaceae	T	Fruits	Food	Fruits are used as food
Rhododendron arboreum Sm.	Dicots	Laligurans	Ericaceae	T	Flower	Medicine	Flower juice is used for intestinal pain
Rhus chinensis Mill.	Dicots	Bhakmello	Anacardiaceae	S	Fruits	Food	Fruits are used as food
Rubus ellipticus Smith	Dicots	Ausaulu	Rosaceae	S	Fruits	Food	Fruits are used as food
Saccharum arundinaceum Retz.	Monocots	Khus	Poaceae	H	Leaves	Religious	Leaves are used in a religious ceremony.
Sapindus mukorossi Gaertn.	Dicots	Reetha	Sapindaceae	T	Fruits	Other	Fruit paste is used to wash clothes as detergents.
Searsia parviflora (Roxb.) F.A.Barkley	Dicots	Ranayal	Anacardiaceae	S	Fruits	Food	Fruits are used as food
Syzygium cumini (L.) Skeels	Dicots	Jamuno	Myrthaceae	T	Fruits, Bark	Multiuse	Fruits are used as food, and the paste of bark is used during the fabrication of body parts.
Terminalia elliptica Willd	Dicots	Harro	Combretaceae	T	Fruits	Food	Fruits are used as food
Tinospora cordifolia (Willd.) Hook.f. & Thomson	Dicots	Gurgo	Menispermaceae	C	Stem	Medicine	Stem juice is used medicine for diabetes and pain.
Toona ciliata M. Roem.	Dicots	Tuni	Meliaceae	T	Stem	Timber	Stem is used as timber for houses, temples
Urtica dioica L.	Dicots	Sesno	Urticeae	H	Young shoot	Food	Young shoot is used as a vegetable as well as fodder to increase the milk of cows and buffalos.
Woodfordia fruticosa (L.) Kurz	Dicots	Dhaiya	Lythraceae	S	Flower	Food	Flower juice is used as food
Zanthoxylum armatum DC.	Dicots	Timur	Rutaceae	S	Fruits	Multiuse	Fruits help make pickles, and are also used for the treatment of cough and fever.
Ziziphus mauritiana Lam.	Dicots	Bayar	Rhamnaceae	S	Fruits	Food	Fruits are used as food

*Invasive alien plant species, T=Tree, S=Shrub, C=Climber, H=Herb

Structural, Vibrational and Electronic Properties with Pharmacokinetics, Drug-likeness, and Molecular Docking of Furandimethanol

Madhab Raj Bhatt*, Govind Bahadur Dhami, Shiv Raj Joshi

Department of Physics, Siddhanath Science Campus, Mahendranagar, Kanchanpure, Tribhuvan University, Nepal

Research Article

ISSN: 3059-9504 (online)
DOI: https://doi.org/10.3136/ajs.v2i1.87746

Article History

Received: September 20, 2025; Revised: October 22, 2025; Accepted: October 29, 2025; Published: December 25, 2025

Keywords

Density functional theory, BHMF, HOMO-LUMO, MESP, UV-Vis, Molecular Docking, Pharmacokinetics, Drug-likeness.

***Corresponding author**

Email: phy.madhab@gmail.com (MR Bhatt)

ABSTRACT

In this study, geometrical parameters, electronic and vibrational properties of furandimethanol (BHMF) have been analyzed by using density functional theory (DFT) at B3LYP/6-31g level. Forty-five normal modes of vibration were obtained and analyzed with their potential energy contributions. The calculated Raman and IR spectra were plotted using scaled wavenumbers. Molecular electrostatic potential surface (MESP), ultraviolet visible (UV-Vis) spectra and Mulliken charges were mapped to understand electronic properties. Swiss ADME web tool was used for prediction of physicochemical, pharmacokinetics, drug-likeness and medicinal properties of titled molecule. Molecular docking studies against 1S5B (2.13 Å resolution), a mutant cholera holotoxin from *Vibrio cholerae*, were performed using Autodock tools like BIOVIA Discovery Studio, PyMOL, Python and Open Babel. The molecular docking study indicates that the furandimethanol is moderate inhibitor of 1S5B.

1. INTRODUCTION

In recent time, a majority of researchers are using computational tools widely used in chemistry to investigate real problems in chemical, pharmaceutical, biotechnology, and material science. They use the results of theoretical calculations, to calculate the structure and properties of molecules and solid materials both in physics and chemistry [1]. Computational chemistry and computational physics are used in the designing of new drugs and materials to solve numerical problems. Nowadays, researchers use various computational programs to predict the molecular structure and physical properties of bioactive molecules [2]. The density functional theory (DFT) is a popular method for defining the structural and electronic properties of atoms and molecules [3]. Furandimethanol, commonly known as 2,3–Bis(hydroxymethyl)furan (BHMF), IUPAC name Furan-2,3-diyl)dimethanol, is a heterocyclic organic compound with oxygen as hetero member. It is a water-soluble furan carrying two hydroxymethyl substituents at the 2-and 3-position and is a member of diol. It is produced from cellulose and has received attention as a bio-feedstock. Its commercial samples can appear yellowish or tan [4]. The Optimized structure of Furandimethanol is presented in Fig. 1.

Compounds classified as heterocyclic probably constitute the largest and most varied family of organic compounds. Among heterocyclic compounds, five-membered heterocycles constitute a wide and differentiated group with a broad spectrum of biological activity. Compounds from this class are present in nature as constituents of nucleic acid, so many important amino acids, alkaloids and hormones [4]. Joshi *et.al* have studied the structure, MESP and HOMO-LUMO of 10-acetyl-10H-phenothiazine-5-oxide using vibrational spectroscopy quantum chemical method [5]. Yadav *et.al* have studied on *ab Initio* and DFT study of HCN: Role of temperature for the formation of HCN molecule in the interstellar medium [6].

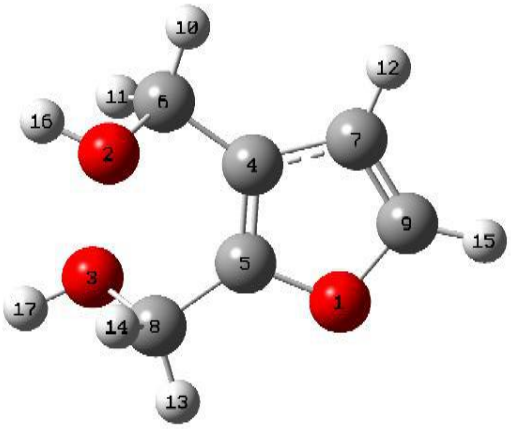

Fig. 1: Optimized Structure of Furandimethanol.

Pharmacokinetics is the branch of pharmacology that deals with the study of what the body does to a drug, summarized by ADME (Absorption, Distribution, Matabolism, Excreation). It focuses at how a drug enters the bloodstream through absorption, how it spreads to tissues and organs through distribution, how the body's enzymes break it down through metabolism, and how it is removed from the body through excretion in urine, bile, or sweat. Drug-likeness is a measure which ensures whether a chemical compound become an effective, safe, and orally active drug in humans.

Molecular docking approach is a computer-aided technique to predict protein-ligand interaction of a drug molecule. It predicts biding modes as well as binding affinity of ligand with target proteins which plays key role in drug design [7,8].

2. METHODOLOGY

Taking initial molecular data available from PubChem database [9], geometry optimization was performed. Taking the optimized parameters, the vibrational spectra were calculated by using B3LYP/6-31g [10, 11], level of theory employing Gaussian 09 program [12] without any constraints on the geometry of molecule [13]. Using the same level of theory, geometrical parameters bond lengths, bond angles and dihedral angles were calculated. The basis set used for the calculations is based on Becke's three-parameter (local, non-local, Hartree-Fock) hybrid exchange functional with Lee-Yang-Parr correlation Functional (B3LYP) [10,11,14, 15].

As the second task, normal modes of vibration and their corresponding Raman activities and IR intensities were calculated by the program Gar2Ped [16]. All the 45 normal modes of vibrations were assigned with their potential energy contributions using internal coordinates recommended by Pulley [17]. The visualization of calculated data is done by using the Gauss View [17].

Raman spectra and IR spectra were plotted using OriginPro 7 programme, UV-visible spectra and molecular electrostatic surface potential (MESP) were plotted using Gauss view. Mulliken atomic charges were plotted using Microsoft excel. Swiss ADME web tool [18] is utilized for prediction of physicochemical, pharmacokinetics, drug-likeness and medicinal chemistry properties of titled molecule. The canonical SMILES of the molecule were retrieved from the PubChem database [9] and fed into the Swiss ADME tool. This tool returns the full set of data including number of hydrogen bond acceptors, number of donors, molar refractivity, polar surface area (PSA), rotatable bonds, AlogP and other crucial parameters.Molecular docking studies were performed using AutoDock Vina [19], AutoDock tools [20], BIOVIA Discovery Studio [21], PyMOL [22], Python and Open Babel. Docking proteins were retrieved from the RCSB Protein Data Bank [23].

The target proteins were retrieved in PDB format from the RCSB Protein Data Bank and then were prepared using BIOVIA Discovery Studio, AutoDock Tools for final docking purpose. In the last step of preparation, polar hydrogen atoms were accurately attached to the target protein structure after deleting all water and unnecessary ligand molecules. The ligand, BHMF, was downloaded from the PubChem database in SDF format and then converted to PDB format using Open Babel [24]. It was prepared using AutoDock tools and saved in PDBQT format which was the same format as that of protein. The molecular docking technique was employed using blind docking, wherein the grid was designed optimally to cover the maximum possible binding sites of the protein. AutoDock Vina was executed to perform molecular docking after the detailed preparation of the protein, ligand, and configuration file. The docking process was initiated using the Vina command, ensuring a precise and systematic approach to the analysis.

The scoring function for AutoDock Vina can be obtained using the following equation

$$\Delta G_{binding} = \Delta G_{H-bond} + \Delta G_{hydrophobic} + \Delta G_{repulsion} + \Delta G_{gauss} + \Delta G_{AutoDock\ Vina\ score} \quad (i)$$

where, ΔG_{H-bond} represents the change in the binding energy due to hydrogen bond, $\Delta G_{hydrophobic}$, due to hydrophobic interaction, due to steric effect, $\Delta G_{repulsion}$(gauss^1 (d) = $e^{-(\frac{d}{0.5\text{Å}})^2}$, gauss^2(d) =$e^{-(\frac{d-3\text{Å}}{2\text{Å}})^2}$ and Repulsion(d) $= \begin{cases} d^2, & d < 0 \\ 0, & d \geq 0 \end{cases}$), due to repulsion and ΔGAutoDock Vina score, due to rotational bonds penalty.

The hydrophobic term equals 1, when d < 0.5 Å; 0, when d > 1.5 Å, and is linearly interpolated between these values. The hydrogen bonding term equals 1, when d < −0.7 Å; 0, when d > 0, and is similarly linearly interpolated in between X- score, we formally treat metals as hydrogen bond donors. In this implementation, all interaction functions $f_{t_i t_j}$ are cut off at r_{ij} = 8 Å (Trott and Olson, 2009)

The conformation-independent function g was chosen to be

$$g(C_{inter}) = \frac{C_{inter}}{1+wN_{rot}} \quad (ii)$$

Where, N_{rot} represents number of active rotatable bonds between heavy atoms in ligand and w is the associated weight.

Results obtained from AutoDock Vina were visualized and analyzed using PyMOL and BIOVIA Discovery Studio.

3. RESULTS AND DISCUSSION

3.1 Geometric parameters

The bond lengths, bond angles and dihedral angles are basic properties of molecules to deal with molecular geometry. In a molecule bond length is defined as the average distance between nuclei of two bonded atoms in it. The value of bond lengths varies from molecule to molecule as it depends upon various factors like types of atoms, orbital hybridization, electronic and steric nature of the substituents. The bond length, bond angle and dihedral angle data for title molecule is listed in Table 1 below:

Table1: Optimized values of Bond length, Bond angle and Dihedral angle.

Bond Length	Optimized value (Å)	Bond Angle	Optimized value (°)	Dihedral Angle	Dihedral angle (°)
O1-C5	1.359	C5-O1-C9	106.62	C9-O1-C5-C4	0
O1-C9	1.359	C6-O2-H16	106.93	C9-O1-C5-C8	-179.96
O2-C6	1.428	C8-O3-H17	106.91	C5-O1-C9-C7	-0.01
O2-H16	0.972	C5-C4-C6	127.11	C5-O1-C9-H15	179.99

O3-C8	1.429	C5-C4-C7	106.12	H16-O2-C6-C4	179.84
O3-H17	0.972	C6-C4-C7	126.77	H16-O2-C6-H10	59.19
C4-C5	1.376	O1-C5-C4	110.57	H16-O2-C6-H11	-58.74
C4-C6	1.474	O1-C5-C8	116.06	H17-O3-C8-C5	-179.88
C4-C7	1.415	C4-C5-C8	133.37	H17-O3-C8-H13	59.2
C5-C8	1.47	O2-C6-C4	107.91	H17-O3-C8-H14	-58.87
C6-H10	1.095	O2-C6-H10	108.52	C6-C4-C5-O1	-179.99
C6-H11	1.095	O2-C6-H11	108.73	C6-C4-C5-C8	-0.03
C7-C9	1.376	C4-C6-H10	111.24	C7-C4-C5-O1	0.01
C7-H12	1.081	C4-C6-H11	111.78	C7-C4-C5-C8	179.96
C8-H13	1.094	H10-C6-H11	108.58	C5-C4-C6-O2	90
C8-H14	1.094	C4-C7-C9	106.13	C5-C4-C6-H10	-151.07
C9-H15	1.08	C4-C7-H12	127.8	C5-C4-C6-H11	-29.51
		C9-C7-H12	126.07	C7-C4-C6-O2	-90
		O3-C8-C5	108.05	C7-C4-C6-H10	28.93
		O3-C8-H13	108.58	C7-C4-C6-H11	150.5
		O3-C8-H14	108.63	C5-C4-C7-C9	-0.01
		C5-C8-H13	111.37	C5-C4-C7-H12	-179.98
		C5-C8-H14	111.42	C6-C4-C7-C9	179.98
		H13-C8-H14	108.71	C6-C4-C7-H12	0.02
		O1-C9-C7	110.57	O1-C5-C8-O3	-90.05
		O1-C9-H15	115.63	O1-C5-C8-H13	29.12
		C7-C9-H15	133.8	O1-C5-C8-H14	150.7
				C4-C5-C8-C3	90
				C4-C5-C8-H13	-150.83
				C4-C5-C8-H14	-29.25
				C4-C7-C9-O1	0.01
				C4-C7-C9-O15	-179.99
				H12-C7-C9-O1	179.98
				H12-C7-C9-H15	-0.02

Generally, the C-C single bond length is 1.54Å, C-H is 1.09Å, C-O is 1.43Å and that of C=C 1.34Å [25]. But, in this study the longest C-C bond was found between C4-C6 with the value 1.474 Å and the shortest C-C bonds were found between C4-C5 and C7-C9 with the same value 1.376Å. The longest C-O bond wsa found between C8-O3 with the value 1.429Å the shortest C-O bonds were found between C9-O1 and C5-O1 with the same value 1.359Å. O-H bond length was found to be 0.972Å and C-H bond length was found in the range 1.080Å -1.095Å. The highest and lowest bond angles were found between C7-C9-H15 and C5-C4-C7 with respective values 133.80° and 106.12°. The dihedral angle is the clockwise angle between two planes, both of which pass through the same bond. Here, the lowest to highest dihedral angles in clockwise directiobs were found in the range 0.01°-179.96°, whereas the lowest to highest dihedral angles in counter-clockwise direction were found in the range 0.00°- 179.99°.

3.2 Vibrational Assignments

Furandimethanol (BHMF) consists of 17 atoms and hence it gives 45 fundamental modes of vibration which are both Raman and IR

active. A complete vibrational analysis of these fundamental vibrational modes was made by using DFT/ B3LYP/6-31g. Also, HF calculations were made using same level of basis set. The PED assignments were given as per the internal coordinate system. The calculated vibrational wavenumbers (in both B3LYP and HF), IR intensity, Raman activity and calculated PED for each normal mode are as shown in Table 2 and IR and Raman spectra are shown in Figs. 2 and 3, respectively.

Table 2: Vibrational wavenumbers (cm^{-1}), Raman activity (km/mol), IR Intensity ($Å^4$/a.m.u) and potential energy distribution.

Wavenumber			Raman Activity	IR Intensity	Potential Energy Distribution (PED)($\geq 5\%$)
Unscaled	Scaled				
DFT	DFT	HF			
49	49	86	0.5774	0.1069	R[υ(CO)](7)+τ(CC)(74)+τ(CO)(7)
94	95	151	0.7297	3.4596	R[υ(C=C)(15)+oop(CC(13)]+ τ(CC)(56)
158	159	216	2.6337	6.0628	R[oop(CC(44)+υ(CC)(15)+δ_{in}(CC)(6)]+δ(COC)(19)
188	189	258	1.9258	7.6907	R[oop(CC(50)+υ(CC)(9)+δ_{in}(CC)(6)]+δ(COC)(17)
237	238	274	1.6805	2.8936	R[δ_{in}(CC)(47)+oop(CC(7)]+υ(CO)(11)+τ(CC)(7)
255	256	343	9.7949	248.580	τ(CO)(92)
337	339	388	8.0452	9.5009	R[υ(CO)](7)+τ(CO)(73)+δ(COC)(12)
358	360	436	2.2902	0.2435	R[δ_{in}(CC)(55)+υ(C=C)(8)+oop(CC(6)]+ δ(COC)(12)
398	398	481	0.8150	11.8220	R[τ′(24)+δ_{in}(CC)(5)+oop(CC(5)]+ δ(COC)(30)
417	417	674	2.6919	1.9238	R[δ](13)+υ(CC)(15)+ oop(CC(11) + δ_{in}(CC)(5)] + δ(COC)(21) +υ(OH)(11)
620	620	711	2.6844	4.6294	R[τ](75)+τ′(9)]+ υ(CO)(6)
673	671	749	6.4752	13.0880	R[τ′(38) + oop(CC(23) +υ(CC)(17) +υ(CO)(6)]
693	691	790	0.2901	23.9430	R[δ(24)+τ′(6)+oop(CC(6)]+υ(CC)(19) +δ(COC)(25)+
734	731	822	3.158	39.6590	R[oop(CH)(27) + τ′(20) +υ(CO)(8)] +oop(CC(13) +υ(CC)(12) + δ(COC)(5)
765	762	887	2.7985	32.2000	R[oop(CH)(36)+τ′(15)+τ(10)+oop(CC(13)]+ υ(CO)(10)
888	883	983	0.9953	5.3747	R[oop(CH)(85) + υ(CO)(7) + τ(5)]
906	900	1046	3.8238	22.8930	R[δ′(57) + υ(CO)(19)]+ ρ(CH_2)(6)
967	960	1057	4.4108	9.3792	R[δ′(13) + υ(CO)(11) + δ(9) + υ(CC)(5)+ υ(C=C)(5)] + ρ(CH_2)(40)
971	964	1072	10.9727	43.3530	υ(CO)(75) + δ(COC)(5)
978	970	1111	6.4668	45.4380	υ(CO)(75) + ρ(CH_2)(5)
1007	999	1122	6.0460	3.7559	R[υ(CO)](5) +ρ(CH_2)(61) + υ(CO)(12)
1041	1033	1146	7.9910	4.3749	R[υ(CO)(65) + δ_{in}(CH)(19)]
1110	1099	1161	2.2426	7.7562	R[δ_{in}(CH)(14) + δ(8) +υ(CO)(14) +υ(CC)(7) + δ_{in}(CC)(7)] + ρ(CH_2)(34)
1161	1149	1219	14.0402	1161.20	R[δ_{in}(CH)](45)+υ(C=C)(12) +υ(CO)(17) +υ(CC)(10)]+ {ρ(7) + γ (6) }(CH_2)
1198	1185	1273	6.9571	7.0379	R[υ(CO) (22) + υ(CC)(26) + δ(10) +υ(C=C)(6)]+ γ(CH_2)(16)
1238	1224	1309	11.6332	26.4070	R[δ_{in}(CH)(12) + δ(7) + υ(CC)(5)] + δ(CHO)(27) + γ(CH_2)(19)+ υ(CC)(11)
1257	1242	1346	3.2808	36.5350	δ(CHO)(63) + ω(CH_2)(26)
1291	1275	1351	8.1630	54.4370	R[δ(5)] + δ(CHO)(36) + ω(CH_2)(26) + γ(CH_2)(17)+ υ(CC)(6)
1306	1290	1397	2.8531	1.3104	R[δ_{in}(CH)](43) + γ(CH_2)(40)
1321	1304	1469	19.8075	6.2351	R[υ(CC)(10) +υ(CO)(10)] + γ(CH_2)(63) +υ(CC)(5)
1419	1399	1516	4.5706	6.9053	R[υ(CC)(20)+δ_{in}(CH)(23)+υ(CO)(5)] +ω(CH_2)(21)
1473	1451	1555	9.8611	7.2197	ω(CH_2)(67) + δ(CHO)(17) + υ(CC)(5)
1478	1455	1568	18.6438	5.1138	R[υ(CC)](6)+ ω(CH_2)(44)+υ(CC)(18)+ δ(CHO)(14)
1507	1483	1640	81.2979	10.3620	R[υ(C=C)](63) + δ_{in}(CH)(17) +δ′(5)+ υ(CC)(5)
1545	1520	1652	24.1001	3.5611	δ(CH_2)(94)
1561	1535	1658	5.4589	7.1581	δ(CH_2)(96)
1655	1624	1765	26.1030	3.8103	R[υ(C=C)](66) +υ(CC)(14)]
3022	2900	3050	89.7099	59.2930	υ(CH_2)(100)

3040	2916	3088	114.072	40.3970	$\upsilon(CH_2)$(99)
3068	2941	3118	50.4533	27.4440	$\upsilon(CH_2)$(99)
3090	2961	3125	59.6634	16.7150	$\upsilon(CH_2)$(99)
3279	3132	3279	69.5059	2.1007	R[υ(CH)](99)
3326	3175	3332	112.266	0.2693	R[υ(CH)](99)
3458	3293	3519	242.713	5.4531	υ(OH)(98)
3463	3298	3656	234.425	3.3227	υ(OH)(99)

3.2.1 Furan ring vibration

Generally, C—H stretching occurs in the region 3100-3000 cm^{-1} [26]. In this study, C-H stretching was calculated at 3132cm^{-1} and 3175cm^{-1} with Raman activity/IR intensity 69.5059/112.2660 and 2.1007/0.2693 units respectively. C-H in plane bending vibrations were recorded at 1399cm^{-1}, 1290cm^{-1}, 1224cm^{-1}, 1099cm^{-1} and 1033cm^{-1} with Raman activity/IR intensity 4.5706/6.9053, 2.8531/1.3104, 11.6332/26.4070, 14.0403/1161.2000, 2.2426/7.7562 and 7.9910/4.3749 units respectively in scaled DFT. The out of plane bending was recorded below 883 cm^{-1}. The ring C-C stretching vibrations are found to be strong in the band from 1600cm^{-1}-1400cm^{-1}[26], here they were recorded at 1624cm^{-1}, 1455cm^{-1} and 1399cm^{-1} with Raman activity/IR intensity 26.1030/3.1803, 18.6438/5.1138 and 4.5706/6.9053 units respectively in scaled DFT.

C=C stretching vibrations are generally occur in the range 1680cm^{-1}-1630cm^{-1} [26], here they were were calculated at 1624cm^{-1}, 1483cm^{-1}, 1149 cm^{-1} with Raman activity/IR intensity 26.1030/3.1803, 81.2979/103620, 14.0403/1161.2000 units in scaled DFT. C-O stretching vibrations were recorded at 1185cm^{-1},1149cm^{-1}, 1099cm^{-1}, 1033cm^{-1}, 900cm^{-1}, 349cm^{-1} with Raman activity/IR intensity 6.9571/7.0379, 14.0403/1161.2000, 2.2426/7.7562, 7.9910/4.3749, 3.8238/22.8930, 8.0452/9.5009 units respectively. Ring deformation vibrations were recorded below 1275cm^{-1} and ring torsion vibrations were recorded below 762 cm^{-1}. In plane bending vibrations of C-C were calculated at 417cm^{-1}, 398cm^{-1}, 360cm^{-1}, 238cm^{-1}, 189cm^{-1}, 169cm^{-1} and 95cm^{-1} with Raman activity/IR intensity 2.6913/1.9238, 0.8150/11.8220, 2.2902/0.2448, 1.6805/2.8926, 1.9258/7.6907, 2.6937/6.0628 and 0.7279/3.4596 units respectively. Similarly, out of plane bending of C-C bending vibrations were recorded at 691cm^{-1}, 671cm^{-1}, 417cm^{-1}, 398cm^{-1}, 360cm^{-1},238cm^{-1}, 189cm^{-1}, 159cm^{-1} and 95cm^{-1} with Raman activity/ IR intensity 0.2901/23.9430, 6.4753/11.0880, 2.6913/1.9238, 0.8150/11.8220, 2.2902/0.2448, 1.6805/2.8926, 1.9258/7.6907, 2.6937/6.0628 and 0.7279/3.4596 units, respectively.

3.2.2 CH_2 vibration

Literature reviews suggest that the asymmetric stretching of CH_2 occurs in the region 3000cm^{-1}-2800cm^{-1} whereas symmetric stretching occurs in the region 2900cm^{-1} -2800 cm^{-1} [27], but here symmetric stretching of CH_2 (pure mode) was recorded at 2900cm^{-1} with Raman Activity/IR intensity 89.7099 and 59.2930 units respectively. Remaining CH_2 stretching vibrations were calculated at 2916cm^{-1}, 2941cm^{-1} and 2961cm^{-1} with Raman activity/ IR intensity 114.0720 /40.3970, 50.4533/27.4440 and 59.6634/ 16.7150 units, respectively. Moreover, bending, wagging, twisting and rocking were recorded below 1520cm^{-1}, 1455 cm^{-1}, 1304cm^{-1} and 1149 cm^{-1}respectively.

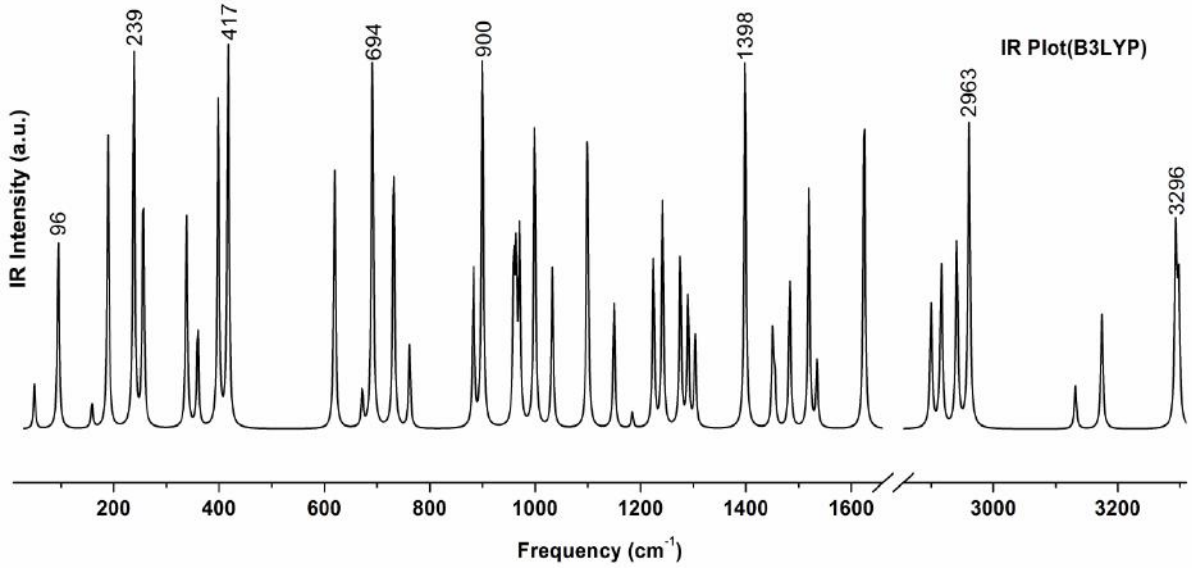

Fig. 2: IR spectra of BHMF between the ranges 10 —3310 cm^{-1} (Intensity of selected characteristic modes are assigned).

3.2.3 OH vibration

The non-hydrogen bonded or free hydroxyl group absorbs strongly in the region 3600cm^{-1}-3550cm^{-1} whereas the existence of hydrogen bond can lower the O-H stretching wave number to 3550cm^{-1}-3200cm^{-1} region with an increase in IR intensity and breadth [28]. The in-plane deformation vibrations appear strong in the region 1440cm^{-1}-1260 cm^{-1} [29]. Here, there are two O-H groups and their symmetric stretching vibrations were recorded at 3519cm^{-1} and 3656 cm^{-1} with Raman activity/ IR activity 242.7130/ 5.4531 and 234.4250/ 3.3227 units respectively. All the C-C and CHO deformations were recorded below 1455 cm^{-1}.

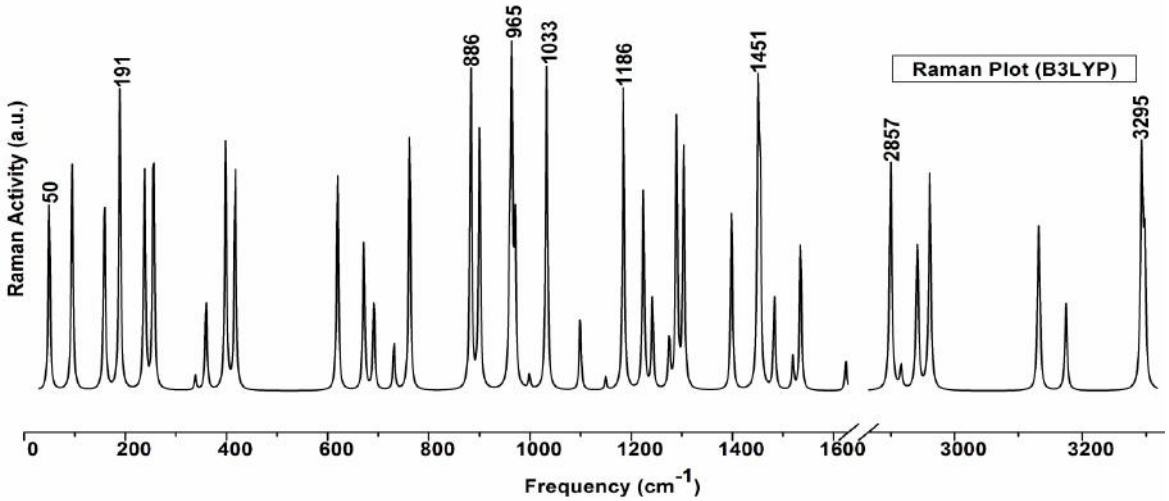

Fig. 3: Raman spectra of BHMF between the ranges 0 —3310 cm^{-1} (Intensity of selected characteristic modes are assigned).

3.3 Electronic Properties

3.3.1 Mulliken Atomic Charges

Mulliken atomic charges are useful in determining the chemical reactivity of compounds. The Mulliken charges for BHMF are listed in the Table 3. From the table, C9 has the highest positive charge of all carbon atoms and are thus predicted to be the target of nucleophilic attack. Also, the oxygen atom O1 has a positive charge and rest two oxygen atoms have negative charges as shown in Fig. 4. All the hydrogen atoms are associated with positive charges.

Table 3: Mulliken charges for BHMF.

Atoms	Mulleken atomic charges
O1	0.507734
O2	-0.554525
O3	-0.554760
C4	-0.003856
C5	0.367248
C6	-0.214200
C7	-0.230092
C8	-0.206398
C9	0.082129
H10	0.180081
H11	0.184916
H12	0.188372
H13	0.197543
H14	0.190897
H15	0.211978
H16	0.333533
H17	0.334868

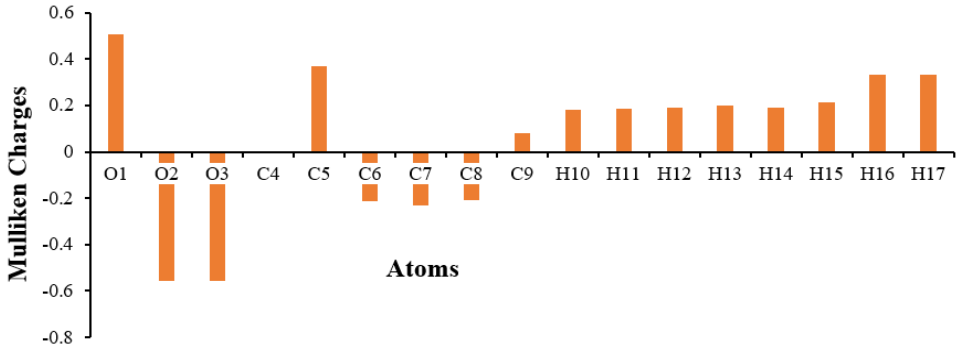

Fig. 4: Mulliken charge plot of BHMF.

3.3.2 Molecular Electrostatic Potential Surface (MESP)

The MESP provides a visual method to understand the relative polarization of molecule [30]. In the surface generated, negative electrostatic potential (shades of red color) corresponds to an attraction of the proton by the concentrated electron density in the molecules and positive electrostatic potential (shades of blue

color) corresponds to repulsion of the proton. The largely white or lighter yellow color shades on the surface indicate that the molecule is mostly non-polar. In the surface generated the deepest red region around the oxygen atoms is global negative site and is favorable for the electrophilic attack. Whereas, the deepest blue regions around the hydrogen atoms are the global positive site and is favorable for nucleophilic attack. The positive potential increases in the order red < orange < yellow <green (Fig. 5). The bonding of any molecule with other molecules depends upon the charge distributions around the molecule. So, MESP play an important role to identify the bonding sites of molecule biologically.

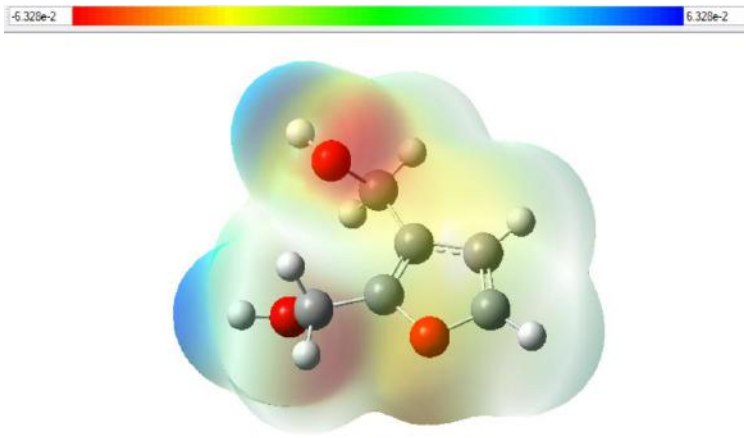

Fig. 5: Molecular electrostatic potential mapped on isogeneity surface in the range -6.328× 10^{-2}(red) to 6.328× 10^{-2}(blue) for BHMF.

3.3.3 UV-Visible spectra

UV-Vis is a spectroscopy which involves the interaction of ultraviolet and visible radiations with matter. It is an analytical technique that measures the number of discrete wavelengths of UV or visible light that are absorbed by or transmitted through a sample [30]. In order to plot the UV-Vis spectra, time dependent density functional theory (TD-DFT) calculations were performed in both gaseous phase as well as solvent (ether) environment. Theoretically plotted UV-Vis absorption spectra are shown in the Figs. 6 and 7 respectively corresponding to gaseous phase and solvent phase.

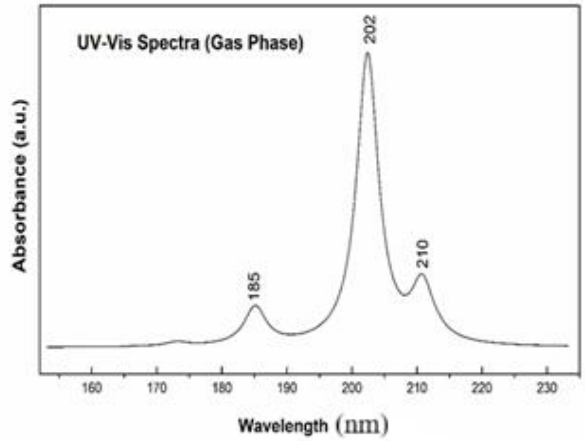

Fig. 6: UV-Vis plot of BHMF in gas phase between the ranges 160-230 cm^{-1}. Sigle peak with the highest absorbance was assigned and it was observed at 202cm^{-1}.

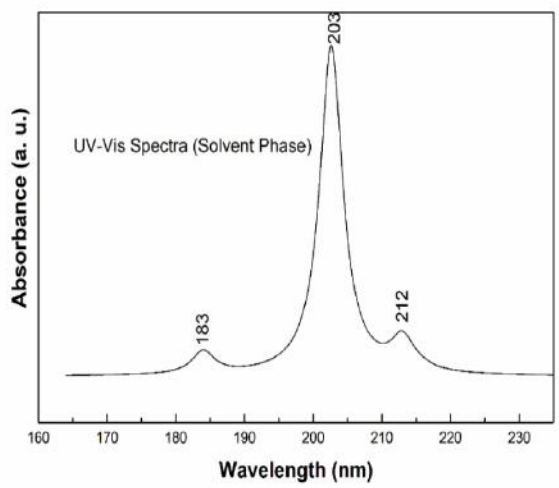

Fig. 7: UV-Vis plot of BHMF in solvent (Eather) phase between the ranges 160-230 cm^{-1}. Sigle peak with the highest absorbance was assigned and it was observed at 203cm^{-1}.

3.4 Physicochemical Properties

Its molar refractivity (30.96) indicates its low polarizability, which is characteristic of the compact aromatic core. Thus, together these descriptors suggest a molecule of suitable polarity (for aqueous solubility) and lipophilicity (for passive absorption), consistent with the physicochemical requirements for oral bio-availability agents. Physicochemical properties of the title compound calculated by the Swiss ADMDE web tool are shown in Table 4.

Table 4: Physicochemical Properties of BHMF.

Physicochemical Properties	
Formula	$C_6H_8O_3$
Molecular weight	128.13 g/mol
Num. heavy atoms	9
Num. arom. heavy atoms	5
Fraction Csp3	0.33
Num. rotatable bonds	2
Num. H-bond acceptors	3
Num. H-bond donors	2
Molar Refractivity	30.96
TPSA	53.60 Å²

3.4.1 Lipophilicity

The title compound possesses low lipophilicity (consensus LogP = 0.07). Calculated from 3D models, predictions range from −0.97 to +1.20; consensus is about neutrality between hydrophilic and lipophilic tendencies. This balanced value of lipophilicity is favorable for oral absorption, distribution and formulation flexibility. However, its low lipophilicity might restrict its ability to penetrate through very lipophilic barriers such as the blood–brain barrier, restricting its therapeutic uses in peripheral targets. The title compound's lipophilicity is displayed Table 5.

Table 5: Lipophilicity of BHMF.

Lipophilicity	
Log $P_{o/w}$ (iLOGP)	1.20
Log $P_{o/w}$ (XLOGP3)	-0.75
Log $P_{o/w}$ (WLOGP)	-0.04
Log $P_{o/w}$ (MLOGP)	-0.97
Log $P_{o/w}$ (SILICOS-IT)	0.94
Consensus Log $P_{o/w}$	0.07

3.4.2 Pharmacokinetics

Furandimethanol is highly absorbed in the gastrointestinal track but not across the blood–brain barrier. it is not P-glycoprotein substrate, and do not inhibit important CYP450 isoenzymes (CYP1A2, CYP2C19, CYP2C9, CYP2D6, and CYP3A4). The skin penetration coefficient (Log Kp = −7.61 cm/s) is indicative of low dermal absorption. The present characteristics support its potential as an orally administrable, but not a CNS-available drug. The lack of CYP450 inhibition decreases its potential for drug–drug interactions, adding to the safety profile.
Pharmacokinetics of title compound are presented in Table 6.

Table 6: Pharmacokinetics of BHMF.

Pharmacokinetics	
GI absorption	High
BBB permeant	No
P-gp substrate	No
CYP1A2 inhibitor	No
CYP2C19 inhibitor	No
CYP2C9 inhibitor	No
CYP2D6 inhibitor	No
CYP3A4 inhibitor	No
Log K_p (skin permeation)	-7.61 cm/s

3.4.3 Drug-likeness

Numerous parameters including molecular weight, hydrogen bond acceptors and donors, molar refractivity, polar surface area, number of rotatable bonds, and ALogP were accessed to study the drug-likeness of the title molecule using Swiss ADMDE web tool. The compound also satisfies all the descriptors of Lipinski's Rule of Five [31] and Veber–Egan filters. But it violated Ghose filter (small size and low molar refractivity) and Muegge's rule (molecular weight >200). The low score of 0.55 suggests moderate yet satisfactory oral bioavailability. Furandimethanol adheres to the basic principles of drug-likeness however its size may be limiting target engagement and metabolic stability, likely requiring structural elaboration during optimization. The result is summarized in Table 7.

Table 7: Drug-likeness Properties of BHMF.

Drug-likeness	
Lipinski	Yes; 0 violation
Ghose	No; 3 violations: MW<160, MR<40, #atoms<20
Veber	Yes
Egan	Yes
Muegge	No; 1 violation: MW<200
Bioavailability Score	0.55

3.4.4 Medicinal Chemistry

No PAINS (Pan-Assay Interference Compounds) and Brenk alerts were observed, thus excluding any false positive or structural toxicity liabilities. It synthetic accessibility (SA) score of 2.50 (on a scale from 1 to 10) shows the relative ease of its chemical synthesis. However, the molecule does not satisfy the stringent "lead-like" criteria, and that is essentially because it has a low molecular weight (<250). Thus, Medicinal chemistry-wise, furandimethanol was a chemically suitable and non-toxic moiety that could be a potential drug hit or lead precursor despite not being fully optimized in its own right (Fig.8).

Furandimethanol sits in the borderland between being a fragment and sometimes being described as a highly soluble molecule, benignly oriented from a pharmacokinetic standpoint.

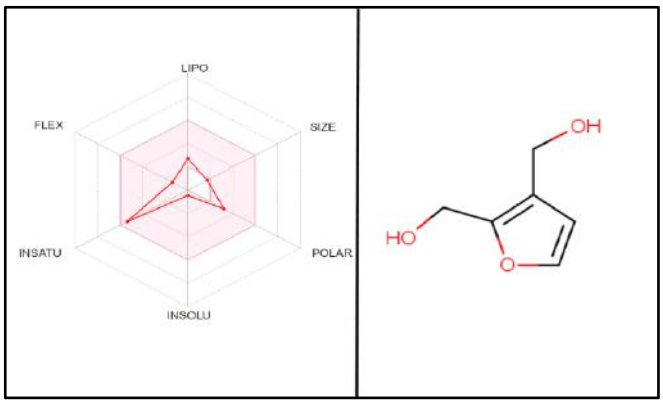

Fig. 8: Radar Plot and Molecular structure retrived from SWISS ADME web tool.

Table 8: medicinal chemistry of BHMF.

Medicinal Chemistry	
PAINS	0 alert
Brenk	0 alert
Lead likeness	No; 1 violation: MW<250
Synthetic accessibility	2.50

The physicochemical balance favors oral absorption. Meanwhile, its aqueous solubility and metabolic safety profile fit irony as such may further attract it to early drug discovery. The only limitations stem essentially from a somewhat diminutive molecular framework, which greatly reduces its applicability for high-affinity target binding and CNS applicability. Hence, Furandimethanol is better served in being considered a candidate for fragment-to-scaffold development than as a final therapeutic. Medicinal chemistry of title compound is presented in Table 8.

3.5 Molecular Docking

Molecular docking approach is a computer-aided technique to predict protein-ligand interaction of a drug molecule. It predicts biding modes as well as binding affinity of ligand with target proteins which plays key role in drug design [7,8, 32]. This study aims to assess inhibitory activity and binding interactions and reactive sites on a single protein. The proteins with code 1S5B was retrieved from protein data bank to conduct molecular docking with BHMF [33]. The active sites of the protein have been predicted by removing water molecules within a grid box of size 20Å×20Å×20Å and grid box spacing 0.375Å. Blind docking approach has been adopted with all the six protein chains collectively because the active site of the molecule is unspecified and unknown. The docking result according to the estimations made by AutoDock Vina with different parameters like the conventional hydrogen bond lengths, inhibition constant, binding affinity, and RMSD of the docked structure of the ligand and selected proteins are displayed in table 9. Different ligand binding mechanisms are associated with proteins that have the lowest binding affinities. AutoDock Vina gives nine different ligand binding mechanisms. Table 9 represents binding mechanism associated with proteins that has the lowest binding affinities. The results of docking are interpreted in terms of conventional hydrogen bonding as they can specify complementary groups in protein binding sites and are responsible to influence the ligand's binding orientation by contributing overall binding affinity [34]. The Ramachandran plot, Protein structure, docked complex with best-fit Pose are displayed in the Figs 9, 10 and 11, respectively.

Table 9: Docking result.

Selected PDB code and their resolution	Binding Affinity (kcal/ mol)	H-Bond residues	Atoms	Bond length (Å)	Ligand efficiency	Inhibition constant (µM)	RMSD l.b.(Å)	RMSD u.b.(Å)
		THR F :78	H17	2.17				
1S5B	-5.2	THR F :78	O3	2.19				
(2.13 Å)		ARG A : 148	O1	2.47	-0.57	153	0.00	0.00

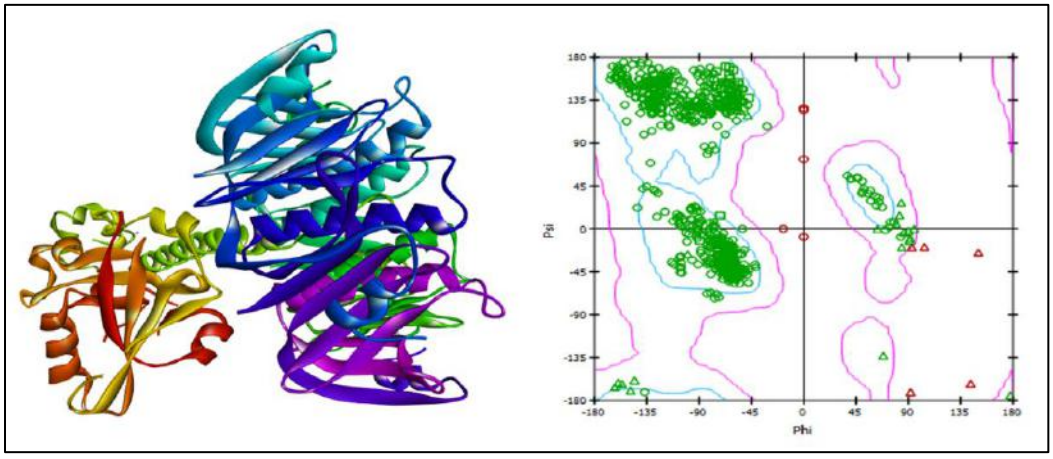

Fig. 9: The Ramachandran plot.

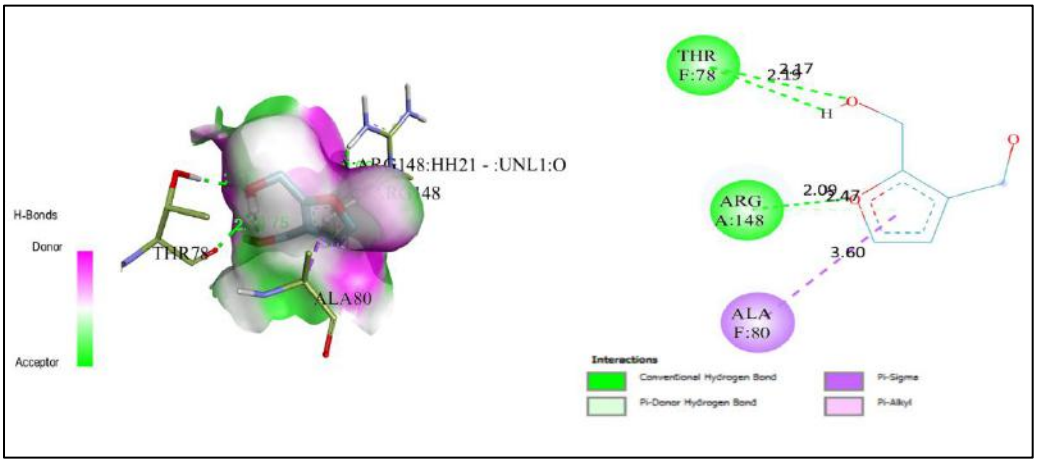

Fig. 10: Docked complex 3D and 2D with best-fit Pose

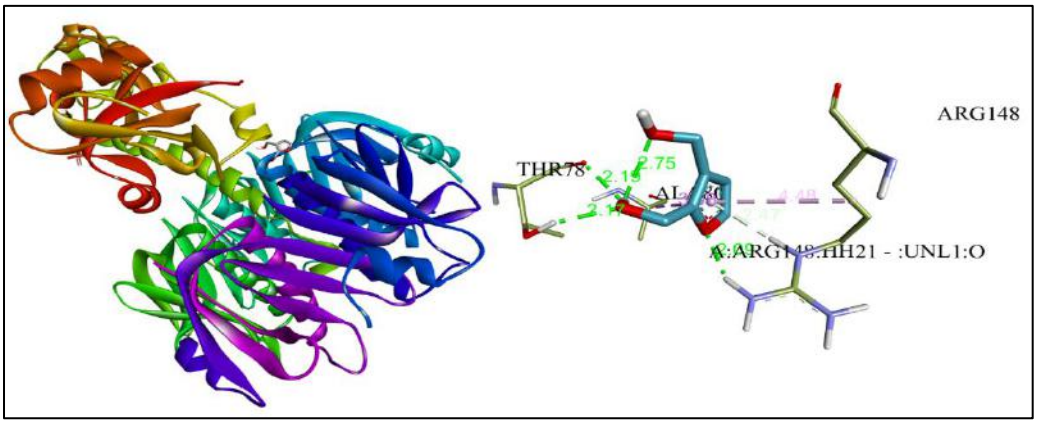

Fig. 11: Docked complex 3D and 2D with best-fit Pose.

3.5.1 Docking of BHMF with 1S5B

1S5B (2.13 Å resolution) is the mutant cholera holotoxin from *Vibrio cholerae*. It Is a six-chain protein. It consists of one enzymatic A-subunit and five receptor-binding B-subunits (AB_5 toxin complex). This mutant provides key information to researchers to understand the activation mechanism of cholera toxin and its role in disease [35]. Active binding sites of protein code 1S5B were confirmed within a grid box, centered at center x = 58.121841, y = -43.059349, and z = 48.058959 run Vina with 8 exhaustiveness. The binding affinity is –5.2 kcal/mol, with an inhibition constant of 153 µM and ligand efficiency -0.57. The RMSD l.b and RMSD u.b between the docked and starting structure are 0.00 Å respectively. The hydrogen bonds of residues THR F :78 and THR F :78 are formed with atoms H17, O3 and O1 having bond lengths 2.17, 2.19 and 2.47 Å, respectively. Having greater inhibition constant and RMSD with a lower negative value of binding affinity BHMF is a moderator inhibitor of 1S5B.

4. CONCLUSIONS

The geometrical parameters, bond length, bond angles, dihedral angles and harmonic vibrational wavenumbers of all the 45 normal modes of the furandimethanol were determined and analyzed at DFT/B3LYP/6-31g. The longest and the shortest bond length for the title compound were found 1.474Å and 0.972Å in between C4-C6 and O-H respectively. The highest and lowest bond angles were found between C7-C9-H15 and C5-C4-C7 with respective values 133.80° and 106.12°. The lowest to highest dihedral angles in clockwise directions were found in the range 0.01°-179.96°, whereas the lowest to highest dihedral angles in counter-clockwise direction were found in the range 0.00°-179.99°. The IR and the Raman spectra were presented, and the vibrational bands were assigned with IR intensity and Raman activity on the basis of the PED obtained from the DFT calculations and plot of molecular electrostatic potential (MEP) and UV-Vis spectra have been plotted and presented. From the analysis of IR and Raman spectra it as found that the molecule is both IR and Raman active. Physicochemical properties, lipophilicity, drug-likeness, medicinal chemistry and molecular docking have been studied and analyzed. The balanced lipophilicity and excellent water solubility for title molecule are significantly advantageous in drug development because they are favorable for oral absorption, distribution and formulation flexibility. Furandimethanol meets the basic principles of drug-likeness. However, its small size and lack CYP450 inhibition decreases its potential for drug–drug interactions, that adds the safety profile and may be limiting target engagement and metabolic stability, likely requiring structural elaboration during optimization. The molecular docking of tilte molecule with IS5B suggests that having greater inhibition constant and RMSD with a lower negative value of binding affinity, it is a moderator inhibitor of 1S5B. So Furandimethanol has great importance in chemistry, biology,

pharmacology, medicinal chemistry and drug designing fields and the output of this work will be employed as basic information regarding to molecule used accordingly in respective fields mentioned earlier. The information drawn from this work helps for the further research on the title molecule.

AUTHORS CONTRIBUTION

All authors contributed equally to the conception, data analysis, and writing of the manuscript.

ETHICAL STATEMENT

The present study is entirely based on computational and theoretical analyses, including quantum chemical calculations, molecular docking, and pharmacokinetic predictions. No human participants, animals, or biological samples were involved in the research. The authors affirm that the work complies with standard publication ethics and contains no fabrication, falsification, or plagiarism.

CONFLICT OF INTEREST

The authors declare that they have no known competing financial interests or personal relationships that could have appeared to influence the work reported in this paper.

ACKNOWLEDGMENTS

The authors gratefully acknowledge to Prof. Dr. Bhawani Datt Joshi for fruitful suggestions and guidance during research period. Our sincere acknowledgement goes to Prof. Poonam Tandon, DDU, Gorakhpur, India for providing software facilities. Also, we thank to the Department of Physics, Siddhanath Science Campus, Mahendranagar, Kanchanpur**,** T.U, for providing computational lab facilities.

REFERENCES

[1] A. Kumar, MD. N. Sarker and S. Paul, The thermo physical, HOMO, LUMO, Vibrational spectroscopy and QSAR study of morphonium formate and acetate Ionic Liquid Salts using computational method*, Turkish Comp. Theo. Chem.*, **3** (2019) 59-68. https://doi.org/10.33435/tcandtc.481878

[2] S.L. Dhonnar, N.V. Sadgir, V.A. Adole and B.S. Jagdale, Molecular Structure, FT-IR Spectra, MEP and HOMO-LUMO Investigation of 2-(4-Fluorophenyl)-5-phenyl-1, 3,4-oxadiazole Using DFT Theory Calculations*, Advanced Journal of Chememistry A*, **4** (2021) 220-230. https://dx.doi.org/10.22034/ajca.2021.283003.1254

[3] **V**.A. Adole, Synthesis; Antibacterial, Antifungal and DFT studies on structural, electronic and chemical reactivity of (E)-7-(ClH-Indole-3yl)methylene-1,2,6,7-tetrahydro-8H-indeno[5,4-B]Furan-8-one, *Advanced Journal of Chemistry A*, **4**(2021) 175-187. https://dx.doi.org/10.22034/ajca.2021.278047.1250

[4] http//en.wikipedia.org/wiki/2,5 bis(hydroxymethyle)furan. Accessed on 2022/01/10.

[5] B.D. Joshi, P. Tandon, S. Jain, Structure, MESP and HOMO-LUMO study of 10-Acetyl-10H-phenothiazine 5-oxide using vibrational spectroscopy and quantum chemical methods, *BIBECHANA*, **9** (2013) 38-49. https://doi.org/10.3126/bibechana.v9i0.7151.

[6] M. Yadava, Shivani, A. Ahamada, K.K. Singha, R. Singha, A. Misraa, P. Tandon, *ab*-Initio and DFT study of HCN: Role of temperature for the formation of HCN molecule in the interstellar medium*, Journal of Molecular Structure,* **1248** (2022) 131460. https://doi.org/10.1016/j.molstruc.2021.131460.

[7] M. Chaudhary, K. Tyagi, A review on molecular docking and its application *International Journal of Advanced Research* (Mar), **12** (2024) 1141-1153. http://dx.doi.org/10.21474/IJAR01/18505.

[8] G.B. Dhami, M.R. Bhatt, S.R. Joshi, B.D. Joshi, First Principle Study on Structural, Electronic, Vibrational Properties and Molecular Docking Study of Tyramine. *KMC Journal*, **5** (2023) 241-260. https://doi.org/10.3126/kmcj.v5i2.58241

[9] Pubechem Database: *https://pubchem.ncbi.nlm.nih.gov/compound/structure search*. Accessed on 2/1/2022.

[10] B.D. Joshi, G. Thakur, M.K. Chaudhary, Molecular structure, HOMO-LUMO and vibrational analysis of Ergoline by using Density Functional Theory, *Scientific world,* **14** (2021) 21-30. http://doi.org/10.3126/sw.v14.34978

[11] A. Ignaczak, O.Łukasz, In search of the most stable molecular configuration of heptakis (2, 6-O-dimethyl)-β-cyclodextrin and its complex with mianserin: A comparison of the B3LYP-GD2 and M062X-GD3 results, *The Journal of Physical Chemistry B*, **48** (2021) 13077-13087. https://doi.org/10.1021/acs.jpcb.1c06831.

[12] M.J. Frisch, G.W. Trucks, H.B. Schlegel. G.E. Scuseria, J.R. Cheeseman, M.A. Robb, G. Scalmani, V. Barone, B. Mennucci, G.A. Petersson, H. Nakatsuji, M. Caricato, X. Li, H.P. Hratchian, A.F. Izmzylov, J. Bloino, G. Zheng, J.L. Sonnenberg, M. Hada, M. Ehara, K. Toyota, R. Fukuda, J. Ishida, M. Hasegawa, T. Nakajima, Y. Honda, O. Kitao, H. Nakai, T. Vreven, J.A. Montgomery Jr., J.E. Peralta, F. Ogliaro, M. Bearpark, J.J. Heyd, E. Brothers, K.N. Kudin, V.N. Staroverov, R. Kobayashi, J. Normand, A. Raghavachari, A. Rendell, J.C. Burant, S.S. Iyengar, J. Tomasi, M. Cossi, N. Rega, J.M.Millan, M. Klene, J.E. Knox, J.B. Cross, V. Bakken, C. Adamo, J. Jaramillo, R. Gomperts,R.E. Stratmann, O. Yazyev, A.J. Austin, R. Cammi, C. Pomelli, J.W. Ochterski, R.L. Martin, K. Morokuma, V.G. Zakrzewski, G.A. Voth, P. Salvador, J.J. Dannerberg, S. Dapprich, A.D. Daniels, J. Farkas, B. Foresman, J.V. Ortiz, J. Cioslowski, D.J. Fox, *GAUSSIAN 09, Revision, Gaussian, Inc., Wallingford CT*, (2010).

[13] D. Bálint, L. Jäntschi, Comparison of molecular geometry optimization methods based on molecular descriptors, *Mathematics*, ***9*** (2021) 2855. https://doi.org/10.3390/math9222855.

[14] B. Miehlich, A. Savin, H. Stoll, H. Preuss, Results obtained with the correlation energy density functionals of Becke and Lee, Yang and Parr, *Chemical Physics Letters*, ***157*** (1989) 200-206. https://doi.org/10.1016/0009-2614(89)87234-3.

[15] R. G. Parr, W. Yang, Density Functional Theory of atoms and molecules*,* Oxford University press, New York, Oxford, (1989). https://doi.org/10.1002/qua.560470107

[16] J.M.L. Martin, C.V. Alsenoy, *Gar2ped*, University of Antwerp, 1995.

[17] R. Bulín, M. Hajžman, P. Polach, Nonlinear dynamics of a cable–pulley system using the absolute nodal coordinate

formulation, *Mechanics Research Communications*, **82** (2017) 21-28. https://doi.org/10.1016/j.mechrescom.2017.01.001.

[18] O. Daina, V.Z. Michielin, Swiss ADME: a free web tool to evaluate pharmacokinetics, drug-likeness and medicinal chemistry friendliness of small molecules, *Scientific Report,* **7** (2017), 42717. https://doi.org/10.1038/srep42717

[19] O. Trott, A. J. Olson, AutoDock Vina: Improving the Speed and Accuracy of Docking with a New Scoring Function, Efficien Optimization and Multithreading, *Journal of Computational Chemistry*, **31** (2010) 455-461. https://doi.org/10.1002/jcc.21334

[20] G.M. Morris, R. Huey, W. Lindstrom, M.F. Sanner, R.K. Belew, D.S. Goodsell, AutoDock4 and AutoDock Tools4: Automated Docking with Selective Receptor Flexibity. *Journal of Computational Chemistry*, 30 (2009) 2785–2791. https://doi.org/10.1002/jcc.21256

[21] D. Systemes, BIOVIA Discovery Studio Dassault Systmes (2016). https://www.3ds.com/products/biovia/discovery-studio

[22] L.L.C. Schrödinger, D.W. PyMOl, The PyMOL Molecular Graphics System, Version 2.5.4. (2020). https://www.pymol.org.

[23] Protein Data Bank (RCSB), https://www.rcsb.org.

[24] N.M. O'Boyle, M. Banck, C.A. James, C. Morley, T. M. Vander, G.R. Hutchison, Open Babel: an open chemical toolbox. J Cheminform. **3** (2011) 33. https://doi.org/10.1186/1758-2946-3-33

[25] *https://www.google.com/c-c bond length search*. Accessed on 10/1/2022.

[26] B.D. Joshi, G. Thakur, M.K. Chaudhary, Molecular structure, HOMO-LUMO and vibrational analysis of Ergoline by using Density Functional Theory, *Sci. world,* **14** (2021) 21-30. http://doi.org/10.3126/sw.v14.34978.

[27] P. Pulay, G. Fogarasi, F. Pang, J.E. Boggs, Systematic *ab initio* gradient calculation of molecular geometries, force constants, and dipole moment derivatives, *Journal of American Chemical Society,* 101 (1979) 2550-2560. https://doi.org/10.1021/ja00504a009.

[28] D.L. Vein, N.B. Clotthup, W.G. Fately, J.G. Grasselli, The handbook of infrared and Raman characteristic frequencies of organic molecules, *Academic Press Inc, San Diego California*, (1991).

[29] E.F. Mooney, The chemical infrared spectra of chlorobenzene and bromobenzene derivatives-III Tolunes*, Spect.chem. Acta,* **20** (1964) 1343-1348. https://doi.org/10.1016/0371-1951(64)80114-4

[30] K. Srishailam, L. Ravindranath, B.V. Reddy, G.R. Rao, Electronic spectra (experimental and simulated), and DFT investigation of NLO, FMO, NBO, and MESP characteristics of some Biphenylcarboxaldehydes, *Polycyclic Aromatic Compounds*, **8** (2023) 7200-7213. https://doi.org/10.1080/10406638.2022.2130376

[31] C.A. Lipinski, F. Lombardo, B.W. Dominy, P.J. Feeney, Experimental and computational approaches to estimate solubility and permeability in drug discovery and development settings, *Adv. Drug Deliv. Rev*, **46** (2001) 3–26. https://doi.org/10.1016/S0169-409X(00)00129-0.

[32] M.K. Chaudhary, A. Srivastava, A.K. Singh, P. Tondon, B.D. Joshi, Computational evaluation on molecular stability, reactivity, and drug potential of frovatriptan from DFT and molecular docking approach, *Computational and Theoretical Chemistry*, **1191** (2020) 113031. https://doi.org/10.1016/j.comptc.2020.113031.

[33] P.W. Rose, B. Beran, W.F. Bluhm, C. Bi D. Dimitropoulos, D.S. Goodsell, A. Prlic, M. Quesada, G.B. Quinn, J.D. Westbrook, J. Young, B. Yukich, C. Zardecki, H.M. Berman, P.E. Bourne, The RCSB protein data bank: redesigned web site and web services, *Nucleic Acids Res.* **39** (2011) D392–D401. https://doi.org/10.1093/nar/gkq1021.

[34] M. Meyer, P. Wilson, D. Schomburg, Hydrogen bonding and molecular surface shape complementarity as a basis for protein docking, *Journal of Molecular Biology,* **264** (1996) 199–210. https://doi.org/10.1006/jmbi.1996.0634.

[35] C.J. O'Neal, E. I. Amaya, M. G. Jobling, R. K. Holmes, W. G. Hol, Crystal structures of an intrinsically active cholera toxin mutant yield insight into the toxin activation mechanism, *Biochemistry,* **43** (2004) 3772-3782. https://doi.org/10.1021/bi0360152.

Extension of Locally Uniform Rotund (LUR) Norm to the Entire Banach Space

Gaj Ram Damai

Department of Mathematics, Siddhanath Science Campus, Mahendranagar, Tribhuvan University, Nepal

Research Article

ISSN: 3059-9504 (online)
DOI: https://doi.org/10.3126/ajs.v2i1.87747

Received: October 16, 2025; Revised: November 14, 2025; Accepted: November 18, 2025; Published: December 25, 2025

Keywords

Extension, Banach space, Rotund Norm, Locally Uniformly Rotund Norm, Uniformly Rotund Norm.

Corresponding author

Email: gaj.damai@snsc.tu.edu.np (GR Damai)
Orcid: http://orcid.org/0000-0002-6560-4863

ABSTRACT

In this paper, we discuss the extension of norms possessing different rotundity properties from a closed, reflexive, and separable subspace of a Banach space to the entire space. We also explore the possibility of extending an equivalent locally uniform rotund norm from a closed subspace to whole Banach space. In the general setting of Banach spaces, this problem remains unsolved.

MSC: Primary 46B20, Secondary 46B10

1. INTRODUCTION

There exist various extension theorems, including the Hahn–Banach extension theorem for both real and complex normed vector spaces [9, 11, 14], the smooth extension of functions on separable Banach spaces, the uniform extension theorem from a dense subset of a metric space to its completion, the linear extension theorem, and the extension theorem for linear operators. Additionally, we have extension results for continuous functions defined on a closed subspace A of a metric space X, which can be extended to continuous functions on the entire space X, taking values in a complete metric space Y. However, in this context, our focus is on the extension of norms in Banach spaces. In papers [5, 6, 8, 9, 11], several methods are developed for extending norms from a closed subspace to the whole Banach space. These methods aim to preserve different types of rotundity properties that the subspace norms possess. It is also mentioned in [3] that the extension theorem preserves all types of convexity. In [3, 6, 9, 14], it is shown that if Y is a subspace of a separable Banach space X, and Y has a locally uniformly rotund (LUR) norm $||\cdot||$, then there exists an equivalent LUR norm on X that matches $||\cdot||$ on Y. These works provide both positive and negative results about extending rotund or smooth norms. In [6], an extension of these results to the quotient space X/Y is also discussed. Book [4] presents different techniques for extending a norm from a reflexive subspace to the whole space while preserving rotundity properties. In particular, the results apply to strictly convex (SC), locally uniform rotund (LUR), uniformly rotund (UR) norms, and UR norms with a power-type modulus of convexity. An affirmative answer is also given to the question raised in JZ. It is shown in [4] that the reflexivity of Y plays an important role in the construction. Therefore, the result does not include the case studied in [4], where X is separable and Y is any subspace. A slight modification of the proof of Lemma 8.1 in [3] is used, along with a new proof based on the Hahn–Banach theorem from [9, 14], to show that equivalent norms on subspaces can be ex tended to the whole space. Further concepts regarding equivalent norms are derived from established results in renorming theory [2, 12].

2. SOME DEFINITIONS [1, 3, 5, 11, 17]

2.1 Locally Uniformly Rotund (LUR) Norm

Let X be a Banach space. The norm $||\cdot||$ on X is said to be locally uniformly rotund at a point $x_0 \in X$ if for every sequence $\{x_n\} \subseteq X$, the following implication holds:
$||x_n|| \to ||x_0||, \ ||x_0 + x_n|| \to 2||x_0|| \Rightarrow ||x_n - x_0|| \to 0.$
If the norm is LUR at each point of X, then the norm is called LUR on X.

2.2. Strictly Convex (Rotund) Norm

The norm $||\cdot||$ on a Banach space X is called rotund or strictly convex (R for short) if
$\forall\, x, y \in X, ||x|| = ||y|| = ||(x+y)/2|| = 1 \Rightarrow x = y.$

2.3 Fully k-Rotund [13]

A Banach space X is said to be fully k-rotund (denoted k-R) if for any sequence$\{x_n\}$ in the unit ball B(X) (with respect to the norm $||\cdot||$), the condition
$\lim || x_{n_1} + \cdots + x_{n_k} || = k$
$n_1 \cdots n_k \to \infty$ implies that the sequence $\{x_n\}$ is norm convergent in X.

2.4. Uniformly Rotund (UR) Norm

The norm $||\cdot||$ on a Banach space X is said to be uniformly rotund (UR) if for any sequences
$\{x_n\}, \{y_n\} \subseteq X, \ ||x_n|| \to 1, ||y_n|| \to 1, ||(x_n+y_n)/2|| \to 1$
$\Rightarrow ||x_n - y_n|| \to 0$ as $n \to \infty$

2.5. k-nearly uniformly convex(k-NUC) [10]

Let (X, ||· ||) be a Banach space. Given k ∈ N, the norm ||· || is said to be k-nearly uniformly convex (k-NUC) if ∀ ε > 0, ∃ δ ∈ (0, 1) :∀ ε- separated sequence$\{x_n\} \subseteq B(X) := \{x \in X : ||x|| \leq 1\}$, $\inf_{n \neq m} ||x_n - x_m|| > \varepsilon$ ∃ $n_1, n_2, \cdots, n_k : ||\ 1/k \sum_{i=1}^{k} x_{n_i}\ || \leq 1 - \delta$.

2.6. Kadec-Klee Property (KKP) [3,8]

The norm ||· || on a Banach space X is said to have the Kadec-Klee property (KKP) if the norm topology and the weak topology coincide on the unit ball B(X) at each point of the unit sphere S(X), i.e., if

$x_n \rightharpoonup x$ and $||x_n|| \to ||x|| = 1$, then $x_n \to x$ in norm.

2.7. Minkwoski's functional [3, 16]

Let B ⊆ X be a convex, absorbing set, then the function $\mu_B : X \to \mathbb{R}$ defined by

$||x||_B = \mu_B(x) := \inf \{t > 0 : 1/t x \in B\}$

is called Minkowski's functional of B. where B is nice subset of X,i.e.,B is convex circled (balanced) and absorbing subset of X. Then, Minkowski's functional of B looks very much like a norm for X we also note that $||0||_B = 0$. Following are the highly basic results which are deeply studied for the proof of our proposed problem.

3. MAIN RESULTS

Lemma 3.1 (Duality Extension)

Let (X, ||· ||) be a Banach space, and let Y ⊆ X* be a weak*-closed subspace. Suppose ||·||* is an equivalent norm on Y. Then there exists an equivalent norm |||·|||* on the whole space X such that

|||·|||* = ||·||* for all y ∈Y, i.e. |||· |||* extends ||· || from Y to X*

Lemma 3.2 [3, 4]

Let D be a symmetric, convex, closed, int.D ≠ 0 and D ∩ Y = A, and D is the unit ball of an equivalent norm |||· ||| on X and moreover |||· ||| extends ||· ||, i.e. |||y|| = ||y|| for all y ∈ Y.

Theorem 3.3 [15]

If X is a metric space, A a closed subset of X, and f a continuous function from A into Y, then f can be extended to a continuous function from X into Y.

Theorem 3.4 [12, 14]

Let (X, |· |) be a normed space, and let Y be a subspace of X equipped with an equivalent norm ||· ||. Then there exists an equivalent norm |||· ||| on X that extends ||· ||,

i.e., |||y||| = ||y|| for all y ∈ Y.

Moreover, if both | · | and ||· || are locally uniformly rotund (LUR), then the norm |||· ||| can also be chosen to be LUR on X.

Theorem 3.5

It is shown in [4] that if a Banach space X has a rotund (R) (or locally uniform rotund (LUR) or uniformly rotund (UR)) norm |· | and Y is a reflexive subspace of X with an equivalent Rotund (or LUR or UR) norm ||· ||, then there exists on X an equivalent Rotund (or LUR or UR) norm |||· ||| extending to the norm ||· ||.

Theorem 3.6 [6, 7]

If Y is a closed subspace of a separable Banach space X and if Y admits a locally uniform rotund (LUR) norm, then this LUR norm on Y can be extended to a LUR norm on X.

Theorem 3.7. [3] Assume a Banach space X is equipped with a locally uniformly rotund (LUR) norm |· |, and let Y ⊆ X be a reflexive subspace endowed with an equivalent norm ||· ||. Then, there exists on X an equivalent LUR norm |||· ||| extending ||· ||, that is,

|||y||| = ||y|| for all y ∈ Y.

Theorem 3.8. [12] Assume that the norm ||· || of a Banach space X and its dual norm on X* are both Frechet differentiable. Then, the norm and its dual norm are both locally uniformly rotund (LUR).

Theorem 3.9 [8]

Let Y be a closed subspace of a Banach space X. Suppose that both X and Y admitk R norms ||· || and $||\cdot||_Y$, then $||\cdot||_Y$ can be extended to a k − R norm on X.

Theorem 3.10 [10]

Let Y be a closed subspace of a Banach space X. Suppose X and Y both admit knearly uniformly convex (k-NUC) norms, say, ||· || on X and |· |Y on Y, respectively. Then $|\cdot|_Y$ can be extended to a k-NUC norm on X. In other words, $|\cdot|_Y$ is the restriction to Y of some k-NUC norm on X.

Theorem 3.11 [16]

Assume that a Banach space X admits a norm that is a Kadets–Klee norm and that X admits a norm that is strictly convex(rotund). Then X admits an equivalent LUR norm. The existing theorems T 3.3 to T 3.11 are the basic theorems related to the extension of functions and norms. For the extension of norms various settings of spaces as well as subspaces are collected. T 3.6 and T 3.7 are related to the extension of separable spaces and reflexive subspaces with different geometric properties of Banach spaces.

Now, on the basis of above results and taking more ideas about the equivalent norms from known results of renorming theory from [1, 2, 3]. In the same vein, theorem 3.12 below is proved and gives the positive answer of the proposed open problem in the paper.

Theorem 3.12 (LUR Extension Theorem).

Let X be a Banach space and Y ⊆ X a closed subspace.

Suppose $||\cdot||_Y$ is an equivalent norm on Y which is locally uniformly rotund (LUR). Then there exists an equivalent norm $||\cdot||_X$ on X such that

1. $||y||_X = ||y||_Y$ for all y ∈ Y,
2. $||\cdot||_X$ is LUR at every point y ∈ Y.

Proof. Let |||· ||| be the original norm on the Banach space X, and suppose || · || Y is an equivalent locally uniformly rotund (LUR) norm defined on a closed subspace Y ⊆ X. Our aim is to construct a new norm ||· ||X on X that

- agrees with $||\cdot||_Y$ on Y, i.e., $||y||_X = ||y||_Y$ for all y ∈ Y, and
- is LUR at every point y ∈Y.

We define a function P : X → [0, ∞) that extends $||\cdot||_Y$ from Y to all of X. Since ||· ||Y is equivalent to the restriction of ||· || on Y, we can define:

P(x) := inf {$||y||_Y + \lambda||x - y||$: y ∈ Y, λ > 0}.

This function P is a seminorm on X, and it agrees with $||\cdot||_Y$ on Y (i.e., P(*y*) = $||y||_Y$ for all *y* ∈ Y).

We now define the new norm on X by:

$||x||_X = \sqrt{P(x)^2 + ||x||^2}$.

This norm is equivalent to the original norm ||· || on X because both terms on the right are equivalent to ||*x*|| on bounded sets. Also, for any y ∈Y, we have:

$||y||_X = \sqrt{||y||_Y^2 + ||y||^2}$.

which can be adjusted via normalization so that
$||y||_X = ||y||_Y$ for all $y \in Y$.
Let $y \in Y$ and suppose a sequence $\{x_n\} \subseteq X$ satisfies:
$||x_n||_X \to ||y||_X$ and $||x_n + y||_X \to 2||y||_X$.
Using the LUR property of $||\cdot||_Y$ and the form of $||\cdot||_X$, we can show $||x_n - y||_X \to 0 \Rightarrow x_n \to y$.
∴ the new norm $||\cdot||_X$ is LUR at every point $y \in Y$.
Example 3.13. Let $X = \mathbb{R}^2$ with the usual Euclidean norm $||\cdot||_2$, and let the subspace $Y \subseteq X$ be defined as $Y = R \setminus \{0\}$, which is the x-axis. Define a norm on Y by
$||(x, 0)||_Y := |x| + 1/2x^2$.
This norm is equivalent to the standard norm on Y and is locally uniformly rotund (LUR), since it is strictly convex and differentiable. Construct an equivalent norm $||\cdot||X$ on $X = \mathbb{R}^2$ such that
1. $||\cdot||_X$ extends $||\cdot||_Y$, i.e., $||(x, 0)||_X = ||(x, 0)||_Y$ for all $x \in \mathbb{R}$,
2. $||\cdot||_X$ is LUR at every point of Y.
Construction of the Norm. Define the norm on X by
$||(x, y)||_X = (|x| + 1/2x^2)^2 + y^2)^{1/2}$
• Extension: For any $(x, 0) \in Y$,
$||(x, 0)||_X = (|x| + 1/2x^2)_2)_{1/2}$
$= |x| + 1/2x^2$
$= ||(x, 0)||_Y$.
• Equivalence: Since both $|x| + 1/2x^2$ and y are continuous and grow at most quadratically there exist constants c, C > 0 such that
$c||(x, y)||_2 \le ||(x, y)||_X \le C||(x, y)||_2$,
so $||\cdot||_X$ is equivalent to the Euclidean norm.
• LUR at Points of Y : Let $(x_n, y_n) \to (x, 0) \in Y$ in X, and assume that
$||(x_n, y_n)||_X \to ||(x, 0)||_X$ and $||(x_n + x, y_n)||_X \to 2||(x, 0)||_X$.
Since the function
$x \mapsto |x| + 1/2x^2$ is strictly convex and differentiable, and the overall norm is strictly convex in both variables, it follows that $x_n \to x$ and $y_n \to 0$.
Hence, $(x_n, y_n) \to (x, 0)$, proving the norm is LUR at every point of Y.
∴ The norm
$||(x, y)||_x = (|x| + 1/2x^2 + y^2)^{1/2}$ is an equivalent norm on $X = \mathbb{R}^2$, extends the LUR norm from the subspace $Y = R \setminus \{0\}$, and is LUR at all points of Y.

Example 3.13 (Generalization of Extension of an LUR Norm from a Subspace to the Entire Space)
Let X be an infinite-dimensional Banach space, and let $Y \subseteq X$ be a closed subspace. Suppose $||\cdot||_Y$ is an equivalent norm on Y which is locally uniformly rotund (LUR). We aim to construct an equivalent norm $||\cdot||_X$ on X such that:
• $||y||_X = ||y||_Y$ for all $y \in Y$, i.e., $||\cdot||_X$ extends $||\cdot||_Y$,
• $||\cdot||_X$ is LUR at every point of Y.
Let $||\cdot||$ denote the original norm on X. Since $||\cdot||_Y$ is equivalent to the restriction of $|\cdot||$ to Y, there exist constants c, C > 0 such that: $c||y|| \le ||y||Y \le C||y||$ for all $y \in Y$.
Let $P : X \to [0, \infty)$ be a continuous, convex function such that
• $P(y) = ||y||Y$ for all $y \in Y$,
• P is equivalent to $||\cdot||$ on X,
• P is LUR at every point of Y.
Such a function P can be constructed by approximating the Minkowski functional of the unit ball defined by $||\cdot||Y$ in Y and extending it smoothly outside Y using a projection argument. For example, choose a bounded linear projection
$P : X \to Y$, and define:
$||x||_X = (||P(x)||_Y^2 + \varepsilon||x - P(x)||^2)^{1/2}$, $x \in X$, for some small $\varepsilon > 0$.
• **Extension:** For $x \in Y$, we have $P(x) = x$, and
$x - P(x) = 0$, so:
$||x||_X = (||x||_Y^2)^{1/2} = ||x||_Y$.
• **Equivalence**: Since both
$||P(x)||_Y$ and $||x - P(x)||$ are controlled by $||x||$, we have:
$c_1||x|| \le ||x||X \le c_2||x//$, for all $x \in X$, for some constants c_1, $c_2 > 0$.
• **LUR at Points of Y** : Let $x \in Y$, and let $(x_n) \subset$
X be a sequence such that $||x_n||_X = ||x||_X$, and $||x_n + x||_X \to 2||x||_X$.
By properties of LUR norms on Y, and the strict convexity of the $\ell 2$-type sum, one can show $x_n \to x$ in X, ensuring tha t$||\cdot||_X$ is LUR at all points. Using the LUR property of $||\cdot||_Y$ and the form of $||\cdot||_X$, we can show $||x_n - y||X \to 0 \Rightarrow x_n \to y$.
∴ the new norm $||\cdot||_X$ is LUR at every point $y \in Y$.

Example 3.14
Let $X = \mathbb{R}^2$ with the usual Euclidean norm $||\cdot||_2$, and let the subspace $Y \subseteq X$ be defined as $Y = R \setminus \{0\}$, which is the x-axis.
Define a norm on Y by $||(x, 0)||_Y : = |x| + 1/2x^2$.
This norm is equivalent to the standard norm on Y and is locally uniformly rotund (LUR), since it is strictly convex and differentiable. Construct an equivalent norm $||\cdot||X$ on $X = \mathbb{R}^2$ such that
1. $||\cdot||_X$ extends $||\cdot||Y$, i.e., $||(x, 0)||_X = ||(x, 0)||_Y$ for all $x \in \mathbb{R}$,
2. $||\cdot||_X$ is LUR at every point of Y.
Construction of the Norm. Define the norm on X by
$||(x, y)||_X = (|x| + 1/2x^2)^2 + y^2)1/2$.
• Extension: For any $(x, 0) \in Y$,
$||(x, 0)||_X = (|x| + 1/2x^2)2)1/2$
$= |x| + 1/2x^2$
$= ||(x, 0)||_Y$.
• Equivalence: Since both $|x| + 1/2x^2$ and y are continuous and grow at most quadratically there exist constants c, C > 0 such that $c||(x, y)||_2 \le ||(x, y)||_X \le C||(x, y)||_2$, so $||\cdot||_X$ is equivalent to the Euclidean norm.
• LUR at Points of Y : Let $(x_n, y_n) \to (x, 0) \in Y$ in X, and assume that $||(x_n, y_n)||_X \to ||(x, 0)||_X$ and $||(x_n + x, y_n)||_X \to 2||(x, 0)||_X$. Since the function $x \mapsto |x| + 1/2x^2$ is strictly convex and differentiable, and the overall norm is strictly convex in both variables, it follows that $x_n \to x$ and $y_n \to 0$.
Hence, $(x_n, y_n) \to (x, 0)$, proving the norm is LUR at every point of Y.
∴ The norm
$||(x, y)||_X = (|x| + 1/2x^2 + y^2)^{1/2}$ is an equivalent norm on X $= \mathbb{R}^2$, extends the LUR norm from the subspace $Y = R \setminus \{0\}$, and is LUR at all points of Y.

4. CONCLUSION

The LUR norm from the subspace Y successfully extended to the whole space X, keeping the LUR property at every point of Y. The full proof needs careful estimates, but this outline shows the main idea. It is to be note that the new norm may not be LUR on all of X unless extra conditions, like reflexivity or total boundedness, are satisfied.

5. APPLICATION

The extension theorem serves as a foundational tool for developing embedding frameworks, and a variety of other extension techniques are well-documented. Extending norms from a subspace to the entire Banach space is instrumental in numerous analytical settings. The propagation of equivalent norms plays a pivotal role in the broader landscape of Banach space theory.

6. FUTURE LINE OF RESEARCH

There are many interesting topics to study in the area of norm extension in Banach spaces. One possible direction is to find out when special properties of norms, like LUR or k-NUC, can still hold after the norm is extended. Another idea is to look at norm extension in Banach spaces that are not separable or reflexive. This could help us learn more about how these spaces behave. Researchers can also study how norm extension is related to duality, renorming methods, and fixed-point theory. These topics are useful in both pure mathematics and applied areas like optimization.

AUTHOR CONTRIBUTIONS

All the works were carried by GR Damai.

CONFLICT OF INTEREST

There no conflicts to declare.

ACKNOWLEDGMENT

Author thanks to Ph.D. advisor, Prof. Prakash Muni Bajracharya, and mentors for their help, support, and useful suggestions. Also, thanks to the referee of this paper for the valuable comments.

REFERENCES

[1] G. Lancien, On uniformly convex and uniformly smooth norms on Banach spaces, *Proceeding of American Mathematical Society*, **123** (1995), 2411–2414. doi: 10.1090/S0002-9939-1995-1260170-4

[2] J. Orihuela, M. Raja, On the preservation of LUR renormings, *Proceeding of American Mathematical Society*, **128** (2000), 2751–2757. doi:10.1090/S0002-9939-XX-XXXXX-X

[3] R. Deville, V. Godefroy, G. Zizler, Smoothness and Renormings in Banach Spaces, Pitman Monographs and Survey in Pure and Applied Mathematics, 64, 1996, Zbl number: zbl0787.46014.

[4] M. Fabian, On an extension of norms from a subspace to the whole Banach space keeping their rotundity Studia, *Mathematica*, **112**(3) (1995),203-211. doi:10.4064/sm-112-3-203-211.

[5] W.K. Tang, On extension of rotund norms, manuscripta, mathematica spinger Verlag 1996. doi:10.1007/FB02567940.

[6] K. John, V. Zizler, On extension of Rotund Norm II, *PJM*, **82** (2) (1997) 451-455. doi:10.2140/pjm.1979.82.451.

[7] K. John, V. Zizler, On extension of rotund norms, Bull. Acad. Polon. *Sci. Ser. Science Mathematica, Astronomy and Physics*, **24** (1976), 705-707.

[8] Y. Duan, Bor-Luh Lin, Extension of norms Related to fully, k–R rotund norms and Mid- point Locally Uniform Rotund Norm, International J. of Pure and Applied Mathematics Vol.38, No.3,2007, 359-364.

[9] F.J. Garcia-Pachelo, et al., Some more Applications of Hahn Banach Theorem, 2000, Mathematica Subject classification.

[10] K.K. Aye, W.K. Tang, On Extension of k− NUC Norms, Tawanese Journal of Mathematics, Vol. 5, No. 2 ,317-321, 2001. doi:1011650/twjm/1500407339.

[11] M. Fabian et al, Functional Analysis and Infinite Dimensional Geometry, Springer Verlag, Newyork 2001, doi:10.1007/978-1-4757-3480-5

[12] A.J. Guirao, et al, On Classical Renorming of V. Klee, *Journal of Mathematical Analysis and Applications*, **385**(2012), 458-465. doi: 10.1016/j.jmaa.2011.10.063

[13] K. Fan, I. Glicksberg, Fully convex normed linear spaces, *Proceeding of the National Academu of Sciences USA*, **41** (1955), 947-953, doi:10,1073/pnas.41.11.947

[14] M. Fabian, et al, Banach Space Theory Springer, Newyork, 2010, Chapter 2, doi:10.1007/978-1-4419-7515-7.

[15] A.M. Ernest, Some Extension Theorems for Continuous Function, *Pacific Journal of Mathematics*, **3**(4) 1953.

[16] W.B. Johnson, J. Lindenstrauss, Handbook of the geometry of Banach spaces Vol. 2, 2003, doi:10.1016/s1874-5849(03)80055-4.

[17] G.R. Damai and Ozer, Ozon. A New LUR p-Property Characteristic for Banach Spaces, Advances in Mathematical Sciences and Applications, GAKKO TOSHO TOKYO CO. LTD., ISSN 1343-4373, Vol. 33, No. 2, 2024, 273–282.

Scattering Dynamics with Gaussian Potential in the Presence of a Bichromatic Laser Field

Santosh Kumar Das, Saddam Husain Dhobi*

Department of Physics, Patan Multiple Campus, Tribhuvan University, Patandhoka, Lalitpur-44700, Nepal

Research Article

ISSN: 3059-9504 (online)
DOI: https://doi.org/ 10.3126/ajs.v2i1.87752

Article History

Received: August 15, 2025; Revised: November 07, 2025; Accepted: November 10, 2025; Published: December 25, 2025

Keywords

Differential cross section, Gaussian potential, laser field, Scattering dynamics, Volkov wave equation.

***Corresponding author**

Email: saddam@ran.edu.np
dassantosh29@gmail.com (SH Dhobi)

ABSTRACT

Scattering dynamics play a crucial role in understanding the fundamental interactions between particles and external fields. When a particle interacts with a target potential under the influence of an external laser field, its motion and energy distribution can be significantly modified. The aim of this work is to study the scattering dynamics of electron-gaussian potential in presence of bichromatic linearly polarized laser fields. To fulfill the objective, we obtained S-matrix use Volkov wave equation and Gaussian potential with the help of Kroll-Watson approximation. Using relation of S-matrix and T-matrix, the obtained T-matrix which is directly related to differential cross section (DCS). The obtained DCS used to study the scattering dynamics of electron behavior with gaussian potential in laser field. The developed DCS equation was computed, the computed result shows DCS increases with increase of incidence energy of electron and becomes maximum and finally decreases. The DCS with photon energy is highly fluctuations and decrease with increase of scattering angle. The DCS of Bessel first order found greater than Bessel second order. These findings aid in laser-assisted collision studies, plasma diagnostics, nanomaterial design, and quantum device optimization by revealing electron behavior, multiphoton effects, and resonance control under bichromatic laser fields.

1. INTRODUCTION

This study investigates DCS in the presence of a linearly polarized laser field, employing Bessel functions of varying orders, with oxygen molecules modeled under the Lennard-Jones potential. The analysis demonstrates that electron energy can be absorbed or emitted during interactions, producing pronounced resonance peaks in the DCS, which indicate potential formation of new particle structures, while minima correspond to strong electron–target coupling and smaller composite formation. The Bessel zero-order exhibits higher DCS values compared to higher orders, and at zero-radian scattering angle, the DCS reaches its minimum, emphasizing enhanced particle interactions at this orientation [1]. Analytical studies using the coupled-channel Lippmann–Schwinger equation for a one-dimensional δ-function potential further show that electrons can absorb or emit energy in integer multiples of the laser frequency, resulting in elastic, inelastic, and superelastic scattering amplitudes with observed stimulated recombination resonances [2]. Accurate modeling of laser-assisted multiphoton transitions also requires consideration of realistic laser field properties, including focusing, pulse structure, multimode behavior, and statistical fluctuations, which significantly affect scattering cross sections in fast electron–atom collisions [3]. Previous studies have explored electron-laser interactions using attractive δ-function potentials, primarily through numerical solutions of the time-dependent Schrödinger equation, focusing on photoionization rates in strong-field regimes (10^9–10^{14} W/cm²), while ultra strong-field domains (≥10^{16} W/cm²) remain less examined. Laser-modified scattering rates for this potential are not well-studied, though related phenomena have been analyzed in other systems, showing stabilization of bound states under high-intensity fields [2]. The Kroll–Watson approximation is widely employed, treating electron-laser interaction nonperturbatively but neglecting direct laser-atom coupling, predicting that the field-free scattering cross section is modified mainly by electron-laser interactions [4]. In strong fields, electrons can undergo scattering, leading to above-threshold ionization, harmonic generation, and further excitations [5], while intense lasers enhance charge exchange in ion-atom collisions under resonant conditions [6]. Quantum-orbit theory effectively describes multistep processes [7] by Milošević et al. Realistic laser models incorporating multimode behavior and pulse shaping are essential for accurate light-matter interaction simulations [8]. Correlated double ionization highlights strong electron correlation in multiphoton ionization [9], and ponderomotive effects dominate electron-photon scattering in high-intensity fields [10]. Beyond fundamental physics, laser microtechnology enables precise fabrication of micrometer-scale structures for optics and electronics applications [11].

The scattering dynamics of particles interacting with a Gaussian potential in the presence of a bichromatic laser field is a complex

phenomenon studied within atomic physics and laser-matter interaction, integrating concepts from quantum mechanics and electromagnetism [12-15]. A Gaussian potential is often employed in theoretical models due to its analytical tractability and its ability to represent localized interactions, such as those occurring in quantum dots or screened atomic potentials. The presence of a bichromatic laser field, which consists of two laser components with different frequencies (e.g., ω and 2ω or ω and 3ω) and a controllable relative phase, introduces a powerful tool for coherent control of scattering processes [16-17]. The theoretical framework for analyzing such interactions typically involves solving the time-dependent Schrödinger equation or employing approximations like the Born approximation, particularly the first and second Born approximations. The Volkov wave functions are often used to describe the states of electrons in the presence of a strong laser field [18]. These approaches allow for the calculation of DCS and total differential cross sections, which are crucial for understanding the probability and angular distribution of scattered particles [19].

Despite extensive studies on laser-assisted scattering using monochromatic fields and simple potentials, the effects of Gaussian potentials under bichromatic laser fields remain underexplored, particularly regarding phase-dependent, multiphoton interactions, and nonlinear frequency-dependent effects. Most prior work has focused on δ-function or Lennard-Jones potentials, often neglecting realistic laser properties and coherent control over electron dynamics. Investigating electron scattering in a bichromatic field composed of two frequencies (e.g., ω and 2ω or ω and 3ω) with a controllable relative phase provides enhanced flexibility, enabling precise manipulation of energy and momentum transfer, resonances, and multiphoton processes. Understanding these dynamics is crucial for laser-assisted collision studies, plasma diagnostics, nanomaterial design, and quantum device optimization, as it reveals detailed electron behavior under realistic experimental conditions and allows coherent control that monochromatic fields cannot achieve.

2. MATERIALS AND METHODS

The time dependent Schrödinger equation can be used to describe the conduction-band electrons dynamics in the (x,y) plane [15, 20] as:

$$\left[\frac{1}{2\mathrm{m}'}\left(\mathbf{p}-\frac{\mathrm{e}}{\mathrm{c}}\mathbf{A}(\mathrm{t})\right)^2+\mathrm{V}(\mathrm{r})\right]X(\mathrm{x},\mathrm{y},\mathrm{t})=\ \mathrm{i}\hbar\frac{\partial X(\mathrm{x},\mathrm{y},\mathrm{t})}{\partial \mathrm{t}} \quad (1)$$

represents the time-dependent Schrödinger equation for an electron in the presence of an external electromagnetic field, where m' is the electron mass, **p** is the momentum operator, e is the electron charge, c is the speed of light, **A**(t) is the time-dependent vector potential, and V(r) is the potential energy. The term $\left(\mathbf{p}-\frac{\mathrm{e}}{\mathrm{c}}\mathbf{A}(\mathrm{t})\right)^2$ accounts for the coupling between the charged particle and the electromagnetic field through the minimal coupling scheme, while the right-hand side describes the time evolution of the wave function $X(\mathrm{x},\mathrm{y},\mathrm{t})$. The corresponding solution of equation (1) is presented in equation (2) [21-24].

$$X(r,t)=\frac{1}{(2\pi)^{\frac{3}{2}}}\exp\left\{i\frac{\boldsymbol{p}}{\hbar}.\left(\boldsymbol{r}+\frac{\mathrm{e}}{\mathrm{m}'}\int\mathbf{A}(\,t)dt\right)-i\frac{E}{\hbar}t-\right.$$
$$\left.i\frac{\mathrm{e}^2}{2\mathrm{m}'\hbar}\int\mathbf{A}^2(t)\,dt\right\} \quad (2)$$

which is known as the Volkov wave function, describing a free electron dressed by the electromagnetic field; here $\boldsymbol{r}$ is the position vector, E is the electron energy, and the exponential terms represent, respectively, the plane-wave contribution, the phase modulation due to the vector potential, and the additional phase shift arising from the field intensity through the $\int\mathbf{A}^2(t)dt$ term. The vector potential for bichromatic linear polarized laser [25].

$$\mathbf{A}(t)=\epsilon_1\left(\frac{\varepsilon_1}{\omega}\right)\cos(\omega t)+\epsilon_m\left(\frac{\varepsilon_m}{m\omega}\right)\cos(m\omega t+\phi) \quad (3)$$

where ϵ_1 and ϵ_m denote the independent polarization vectors. For simplicity, both fields are assumed to have the same linear polarization. Here, ε_1 and ε_m represent the corresponding electric field strengths, while ϕ indicates the relative phase. In practical applications, the parameter m typically takes the values 2 or 3, corresponding to the second and third harmonics. Experimentally, the achievable ratio $\varepsilon_m/\varepsilon_1$ is usually around 10% in nonlinear media, and this ratio is even smaller for the third harmonic. Now putting value of **A**(t) form equation (3) in equation (2) and solving as:

$$X(r,t)=\frac{1}{(2\pi)^{\frac{3}{2}}}\exp\left\{i\frac{p}{\hbar}.\left(r+\frac{e}{m'}\int\boldsymbol{\epsilon_1}\ \left(\frac{\epsilon_1}{\omega}\right)\boldsymbol{cos}\omega t+\right.\right.$$
$$\left.\epsilon_m\left(\frac{\epsilon_m}{m\omega}\right)cos(m\omega t+\phi)\,dt\right)-i\frac{E}{\hbar}t-$$
$$\left.i\frac{e^2}{2m'\hbar}\int\left(\boldsymbol{\epsilon_1}\left(\frac{\epsilon_1}{\omega}\right)\boldsymbol{cos}\omega t+\ \epsilon_m\left(\frac{\varepsilon_m}{m\omega}\right)cos(m\omega t+\phi)\right)^{\mathbf{2}}\right\} \quad (4)$$

Equation (4) represents the wavefunction of a charged particle in an oscillating electromagnetic field, known as the Volkov-type solution. Physically, it describes how the particle's phase and motion are modified by the presence of combined laser fields the fundamental frequency ω and its harmonic $m\omega$ (usually $m=2$ or 3). On integration Equation (4) and solving with omitting last term of equation (4) because it is very small in magnitude and it doesn't play the vital role. When system is unperturbed due to laser field then we apply Kroll-Watson Approximation for perturbation. S-matrix is used to get the system information and it is also used when times tends to infinity

$$X(r,t)=\frac{1}{(2\pi)^{\frac{3}{2}}}\exp\left\{iprcos\theta+ip\left[\epsilon_1\left(\frac{\varepsilon_1}{\omega^2}\right)\sin(\omega t)-\right.\right.$$
$$\left.\left.\epsilon_m\left(\frac{\varepsilon_m}{m\omega^2}\right)\sin(m\omega t+\phi)\right]-iEt\right\} \quad (5)$$

Physically, this equation emphasizes how the particle's position and phase vary with time due to the external electric fields, while neglecting the overall phase factor that has no observable effect. The term $prcos\theta$ accounts for the propagation of the wave in space, and the sine-dependent terms represent the field-driven

displacement of the electron caused by the oscillating components of the electric field. Thus, equation (5) captures the essential dynamic behavior of the system in a simplified form, focusing only on the physically meaningful, time-dependent motion. Now using Kroll-Watson Approximation S-matrix [26-28] is defined as

$$S_{fi}^{E} = \delta_{fi} - \frac{i}{\hbar}\int_{-\infty}^{\infty} \langle X_f(r,t)|V(r)|X_i(r,t)\rangle \, dt \qquad (6)$$

Where Equation (6) represents, the S-matrix with transition amplitude [second term of Equation (6)] between an initial quantum state $X_i(r,t)$ and a final state $X_f(r,t)$ under the influence of an interaction potential $V(r)$. Physically, this equation comes from time-dependent perturbation theory and describes how an external field or potential induces a transition between two quantum states. The first term, δ_{fi}, corresponds to the case where no interaction occurs (the system remains in the same state), while the second term gives the probability amplitude for transition due to the perturbing potential. The integral over time accounts for the accumulated effect of the interaction throughout the field's duration. The second term of equation (6) for transition matrix or T-matrix is obtained with the help of Equation (7),

$$T_{fi} = \int_{-\infty}^{\infty} \left\langle X_f(r,t)\middle|V(r)|X_i(r,t)\right\rangle dt \qquad (7)$$

Physically, it quantifies how strongly and effectively the interaction couples the two states over time. A larger value of T_{fi} indicates a higher probability of transition, meaning the potential $V(r)$ strongly influences the particle's motion. In laser–matter or scattering processes, this term is crucial for determining transition probabilities, cross-sections, and emission or absorption rates, reflecting how external fields or potentials drive the exchange of energy between the system and its environment. After putting the value of wave function equation (5) on equation (7) and solving we get,

$$T_{fi} = \int d^3r \int_{-\infty}^{\infty} \left(\frac{1}{(2\pi)^{\frac{3}{2}}} \exp\left\{ -ip_f r cos\theta - ip_f \left(\epsilon_1 \left(\frac{\varepsilon_1}{\omega^2}\right) \sin(\omega t) - \epsilon_m \left(\frac{\varepsilon_m}{m\omega^2}\right) \sin(m\omega t + \phi) \right) + iE_f t \right\} V(r) \; \frac{1}{(2\pi)^{\frac{3}{2}}} \exp\left\{ ip_i r cos\theta + ip_i \left(\epsilon_1 \left(\frac{\varepsilon_1}{\omega^2}\right) \sin(\omega t) - \epsilon_m \left(\frac{\varepsilon_m}{m\omega^2}\right) \sin(m\omega t + \phi) \right) - iE_i t \right\} \right) dt \qquad (8)$$

After performing the time integral with the Jacobi–Anger expansion, the oscillatory factors turn into sums of Bessel functions (J_n) and the time integral produces a Kronecker/Dirac delta enforcing discrete energy balance in Equation (8). Physically that result has two immediate meanings: (a) the Bessel functions give the amplitude for absorbing/emitting n photons from a given harmonic component, so they set the relative strength of each multiphoton channel; and (b) the Kronecker/energy delta implements energy conservation. The final equation (8) after solving we get equation (9) as,

$$T_{fi} = \frac{1}{(2\pi)^3} \int \{ \exp(ikr) \times J_n(dn_1) \times J_n(dn_2) \exp(in\phi) \} V(r) d^3r \qquad (9)$$

Where $dn_1 = k\epsilon_1 \left(\frac{\varepsilon_1}{\omega^2}\right)$ *and* $dn_2 = -\epsilon_m \left(\frac{\varepsilon_m}{m\omega^2}\right)$ and $d^3r = r^2 sin\theta \; d\theta \; d\phi \; dr$ represent the volume for spherical coordinate system and $k = k_f - k_i$. On putting the value of V(r) which is known as Gaussian potential [29] defined in Equation (10) as,

$$V(r) = V_0 \exp\left\{ -\left(\frac{r}{R}\right)^2 \right\} \qquad (10)$$

Physically, V_0 defines the depth or strength of the potential well, while R specifies its spatial extent or characteristic range, the region within which the interaction is significant. The exponential decay ensures that the potential rapidly approaches zero as r increases, meaning the particle experiences a strong interaction only near the center and is essentially free beyond that region. On substituting the value form equation (10) to equation (9) and solving we get the T-matrix as

$$T_{fi} = -\frac{V_0 J_n(dn_1) J_n(dn_2) \exp(in\phi)}{4\pi^2 ik} \left\{ \begin{array}{c} \sqrt{\pi} \; (ikcos\theta) \exp\left(-\frac{(kcos\theta)^2 R^2}{4} \right) \frac{R^3 \, erf\left(\frac{2r}{R^2} - ikcos\theta\right)}{8\sqrt{ikcos\theta}} - \\ \frac{R^2 \exp\left(r \left\{ ikcos\theta - \frac{r}{R^2} \right\} \right)}{2} \end{array} \right\} \qquad (11)$$

Equation (11) is final equation of transition matrix which is directly related to DCS and this transition matrix is used to study the scattering dynamics of electron with gaussian potential in laser field. Since we have relation of DCS and transition matrix [30-32] we have,

$$\frac{d\sigma}{d\Omega} = \frac{k_f}{k_i} \left| T_{fi} \right|^2 \qquad (12)$$

Equation (12) shows relationship between the transition matrix element and the DCS, which quantifies the probability of an electron being scattered into a specific solid angle $d\Omega$. Physically, this equation shows that the DCS depends on the magnitude squared of the transition amplitude, representing the strength of interaction between the incoming and outgoing states. The transition matrix T_{fi}, derived from equation (11), encapsulates all the effects of the laser field, Gaussian potential, and multiphoton interactions. Now substituting value from equation (11) to equation (12) we get final equation (13) to study the scattering dynamics of electron and gaussian potential as

$$\frac{d\sigma}{d\Omega} = \frac{k_f}{k_i} \left| -\frac{V_0 J_n(dn_1) J_n(dn_2) \exp(in\phi)}{4\pi^2 ik} \left\{ \sqrt{\pi} \; (ikcos\theta) \exp\left(-\frac{(kcos\theta)^2 R^2}{4} \right) \frac{R^3 \, erf\left(\frac{2r}{R^2} - ikcos\theta\right)}{8\sqrt{ikcos\theta}} - \frac{R^2 \exp\left(r \left\{ ikcos\theta - \frac{r}{R^2} \right\} \right)}{2} \right\} \right|^2 \qquad (13)$$

Equation (13) gives the DCS for an electron scattering from a Gaussian potential in the presence of a two-color laser field. Physically, it combines the effects of the laser-driven multiphoton processes (through Bessel functions and the relative phase ϕ), the spatial characteristics of the Gaussian potential (strength V_0 and range R, including error-function and exponential terms from spatial integration), and the kinematic/angular dependence of the scattering ($k_i, k_f, \cos\theta$). The modulus squared represents the probability of the electron being scattered into a specific angle, showing how the laser field, potential shape, and scattering geometry together control the angular distribution and intensity of the scattered electrons.

3. RESULTS AND DISCUSSION

Computational detail: Change in momentum (1-4) eV, strength of the potential well 2.7× 10^{-10}mV, Bessel order (1-5), harmonic order (2-3), $r = 1$ Å, $R = 0.6 - 0.8$ Å, scattering angle (0-120°), polarization vectors ($\epsilon_1 = \epsilon_m = 1$), electric field strength ($\varepsilon_1 = 1\ a.u.$ and $\varepsilon_m = 2\ a.u.$), phase angle (5.7° and 57°). Figure 1 illustrates the variation of the DCS with photon incidence energy in the presence of a laser field for the Bessel first-order. The analysis revealed that Figure 1(a) corresponds to the second-order harmonic ($m = 2$), while Figure 1(b) represents the third-order harmonic ($m = 3$). Also, the harmonic order of the laser field increases, the DCS decreases for the Bessel first-order. This reduction is attributed to the decrease in field amplitude at higher harmonic orders. Furthermore, shift in maxima peak towards lower photon incidence energy is observed with increasing harmonic order. On the other hand, the maxima peak for the $m = 2$ appears at approximately 1.7 eV and the $m = 3$ around 1.9 eV. The peak was due to superposition of amplitude of projected, target and laser where project is nearer to target.

The demonstrate shows dependency of the DCS on the harmonic order of the applied laser field. The increasing in harmonic order shows the DCS decreases due to the reduction in field amplitude as it is directly related to DCS. The maxima peak for $m = 2$ and $m = 3$, suggests lower-order harmonics the probability of scattering is higher means weaker interaction while higher-order harmonic the probability of scattering is lower and interaction is higher. This means scattering dynamic of electron with gaussian potential is higher for lower order harmonic. In lower energy region below 10 eV [33] show that DCS initially increase with increasing in scattering electron energy and become maximum and then decrease for electron-atom in two polarized colors. Also Figure 1 and Figure 2 has similar nature obtained by Bartschat et al. [34] where they study quantum-mechanical calculations of cross sections for electron collisions with atoms and molecules.

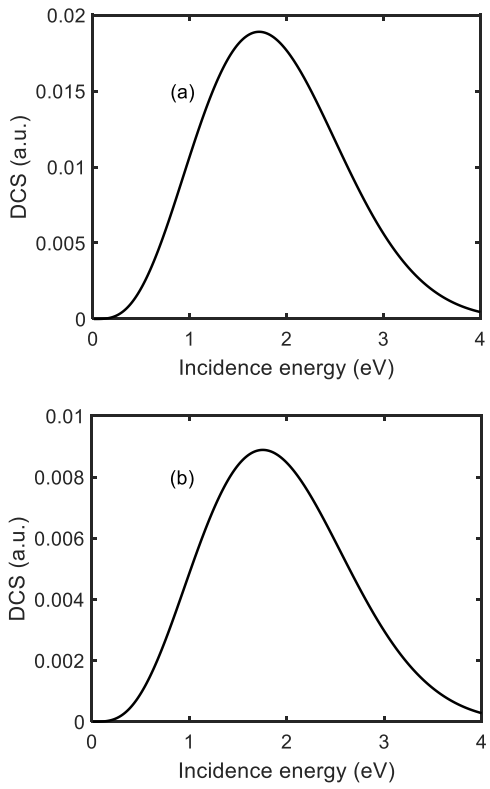

Fig. 1: DCS with incidence energy of electron (a) $m = 2$ and (b) $m = 3$ for Bessel first-order

Fig. 2 presents the variation of the DCS with photon incidence energy for the Bessel second-order and similar nature to Figure 1 but shifting of maxima peak was observed around 3 eV [34] for the $m = 2$ and m=3. On comparing the DCS between harmonic orders, the DCS for the second-order harmonic is consistently lower than that of the first-order harmonic. Also comparing the DCS with Bessel order it is found that Bessel first-order has higher than second order. This is because on compare the amplitude of field Bessel second-order has lower ampltiude than first order and as we known field ampltiude is DCS is directly related.

Fig. 3 illustrates the behavior of the DCS with photon energy of the laser field for the Bessel first-order at $m = 2$ and $m = 2$. The DCS exhibits two major peaks when the photon energy exceeds 0.4 eV, as shown in Figure 3(a). In contrast, for the $m = 3$, three distinct peaks are observed when the photon energy exceeds 0.3 eV, as presented in Figure 3(b). The comparative analysis shows that the DCS corresponding to $m = 2$ is consistently higher than that of $m = 3$. DCS is directly proportional to the amplitude of the laser field, higher harmonic orders lead to lower DCS values. Furthermore, the observed peaks are attributed to superpostion interactions of electrons with the laser field in the vicinity of the

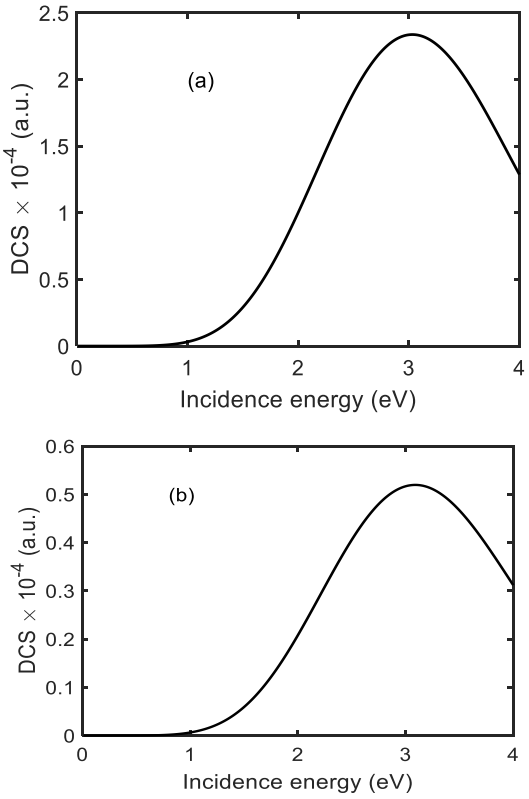

Fig. 2: DCS with incidence energy of electron (a) m=2 and (b) m=3 for Bessel second-order

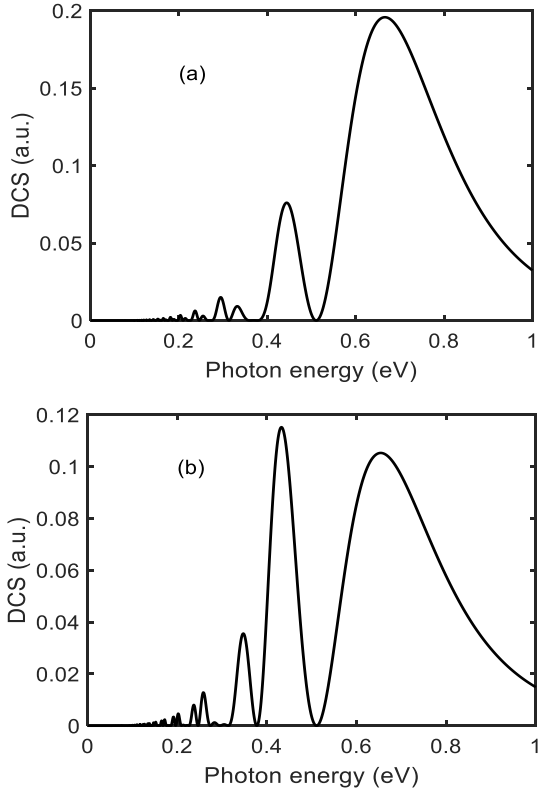

Fig. 3: DCS with photon energy (a) $m = 2$ and (b) $m = 3$ for Bessel first-order

target. The sharp and high peak of DCS is due to field amplitude of scattering particles. The analysis of Figure 3 reveals that the number of peaks in the DCS increases with harmonic order: two major peaks for $m = 2$ and three peaks for $m = 3$. However, the overall amplitude of the DCS decreases with higher harmonic order due to the reduction in field oscillation strength. These findings highlight the intricate role of harmonic order and superposition effects in shaping scattering dynamics under a laser-assisted environment.

Fig. 4 presents the DCS as a function of photon energy for the Bessel second-order. The overall trend is similar to that observed in Fig. 3 with larger number of small peaks the small peaks are the superpostion of smaller amplitude of scattering particle because the particle during scattering looses and gain the energy.
Figus. 4(a) and 4(b) reveal that as the harmonic order increases, smaller peaks become more pronounced. Another key observation is the shift of the peaks towards lower photon energies with increasing harmonic order. For instance, at $m = 3$, a peak appears below 0.4 eV, accompanied by several small-amplitude oscillatory peaks at even lower photon energies.

The combined influence of harmonic order and Bessel order enhances oscillatory structures in the DCS, while simultaneously reducing the overall amplitude due to diminished field strength. The observed peak shifts toward lower photon energies with increasing harmonic order highlight the sensitivity of scattering dynamics to multiphoton resonance processes.

Fig. 5 illustrates the variation of the DCS with scattering angle for the Bessel first-order at different harmonic orders. The results show that the DCS decreases for both the $m = 2$ and $m = 3$, as seen in Figures 5(a) and 5(b), respectively. The DCS for the $m = 2$ is consistently higher than that of $m = 3$, which can be explained by the reduction in field amplitude with increasing harmonic order. Physically, a lower DCS indicates stronger interactions between scattering particles and a reduced probability of scattering, as the interacting particles are closer together. Conversely, a higher DCS corresponds to weaker interactions and a greater probability of scattering, since the particles are relatively farther apart. Das and Dhobi [35] study the differential cross-section of scattering by using Gaussian potential in presence of laser and with linear polarization found decrease with scattering angle. Ghoshal and Ho [36] study positron scattering from hydrogen atomembedded in weakly-coupled plasmas and found the DCS decrease with incresing scattering angle.

This behavior arises because as the Bessel order increases, the amplitude of the field oscillation decreases. Interestingly, after a certain Bessel order, the DCS becomes nearly constant. This suggests that at this regime the interacting particles no longer move closer to each other, as the electrostatic interaction energy between them reaches a value comparable to the rest energy of the particles. This point acts as a reference threshold beyond which the incident particles cannot penetrate or approach the target field any further. In other words, the target field becomes dominant over the incident field, leading to a saturation of the scattering process.

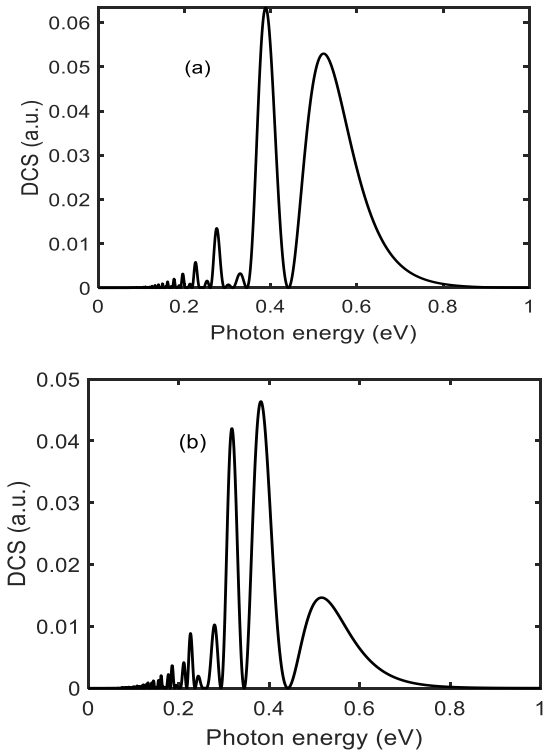

Figure 4: DCS with photon energy (a) $m = 2$ and (b) $m = 3$ for Bessel second-order

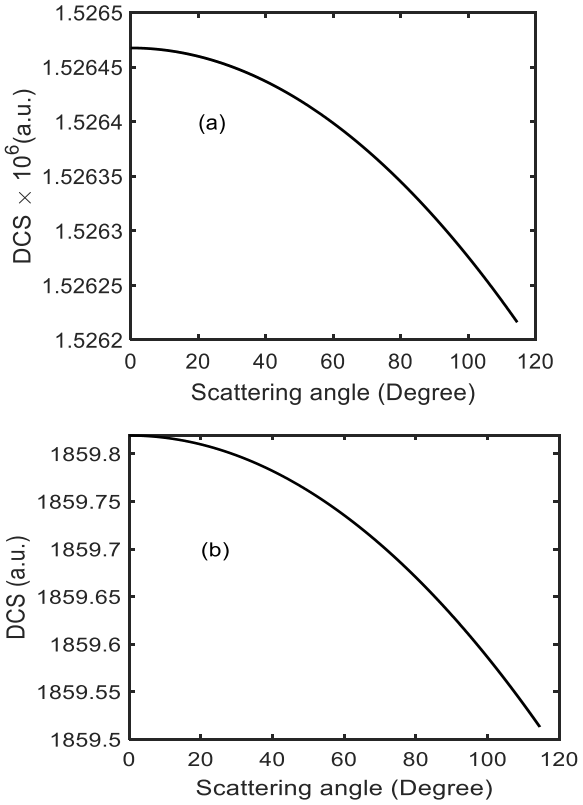

Fig. 5: DCS with scatterionga angle (a) n=1 and (b) n=2 for Bessel order.

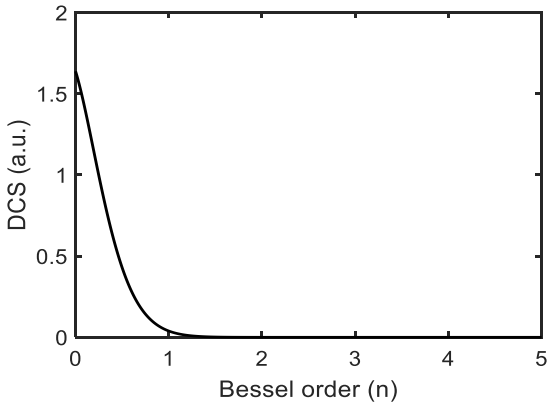

Fig. 6: DCS with different order Bessel order

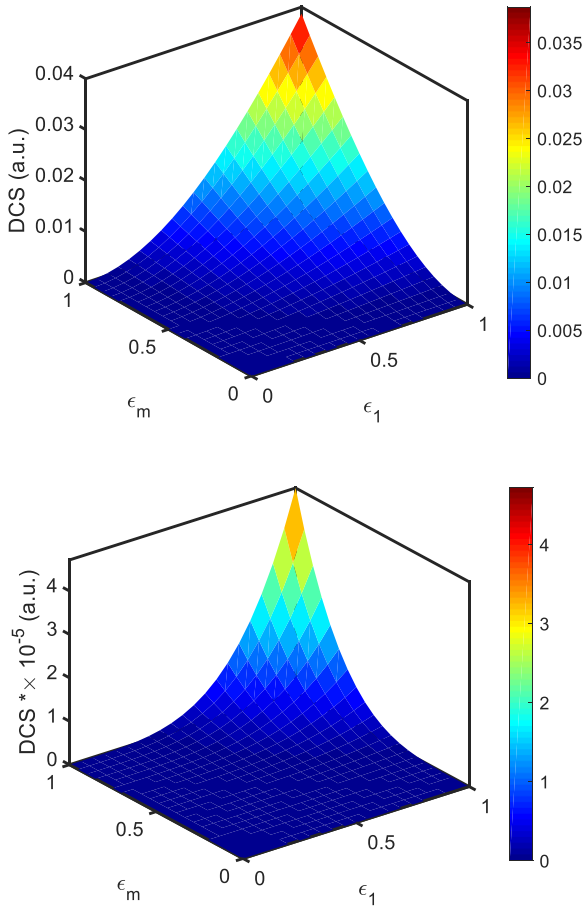

Fig. 7: 3D DCS with polarization vector at n=1 (upper-side) and n=2 (lower side).

Fig. 6 shows the variation of the DCS with increasing order of the Bessel order for both lower and higher harmonic orders. The obseravtion shows the DCS decreases with increasing Bessel order, and the magnitude of the DCS for the lower harmonic order is

consistently higher than that for the higher harmonic order. This behavior arises because as the Bessel order increases, the amplitude of the field oscillation decreases. Interestingly, after a certain Bessel order, the DCS becomes nearly constant. This suggests that at this regime the interacting particles no longer move closer to each other, as the electrostatic interaction energy between them reaches a value comparable to the rest energy of the particles. This point acts as a reference threshold beyond which the incident particles cannot penetrate or approach the target field any further. In other words, the target field becomes dominant over the incident field, leading to a saturation of the scattering process.

Fig. 7 presents the three-dimensional distribution of the DCS as a function of unit vectors for the Bessel first- and second-order. The results show that when the magnitude of the unit vector is lower, the DCS attains higher values, indicating stronger scattering at smaller vector components. A comparison between Bessel order eveals that the DCS for the Bessel first-order is consistently higher than that of the second order. Similarly, when comparing harmonic orders, the DCS corresponding to lower-order harmonics is higher than that of higher-order harmonics. This behavior aligns with the general trend that increasing either the Bessel order or the harmonic order reduces the field amplitude, and consequently decreases the DCS.

4. CONCLUSION

The present analysis reveals that harmonic and Bessel order fundamentally govern the strength and angular characteristics of electron scattering in bichromatic laser fields. The observed correlation between field amplitude reduction and diminishing DCS values highlights the tunability of scattering processes through external laser parameters. This tunability offers potential control mechanisms for designing precise electron–laser interaction systems, relevant to plasma diagnostics, nanostructure fabrication, and high-resolution spectroscopy. Physically, the shift and broadening of resonance peaks with increasing harmonic order indicate altered energy absorption dynamics that can be exploited for studying nonlinear multiphoton processes. Future extensions of this work could incorporate Coulomb potentials to account for long-range interactions, relativistic corrections for high-energy regimes, and comparisons with experimental data to validate the theoretical framework. Such developments would deepen understanding of laser-assisted collision phenomena and support the advancement of next-generation light–matter interaction technologies.

AUTHOR CONTRIBUTIONS

S.K. Das and S.H. Dhobi equally contributed to identifying the research problem, designing the methodology, preparing the original draft, performing computations, and preparing the reviewer report.

FUNDING SOURCES

No fund.

ETHICAL ISSUES

This study did not involve human participants or animal experiments. The research complies with ethical standards for theoretical and computational studies, and all data presented are original.

ACKNOWLEDGMENTS

The authors would like to thank all faculty members of the Department of Physics, Patan Multiple Campus, Tribhuvan University, Patandhoka, Lalitpur, Nepal, for providing a peaceful environment and necessary research facilities during the course of this study.

REFERENCES

[1] N.B. Shrestha, S.P. Gupta, Y. Poudel, K. Yadav, S.H. Dhobi, J.J. Nakarmi, Laser assist scattering in Lennard–Jones potential, *Hadronic Journal*, **46** (4) (2023) 459-462. https://doi.org/10.29083/HJ.46.04.2023/SC459

[2] K.J. LaGattuta, Laser-assisted scattering from a one-dimensional δ-function potential: an exact solution, *Physical Review A*, **49** (3) (1994) 1745. https://doi.org/10.1103/PhysRevA.49.1745

[3] P. Francken, C.J. Joachain, Theoretical study of electron–atom collisions in intense laser fields, *Journal of the Optical Society of America B*, **7**(4) (1990) 554–563. https://doi.org/10.1364/JOSAB.7.000554

[4] B. Wallbank, J.K. Holmes, Laser-assisted elastic electron–atom collisions, *Physical Review A*, **48** (4) (1993) R2515. https://doi.org/10.1103/PhysRevA.48.R2515

[5] K.C. Kulander, J. Cooper, K.J. Schafer, Laser-assisted inelastic rescattering during above-threshold ionization, *Physical Review A*, **51** (1) (1995) 561. https://doi.org/10.1103/PhysRevA.51.561

[6] F. Anis, V. Roudnev, R. Cabrera-Trujillo, B.D. Esry, Laser-assisted charge transfer in He^{2+} + H collisions, *Physical Review A*, **73** (4) (2006) 043414. https://doi.org/10.1103/PhysRevA.73.043414

[7] D.B. Milošević, D. Bauer, W. Becker, Quantum-orbit theory of high-order atomic processes in intense laser fields, *Journal of Modern Optics*, **53** (1–2) (2006) 125–134. https://doi.org/10.1080/09500340500186099

[8] R. Daniele, G. Ferrante, Particle scattering in the presence of a strong multimode laser field, *Journal of Physics B: Atomic and Molecular Physics*, **14** (20) (1981) L635. DOI 10.1088/0022-3700/14/20/004

[9] G.L. Yudin, M.Y. Ivanov, Physics of correlated double ionization of atoms in intense laser fields: quasistatic tunneling limit, *Physical Review A*, **63** (3) (2001) 033404. https://doi.org/10.1103/PhysRevA.63.033404

[10] P.H. Bucksbaum, M. Bashkansky, T.J. McIlrath, Scattering of electrons by intense coherent light, *Physical Review Letters,* **58** (4) (1987) 349. https://doi.org/10.1103/PhysRevLett.58.349

[11] S.M. Metev, V.P. Veiko, *Laser-Assisted Microtechnology*, **19**, Springer Sci. & Bus. Media, 2013.

[12] S. Varró, F. Ehlotzky, Potential scattering of electrons in a bichromatic laser field of frequencies ω and 2ω or ω and

3ω, *Optics Communications*, **99** (3–4) (1993) 177–184. https://doi.org/10.1016/0030-4018(93)90075-G.

[13] A. Cionga, F. Ehlotzky, M. Florescu, M. Iacomi, One-dimensional potential scattering of electrons in a bichromatic laser field, *Journal of Physics B: Atomic, Molecular and Optical Physics*, **34** (20) (2001) 3951–3962. https://doi.org/10.1088/0953-4075/34/20/307.

[14] D.B. Milošević, Potential scattering in a strong multicolour laser field, *Journal of Physics B: Atomic, Molecular and Optical Physics*, **29** (4) (1996) 875–893. https://doi.org/10.1088/0953-4075/29/4/024.

[15] R.P. Kurmi, K. Yadav, A. Shrestha, S.H. Dhobi, Laser assist quantum dot scattering with Gaussian potential, *Physics Open*, **23** (2025) 100267. https://doi.org/10.1016/j.physo.2025.100267.

[16] S.T. Zhang, J. Chen, L. Shu-min, The intensity dependence of the free-free transition in a bichromatic laser field, *Canadian Journal of Physics,* **80** (9) (2002) 969–977. https://doi.org/10.1139/p02-052.

[17] S. Kerbstadt, K. Eickhoff, T. Bayer, M. Wollenhaupt, Bichromatic control of free electron wave packets, *In Progress in Ultrafast Intense Laser Science XV, Cham: Springer International Publishing* (2020) 43–76. https://doi.org/10.1007/978-3-030-47098-2_3.

[18] B. Zhou, M.-Y. Zheng, D.-Y. Wen, The second Born approximation of electron–argon elastic scattering in a bichromatic laser field, *arXiv* (2013). https://doi.org/10.48550/arXiv.1301.4661.

[19] Z. Zun-Lue, L. Ming-Chao, S. Jin-Feng, Electron–helium atom collisions in the presence of a bichromatic laser field, *Communications in Theoretical Physics,* **50** (2) (2008) 477–480. https://doi.org/10.1088/0253-6102/50/2/39.

[20] P. Liu, Q. Wang, X. Li, Studies on CdSe/L-cysteine quantum dots synthesized in aqueous solution for biological labeling, *The Journal of Physical Chemistry C*, **113** (18) (2009) 7670–7676. https://doi.org/10.1021/jp901292q.

[21] J. Maurer, U. Keller, Ionization in intense laser fields beyond the electric dipole approximation: concepts, methods, achievements and future directions, *Journal of Physics B: Atomic, Molecular and Optical Physics*, **54** (9) (2021). DOI 10.1088/1361-6455/abf731

[22] S.H. Dhobi, S.P. Gupta, K. Yadav, A.K. Jha, Scattering dynamics in thermal environments around PEMFC electrode, *International Energy Journal,* **25** (1A) (2025) 123-132. http://rericjournal.ait.ac.th/index.php/reric/article/view/3082/pdf

[23] S.H. Dhobi, K. Yadav, S.P. Gupta, J.J. Nakarmi, A.K. Jha, Non-monochromatic laser assist scattering in thermal environment, *Journal of the Nigerian Society of Physical Sciences,* **7** (1) (2025) 2345–2345. https://doi.org/10.46481/jnsps.2025.2345

[24] S.H. Dhobi, S.P. Gupta, K. Yadav, J.J. Nakarmi, A.K. Jha, Differential cross section with Volkov–thermal wave function in Coulomb potential, *Atom Indonesia*, **50** (1) (2024) 19–25. https://doi.org/10.55981/aij.2024.1309

[25] I.F. Barna, S. Varró, Laser-assisted proton collision on light nuclei at moderate energies, *Laser and Particle Beams,* **33** (2) (2015) 299–305. https://doi.org/10.1017/S0263034615000191

[26] N.M. Kroll, K.M. Watson, Charged-particle scattering in the presence of a strong electromagnetic wave, *Physical Review A*, **8** (1973) 804–809. https://doi.org/10.1103/PhysRevA.8.804

[27] S.H. Dhobi, S.P. Gupta, J.J. Nakarmi, B. Koirala, K. Yadav, S.K. Oli, M. Gurung, Scattering of free electrons with hydrogen atoms in proton exchange membrane fuel cell system, *International Annals of Science*, **13** (1) (2023) 22–28. https://doi.org/10.21467/ias.13.1.22-28

[28] S.H. Dhobi, J.J. Nakarmi, K. Yadav, S.P. Gupta, B. Koirala, A.K. Shah, Study of thermodynamics of a thermal electron in scattering, *Heliyon*, **8** (12) (2022). https://doi.org/10.1016/j.heliyon.2022.e12315

[29] B.K. Agrwal, H. Prakash, *Quantum Mechanics*, Prentice Hall of India Pvt. Ltd., New Delhi (2002).

[30] K. Kavazović, A. Čerkić, D.B. Milošević, Electron–molecule scattering in a bichromatic elliptically polarised laser field: plateau structures and two-centre interference minima, *Molecular Physics*, **119** (14) (2021) e1948123. https://doi.org/10.1080/00268976.2021.1948123

[31] S.H. Dhobi, K. Yadav, S.P. Gupta, J.J. Nakarmi, B. Koirala, Differential cross-section in the presence of a weak laser field for inelastic scattering, *Ukrainian Journal of Physics,* **67** (4) (2022) 227–227. https://doi.org/10.15407/ujpe67.4.227

[32] S.H. Dhobi, K. Yadav, A.K. Jha, B. Karki, J.J. Nakarmi, Free electron–ion interaction and its effect on output current of permeable exchange membrane hydrogen fuel, *ECS Trans.*, **107**(1) (2022) 8457. https://doi.org/10.1149/10701.8457ecst

[33] D. Habibović, A. Čerkić, D.B. Milošević, Laser-assisted electron–atom scattering in an orthogonally polarized two-color laser field, *The European Physical Journal D*, **79**(11) (2025) 136. https://doi.org/10.1140/epjd/s10053-025-01087-7

[34] K. Bartschat, J. Tennyson, O. Zatsarinny, Quantum-mechanical calculations of cross sections for electron collisions with atoms and molecules, *Plasma Processes and Polymers*, **14**(1–2) (2017) 1600093. https://doi.org/10.1002/ppap.201600093

[35] S.K. Das, S.H. Dhobi, Study of the differential cross-section of scattering by using Gaussian potential in presence of laser, *Patan Prospective Journal*, **5** (1) (2025) 120–132. https://doi.org/10.3126/ppj.v5i1.85843

[36] A. Ghoshal, Y.K. Ho, Positron scattering from hydrogen atom embedded in weakly-coupled plasmas, *The European Physical Journal D*, **55** (3) (2009) 581–589. https://doi.org/10.1140/epjd/e2009-00238-x

Translating Nepal's National AI Policy into Action: Strategic Roadmap for Education, Industry, Infrastructure, and Digital Diplomacy

Yagya Raj Pandeya[1,3,4*], Bhaskar Bhatt[2,3*]

[1]Department of Artificial Intelligence, Kathmandu University, Dhulikhel, Nepal
[2]AI Research Unit, DigNep Group Pvt. Ltd., Kathmandu, Nepal
[3]Global Society of Advanced Research and Publication (GSARP), Lalitpur, Nepal
[4]AI Research and Development Division, Guru Technology Pvt. Ltd., Kathmandu, Nepal

Research Article

ISSN: 3059-9504 (online)
DOI: https://doi.org/ 10.3126/ajs.v2i1.87754

Article History

Received: October 16, 2025; Revised: November 14, 2025; Accepted: November 18, 2025; Published: December 25, 2025

Keywords

AI policy and strategy of Nepal, AI in education, Industry value chain, Digital infrastructure, Digital diplomacy, Sectoral AI applications.

***Corresponding Author**

Email: yagyapandeya@gmail.com (YR Pandey), bhaskar@dignep.com.np (B Bhatt)
Orcid: https://orcid.org/0000-0002-9842-8704

ABSTRACT

Artificial intelligence is fundamentally transforming Nepal's socio-economic landscape, with far- reaching implications across diverse sectors. Recognizing this transformative potential, the Government of Nepal published an AI Concept Paper in 2024, followed by the National AI Policy in 2025. However, translating policy frameworks into tangible outcomes requires developing comprehensive short-term and long-term AI strategies that deliver public value. Education, digital infrastructure, industry, and digital diplomacy emerge as pivotal sectors where AI can advance national interests, accelerate sectoral development, and address critical cybersecurity challenges. This study examines AI-driven opportunities and risks across four key domains: industrial value chains, education, digital infrastructure, and digital diplomacy. Each sectoral analysis explores current conditions, potential use cases, associated risks, and emerging opportunities for AI integration. This study employed a multi-method approach combining extensive desk reviews, iterative report evaluations, focused group discussions, and stakeholder consultations. This methodology incorporates diverse perspectives and draws upon global best practices in AI adoption to ensure comprehensive and contextually relevant findings. The study reveals that each sector requires a holistic and adaptive framework that integrates customized AI implementation strategies, proactive risk management strategies, sustainable funding mechanisms, and robust evaluation systems. Critical priorities identified across sectors include enacting data privacy legislation, investing in workforce upskilling programs, developing essential digital infrastructure, implementing AI risk mitigation protocols, strengthening digital diplomacy capabilities, and enhancing cybersecurity measures. These interconnected priorities collectively shape Nepal's evolving position within the global AI ecosystem and determine its capacity to leverage AI for inclusive development. This study provides policymakers with strategic insights, evidence-based analysis, and practical implementation tools to formulate effective AI policies, address critical infrastructure and governance gaps, and foster inclusive capacity building across sectors.

1. INTRODUCTION

Nepal is embarking on an ambitious journey to shape its future through the strategic implementation of a national AI policy. Recognizing the transformative potential of artificial intelligence in driving socio-economic growth, the Ministry of Communication and Information Technology (MoCIT) published a AI concept paper on June 30, 2024 [1] outlining the use and practice of AI to establish a foundation for developing relevant policies and legislation. Subsequently, the National AI Policy of Nepal [2] was published on August 14, 2025, marking a significant step toward guiding the ethical use, regulation, and advancement of AI across diverse sectors.

This study explores the multifaceted implications of Artificial Intelligence (AI) across four critical domains—Education, Industry, Digital Diplomacy, and Policy Infrastructure—each representing a fundamental pillar of Nepal's evolving AI ecosystem. Together, they provide a holistic understanding of how AI can serve as a transformative force for national development, innovation, and governance. The AI in Education study examines how AI technologies are reshaping teaching, learning, and skills development across educational institutions. It emphasizes institutional readiness, the importance of equitable access, and the challenges posed by the digital divide. By assessing the integration of AI in classrooms and curricula as in [3] the study highlights both opportunities for personalized learning and the need for digital infrastructure and teacher training to support effective adoption. The AI effect analysis on Industry Value Chain study analyzes the influence of AI on industrial productivity, innovation, and workforce transformation as recommended by [4-6]. It explores how automation, data-driven decision-making, and intelligent manufacturing can enhance efficiency and competitiveness. At the same time, it underscores the urgency of reskilling and upskilling workers to adapt to rapidly changing economic conditions and to prevent

workforce displacement. There are several news regarding the importance of digital diplomacy in Nepal [7,8]. The Digital Diplomacy component investigates how AI is transforming international relations and governance. It focuses on the growing importance of AI in diplomatic engagement, cybersecurity defense, and global cooperation. The study highlights Nepal's need to strengthen its digital diplomacy capabilities as discussed in [9] to effectively participate in global AI governance and safeguard national interests. Finally, the Policy Infrastructure study evaluates the state of Nepal's digital infrastructure, data governance frameworks, and cybersecurity systems. It identifies critical policy and regulatory gaps that may hinder responsible AI development and proposes actionable interventions to enhance institutional coordination, data protection, and digital resilience. Together, these four studies provide a comprehensive foundation for shaping Nepal's National AI Strategy— bridging technological potential with policy readiness, and ensuring that AI contributes to inclusive, secure, and sustainable national growth.

We examined four key sectors, analyzing their existing scenarios, challenges, and opportunities in adapting Artificial Intelligence (AI). Throughout the process, we collaborated with multiple stakeholders and integrated their insights and recommendations into a unified strategic framework. Continuous engagement with government and non-government agencies was maintained to foster trust, ensure policy alignment, and strengthen coordination toward achieving national AI objectives.

Drawing upon expert consultations, literature reviews, and contextual analysis, these studies offer a comprehensive assessment of Nepal's readiness for AI integration. They identify key strengths, constraints, and opportunities within each sector, ultimately contributing to an actionable roadmap for implementing Nepal's National AI Strategy. Collectively, this work provides both analytical depth and practical guidance—bridging academic insight with policy relevance—to support Nepal's strategic vision for an inclusive, secure, and innovation-driven AI future.

2. SCOPE OF WORK

2.1 Review of Sectoral Studies

The research was meticulously designed to ensure the quality, relevance, and coherence of the four sectoral studies. This was achieved through a comprehensive, multi-faceted review process focusing on four critical areas. First, the process involved a rigorous Assessment of each study's technical foundation, which included evaluating the quality of the research design, data collection methodologies, and analysis methods employed. This ensured that the conclusions drawn were structurally sound and scientifically credible. Concurrently, the review focused on Content Quality, examining the studies' findings and recommendations to confirm they were evidence-based, highly relevant to the local context, and appropriately aligned with Nepal's overall AI readiness goals. Beyond quality checks, the process prioritized iterative improvement. This involved providing Constructive Feedback, which offered detailed critiques aimed at enhancing the clarity of the presentation, increasing the depth of the analysis, and strengthening the practical implications of each study's recommendations. Finally, Cross-Sector Considerations were paramount to the design. This step ensured that the studies did not exist in silos but rather incorporated broad perspectives that would enable policy coherence, strategic alignment, and synergy across the different sectors being examined. Through this entire rigorous review process, the overarching goal was to provide valuable, grounded insights and actionable recommendations that would directly support the development of a robust and effective national AI strategy for Nepal.

2.2 Fostering Cross-Sector Collaboration

To ensure a cohesive and well-integrated approach, we undertook a series of coordination activities aimed at fostering collaboration among sectoral study teams and key stakeholders. These efforts were focused on streamlining research methodologies, resolving inconsistencies, and aligning recommendations to support a unified national AI strategy. Through these coordinated activities, we strengthened cross-sector collaboration, improved research integration, and ensured that AI policy recommendations reflect a unified and strategic approach to fostering AI-driven growth and innovation in Nepal.

We organized virtual meetings with each sectoral study team, providing a structured platform to present interim findings, identify overlapping themes, and refine study integration. These discussions enabled teams to exchange ideas, address methodological differences, and ensure that research findings were coherent and aligned with national AI policy objectives. The real-time feedback from these sessions was instrumental in resolving discrepancies and enhancing the clarity of sector-specific insights.

In addition to virtual discussions, we participated in in-depth workshops and meetings that brought together researchers, industry experts, policymakers, and other key stakeholders. These sessions facilitated open dialogue, collaborative problem-solving, and the exchange of best practices. By addressing inconsistencies across studies, stakeholders collectively refined recommendations, ensuring they were practical, actionable, and aligned with both national priorities and international AI governance frameworks.

We served as a bridge between the Ministry of Communication and Information Technology (MoCIT) and e-governance board (EGB), the sectoral research teams, and academic institutions, ensuring that the studies adhered to both MoCIT's strategic vision and rigorous academic standards.

3. METHODOLOGY

3.1 Desk Review

The desk review evaluates Nepal's AI-driven digital ecosystem by analyzing existing research, reports, and national policies. It examines the country's ICT and AI landscape, covering policy frameworks, regulatory measures, and international best practices. The study assesses internet connectivity, data centers, cloud services, and data policies, emphasizing privacy, security, and data quality—key factors for AI development. Additionally, it explores Nepal's ICT history, AI policies, and governance structures, comparing them with global standards

to identify gaps and opportunities [10,11]. The findings provide a structured foundation for understanding Nepal's digital infrastructure and its alignment with AI ecosystem growth.

Scholars and policymakers have investigated ways to help states devise foreign policy, national security strategies, and diplomatic strategies that address these challenges, opportunities, and role of AI in global affairs. The literature review [12-14] on impact of AI on industry value chains shows that AI technologies are transforming industry value chains, leading to job displacement, job creation, and reskilling requirements. In the education sector, the application of artificial intelligence has expanded beyond the traditional notion of AI as a supercomputer to encompass embedded computer systems [3]. A key objective of AI in education is to deliver personalized learning support tailored to each student's learning progress, preferences, and individual characteristics [15,16].

3.2 Data Collection

The research questions and survey instruments were developed based on gaps identified during the desk review and the defined research scope, ensuring a focused and targeted approach to data collection. These tools formed the foundation for gathering both qualitative and quantitative insights into Nepal's AI-driven digital ecosystem.

Primary data collection played a crucial role in capturing first-hand perspectives on the current state of AI, digital infrastructure, and data policies in Nepal. This process involved direct engagement with key stakeholders, including government officials, industry leaders, academics, civil society representatives, and regulatory bodies, through surveys, focus group discussions (FGDs), and key informant interviews (KIIs). Such interactions helped identify policy gaps, challenges, and opportunities while providing a holistic understanding of AI adoption and its impact on Nepal's economic and technological landscape.

Surveys were employed to collect quantitative data from a broad range of stakeholders, ensuring representation across sectors. The responses offered valuable insights into AI awareness, adoption levels, regulatory challenges, and infrastructure readiness, forming a critical basis for subsequent analysis. To develop comprehensive AI strategy and policy recommendations, multiple FGDs were conducted with stakeholders from diverse sectors. These discussions provided a collaborative platform for addressing key concerns, ensuring that policy recommendations reflected balanced viewpoints. The FGDs also facilitated the integration of technical, ethical, and regulatory considerations into Nepal's AI policies, promoting informed and inclusive decision-making.

The study employs a mixed-methods approach, including desk reviews and stakeholder consultations. For the industry value chain research, data were collected through 25 Key Informant Interviews, Focus Group Discussions with 31 participants, and structured surveys administered to 278 respondents. In the context of AI in education, surveys targeted 1,000 students, 150 faculty members, and 50 administrators across the Kathmandu Valley. For digital infrastructure development, surveys captured quantitative data from a broad range of stakeholders to ensure diverse representation across sectors. A total of 223 participants took part, representing government agencies, private sector organizations, regulatory bodies, technical communities and associations, research institutes, academia, civil society organizations and media, NGOs/INGOs, consultants, students and end users, and other relevant stakeholders. The survey responses provide valuable insights into AI awareness, adoption levels, regulatory challenges, and infrastructure readiness, forming a critical foundation for further analysis.

3.3 Stakeholder Consultation

A central component of this research was extensive stakeholder consultation, aimed at ensuring that the study captured diverse perspectives and produced practical, actionable recommendations for Nepal's AI ecosystem. Engaging stakeholders provided first-hand insights into the current state of AI adoption, regulatory frameworks, infrastructure readiness, and sector-specific challenges, while also identifying opportunities for strategic interventions. We convened both in-person and virtual meeting with various stakeholders from government and non-government organization to promote collaboration and ensure the coherence of their interim findings.

The consultation process involved multiple approaches. Key informant interviews were conducted with government officials, policymakers, industry leaders, academics, and representatives from civil society and regulatory bodies. These interviews offered in-depth perspectives on policy gaps, technological barriers, and sectoral priorities. Focus group discussions (FGDs) brought together participants from different sectors to foster interactive dialogue, enabling stakeholders to discuss shared challenges, exchange best practices, and collaboratively refine recommendations.

In addition, workshops and thematic meetings were organized to validate findings, discuss interim results, and align recommendations with national priorities and international AI governance standards. These forums provided stakeholders with opportunities to contribute their expertise, ensuring that the research outputs reflected balanced viewpoints and addressed technical, ethical, and regulatory considerations.

Through this structured stakeholder consultation process, the research achieved a holistic understanding of Nepal's AI landscape, strengthened cross-sector collaboration, and ensured that policy recommendations were relevant, inclusive, and implementable, supporting a coherent and strategic national AI roadmap.

4. RESULT AND DISCUSSION

This study identifies and analyzes four cross-sectoral considerations fundamental to developing effective AI policy and strategy in Nepal. Our research explores the transformative potential and implementation challenges of artificial intelligence across four pivotal domains: AI in education, digital infrastructure readiness, effects of AI on industry value chains, and digital diplomacy. These sectors represent critical pillars where AI integration can advance national interests while requiring coordinated policy frameworks that address sector-specific needs within a coherent national strategy.

4.1 AI in education

The study AI in Education explores the role and impact of

artificial intelligence on education and skills development in Nepal, with a focus on institutional readiness, faculty preparedness, and student engagement. Using a combination of surveys with administrators, focus group discussions involving education leaders and industry professionals, and data analysis, the study provides a comprehensive overview of the current educational landscape. The findings reveal that around 70% of students view AI as a useful tool for organization and learning enhancement, while faculty members recognize its potential but stress the need for institutional support, structured training, and policy backing. Industry representatives further emphasize the importance of aligning AI education with evolving market needs.

The report underscores the urgency of ensuring equitable access to AI tools and reliable internet connectivity in all classrooms, particularly in rural and underserved areas. It calls for updated and enforceable AI-specific policies to advance AI education and innovation nationwide. However, several limitations are evident, including a small and geographically narrow sample size, minimal involvement of teachers, parents, and education experts, and an urban-centric focus—mainly around Kathmandu. The study also lacks essential statistical data on AI courses, student enrollment, infrastructure, instructor availability, and projected graduate output, which are crucial for informed policy and strategy development. Additionally, it overlooks key aspects such as teacher training, curriculum enhancement, risk mitigation, and integration of international best practices, while failing to identify sustainable funding mechanisms.

To enhance future research, the study recommends adopting a more inclusive and methodologically robust approach that ensures geographical representation, diverse stakeholder participation, and a clearer framework for assessing institutional readiness. Strengthening these areas will be vital for effectively integrating AI into Nepal's education system and building a future-ready workforce.

4.2 Digital Infrastructure Readiness for AI

The study on Nepal's digital ecosystem provides an in-depth exploration of the country's ICT history, existing policies, AI practices, data privacy measures, digital infrastructure, and alignment with international benchmarks. The analysis identified significant gaps in AI governance, data protection, cybersecurity, and infrastructure development, all of which pose challenges to the growth of Nepal's AI ecosystem. To capture a broad range of perspectives, the study employed surveys, focus group discussions (FGDs), and key informant interviews (KIIs) with stakeholders from various sectors. Insights from these engagements were systematically analyzed to ensure a holistic understanding of Nepal's AI landscape.

The findings underscore the need to strengthen legal frameworks for data privacy, establish cross- border data-sharing regulations, and promote AI education and workforce development. Addressing algorithmic bias, improving cybersecurity, and setting up robust regulatory oversight mechanisms are also vital to building a trustworthy AI ecosystem. The study recommends developing a national AI roadmap that outlines both short- and long-term goals, focusing on scalable digital infrastructure, regulatory governance, and ethical AI practices. Policies should support local data availability for AI-driven innovations and foster a research ecosystem tailored to Nepal's specific needs. A well-defined AI strategy—anchored in strong governance, public–private partnerships, and stakeholder collaboration—will be critical in positioning Nepal as a competitive player in the global AI landscape.

The report on AI Digital Infrastructure further emphasizes the importance of an integrated approach that incorporates sector-specific AI policies, data-sharing frameworks, enhanced data privacy laws, ethical AI standards, and inclusive workforce development. However, several limitations were noted, including a small and geographically unrecorded sample, lack of adherence to global research standards, and limited inclusion of defense and security institutions. The reliance on self-reported data also limits the objectivity of findings. Moreover, the report does not clearly define national AI priority sectors, lacks sufficient integration of international best practices, and omits sector-specific risk assessment methodologies and funding strategies. Additionally, it fails to address high-risk sector contexts relevant to Nepal. Strengthening these areas will be essential for developing a comprehensive and future-ready AI digital infrastructure strategy.

4.3 Industrial value chain optimization using AI

The study on the effects of AI on industry value chains examines the implications of artificial intelligence for employment, automation, and reskilling in Nepal. It identifies sectors most vulnerable to job displacement due to automation and proposes strategies to support workforce adaptation and inclusive growth. Using a mixed-methods approach—including desk reviews, stakeholder consultations, and structured surveys—the study provides a comprehensive analysis of AI's impact on different sectors. It highlights that marginalized communities, particularly those with limited digital literacy and access to technology, are at greater risk of being left behind. Sectors characterized by high routine and low-skilled tasks are identified as the most susceptible to displacement, while new opportunities are emerging in high-skilled domains such as healthcare, finance, and AI development. The Effects of AI on Industry Value report underscores AI's transformative potential across Nepal's industrial sectors and recommends targeted initiatives such as reskilling programs, ethical AI frameworks, public–private partnerships, AI infrastructure development, and faculty capacity building. It emphasizes the need for strong collaboration among industry, government, and educational institutions to ensure effective AI integration and workforce preparedness. However, the report's scope is limited by a small and geographically unrecorded sample, lack of adherence to international survey standards, and an overemphasis on the IT sector—while underrepresenting agriculture, tourism, and labor-intensive industries. Furthermore, it does not clearly define Nepal's AI priority sectors or adequately address issues of job displacement, workforce adaptation, and the potential impact on remittance flows. The absence of comprehensive data on AI adoption, sector- specific risk assessments, international best practices, and funding mechanisms further limits its policy utility. Future research should adopt a broader and more inclusive approach, incorporate detailed risk assessments and clearly define

stakeholder roles to support sustainable and equitable AI-driven industrial transformation in Nepal.

4.4 Digital Diplomacy

The Digital Diplomacy study explores the implications of artificial intelligence (AI) on national security, geopolitics, and foreign policy, providing an in-depth overview of the global AI policy landscape and international cooperation mechanisms. It examines how AI is reshaping geopolitical rivalries and influencing international relations, with particular attention to what these shifts mean for Nepal's national security and foreign policy. The study also analyzes Nepal's existing AI landscape and offers targeted policy recommendations to strengthen the country's AI diplomacy. The research adopted a qualitative approach, combining an extensive review of academic literature, government documents, reports from non-governmental and multilateral agencies, and media sources. It also incorporated semi-structured interviews, focus group discussions, and case studies of five key international actors—the United States, China, India, the European Union, and Bangladesh. The findings highlight a polarized global AI ecosystem, largely divided between the US/Western bloc and China, while identifying opportunities for Nepal to engage in international cooperation on AI development, regulation, and ethical governance. The study also explores the intersection of AI with cybersecurity and national security, emphasizing the growing importance of diplomatic readiness in the AI era.

The Digital Diplomacy report recommends that Nepal enhance its AI diplomacy through three strategic pillars: knowledge transfer, coordination on data protection, and promotion of innovation—all supported by a participatory and inclusive policy development process. However, several limitations were noted, including a small and under-documented interview sample, lack of defined participant roles, and the absence of comprehensive frameworks for national interests, cybersecurity, and AI applications in diplomacy. The report also does not establish parameters for maintaining geopolitical neutrality or strategies for leveraging AI in diplomatic practice. Furthermore, it lacks a risk assessment framework for digital diplomacy and fails to identify associated risk factors.

To advance Nepal's AI diplomacy, future research should emphasize both "AI for Diplomacy"— the use of AI technologies to enhance diplomatic processes—and "Diplomacy for AI"—the use of diplomatic channels to foster AI development and innovation. A stronger assessment of Nepal's AI readiness, informed by its digital infrastructure and alignment with international best practices, will be essential for shaping an effective and forward-looking AI diplomacy strategy.

4.5 Limitations and Recommendations

The four sector-specific studies on the effects of AI adoption place strong emphasis on quantitative data, primarily to support qualitative insights and ensure alignment with global best practices. Future research should develop detailed implementation strategies, including clear frameworks for resource allocation and monitoring. The studies also require more comprehensive recommendations for curriculum development and teacher training, emphasizing specific AI skills. Alignment with international standards—particularly regarding data privacy and cross-border data sharing—needs to be more explicitly articulated, and practical resource requirements, including funding and technical expertise, should be clearly defined. The analysis of emerging AI technologies, such as generative AI, should be strengthened, alongside improvements in data availability, quality, and ethical governance frameworks. Greater international collaboration and benchmarking against global standards are essential. The studies are further limited by the absence of a pre-study AI readiness index, lack of adherence to international survey standards, and insufficient documentation of data sources, participant demographics, and geographical coverage. Additionally, the small and unrepresentative data samples reduce the generalizability of findings, while the studies fail to clearly outline their limitations and provide guidance for future research directions.

To enhance the quality of future research and policy development, several key methodological improvements are recommended. First, the development and integration of an AI Readiness Index would enable a comprehensive, cross-sectoral assessment of Nepal's current capabilities, helping to identify priority areas for intervention. Second, survey methodologies should be standardized and aligned with established international frameworks—such as the UNESCO guidelines—to strengthen data validity, reliability, and comparability. Third, ensuring data transparency through detailed documentation of data sources, participant demographics, and geographical coverage is essential for promoting research integrity and reproducibility. Finally, future studies should clearly outline their limitations and propose specific, evidence-based recommendations to guide subsequent research efforts and address existing knowledge gaps effectively.

5. CONCLUSION

The four sector-specific studies on the effects of AI in education, industry value chains, digital infrastructure, and diplomacy provide a comprehensive understanding of Nepal's current AI landscape, highlighting both opportunities and challenges for sectoral development and national policy formulation. In education, AI shows potential to enhance personalized learning, improve organizational efficiency, and strengthen skill development, but gaps in curriculum, teacher training, and equitable access—particularly in rural areas—need urgent attention. In the industry value chain, AI adoption can drive productivity, innovation, and high-skilled employment, yet issues such as job displacement, workforce reskilling, sector prioritization, and alignment with global best practices require structured strategies and stakeholder coordination. The digital infrastructure study underscores the necessity of robust data governance, ethical frameworks, inclusive policies, and cross-institutional collaboration, while identifying critical weaknesses in AI readiness, data quality, and infrastructure scalability. Finally, in digital diplomacy, AI is emerging as a tool for enhancing Nepal's international engagement, knowledge transfer, and innovation promotion, but gaps remain in strategic frameworks, risk management, neutrality, and alignment with international norms. These studies emphasize that Nepal's AI ecosystem requires a cohesive and cross-sectoral approach, combining policy alignment, workforce development, infrastructure investment, and ethical governance. Strengthening institutional capacity,

adopting standardized methodologies, and fostering international collaboration will be crucial to leveraging AI effectively. By addressing these gaps and building on identified opportunities, Nepal can position itself to harness AI for sustainable development, economic growth, and strategic global engagement.

AUTHOR CONTRIBUTIONS

All the authors contributed equally.

CONFLICT OF INTEREST

The author declares no known conflicts of interest.

ACKNOWLEDGMENTS

We sincerely thank The Asia Foundation for their generous financial support, which made the completion of this study possible. We are also grateful to Global Society for Advanced Research and Publication (GSARP), Guru Technology Pvt. Ltd. and DigNep Group Pvt. Ltd. for their invaluable assistance in data collection and peer review. Our special thanks go to all the stakeholders who contributed their time and insights through surveys, consultations, and recommendations, helping us identify and correct errors. Their support was crucial in ensuring the quality, accuracy, and relevance of this research.

REFERENCES

[1] Government of Nepal, AI concept paper (2081). https://mocit.gov.np/content/12663/12663nepal/

[2] Government of Nepal. (2024). National AI policy (2081). https://mocit.gov.np/content/13001/relations-of-artifacial-intelligence-policy-2081-to/

[3] L. Chen, P. Chen, Z. Lin, (2020). Artificial intelligence in education: A review. *IEEE Access*, **8** (2020) 75264-75278, 2020. https://doi.org/10.1109/ACCESS.2020.2988510.

[4] Y. Liang, The impact of artificial intelligence on employment and income distribution. Journal of Education, *Humanities and Social Sciences* (2024), https://doi.org/10.54097/2a7a8830

[5] L. Babashahi, C.E.Barbosa, Y. Lima, A. Lyra, H.S. dos Santos, M. Argôlo, M.A. de Almeida, J.M. de Souza, AI in the workplace: A systematic review of skill transformation in the industry. *Administrative Sciences*, **14** (6) (2014) 127. https://doi.org/10.3390/admsci14060127

[6] S.K. Lodhi, A.Y. Gill, I. Hussain, AI-powered innovations in contemporary manufacturing procedures: An extensive analysis. *International Journal of Multidisciplinary Sciences and Arts*, **3**(4) (2024) 15–25. https://doi.org/10.47709/ijmdsa.v3i4.4616

[7] A.R. Mulmi, Nepal needs to play catch-up. The Kathmandu Post December **9**, 2022). https://kathmandupost.com/columns/2022/12/08/nepal-needs-to-play-catch-up

[8] M. Shrestha, Artificial intelligence: Strategic tool in diplomacy. The Himalayan Times, (September 23, 2021). https://thehimalayantimes.com/opinion/artificial-intelligence-strategic-tool-in-diplomacy

[9] G.P. Aacharya, (Impact of artificial intelligence on new global order: A Nepalese security perspective. *Unity Journal,* (2024). https://www.nepjol.info/index.php/unityj/article/view/63189

[10] I. Rossomakha, O.N. Kyrylenko, A. Borysiuk, The impact of artificial intelligence on the labor market in the world and particularly in Ukraine. Ekonomìka, Fìnansi, Pravo, (2) (2024) 6. https://doi.org/10.37634/efp.2024.2.6

[11] International Telecommunication Union. (2024). United Nations activities on artificial intelligence (AI) 2023. ITU Publications.

[12] A. Zirar, S.I. Ali, N. Islam, Worker and workplace artificial intelligence (AI) coexistence: Emerging themes and research agenda. *Technovation*, **124** (2013) 102747.

[13] Danish Trade Union Development Agency. (2023). Nepal labour market profile 2022/2023. DTDA.

[14] H. Zhang, Economic impacts of generative artificial intelligence: A comprehensive review of the literature. *International Business & Economics Studies*, **6**(5) (2024) 69. https://doi.org/10.22158/ibes.v6n5p69

[15] G.J. Hwang, Definition, framework and research issues of smart learning environments: A context-aware ubiquitous learning perspective. *Smart Learning Environment,* **1** (2014) 4. https://doi.org/10.1186/s40561-014-0004-5

[16] Hwang, G. J., Xie, H., Wah, B. W., Gašević, D. (2020). Vision, challenges, roles and research issues of artificial intelligence in education. Computers and Education: Artificial Intelligence, https://doi.org/10.1016/j.caeai.2020.100001

First-principles Insights Into the Structural, Mechanical, Optical, Magnetic, Electronic, and Dynamical Properties of Hf_2CdN MAX phase Compound

Suraj Timsina, Bibek Dhital[1], Sushil Shrestha, Dipesh Dhital, Ganesh Paudel, Om Shree Rijal, Hari Krishna Neupane*

Amrit Campus, Institute of Science and Technology, Tribhuvan University, Kathmandu, Nepal

Research Article

ISSN: 3059-9504 (online)
DOI: https://doi.org/ 10.3126/ajs.v2i1.87758

Article History

Received: October 02, 2025; Revised: November 05, 2025; Accepted: November 15, 2025; Published: December 25, 2025

Keywords

DFT, dynamical properties, electronic properties, magnetic moment, mechanical stability, optical properties.

***Corresponding author**

Email: hari.neupane@ac.tu.edu.np
Orcid: https://orcid.org/0000-0001-8547-1183

ABSTRACT

The MAX phase compounds possess both ceramic and metallic properties and have attracted great attention from researchers. In this work, we studied the structural, mechanical, optical, magnetic, electronic, and dynamical properties of the Hf_2CdN MAX phase compound using the density functional theory (DFT) method through the Quantum ESPRESSO as a computational tool. The low value of ground-state energy confirms the structural stability of our compound. The calculated elastic constants of Hf_2CdN satisfy Born's stability criteria, indicating that it is mechanically stable. Based on the estimated mechanical parameters, Hf_2CdN exhibits anisotropic behavior, metallic-like bonding, and a brittle nature. The phonon frequency curve shows positive values, confirming that the compound is dynamically stable. From the analysis of band structure and density of states (DOS) plots, it reveals that some energy bands cross the Fermi level, indicating metallic behavior. A high absorption coefficient is observed in the visible and UV regions, suggesting potential applications in optoelectronic devices. The strong reflectivity in the UV region further highlights its suitability for radiation shielding and UV mirror materials. Additionally, the high refractive index in the infrared region suggests possible use in optoelectronic applications. From the partial and total, density of states (PDOS and TDOS) analyses, we confirm that Hf_2CdN is nonmagnetic due to the symmetric distribution of spin-up and spin-down electron states near the Fermi level. Overall, our findings provide fundamental insights into the properties of Hf_2CdN and its potential applications in various technological fields, such as it would be used in the fields of optoelectronic devices, UV radiation detectors, mirror coatings in UV lasers, and thermal imaging coatings.

1. INTRODUCTION

MAX phase compounds have a wide range of applications due to their interesting and unique combination of metallic and ceramic properties [1]. High-temperature coatings, magnetic sensors, and energy storage devices are some of their application areas [2, 3]. In general, MAX phases are denoted by the formula $M_{n+1}AX_n$, where M is an early transition metal, A is a group A element, and X is carbon or nitrogen [4]. Hf_2CdN is a 211-type MAX phase compound, where Hf, Cd, and N correspond to M, A, and X, respectively. The electronic configurations of Hf, Cd, and N are [Xe] $4f^{14}5d^26s^2$, [Kr] $4d^{10}5s^2$, and $1s^22s^22p^3$, respectively. This compound crystallizes in a hexagonal structure with space group $P6_3/mmc$ (No. 194) [5]. In this structure, Hf layers alternate with Cd layers, and N atoms located inside the Hf-centered octahedra form Hf–N bonds. Hadi and co-authors in 2015, investigated the fundamental properties of Mo_2GaC, Nb_2AsC, Nb_2InC, and Ti_2GeC using the plane-wave pseudopotential method [6]. Ali and co-authors studied the physical properties of a new MAX phase compound, Mo_2TiAlC_2, using the density functional theory (DFT) method [7]. Roknuzzaman and co-workers in 2017, explored the first Hf-based 312 MAX phase compound using a first-principles approach [8]. Sultan and co-authors in 2018, examined the physical properties of M_2InC (M = Zr, Hf, Ta) using the DFT approach [9]. In 2019, Hadi and co-authors studied the physical, lattice thermal conductivity, and vibrational properties of Lu_2SnC [10]. The computational prediction of boron-based MAX phases and MXene derivatives is carried out by Miao and co-authors [11]. Using a first-principles approach, Yang and his team in 2022, studied the elastic properties, tensile strength, damage tolerance, and electronic and thermal properties of TM_3AlC_2 (TM = Ti, Zr, and Hf) MAX phase compounds [12]. Belkacem and co-authors in 2022, investigated the stability and efficiency of the new MAX phase compounds M_3GaC_2 (M = Ti or Zr) [13]. Rougab and Gueddouh in 2023, explored the structural stability, elastic anisotropies, and mechanical and thermodynamic properties of Hf_2GeX (X = C, N, and B) using first-principles calculations [14]. Haq and his team in 2024, studied the physical properties of Cr_2PX (X = C and N) MAX phase compounds using a first-principles calculations [15]. Rijal and co-authors in 2025, investigated the physical properties of Ti_2CdC and Ti_2SC MAX phase compounds using the DFT method [16]. From these studies, it can be inferred that MAX phase ompounds have potential applications in thermal barrier coatings, optoelectronic devices, thermal shock-resistant materials, solar heating, and coating technologies. Among the reviewed literature on MAX phase compounds, to the best of our knowledge, the structural, mechanical, magnetic, optical, dynamical, and electronic properties of the Hf_2CdN MAX phase compound have not yet been explored. Therefore, our study is motivated by the need to investigate these properties of Hf_2CdN using first-principles calculations with in Quantum ESPRESSO (QE) as a computational tool [14, 15].

2. METHODOLOGY

The structural, mechanical, dynamical, electronic, magnetic, and optical properties of the Hf_2CdN MAX phase compound were investigated using the density functional theory (DFT) method [17]

implemented in the Quantum ESPRESSO (QE) as a computational tool [18]. All calculations are performed using the Perdew–Burke–Ernzerhof (PBE) functional with ultrasoft pseudopotentials (USPs) [19]. For the structural visualizations and graphical exploration, we have used XCrysDen and XmGrace [20, 21]. The structural parameters of the MAX phase compound are optimized using a plane-wave-based DFT method within the GGA-PBE approximation, where the exchange–correlation functional is treated using ultrasoft pseudopotentials (USPs). A kinetic energy cutoff of 520 eV and a Monkhorst–Pack (MP) [22] k-point mesh of (8 × 8 × 8) for band structure and (16 × 16 × 16) for the density of states (DOS) and partial DOS (PDOS) calculations are used. The lattice constants and atomic positions are fully relaxed until the residual forces are less than 0.01 eV/Å and the total energy converged within 10^{-7} eV. After structural optimization, the bond lengths are determined. Based on the M–X and M–A bond lengths, the nature of atomic bonding (ionic or metallic) is analyzed. The elastic constants C_{ij} are calculated using the stress–strain method within DFT [23]. For the hexagonal crystal system, the five independent elastic constants C_{11}, C_{12}, C_{13}, C_{33}, and C_{44} are computed. The Voigt–Reuss–Hill approximations [24, 25, 26] are employed to derive various mechanical properties, including the bulk modulus (B), shear modulus (G), and Young's modulus (E). To assess ductility or brittleness, Poisson's ratio (ν) and Pugh's ratio (B/G) are calculated. The universal anisotropic index [27] is used to evaluate elastic anisotropy (isotropic or anisotropic nature). Additionally, Kleinman's parameter [28] is computed to characterize the bonding nature in terms of stretching or bending. For the hardness properties, the Vickers hardness is calculated. The highly symmetric points within the Brillouin zone are determined using QE. To confirm dynamical stability, phonon frequency plots are generated along these high-symmetry points, and the nature of the phonon dispersion is analyzed. The electronic structure is calculated using DFT, plotting the band structure along the high-symmetry points and the density of states (DOS) to investigate the electronic response. To study magnetic behavior, the spin-up and spin-down electron distributions near the Fermi level are examined using the DOS versus energy plot. The partial density of states (PDOS) is analyzed to identify which orbitals contribute most or least to the electronic states. Based on the DFT-derived electronic structure, the frequency-dependent dielectric function ε(ω) is computed using the random phase approximation (RPA) [29, 30]. The real part, $\varepsilon_1(\omega)$, is obtained via the Kramers-Kronig relation [31], while the imaginary part, $\varepsilon_2(\omega)$, is derived from direct inter-band transitions. These dielectric functions are further used to calculate optical conductivity, reflectivity, energy-loss function, extinction coefficient, absorption coefficient, and refractive index. Optical anisotropy is assessed by analyzing these properties along different principal components of the dielectric tensor (E_{xx}, E_{yy}, E_{zz}).

3. RESULTS AND DISCUSSION

In this section, we discuss the key findings of the present study.

3.1 Structural Properties

The unit cell of the Hf_2CdN MAX-phase compound belongs to the space group $P6_3/mmc$ is shown in Fig. 1.

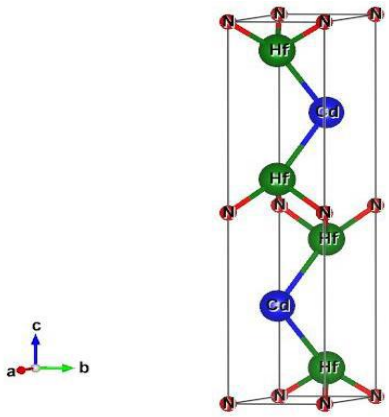

Fig. 1: (Colour online) the optimized and relaxed unit cell structure of Hf_2CdN MAX phase compound.

By analyzing the lattice parameters, bond lengths, and minimum ground-state energies, we studied the structural properties of Hf_2CdN. The calculations are performed using the GGA with PBE functional. The relaxed structure of Hf_2CdN is prepared for these calculations. The lattice parameters are initially calculated using the PBE functional and found to be a=b=3.295 Å and c=15.05 Å. The bond lengths between Hf–Cd, Cd–N, and Hf–N are also calculated using the PBE functional and found to be 3.155 Å, 4.217 Å, and 2.273 Å, respectively, before relaxation. After relaxation, the lattice parameters are determined to be a=b=3.2598 Å and c=14.6725 Å, while the bond lengths between Hf–Cd, Cd–N, and Hf–N are 3.1058 Å, 4.122 Å, and 2.230 Å, respectively.

Table 1: The estimated values of lattice parameters and bond lengths of nearest two atoms present in the material for PBE functional of optimized and relaxed structures of Hf_2CdN.

Estimated parameters	Present work Hf_2CdN	Reported work [33]
Lattice Parameter a = b (Å)	3.2598	3.1760
Lattice Parameter c (Å)	14.6725	14.4530
Bond Length Hf-Cd(Å)	3.1058	
ond Length Cd-N(Å)	4.1220	
Bond Length Hf-N(Å)	2.2300	
Bond Length Hf-C(Å)		
Bond Length Cd-C(Å)		

These values are in good agreement with previously reported values for211-based MAX-phase compounds [32]. In addition, the ground-state energy of Hf_2CdN is calculated using the PBE functional and found to be –64.716 eV, which is in good agreement with previously reported values [32]. This relatively low energy indicates a high binding energy, as binding energy and ground-state energy are inversely related. This reflects a tightly bound structure, confirming that the material is structurally stable. Based on the calculated bond lengths, lattice parameters, and ground-state energy, the stability of the material is further confirmed. All the estimated structural data are presented in Table 1.

3.2 Mechanical Properties

The mechanical properties are investigated based on the values of elastic parameters and the modulus of rigidity. The mechanical stability and strength of the MAX phase compound under compression are analyzed after applying a certain amount of pressure to the material. In the present work, we have explored the mechanical properties of the Hf_2CdN MAX phase compound using different elastic constants. The mechanical stability of the MAX phase compound can be confirmed by the Born stability criterion. Since the Hf_2CdN compound has a hexagonal structure, it consists of five independent elastic constants: C_{11}, C_{12}, C_{13}, C_{33}, and C_{44}. The compound is considered mechanically stable if it satisfies the Born stability criteria given by equations (1), (2), (3) & (4), [34]:

$C_{11} > |C_{12}|$ . . . (1)

$2C^2_{13} < C_{33}(C_{11} + C_{12})$ . . . (2)

$C_{44} > 0$ . . . (3)

$C_{66} > 0 >$ . . . (4)

The elastic constants of the Hf_2CdN compound satisfy the Born stability criteria and, hence, the material is mechanically stable. For evaluating different mechanical properties, we used the Voigt-Reuss-Hill approximations [24, 25, 26]. The bulk modulus (B), shear modulus (G), and Young's modulus (E) collectively referred to as moduli of rigidity are calculated using equations (5), (6), and (7), respectively [35]:

$B = \frac{2}{9}(c_{11} + c_{12} + \frac{2C_{12}+C_{33}}{2})$ . . . (5)

$G = \frac{1}{30}(7C_{11} + 2C_{12} - 4C_{13} - 5C_{12} + 12C_{44})$ . . . (6)

$E = \frac{9BG}{3B+G}$ . . . (7)

Using the PBE functional, the values of B, G, and E for the Hf_2CdN compound are found to be 143.72 GPa, 90.44 GPa, and 224.28 GPa, respectively. The high values of the module of rigidity indicate that a large amount of force is required to deform the material. Thus, the Hf_2CdN compound exhibits high rigidity, meaning it resists deformation and tends to retain its original shape. The positive or negative value of the Cauchy pressure denotes the bonding nature of any MAX phase compound [36]. For Hf_2CdN, the Cauchy pressure is found to be -2.8 GPa (negative), indicating metallic-like bonding. The anisotropic nature of the compound is determined by the universal anisotropic index, given by equation (8), [27]:

$A_u = 5(\frac{G_V}{G_R}) + (\frac{B_V}{B_R}) - 6$ . . . (8)

Here, G_V and $G_R$represent the shear modulus, while B_V and $B_R$represent the bulk modulus for the Voigt and Reuss approximations, respectively. If the value of the universal anisotropic index is positive, the compound is considered anisotropic [27]. We found the value of the universal anisotropic index to be 0.12, indicating the anisotropic nature of Hf_2CdN. The Vickers hardness coefficient, which measures the hardness of a compound, is given by equation (9) [37]:

$$H_v = 0.92\left(\frac{G}{B}\right)^{1.137} G^{0.708} \quad \ldots . (9)$$

Typically, MAX phase compounds have a Vickers hardness greater than 2 GPa [37]. Supporting this fact, the Vickers hardness (H_v) is found to be 13.188 GPa, 12.818 GPa, and 13.866 GPa using the Voigt, Reuss, and Hill approximations, respectively. These values further confirm the hardness of the Hf_2CdN compound. Based on the Kleinman parameter (ζ), the resistance to deformation (either bending or stretching) can be determined. If the value of ζ is greater than 0.5, the material exhibits stretching behavior, whereas a value less than 0.5 indicates bending behavior [37]. The parameter is given by equation (10) [37, 38]:

$\zeta = \frac{2C_{11}+8C_{12}}{7C_{11}+2C_{12}}$ . . . (10)

The ζ value of 0.48 for Hf_2CdN, being less than 0.5, indicates a bending-resistant nature for the PBE functional. Using Pugh's ratio and Poisson's ratio, we can determine whether the compound is brittle or ductile [39]. Pugh's and Poisson's ratios are given by equations (11) and (12), respectively [39]:

Pugh's ratio = $\frac{B}{G}$ . . . . (11)

Poisson's ratio (б) = $\frac{3B-2G}{2(3B+G)}$ . . . . (12)

Poisson's ratio greater than 0.26 indicates the ductile nature of a MAX phase compound, while a value less than 0.26 signifies brittleness [39]. Based on our analysis, the Poisson's ratios are found to be 0.240, 0.241, and 0.241 for the Voigt, Reuss, and Hill approximations, respectively, confirming the brittle nature of the Hf_2CdN compound. Similarly, for Pugh's ratio, a value less than 1.75 indicates brittleness, whereas a value greater than 1.75 represents ductility [39]. We obtained Pugh's ratio values of 1.59, 1.61, and 1.59 for the Voigt, Reuss, and Hill approximations, respectively. These values indicate that the compound under investigation exhibits a brittle nature. The Table 2 and Table 3 presents the stiffness tensor and estimated value of modulus of rigidities, Poisson ratio, Pugh's ratio, and Vickers Hardness coefficient with Voigt, Reuss, and Hill approximations of the Hf_2CdN MAX phase compound.

Table 2: the estimated values of stiffness tensors (C_{ij}) GPa of Hf_2CdN MAX phase compound for PBE functional.

C_{ij} (i/j)	1	2	3	4	5	6
1	289.16	76.77	83.71	0.00	0.00	0.00
2	76.77	289.19	83.71	0.00	0.00	0.00
3	83.71	83.71	226.72	0.00	0.00	0.00
4	0.00	0.00	0.00	79.52	0.00	0.00
5	0.00	0.00	0.00	0.00	79.52	0.00
6	0.00	0.00	0.00	0.00	0.00	106.21

Table 3: the calculated values of bulk modulus (B), Young modulus (E), shear modulus (G) Poisson ratio (б), Pugh's ratio (B/G), and Vickers Hardness coefficient (H_v) of Hf_2CdN compound with Voigt, Reuss, and Hill approximations.

Mechanical Properties	Voigt	Reuss	Hill
B (Gpa)	143.72	142.31	143.01
E (Gpa)	224.28	219.95	222.12
G (Gpa)	90.44	88.52	89.41
б	0.24	0.24	0.24
B/G	1.59	1.61	1.59
H_v(Gpa)	13.11	12.69	12.90

3.3 Optical Properties

When electromagnetic radiation interacts with the surface of a material, phenomena such as reflection, refraction, and polarization occur [40]. A detailed and precise study of optical properties opens the door to numerous potential applications in various sectors, including energy storage, optoelectronics, and

sensing devices [2, 23]. In this work, based on the electronic structure derived from DFT, the random phase approximation (RPA) is used to compute the frequency-dependent dielectric function, ε(ω) [41]. In this section, we discuss the optical properties of the Hf_2CdN MAX phase compound by analyzing its dielectric functions (tensors), reflection coefficient, refraction coefficient, energy loss function, and extinction coefficient. We analyzed the real and imaginary parts of the dielectric function over a photon energy range of 0 to 25 eV. For other optical properties, different ranges of photon energies are used. In each plane, the dielectric tensor is an important concept that measures the dielectric response when an electric field is applied. Mathematically, the complex dielectric function is expressed as;

$$\varepsilon(\omega) = \varepsilon_1(\omega) + i\varepsilon_2(\omega) \ldots \quad (13)$$

where $\varepsilon_1(\omega)$is the real part of the dielectric function (real component of the dielectric tensor) and $\varepsilon_2(\omega)$is the imaginary part (imaginary component of the dielectric tensor) [42]. The real part, $\varepsilon_1(\omega)$, is obtained using the Kramers–Kronig relation, while the imaginary part, $\varepsilon_2(\omega)$, was evaluated from direct inter-band transitions [31]. These components are used to calculate optical conductivity, reflectivity, energy-loss function, extinction coefficient, absorption coefficient, and refractive index, which are essential for investigating optical properties. We analyzed these optical properties for the different principal components of the dielectric tensor (E_{xx}, E_{yy}, E_{zz}) to confirm the optical anisotropy of the material. Mathematically the real dielectric function $\varepsilon_1(\omega)$ and imaginary dielectric function $\varepsilon_2(\omega)$ is given by equations (14) & (15) respectively, [43, 44]:

$$\varepsilon_1(\omega) = 1 + \frac{2}{\pi} p \int_0^{\infty} \frac{\omega' \varepsilon_2(\omega')}{\omega'^2 - \omega^2} d\omega' \quad \ldots (14), \text{ and}$$

$$\varepsilon_2(\omega) = \frac{8}{2\pi\omega^2} \int \sum_{fi} \{Pfi(K)\}^2 \frac{\mathrm{dsk}}{\nabla\omega fi(K)} \quad \ldots (15)$$

The real part of the dielectric tensor, or the real dielectric function, describes the energy-storing capacity or polarization of a material. Figure 2 shows the real dielectric function versus photon energy, with the dielectric function plotted on the y-axis and the corresponding photon energies on the x-axis. We analyzed the graph in two cases: first, the variation of dielectric properties when the applied field is perpendicular to the plane of the material (E_{xx}, E_{yy} in-plane) and second, when the applied field is parallel to the plane of the material (E_{zz} out-of-plane). When a material is subjected to an electric field, its ions become polarized and shift slightly. The greater the applied field, the greater the polarization, and consequently, the higher the energy-storing capacity. The plot shows a non-zero value of the real dielectric function at zero photon energy, indicating that the material can store energy even in the absence of light. This behavior is due to the presence of metallic bonding between Hf and N and the bond between Hf and Cd. Several peaks appear in the (0-3) eV photon energy range, and the peak values of the real dielectric function arise due to resonance effects. At low frequencies, the energy is small, which allows both lighter and bound electrons to contribute to polarization, resulting in maximum polarization. Conversely, at high frequencies, the heavier or tightly bound electrons cannot respond effectively to the applied field, leading to reduced polarization. Beyond a certain frequency, the material no longer interacts with light and becomes transparent. The negative values observed at the plasma frequency indicate the metallic nature of the compound. In these regions, the material does not store energy. We found that the real dielectric function reaches its maximum value of 39.80 at nearly 0 eV photon energy for $E_{xx} = E_{yy}$. The graph then sharply decreases, showing some peaks in the infrared region, and becomes negative in the visible region. For E_{zz}, the graph starts from zero, reaches a maximum value of 33.21 at approximately 1.30 eV photon energy, and then sharply decreases, becoming negative at 1.75 eV. As the photon energy increases further, the graph exhibits several peaks in the visible and ultraviolet regions. Beyond this range, the dielectric function gradually disappears. From the analysis, we found that the maximum dielectric function occurs for $E_{xx} = E_{yy}$. Fig. 2 illustrated the variation of real dielectric function with the different values of photon energies of considered compound.

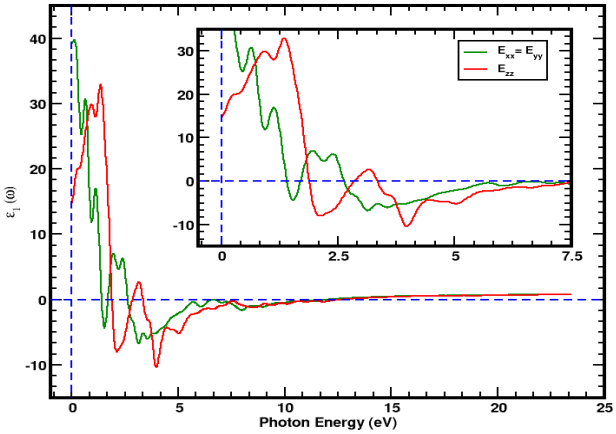

Fig. 2: (Colour online) the variation of real dielectric function with the photon energy of Hf_2CdN MAX phase compound for PBE functional. The inset represents the zoom scale of the real dielectric function versus photon energy plot.

The imaginary part of the dielectric function describes the absorption or energy loss that occurs when the electrons in a material are exposed to light (photons). This phenomenon arises due to inter-band transitions [45], which occur when the photon energy is exactly equal to the energy required for electrons to jump from the occupied valence band to the unoccupied conduction band. At this point, resonance occurs, resulting in peaks appearing in the (0-3) eV range, corresponding to the low-frequency region. The negative value near 0 eV photon energy indicates the metallic nature of the compound. Beyond a photon energy of approximately 10 eV, the material becomes transparent, meaning that light no longer affects the material and no energy loss occurs. A zero value of the imaginary dielectric function indicates that no inter-band transitions occur at that photon energy. For $E_{xx} = E_{yy}$, the graph exhibits several peaks in the infrared and visible regions, reaching a maximum of 28.54 at around 1.8 eV photon energy. For Ezz, the curve starts from a negative value, rises sharply to a maximum of 38.57 at approximately 2.3 eV, and then begins to decrease. Several peaks are also observed in the ultraviolet region; however, at higher photon energies, the curve vanishes. The maximum value of the imaginary dielectric function is found for E_{zz}. In both cases of the dielectric function, we found from the graphs that the dielectric function responds primarily at low photon energy. Fig. 3 Illustrated the variation of imaginary dielectric function with the different values of photon energies of considered compound.

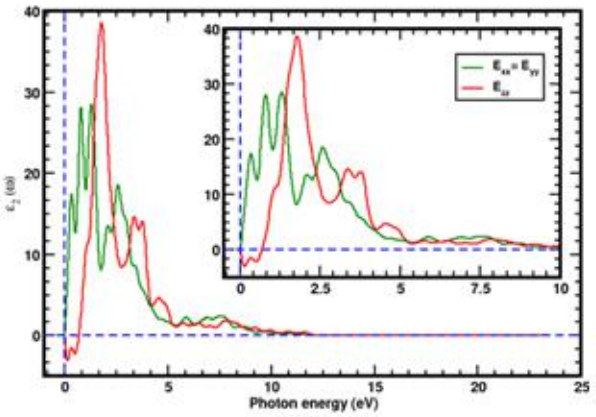

Fig. 3: (Colour online) the variation of imaginary dielectric function with the photon energy of Hf_2CdN MAX phase compound for PBE functional. The inset represents the zoom scale of the imaginary dielectric function versus photon energy plot.

The absorption coefficient determines how strongly a material absorbs light at a given photon energy [46]. A high absorption coefficient means that photons are quickly absorbed by the material, whereas a low absorption coefficient indicates that photons of that frequency can penetrate deeper into the material. Several peaks also appear in the spectrum due to inter-band transitions. The plot of the absorption coefficient, α(ω), versus photon energy is shown in Fig. 4.

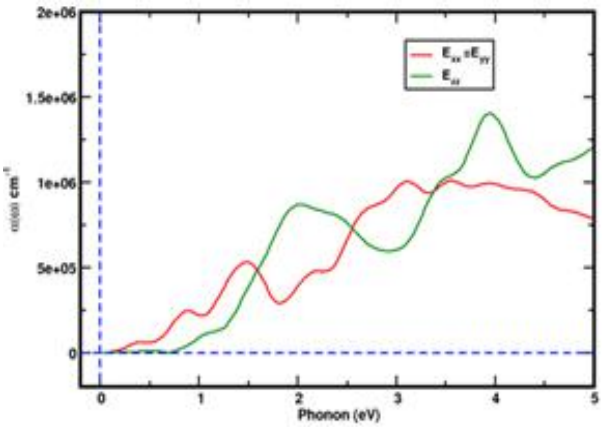

Fig. 4: (Colour online) the variation of absorption coefficient with the photon energy of Hf_2CdN MAX phase compound for PBE functional**.**

The absorption coefficient, α(ω), is plotted along the y-axis against photon energy on the x-axis. We calculated α(ω) using the following equation (16), [40]:

$$(\omega) = \frac{2\omega}{C}\left(\frac{\sqrt{\varepsilon_1^2+\varepsilon_2^2}}{2} - \frac{\varepsilon_1}{2}\right) \quad \ldots (16)$$

Analyzing the graph, the absorption coefficient of Hf_2CdN reaches a maximum in the ultraviolet region, with a value of 1.0024×10^6 for $E_{xx} = E_{yy}$. For E_{zz}, the maximum value is 1.4305×10^6, observed in both the ultraviolet and visible regions. The highest peak occurs for E_{zz} in the ultraviolet region.

Reflectivity determines how much light is reflected from the surface of a material when electromagnetic waves interact with it [32]. It also provides information about the electronic and optical response of the material [40]. A non-zero reflectivity indicates the presence of free electrons, suggesting metallic character. The reflectivity at 0 eV photon energy is called the static reflectivity, which Hf_2CdN exhibits. Several peaks appear in the spectrum due inter-band transitions. The plot of reflectivity, R(ω), versus photon energy is shown in Fig. 5.

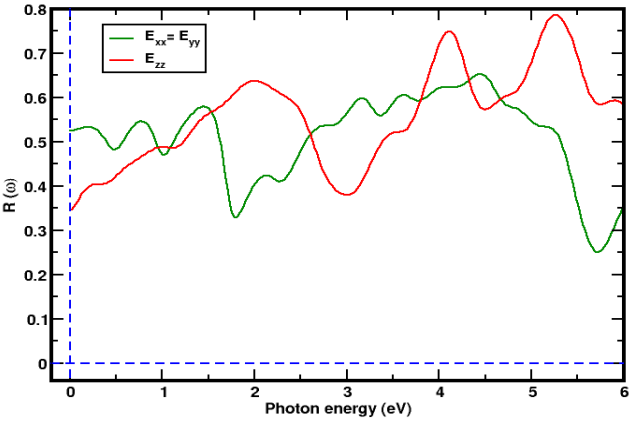

Fig. 5: (Colour online) the variation of reflection coefficient with the photon energy of Hf_2CdN MAX phase compound for PBE functional.

The reflectivity is plotted along the y-axis, and the corresponding photon energy is plotted along the x-axis. The reflection coefficient, R(ω), is calculated by equation (17), [47]:

$$R(\omega) = \frac{(\eta-1)^2+K^2}{(\eta+1)^2+K^2} \quad \ldots (17)$$

It is observed that the maximum reflectivity of Hf_2CdN for $E_{xx} = E_{yy}$ occurs in the ultraviolet region, with a value of 0.65, meaning that 35% of the light is absorbed by the material. For E_{zz}, the maximum reflectivity occurs at 5.5 eV photon energy, beyond the ultraviolet region, with a value of 0.78, indicating that 22% of the light is absorbed. For both $E_{xx} = E_{yy}$ and E_{zz}, several peaks are observed in the infrared, visible, and ultraviolet regions. The maximum reflectivity is found for E_{zz}.

The energy-loss function measures the inelastic scattering of electrons, since the imaginary part of the dielectric function describes how a material absorbs energy [40]. The important optical property, the energy-loss function characterizes the energy lost by an electron as it moves rapidly through a material, indicating how electrons (or photons) dissipate energy within the material. Due to the static response, the energy loss is very low at low frequencies or low photon energy. Figure 6 shows the plot of the energy-loss function, L(ω), versus photon energy, with L(ω) plotted along the y-axis and photon energy along the x-axis. The energy-loss function is mathematically expressed by equation (18), [38, 40]:

$$L(\omega) = \frac{\varepsilon_2}{\varepsilon_1^2+\varepsilon_2^2} \quad \ldots (18)$$

In the photon energy range of approximately (6-7) eV, we found the maximum energy-loss value for $E_{xx} = E_{yy}$, which is 0.68. Similarly, for E_{zz}, the maximum energy loss value is 0.50, observed in the (7-8) eV range. For all response axes, the maximum energy loss occurs in the (5-7) eV region. Overall, the highest energy-loss value is found for $E_{xx} = E_{yy}$.

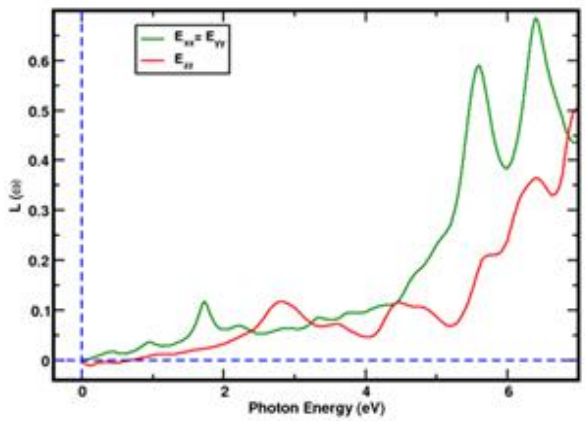

Fig. 6: (Colour online) the variation of energy loss function with the photon energy of Hf_2CdN MAX phase compound for PBE functional.

The refractive index describes how light propagates through a material [44]. It is directly related to the real part of the dielectric function, and the extinction coefficient [48]. Due to the metallic nature of the material, the refractive index is non-zero at 0 eV photon energy, which is referred to as the static refractive index. A high refractive index indicates that light travels more slowly inside the material than in a vacuum. By analyzing the refractive index of a material, we can predict the bending behavior of light and electromagnetic radiation as it passes through the material. The refractive index of considered material is calculated by using equation (19), [40]:

$$\eta(\omega) = \left(\frac{\sqrt{\varepsilon_1^2+\varepsilon_2^2}}{2} + \frac{\varepsilon_1}{2}\right)^{\frac{1}{2}} \quad \ldots (19)$$

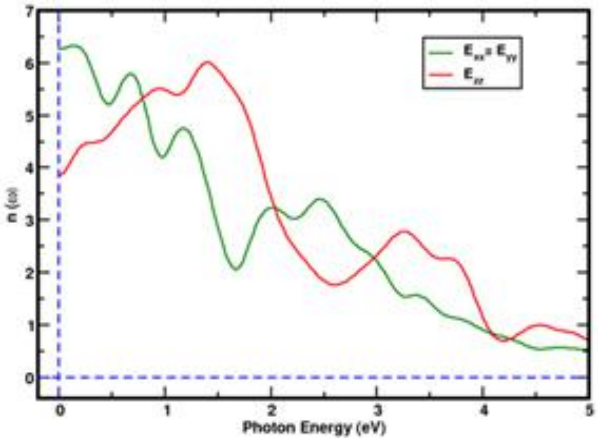

Fig. 7: (Colour online) the variation of refractive index with the photon energy of Hf_2CdN MAX phase compound for PBE functional.

Fig. 7 shows the plot of the refractive index η(ω), versus the corresponding photon energy. The maximum refractive index is observed in the infrared region, with a value of approximately 6.34 for $E_{xx} = E_{yy}$. For E_{zz}, the maximum value is about 6.04, also in the infrared region. Several peaks appear as the photon energy increases. Overall, the refractive index is highest for $E_{xx} = E_{yy}$.

The extinction coefficient describes the level of absorption loss experienced by electromagnetic waves as they travel through a material. Fig. 8 shows the plot of the extinction coefficient versus photon energy, with the extinction coefficient plotted along the y-axis and the corresponding photon energy along the x-axis. The extinction coefficient is calculated using the equation (20), [40]:

$$K(\omega) = \left(\frac{\sqrt{\varepsilon_1^2+\varepsilon_2^2}}{2} - \frac{\varepsilon_1}{2}\right)^{\frac{1}{2}} \quad \ldots (20)$$

For $E_{xx} = E_{yy}$, the maximum value of the extinction coefficient is observed to be approximately 3.95 in the (1-2) eV region, whereas for E_{zz}, the maximum value is around 4.34 in the visible region. At nearly 0 eV photon energy, a non-zero extinction coefficient is observed, reflecting the metallic nature of the compound. The higher value of E_{zz} compared to $E_{xx} = E_{yy}$ indicates the layered nature of the crystal, where electronic states along the c-axis couple differently. From all the plots and values presented, we conclude that the Hf_2CdN compound exhibits anisotropic properties, as $E_{xx} = E_{yy}$ but is not equal to E_{zz}, based on the PBE functional.

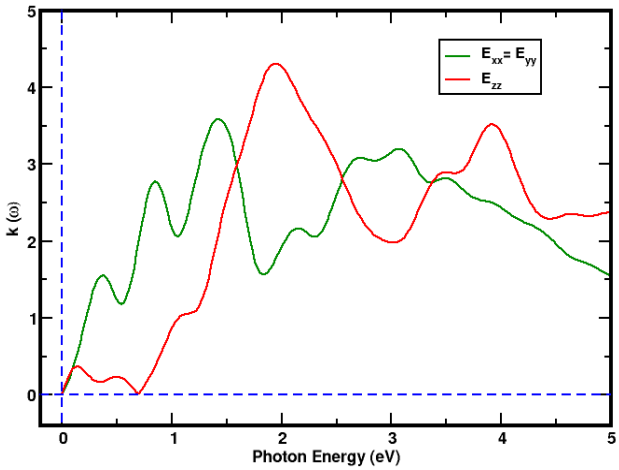

Fig. 8: (Colour online) the variation of extinction coefficient with the photon energy of Hf_2CdN MAX phase compound for PBE functional.

3.4 Magnetic Properties

Magnetic materials have a wide range of applications in both academic and industrial fields [49, 50]. In this work, we examined the magnetic properties of the Hf_2CdN MAX phase compound using density of states (DOS) and partial density of states (PDOS) plots, employing the PBE functional in DFT calculations. Each atomic orbital in the material contains electrons with up- and down-spin states. The distribution of these spin states determines the magnetic moment of the material. At the Fermi energy level, if the up- and down-spin states are distributed symmetrically, the material will have a zero magnetic moment, indicating that the material is non-magnetic [51, 52]. Similarly, if the up- and down-spin states of electrons are not distributed symmetrically around the Fermi energy level, the material will have a nonzero magnetic moment, indicating that it is magnetic. The DOS plot of Hf_2CdN, with energy (eV) on the x-axis and density of states (DOS) on the y-axis, is shown in Fig. 9.

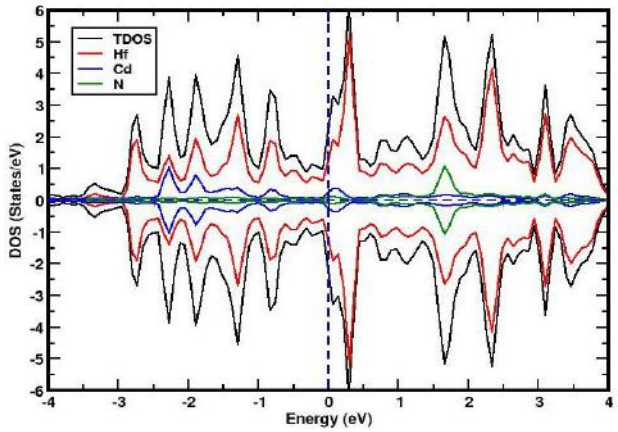

Fig. 9: (Color online) density of states (DOS) of Hf_2CdN MAX phase compound, where vertical blue dotted line represents Fermi energy level and horizontal blue dotted line separates up- and down-spin states.

The vertical blue dotted line represents the Fermi energy level, and the horizontal blue dotted line separates the up- and down-spin states. From the DOS plot computed using the PBE functional, around the Fermi energy level, the up- and down-spin states of electrons are distributed symmetrically. Therefore, we conclude that the material is non-magnetic. The total density of states (TDOS), represented by the black curve in the plot, also shows a symmetrical distribution of up- and down-spin states, confirming the non-magnetic nature of the Hf_2CdN compound.

Furthermore, the magnetic properties of a material arise from the different spin states (up and down) of its electrons. The partial density of states (PDOS) provides insight into the contributions of specific electron orbitals to the magnetic moment. Fig. 10 shows the PDOS plot of Hf_2CdN calculated using the PBE functional. From the plot, it is evident that the 6s, $5p_x$, $5p_y$, $5p_z$, $5d_{xy}$, $5d_{x^2-y^2}$, $5d_{xz}$, $5d_{yz}$ orbitals of the Hf atom have spin states distributed symmetrically around the Fermi level.

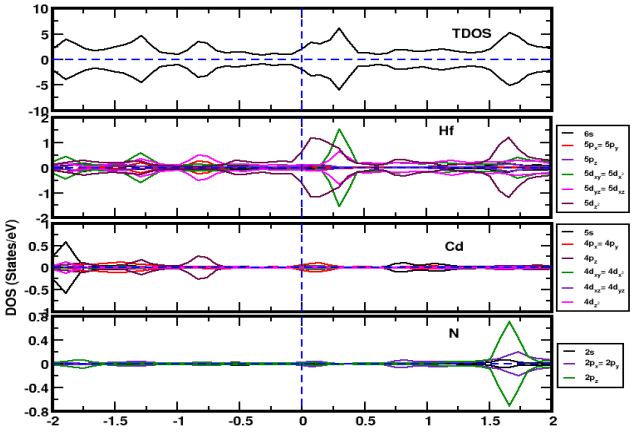

Fig. 10: (Color online) partial density of states (PDOS) of Hf_2CdN MAX phase compound, where vertical blue dotted line represents Fermi energy level and horizontal blue dotted line separates up- and down-spin states.

Although the $5d_z^2$ orbital of Hf also has a symmetrical distribution around the Fermi level, it contributes the highest magnetic moment, with values of $0.31\mu_B$/cell and $-0.31\mu_B$/cell for the up- and down-spin states, respectively. Similarly, the 5s, $4p_x$, $4p_y$, $4p_z$, $4d_{xy}$, $4d_{x^2-y^2}$, $4d_{xz}$, $4d_{yz}$, $4d_z^2$ orbitals of Cd and the 2s, $2p_x$, $2p_y$, $2p_z$ orbitals of N show symmetrical contributions around the Fermi level. Notably, the orbitals of the N atom contribute almost nothing to the magnetic moment, with the $2p_z$ orbital giving the maximum contribution of 0.05 μ_B/cell. For the Cd atom, the $4p_z$ orbital has the maximum contribution of 0.04 μ_B/cell for both spin-up and spin-down electrons. As a result, the Hf_2CdN compound exhibits non-magnetic properties.

The Table 4 shows the magnetic moments contributed by the individual orbital of Hf, Cd, and N atoms in the Hf_2CdN MAX phase compound.

Table 4: The calculated values magnetic moment (μ) contributed by each orbital of Hf, Cd and N atom in Hf_2CdN compound.

Orbitals	μ of up-spin (μ_B/cell)	μ of down-spin (μ_B/cell)	μ of Resultant (μ_B /cell)
2s of N	0.0087	-0.0087	0.0000
$2p_x$ of N	0.0321	-0.0321	0.0000
$2p_y$ of N	0.0321	-0.0321	0.0000
$2p_z$ of N	0.0518	-0.0518	0.0000
5s of Cd	0.0474	-0.0474	0.0000
$4p_x$ of Cd	0.0319	-0.0319	0.0000
$4p_y$ of Cd	0.0319	-0.0319	0.0000
$4p_z$ of Cd	0.0400	-0.0400	0.0000
$4d_{xy}$ of Cd	0.0083	-0.0083	0.0000
$4d_x^2$ of Cd	0.0083	-0.0083	0.0000
$4d_{yz}$ of Cd	0.0072	-0.0072	0.0000
$4d_{xz}$ of Cd	0.0072	-0.0072	0.0000
$4d_x^2$ of Cd	0.0110	-0.0110	0.0000
6s of Hf	0.0524	-0.0524	0.0000
$5p_x$ of Hf	0.0448	-0.0448	0.0000
$5p_y$ of Hf	0.0448	-0.0448	0.0000
$5p_z$ of Hf	0.0428	-0.0428	0.0000
$5d_x^2$ of Hf	0.2260	-0.2260	0.0000
$5d_{xy}$ of Hf	0.2260	-0.2260	0.0000
$5d_{xz}$ of Hf	0.2033	-0.2033	0.0000
$5d_{yz}$ of Hf	0.2033	-0.2033	0.0000
$5d_z^2$ of Hf	0.3100	-0.3100	0.0000

3.5. Electronic Properties

To predict the electronic properties of a material, it is essential to analyze its band structure and density of states (DOS) plots. In the present work, we computed and analyzed the band structure and DOS of Hf_2CdN using the DFT method with the PBE functional. Fig. 11 shows the band and DOS plots of the compound under consideration.

High-symmetry points are plotted along the x-axis, while the corresponding energies are plotted along the y-axis. The vertical green dotted lines parallel to the y-axis represent the high-symmetry points (Γ, H, K, Γ, A, L, H). The horizontal green line parallel to the x-axis represents the Fermi level, which separates

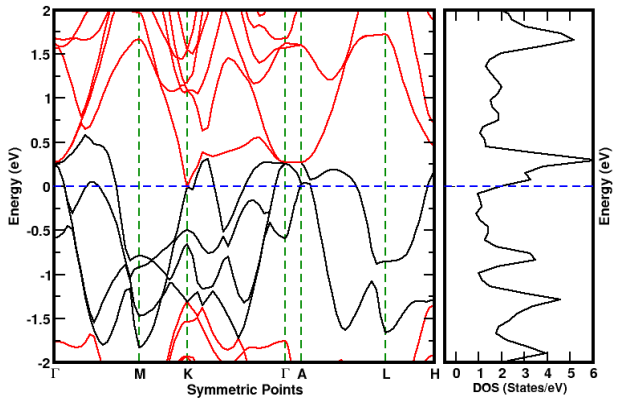

Fig. 11: (Color online) band structure and density of states (DOS) plots of Hf_2CdN MAX phase compound, where horizontal dotted line separates the electronic band in band structure and vertical dotted lines represent the highly symmetrical points.

the valence and conduction bands. The valence band is located below the Fermi level, and the conduction band is located above it. Analyzing the band and DOS plots, it is observed that some of the bands, shown in black, cross the Fermi energy level. This indicates that the valence band maximum and the conduction band minimum are identical, implying a zero-band gap, which reflects the metallic nature of the material. In the band structure, several bands cross the Fermi energy level, indicating the presence of charge carriers (electrons or ions) that can move freely across the Fermi level. Additionally, the DOS plot shows unoccupied energy states appeared near the Fermi level, suggesting a probability of charge carriers occupying these states. These observations further confirm that the Hf_2CdN compound is metallic. Based on the results from both the DOS and band structure plots, we concluded that Hf_2CdN exhibits metallic behavior.

The band structure and DOS analyses confirm the metallic character of the compound, which arises from the presence of free electrons at the Fermi level. These charge carriers play a key role in determining the material's optical behavior. In metals, the lack of a band gap results in strong intrabank transitions, causing high reflectivity and low transmittance in the low-energy region. Additionally, the negative real part of the dielectric function at lower photon energies further supports the metallic nature. Thus, the optical response of the material is in good agreement with its electronic structure, where the high density of electronic states near the Fermi level governs the observed absorption and reflectivity features.

3.6. Dynamical Properties

The dynamical stability of the Hf_2CdN MAX phase compound is examined using its phonon dispersion curve. Fig. 12 shows the phonon frequency curve of the Hf_2CdN compound.

The highly symmetric points (Γ, H, K, Γ, A, L, H) are plotted along the x-axis, with phonon frequencies plotted along the y-axis. In the curve, each vertical dotted line corresponds to a high-symmetry point. The dynamical stability of the compound is evaluated using the phonon frequency curve at each symmetric point [46]. We observed that all frequencies are positive, indicating dynamical stability. Each unit of the MAX phase contains eight atoms, resulting in a total of twenty-four phonon branches, of which there are acoustic and twenty-one are optical. The optical branches, located at the higher frequency range, determine the optical behavior of the compound, while the acoustic branches, located at the lower frequency range, correspond to coherent vibrations of atoms. Optical vibrations arise from out-of-phase atomic motions, whereas acoustic vibrations result from in-phase atomic motions [46]. For Hf_2CdN, the optical branches appear above 2 cm^{-1}. From the phonon frequency curve, all frequencies at every symmetric point are positive, confirming the dynamical stability of the compound. In Figure 12, the green curve represents the acoustic bands, and the red curve represents the optical bands. This confirms that the Hf_2CdN compound is dynamically stable. Additionally, we observe that the frequency of the acoustic modes for Hf_2CdN is zero at the Γ point, which further confirms the dynamical stability of the compound.

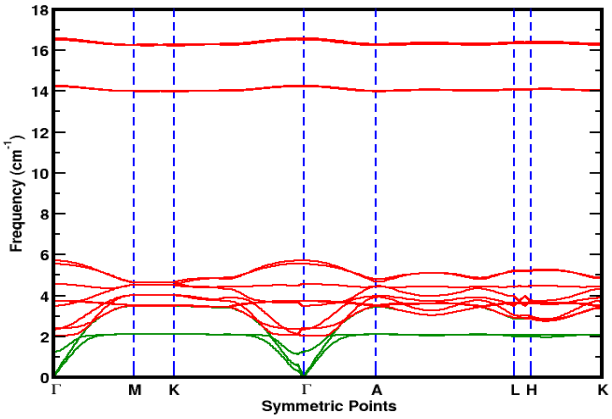

Fig. 12: (Color online) phonon frequency curve of Hf_2CdN MAX phase compound, highly symmetric points (Γ, H, K, Γ, A, L, H) are plotted along the x axis and corresponding photon frequency are plotted along the y-axis.

4. CONCLUSIONS

We have investigated the structural, mechanical, optical, magnetic, electronic, and dynamical properties of Hf_2CdN compound by employing density functional theory (DFT) with the GGA–PBE functional. For the structural properties, we computed the bond lengths, lattice parameters, and ground-state energy. The computed values are in good agreement with those reported values for other stable 211 MAX phase compounds, confirming that Hf_2CdN is structurally stable. For mechanical stability, we calculated and analyzed various moduli and elastic constants. The Born stability criteria are satisfied by Hf_2CdN, indicating that the compound is mechanically stable. The Zener anisotropy index is found to be -3.03, which deviates from 1, suggesting anisotropic behavior. The Cauchy pressure is computed -2.80, implying metallic-like bonding. Pugh's ratio and Poisson's ratio are less than 1.75 and 0.26, respectively, confirming the brittle nature of the compound. Based on the Vickers hardness and Kleinman parameter, we conclude that Hf_2CdN exhibits significant hardness and bond-stretching characteristics. For optical properties, we plotted the variation of photon energy with the real dielectric function, extinction coefficient, reflection, absorption coefficient, refractive index, and energy loss function. The maximum energy loss occurs in the UV region and beyond, compared to the infrared and visible regions. The refractive index and extinction coefficient

are higher in the infrared region, suggesting high optical conductivity. The reflectivity analysis shows that Hf_2CdN has a high reflection coefficient at low photon energies and in the UV region, indicating its potential use as a radiation-shielding material. A high absorption coefficient is observed in the visible and UV regions, suggesting possible applications in optoelectronic devices. The strong reflectivity in the UV region further highlights its suitability for UV mirrors and radiation-shielding materials. The high refractive index in the infrared region also supports its potential for optoelectronic applications. Overall, the compound shows strong optical response even at low photon energy. Since the phonon frequency curve exhibits only positive frequencies at all high-symmetry points, Hf_2CdN is dynamically stable. The electronic properties are investigated using band structure and DOS plots. The band structure reveals several bands crossing the Fermi energy level, indicating a very small or nearly zero bandgap energy. The DOS at the Fermi level is nonzero, confirming good electrical conductivity. From the DOS and PDOS analyses, we conclude that the compound is nonmagnetic due to the symmetrical distribution of spin-up and spin-down electron states around the Fermi energy level.

ACKNOWLEDGEMENTS

Authors would like to thank the condensed matter research lab CDP TU Kirtipur for conducting the computational work.

AUTHOR CONTRIBUTIONS

S. Timsina: Gathering information, data analysis and interpreting, making figures, writing the original manuscript. B. Dhital: Contribution to Formal analysis. Sushil Shrestha: Contribution to Formal analysis and editing the manuscript. D. Dhital: Contribution to Formal analysis. G. Paudel: Contribution to Formal analysis and editing the manuscript. O.S. Rijal: Contribution to Formal analysis and editing the manuscript. H.K. Neupane: Developed the concept, Supervised the investigation, analyzed the results, and implemented extensive revisions to the manuscript.

DATA AVAILABILITY

The data used to generate the figures and tables are available from the corresponding author upon request.

DECLARATIONS AND CONFLICT OF INTEREST

The author declares no known conflicts of interest.

REFERENCES

[1] M.S. Alam, M.A. Chowdhury, T. Khandaker, M.S. Hossain, M.S. Islam, M.M. Islam, M.K. Hasan, Advancements in MAX phase materials: structure, properties, and novel applications, *RSC Advances,* **14**(37) *(2024)* 1426995–7041. DOI: 10.1039/D4RA03714F

[2] H.K. Neupane, O.S. Rijal, R.K. Neupane, G. Paudel, P. Shrestha, S. Sharma, L.P. Joshi, R. Parajuli, Structural, dynamical, thermomechanical, electronic, magnetic, and optical properties of M_2 AC (M = Ta, Sc; A = Al, Cd) MAX phase compound Via DFT approach, *Physica Scripta,* **100** (2025) 095921. DOI 10.1088/1402-4896/adffc6

[3] [3] M.S. Alam, M.A. Chowdhury, M.A. Kowser, M.S. Hossain, M.S. Islam, M.M. Islam, M.K. Hasan, T. Khandaker, Advances of MAX phases: Synthesis, characterizations and challenges, *Engineering Reports,* **6** (2024) e12911. DOI: https://doi.org/10.1002/eng2.12911

[4] M.W. Barsoum, The $M_{N+1}AX_N$ phases: A new class of solids *Progress in Solid State Chemistry,* **28** (2000) 201–81. DOI: https://doi.org/10.1016/S0079-6786(00)00006-6

[5] P. Eklund, M. Beckers, U. Jansson, H. Högberg, L. Hultman, The $M_{N+1}AX$ phases: Materials science and thin-film processing *Thin Solid Films,* **518** (2010) 1851–78. DOI:https://doi.org/10.1016/j.tsf.2009.07.184

[6] M.A. Hadi, M.S. Ali, S. H. Naqib, A.K.M.A. Islam, Band structure, hardness, thermodynamic and optical properties of superconducting Nb_2AsC, Nb_2InC and Mo_2GaC, *International Journal of Computational Materials Science and Engineering,* **02** (2013) 1350007. DOI: https://doi.org/10.1142/S2047684113500073

[7] M. S. Ali, M. A. Rayhan, M. A. Ali, R. Parvin, and A. K. M. A. Islam, New MAX Phase Compound Mo_2TiAlC_2: First-principles Study, *arXiv Preprint arXiv:* **1603** (2016) 04215. DOI: https://doi.org/10.48550/arXiv.1603.04215.

[8] M. Roknuzzaman, M.A. Hadi, M.A. Ali, M.M. Hossain, N. Jahan, M.M. Uddin, J.A. Alarco, K. Ostrikov, First hafnium-based MAX phase in the 312 family, Hf_3AlC_2: A first-principles study *Journal of Alloys and Compounds,* **727** (2017) 616–26. DOI: https://doi.org/10.1016/j.jallcom.2017.08.151

[9] F. Sultana, M.M. Uddin, M.A. Ali, M.M. Hossain, S.H. Naqib, and A.K.M.A. Islam, First principles study of M_2InC (M = Zr, Hf and Ta) MAX phases: The effect of M atomic species, *Results in Physics*, **11** (2018) 869–876. DOI: https://doi.org/10.1016/j.rinp.2018.10.044

[10] M.A. Hadi, N. Kelaidis, S.H. Naqib, A. Chroneos, A.K.M.A. Islam, Mechanical behaviors, lattice thermal conductivity and vibrational properties of a new MAX phase Lu_2SnC, *Journal of Physics and Chemistry of Solids*, **129** (2019)162–171. DOI: https://doi.org/10.1016/j.jpcs.2019.01.009

[11] N. Miao, J. Wang, Y. Gong, J. Wu, H. Niu, S. Wang, K. Li, A. R. Oganov, T. Tada, H. Hosono, Computational Prediction of Boron-Based MAX Phases and MXene Derivatives, Chemistry of Materials, **32** (2020) 6947–6957. DOI: https://doi.org/10.1021/acs.chemmater.0c02139

[12] A. Yang, Y. Duan, L. Bao, M. Peng, L. Shen, Elastic properties, tensile strength, damage tolerance, electronic and thermal properties of TM_3AlC_2 (TM = Ti, Zr and Hf) MAX phases: A first-principles study, *Vacuum,* **206** (2022) 111497. https://doi.org/10.1016/j.vacuum.2022.111497

[13] A.A. Belkacem, H. Rached, M. Caid, Y. Rached, D. Rached, N. T. Mahmoud, N. Benkhettou, The stability analysis and efficiency of the new MAX-phase compounds M_3GaC_2 (M: Ti or Zr): A first-principles assessment, *Results in Physics,* **38** (2022) 105621. DOI: https://doi.org/10.1016/j.rinp.2022.105621

[14] M. Rougab, A. Gueddouh, First-principles insights into structural stability, elastic anisotropies, mechanical and thermodynamic properties of the Hf_2GeX (X = C, N, and B) 211 MAX phases, *Journal of Physics and Chemistry of Solids,* **176** (2023) 111251. https://doi.org/10.1016/j.jpcs.2023.111251

[15] B. Ul Haq, S.-H. Kim, A. Alqahtani, R. Ahmed, A.R. Chaudhry, Y.A.H. Obaidat, M.B. Kanoun, S. Goumri-Said, Investigations of the physical behavior of Cr_2PX (X = C and N) MAX phases through first-principles calculations, *Computational Condensed Matter,* **40** (2024) e00937. DOI: https://doi.org/10.1016/j.cocom.2024.e00937

[16] O.S. Rijal, H. K. Neupane, D. Oli, R.K. Neupane, P. Shrestha, S. Sharma, L.P. Joshi, R. Parajuli, A first-principles investigation of the structural, mechanical, dynamic, electronic, magnetic, and optical properties of Ti_2AC (A = Cd, S) MAX phase compounds, *J0urnal of Physics D: Applied Physics,* **58** *(2025)* 125102. DOI: 10.1088/1361-6463/ada808

[17] K.B. Lipkowitz, D.B. Boyd, *Reviews in Computational Chemistry*, **7** (1996). DOI:10.1002/9780470890905

[18] P. Giannozzi, O. Baseggio, P. Bonfà, D. Brunato, C. Car, I. Carnimeo, C. Cavazzoni, S. De Gironcoli, P. Delugas, F. Ferrari Ruffino, A. Ferretti, N. Marzari, I. Timrov, A. Urru, S. Baroni, QUANTUM ESPRESSO toward the exascale, *Journal of Chemical Physics,* **152** (2020) 154105. DOI: https://doi.org/10.1063/5.0005082

[19] B. Hammer, L.B. Hansen, J.K. Nørskov, Improved adsorption energetics within density-functional theory using revised Perdew–Burke–Ernzerhof functionals, *Physical Review B,* **59** (1999) 7413–7421. DOI: https://doi.org/10.1103/PhysRevB.59.7413

[20] A. Kokalj, XCrySDen-a new program for displaying crystalline structures and electron densities, *Journal of Molecular Graphics and Modeling,* **17** (1999) 176–179. DOI:https://doi.org/10.1016/S1093-3263(99)00028-5

[21] B.K.R. Sanapalli, V. Yele, S. Jupudi, V.V.S.R. Karri, Ligand-based pharmacophore modeling and molecular dynamic simulation approaches to identify putative MMP-9 inhibitors, *RSC Advances*, **11** (2021) 26820–26831. DOI: 10.1039/D1RA03891E

[22] H.J. Monkhorst, J. D. Pack, Special points for Brillouin-zone integrations, *Physical Review B,* **13** (1976) 5188–5192. DOI: https://doi.org/10.1103/PhysRevB.13.5188

[23] İ. Kars Durukan, Mechanical, vibration, and optical properties of IrAl intermetallic compound via DFT calculations: high-pressure effect, *Physica Scripta,* **98** (2023) 075903. DOI: 10.1088/1402-4896/acd904

[24] W. Voigt, Ueber die Beziehung zwischen den beiden Elasticitätsconstanten isotroper Körper, *Annals of Physics,* **274** (1889) 573–587. DOI: https://doi.org/10.1002/andp.18892741206

[25] A. Reuss, Berechnung der Fließgrenze von Mischkristallen auf Grund der Plastizitätsbedingung für Einkristalle, *Zeitschrift für Angewandte Mathematik und Mechanik,* **9** (1929) 49–58. DOI: https://doi.org/10.1002/zamm.19290090104

[26] R. Hill, The Elastic Behaviour of a Crystalline Aggregate, *Proceedings of the Physical Society A,* **65** (1952) 349–354. DOI 10.1088/0370-1298/65/5/307

[27] S.I. Ranganathan, M. Ostoja-Starzewski, Universal Elastic Anisotropy Index, *Physical Review Letters,* **101** (2008) 055504. DOI: https://doi.org/10.1103/PhysRevLett.101.055504

[28] L. Kleinman, Deformation Potentials in Silicon. I. Uniaxial Strain, *Physics Review,* **128** *(1962)* 2614–2621. DOI: https://doi.org/10.1103/PhysRev.128.2614

[29] W. Körner, C. Elsässer, First-principles density functional study of dopant elements at grain boundaries in ZnO, *Physics Review B,* **81** (2010*)* 085324. DOI: https://doi.org/10.1103/PhysRevB.81.085324

[30] G.P. Chen, V.K. Voora, M.M. Agee, S.G. Balasubramani, F. Furche, Random-Phase Approximation Methods, *Annual Review of Physical Chemistry,* **68** (2017) 421–445. DOI: https://doi.org/10.1146/annurev-physchem-040215-112308

[31] X. Li, H. Cui, R. Zhang, First-principles study of the electronic and optical properties of a new metallic MoAlB, *Scientific Reports,* **6** (2016) 39790. DOI: 10.1038/srep39790

[32] H.K. Neupane, D. Oli, O.S. Rijal, R.K. Neupane, P. Shrestha, S. Sharma, L.P. Joshi, R. Parajuli, Exploring the structural, dynamical, mechanical, electronic, magnetic, and optical properties of Ta_2AlN, Ti_2AlN & Ti_2GaN MAX phase compounds: First-principles study, *Heliyon,* **11** (2025) e42962. DOI: 10.1016/j.heliyon.2025.e42962

[33] M. Mebrek, A. Mokaddem, B. Doumi, A. Yakoubi, A. Mir, Novel theoretical prediction of structural properties, ferromagnetic ordering, and electronic structure of Fe_2PbC MAX phase, *Journal of Superconductivity and Magnetism*, **31** (2018) 2485–2490. DOI: https://doi.org/10.1007/s10948-017-4506-6

[34] M. Born, On the stability of crystal lattices. I, *Mathematical Proceedings of the Cambridge Philosophical Society,* **36** (1940) 160–172. DOI: https://doi.org/10.1017/S0305004100017138

[35] M. Born and R. Fürth, The stability of crystal lattices. III: An attempt to calculate the tensile strength of a cubic lattice by purely static considerations, *Mathematical Proceedings of the Cambridge Philosophical Society,* **36** (1940) 454-465. DOI: https://doi.org/10.1017/S0305004100017503

[36] S.-C. Wu, G.H. Fecher, S. Shahab Naghavi, C. Felser, Elastic properties and stability of Heusler compounds: Cubic Co_2YZ compounds with $L2_1$ structure, *Journal of Applied Physics,* **125** (2019*)* 082523. DOI: https://doi.org/10.1063/1.5054398

[37] Y. Tian, B. Xu, and Z. Zhao, Microscopic theory of hardness and design of novel superhard crystals, *The International Journal of Refractory Metals and Hard Materials,* **33** (2012*)* 93–106. DOI: https://doi.org/10.1016/j.ijrmhm.2012.02.021

[38] D.R. Lawati, H.K. Neupane, D.K. Chaudhary, P. Shrestha, R. P. Adhikari, L.P. Joshi, R. Parajuli, Structural, mechanical, electronic and optical properties of $MgZnO_3$ perovskite: First-principles study, *ornal of Physics and Chemistry of Solids,* **181** (2023) 111547. DOI: https://doi.org/10.1016/j.jpcs.2023.111547

[39] G.N. Greaves, A.L. Greer, R.S. Lakes, T. Rouxel, Poisson's ratio and modern materials, *Nature Materials.,* **10** (2011) 823–837. DOI: https://doi.org/10.1038/nmat3134

[40] J. Singh, *Optical Properties of Condensed Matter and Applications*, John Wiley & Sons, **6** (2006). DOI: 10.1002/0470021942

[41] H. Eshuis, J.E. Bates, F. Furche, Electron correlation methods based on the random phase approximation, *Theoretical Chemistry Accounts,* **131** (2012) 1084.

DOI: https://doi.org/10.1007/s00214-011-1084-8

[42] Y. Wu, X. Wang, Y. Wang, Y. Duan, M. Peng, Insights into electronic and optical properties of $AGdS_2$ (A = Li, Na, K, Rb and Cs) ternary gadolinium sulfides, *Optical Matererials,* **114** (2021) 110963. DOI: https://doi.org/10.1016/j.optmat.2021.110963

[43] C. Ambrosch-Draxl, J.O. Sofo, Linear optical properties of solids within the full-potential linearized augmented planewave method, *Computer Physics Communications,* **175** (2006) 1–14. DOI: https://doi.org/10.1016/j.cpc.2006.03.005

[44] B. Amin, I. Ahmad, M. Maqbool, S. Goumri-Said, R. Ahmad, *Ab initio* study of the bandgap engineering of $Al_{1-x}Ga_xN$ for optoelectronic applications, *Journal of Applied Physics,* **109** (2011) 023109. DOI: https://doi.org/10.1063/1.3531996

[45] M. Davies, Dielectric absorption, *Quarterly Reviews Chemical Society,* **8** (1954) 250. DOI: 10.1039/QR9540800250

[46] M.W. Qureshi, X. Ma, G. Tang, R. Paudel, *Ab initio* predictions of structure and physical properties of the Zr_2GaC and Hf_2GaC MAX phases under pressure, *Scientific Reports,* **11** (2021) 3260. DOI: https://doi.org/10.1038/s41598-021-82402-1

[47] B. Ul Haq, S.-H. Kim, S. AlFaify, M.A. Javed, R. Ahmed, K. Alam, A.R. Chaudhry, Physical properties of 211-type MAX phases based on Mn_2AlX (X = C, N, and F) through first-principles approaches, *Mater. Today Commun.,* **37** (2023) 107384. DOI: https://doi.org/10.1016/j.mtcomm.2023.107384

[48] M.A. Ali, M.T. Nasir, M.R. Khatun, A.K.M. A. Islam, S.H. Naqib, *Ab initio* investigation of vibrational, thermodynamic, and optical properties of Sc_2AlC MAX compound, *Chinese Physics B,* **25** (2016) 103102. DOI: 10.1088/1674-1056/25/10/103102

[49] H.K. Neupane, N.P. Adhikari, Structure, electronic and magnetic properties of 2D Graphene–Molybdenum diSulphide (G–MoS_2) heterostructure (HS) with vacancy defects at Mo sites, *Computational Condensed Matter,* **24** (2020) e00489. DOI: https://doi.org/10.1016/j.cocom.2020.e00489

[50] M.V. Makarova, Y. Akaishi, T. Ikarashi, K.S. Rao, S. Yoshimura, H. Saito, Alternating magnetic force microscopy: Effect of Si doping on the temporal performance degradation of amorphous FeCoB magnetic tips, *Journal of Magnetism and Magnetic Materials,* **471** (2019) 209–214. DOI: https://doi.org/10.1016/j.jmmm.2018.09.046

[51] M. Nepal, G. Paudel, S. Aryal, A. Devkota, H.K. Neupane, Adsorption of water on vacancy defective h-BN bilayer at B and N sites: First-principles calculation, *BIBECHANA,* **21** (2024) 129–141. DOI: https://doi.org/10.3126/bibechana.v21i2.62607

[52] G. Paudel, M. Nepal, S. Aryal, A. Devkota, H.K. Neupane, Effect of water adsorption on bilayer h-BN: First-principles study, *Journal of Nepal Physical Society,* **9** (2023) 56–62. DOI: https://doi.org/10.3126/jnphyssoc.v9i2.62323

Relationship between Geomagnetic Indices (Kp, Ap) and Solar Activity (Sunspot Number)

Debasri Samanta[1*], Rajib Kumar Dolai[2]

[1]Department of Physics, Vidyasagar University, Midnapore, West Bengal, India
[2]Department of Economics, Tamralipta Mahavidyalaya, Tamluk, West Bengal, India

Research Article

ISSN: 3059-9504 (online)
DOI:https://doi.org/ 10.3126/ajs.v2i1.87768

Article History

Received: October 16, 2025; Revised: November 14, 2025; Accepted: November 16, 2025; Published: December 25, 2025

Keywords

Sunspot Number (SSN), Kp, Ap, Time-series decomposition, Power spectral density (PSD), Cumulative distribution function (CDF).

Corresponding Author

Email: debasri94s@gmail.com (D Samanta)
Orcid: https://orcid.org/0000-0002-1333-1189

ABSTRACT

This study examines the relationship between solar activity (Sunspot Number) (SSN) and geomagnetic indices (Kp and Ap) using time-series decomposition, distribution analysis, and correlation analysis. The results show an inverse relationship between Kp, Ap, and SSN up to 1990, followed by a strong positive correlation thereafter. Distribution analysis indicates that SSN is dominated by low-frequency components, whereas Kp and Ap capture both long-term trends and shorter-term variations, such as the ~ 27-day solar rotation cycle. Correlation analysis reveals weak overall correlations but strong trend correlations, particularly during the 12:00–15:00 UT interval for Kp and Ap with SSN.

1. INTRODUCTION

The Sun, our nearest star, continuously emits electromagnetic radiation and charged particles into space, a process collectively referred to as solar activity. Phenomena such as sunspots, solar flares, high-speed solar wind streams, and coronal mass ejections (CMEs) influence the Earth's space environment and interact with the magnetosphere and ionosphere. When energetic solar wind plasma and interplanetary magnetic field (IMF) structures encounter Earth's geomagnetic field, they can trigger geomagnetic storms—temporary but intense disturbances in the geomagnetic field. The magnitude of these disturbances largely depends on solar wind parameters, including wind speed, density, and particularly the southward component of the IMF.

Geomagnetic activity is commonly monitored through standardized indices. The Kp index, ranging from 0 to 9, measures global geomagnetic disturbances over 3-hour intervals, whereas the Ap index represents a daily linear-scaled measure of geomagnetic activity. Solar activity is typically represented by the Sunspot Number (SSN), which varies over an approximately 11-year solar cycle. Higher SSN values correspond to solar maximum phases characterized by frequent and intense solar eruptions, while solar minimum periods reflect relatively quiet geomagnetic conditions.

The scientific literature highlights strong relationships between solar activity, solar wind conditions, and geomagnetic disturbances. Svalgaard [1] corrected the long-term Ap index to better represent geomagnetic variability, particularly during polarity intervals of the interplanetary magnetic field. Venkatesan et al. [2] identified a distinctive two-peak structure in geomagnetic activity near solar maxima. Rangarajan et al. [3] demonstrated that Kp and Ap indices exhibit seasonal and solar cycle variations linked to solar wind dynamics, and subsequently showed that trends in Kp-based activity could be used to estimate upcoming sunspot maxima [4].

Further developments include multifractal scaling properties in geomagnetic indices reported by Yu et al. [5], and investigations by Urata et al. [6] connecting geomagnetic activity with seismic precursors, later extended by Akyol et al. [7] using ionospheric signals. Singh et al. [8] projected geomagnetic patterns for Solar Cycle 25, while Echer et al. [9] identified not only the well-known 11-year solar cycle but also a shorter 4.4-year periodicity in geomagnetic activity. Recent progress includes documentation of secular changes in the Kp index and the development of nowcast models by Matzka et al. [10], hemispheric asymmetry in solar indices reported by El-Borie et al. [11], and strong correlations between solar flare indices and geomagnetic disturbances demonstrated by Ozguc et al. [12]. Additionally, Uga et al. [13] observed significant suppression of cosmic ray intensity during geomagnetic storms, particularly at low-latitude stations, and Samanta et al. [14] applied stochastic modelling and Monte-Carlo methods in astrophysical datasets, illustrating the relevance of such methods for uncertainty estimation in space-weather analysis.

The objective of this study is to analyze the relationship between solar activity (SSN) and geomagnetic disturbances (Kp and Ap indices) using time-series analysis, distribution analysis, and correlation analysis.

2. METHODOLOGY

2.1 Data Collection

The present study utilizes complete historical time-series data, rather than sampled survey data. Therefore, population and sampling size definitions are not applicable, as the full

observational record was used to avoid any sampling bias. Daily values of the geomagnetic indices Kp and Ap were obtained from the National Centers for Environmental Information (NCEI), operated by the National Oceanic and Atmospheric Administration (NOAA). These indices are generated every three hours and subsequently aggregated to daily values. Additionally, daily Sunspot Number (SSN) data, representing solar activity levels, were sourced from the Space Weather Prediction Center (SWPC), also part of NOAA. The dataset covers the period 1932–2020, ensuring robust long-term coverage for investigating the relationship between solar activity and geomagnetic responses. Data are publicly accessible through the NOAA-NCEI geomagnetic archive (https://www.ngdc.noaa.gov/stp/geomag/kp_ap.html) and the NOAA-SWPC solar cycle database (https://www.swpc.noaa.gov/products/solar-cycle-progression).

2.2 Seasonal-Trend Decomposition Method

To extract long-term patterns and recurring seasonal behavior from the time-series data, we applied the Seasonal-Trend decomposition using Loess (STL) [15] technique. STL is a robust, non-parametric framework that decomposes a time series into three components: a trend component T_t capturing long-term changes, a seasonal component S_t representing periodic fluctuations, and a residual component R_t that accounts for random irregular variations. Mathematically, the series Y_t at time t is represented as

$$Y_t = T_t + S_t + R_t \quad \text{..... (1)}$$

Each component is estimated independently, allowing the decomposition to adapt flexibly to non-linear structures present in geomagnetic and solar data.

2.3 Distribution Method

To study the frequency structure and statistical distribution of geomagnetic indices (Kp, Ap) and solar activity (SSN), we employed Power Spectral Density (PSD) and Probability Density Function (PDF) analysis. Daily Kp and Ap values were computed as the mean of eight 3-hour measurements recorded each day.

The PSD quantifies how variance (power) is distributed across frequency components, enabling identification of dominant periodicities. PSD was estimated using Welch's method, where the signal is segmented, windowed, and Fourier-transformed. For a segment index k and frequency f, the spectral estimate is

$$P_{xx}(f) = \frac{1}{N}\sum_{k=1}^{K}|X_k(f)|^2 \quad \text{..... (2)}$$

where:

- $P_{xx}(f)$ is the estimated power at frequency f,
- N is the number of segments into which the time series is divided,
- K is the total number of segments,
- $X_k(f)$ is the Fourier transform of the k-th segment of the time series.

The PDF describes the probability of the time-series variable taking a particular value. For observations X_i and bin width Δx, the PDF is defined as

$$PDF\ (x) = \frac{1}{N\Delta x}\sum_{i=1}^{N}\delta(x - X_i) \quad \text{..... (3)}$$

where:

- $PDF\ (x)$ is the probability density at value x,
- N is the total number of observations,
- Δx is the bin width,
- X_i represents each individual observation in the time series,
- $\delta(x - X_i)$ is an indicator function that counts the occurrences of values in the range of bin x.

Additionally, the Cumulative Distribution Function (CDF) of the PSD evaluates the cumulative contribution of frequencies to total power. For frequencies $f' \le f$, the CDF is expressed as

$$\mathrm{CDF_{PSD}(f)} = \frac{\sum_{f' \le f} P_{xx}(f')}{\sum_{f'} P_{xx}(f')} \quad \text{..... (4)}$$

which enables quantification of low- versus high-frequency dominance in geomagnetic variability.

2.4 Correlation Method

To examine the statistical association between geomagnetic activity (Kp and Ap) and solar activity (SSN), we employed the Pearson correlation coefficient, which measures the linear dependence between two variables. For paired observations X_i (e.g., daily Kp or Ap) and Y_i (daily SSN), the coefficient r is given by

$$r = \frac{\sum_{i=1}^{n}(X_i - \bar{X})(Y_i - \bar{Y})}{\sqrt{\sum_{i=1}^{n}(X_i - \bar{X})^2}\sqrt{\sum_{i=1}^{n}(Y_i - \bar{Y})^2}} \quad \text{..... (5)}$$

where $\bar{X}$ and $\bar{Y}$ represent the mean values of the respective series and n is the number of paired observations. The value of r ranges between -1 and $+1$, indicating negative, positive, or no linear correlation.

3. RESULTS AND DISCUSSION

The analysis begins by examining the long-term variability of solar activity and its connection with geomagnetic indices. As shown in Fig. 1, the Sunspot Number (SSN) exhibits a strong linkage with the Kp and Ap indices. Peaks in SSN, corresponding to solar maxima, generally coincide with elevated values of Kp and Ap, confirming that periods of intense solar activity are accompanied by enhanced geomagnetic disturbances. This suggests that increases in SSN, reflecting higher sunspot activity, are associated with corresponding rises in Kp and Ap due to the intensified impact of solar forcing on Earth's magnetosphere. The characteristic ~11-year solar cycle observed in SSN is also mirrored in the variations of Kp and Ap, indicating a recurring pattern of enhanced geomagnetic activity that aligns with solar cycle phases. To explore these relationships in greater detail, time-series decomposition, distributional characteristics, and correlation analyses were conducted.

3.1 Time-Series Decomposition Analysis

The decomposition of the data provides insights into long-term trends, seasonal cycles, and irregular variations of SSN, Kp, and Ap indices.

The long-term trends of the Kp and Ap geomagnetic indices, alongside SSN, show distinct behaviors across the observation period. While Kp and Ap display pronounced fluctuations with peaks and troughs reflecting changing levels of geomagnetic activity, they also reveal a gradual downward trend toward the end of the series. In contrast, SSN exhibits a steady overall decline in solar activity. A closer look at the SSN trend reveals three distinct segments: (i) a sharp decline until 1960, (ii) a moderate decline between 1960 and 1990, and (iii) a rapid decline after 1990. When compared with the geomagnetic indices, contrasting patterns emerge in the earlier periods. During the first segment, while SSN declines sharply, Kp and Ap increase significantly. Between 1960 and 1990, Kp and Ap continue to rise, though at a slower rate, whereas SSN declines moderately. In the final period (1990–2020), all three indices exhibit a synchronized downward trend, indicating strong alignment between solar and geomagnetic activity in recent decades (Fig. 2).

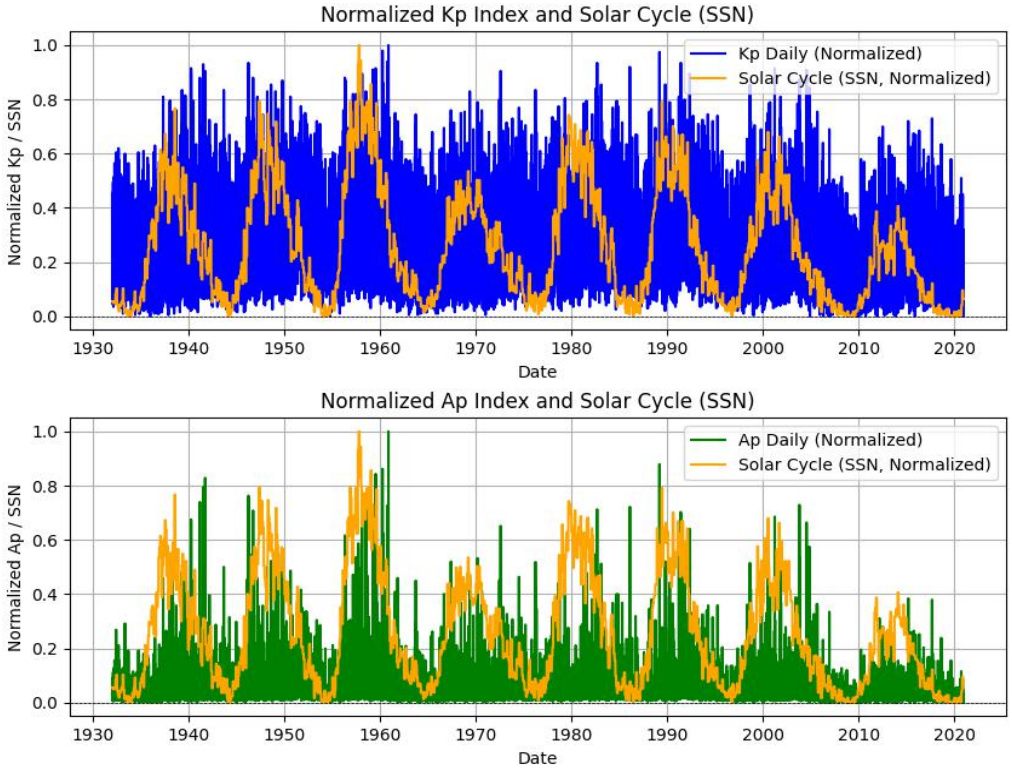

Fig. 1: Normalized Sunspot Number (SSN) and Geomagnetic Indices (Kp and Ap) [**Source:** Designed by the authors (Using python)]

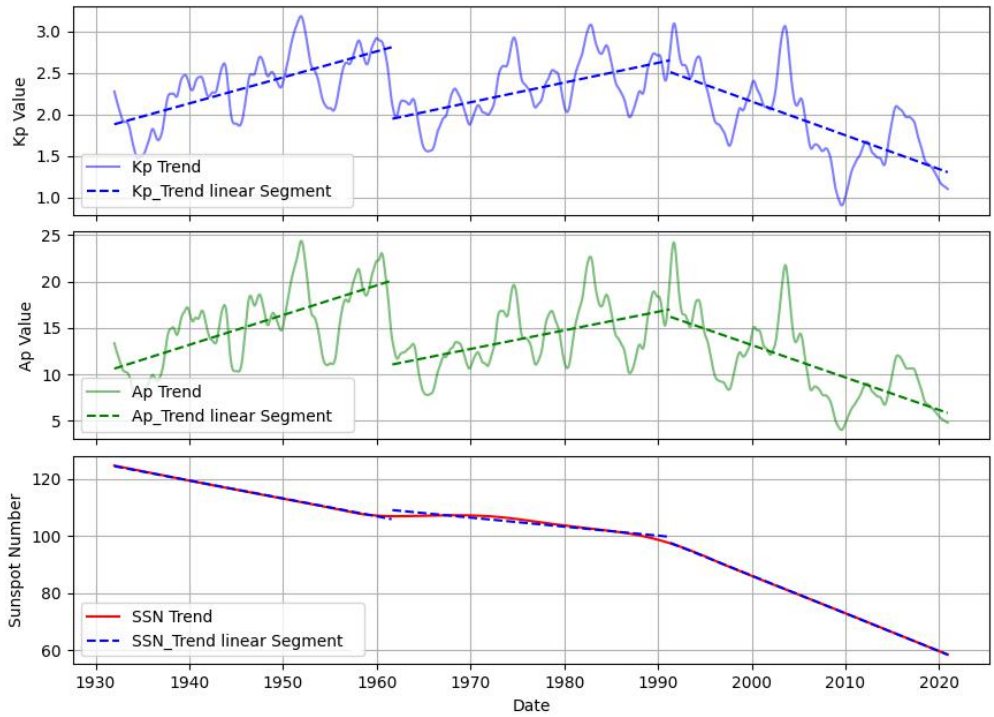

Fig. 2: Trends Components in Kp, Ap, and SSN [**Source:** Designed by the authors (Using python)]

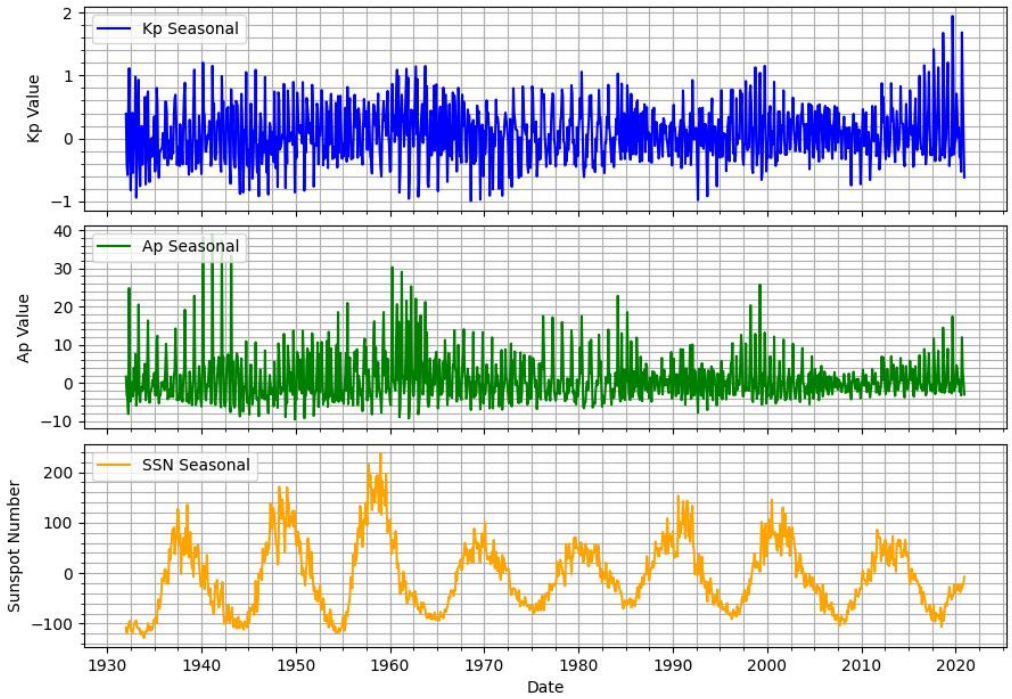

Fig. 3: Seasonal Components in Kp, Ap, and SSN [**Source:** Designed by the authors (Using python)]

The seasonal decomposition highlights the cyclical behavior of solar and geomagnetic indices. The Kp index exhibits consistent semi-annual oscillations, reflecting Earth's orbital position relative to solar wind input. The Ap index also displays a seasonal pattern, but with greater amplitude, indicating heightened sensitivity to intense geomagnetic disturbances, likely driven by strong solar wind streams or coronal mass ejections. SSN, in turn, mirrors the ~11-year solar cycle, with peaks corresponding to solar maxima and troughs to minima (Fig. 3). These seasonal components demonstrate the close coupling between solar cycles and geomagnetic responses, with notable impacts observed during the 1960s, 1990s, and 2000s, when solar maxima significantly amplified geomagnetic activity (Fig. 4).

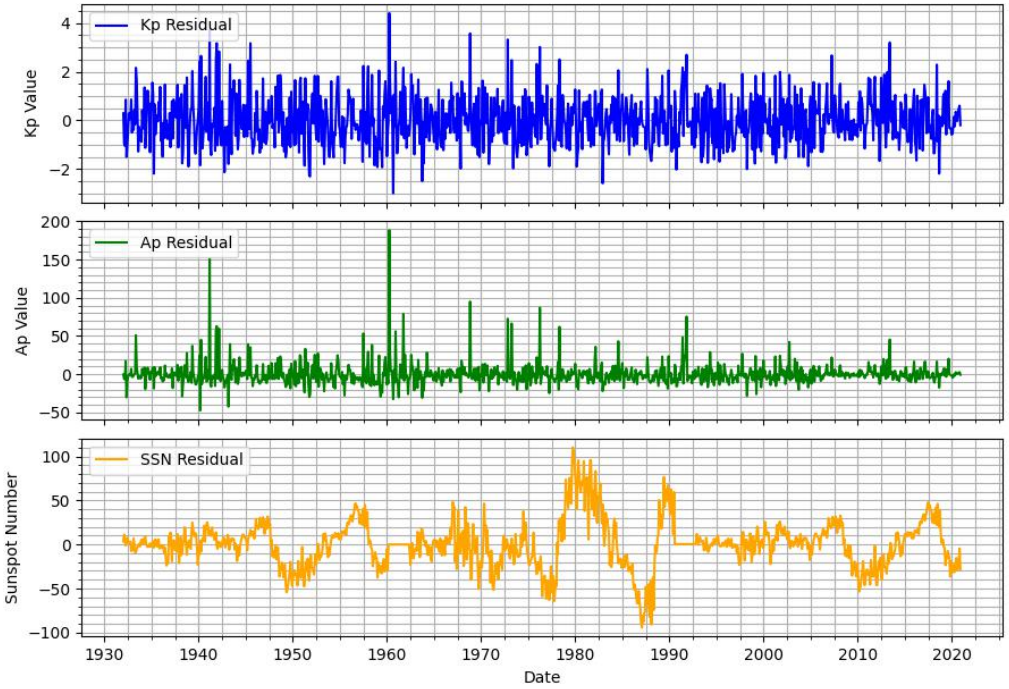

Fig. 4: Residual Components of Kp, Ap, and SSN Indices After Decomposition [**Source:** Designed by the authors (Using python)]

The residuals capture irregular, non-periodic fluctuations beyond the trend and seasonal components. Kp residuals remain relatively stable, with small random deviations, suggesting that the decomposition captures most of its variability. By contrast, Ap residuals display sharp spikes, reflecting episodic geomagnetic disturbances such as geomagnetic storms triggered by solar eruptions. SSN residuals show irregular anomalies and bursts, pointing to deviations from the expected solar cycle and potential disruptions in typical solar activity patterns. These irregularities underline the complex and sometimes unpredictable nature of solar–terrestrial interactions.

3.2 Distribution Analysis

In the distribution analysis of the Kp and Ap indices, as well as SSN, the patterns of geomagnetic and solar activity are examined. Fig. 5 shows the Power Spectral Density (PSD) and Probability Density Function (PDF) for these indices, highlighting their temporal dynamics and distributions. The PSD plots for Kp and Ap reveal prominent peaks at frequencies around 0.02–0.1 cycles per day, corresponding to periodic phenomena such as the ~27-day solar rotation and transient geomagnetic disturbances. In contrast, the SSN PSD is dominated by low frequencies, reflecting the influence of long-term solar cycles, such as the 11-year solar cycle. The ~27-day solar rotation period is calculated from the PSD as the reciprocal of the frequency ($p = 1/f$) where a peak is observed, typically around 0.037 cycles per day, yielding a period of approximately 27 days. This reflects the synodic rotation of the Sun, where active regions like coronal holes and sunspots reappear periodically, influencing solar wind patterns and driving geomagnetic activity. The broader peaks in the PSD of Ap and Kp imply cumulative effects from prolonged solar influences, such as recurrent geomagnetic storms or extended solar wind interactions.

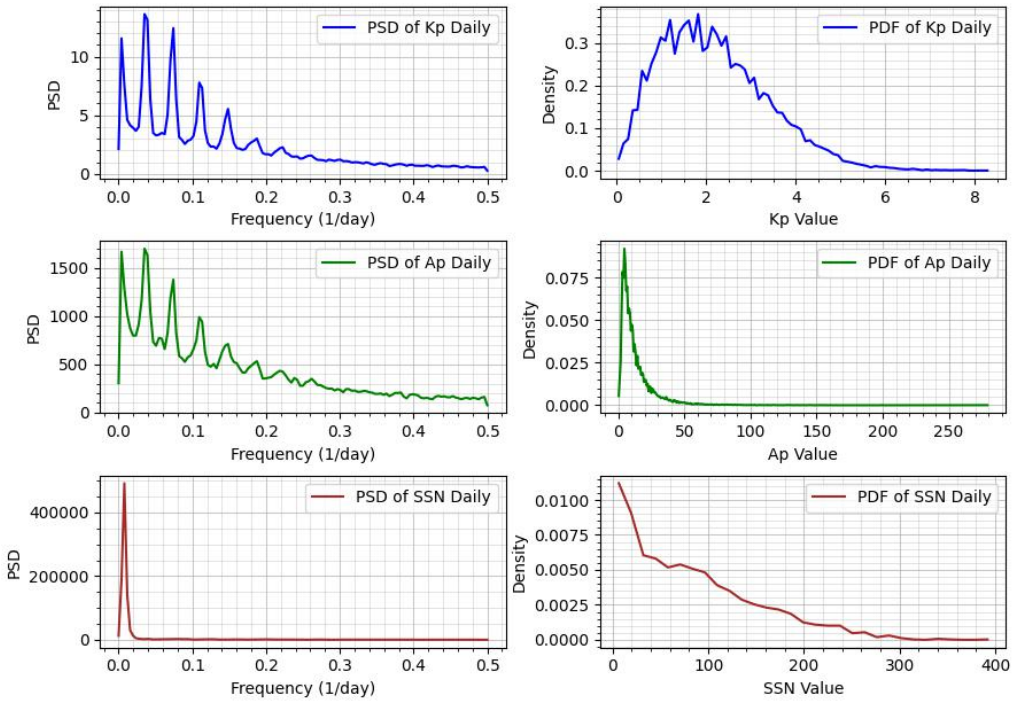

Fig. 5: Power Spectral Density and Probability Density Functions of Kp, Ap, and SSN Indices [**Source:** Designed by the authors (Using python)]

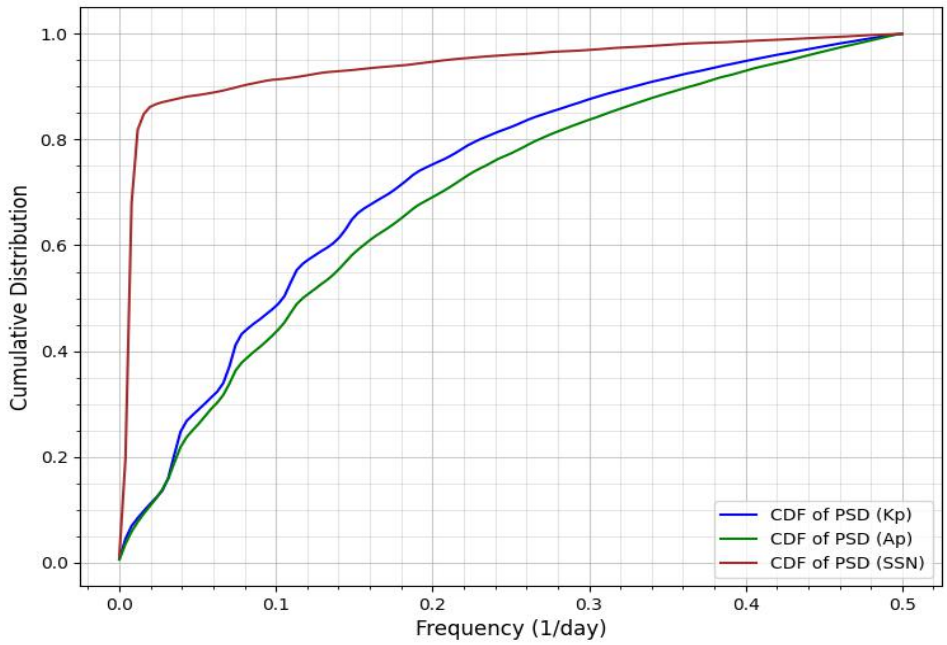

Fig. 6: Cumulative Distribution of PSD for Kp, Ap, and SSN Indices [**Source:** Designed by the authors (Using python)]

The PDFs indicate that Kp and Ap values are concentrated at lower magnitudes, reflecting the predominance of moderate geomagnetic activity. Their longer tails capture the occurrence of infrequent but extreme events, particularly for Ap, which reflects

planetary-scale geomagnetic disturbances. The density of Kp values is most prominent in the range of 0.99–2.45, whereas Ap shows stronger concentration between 3.16 and 4.57. In contrast, the SSN PDF displays a gradual decline, with most values clustered at lower sunspot counts, consistent with the prevalence of relatively quiet solar periods. These results suggest that while SSN primarily governs long-term geomagnetic trends, Kp and Ap are strongly shaped by short-term solar and interplanetary dynamics, with Ap being especially sensitive to extreme geomagnetic events.

The cumulative distribution function (CDF) of the power spectral density (PSD) for the Kp, Ap, and SSN indices reveals distinct differences in the frequency characteristics of solar and geomagnetic activity. For the Sunspot Number (SSN), the CDF shows a sharp rise at very low frequencies, confirming that most of its spectral power is concentrated in this range. This reflects the dominance of long-term periodicity, particularly the 11-year solar cycle, and indicates that sunspot activity evolves gradually under the influence of slow, decadal-scale solar magnetic processes with limited higher-frequency contributions. In contrast, the CDFs of Kp and Ap increase more gradually across a wider frequency band, demonstrating that geomagnetic activity is driven not only by the solar cycle but also by short-term variations. These include the quasi-27-day solar rotation, seasonal modulations, and transient solar disturbances such as coronal mass ejections (CMEs) and high-speed solar wind streams, which induce rapid fluctuations in Earth's magnetosphere. Furthermore, the Ap CDF is slightly less steep at low frequencies compared to Kp, suggesting that Ap captures a broader spectrum of geomagnetic disturbances, including cumulative or prolonged activity, whereas Kp is more sensitive to intermittent variations (Fig. 6).

Correlation Analysis

To better understand the relationship between solar activity and geomagnetic disturbances, correlations were computed between the Sunspot Number (SSN) and the geomagnetic indices Kp and Ap, considering their overall, trend, seasonal, and residual components (Table 1). The overall correlations are relatively weak, with Kp–SSN at 0.1948 and Ap–SSN at 0.1564, suggesting only a mild positive association between geomagnetic activity and solar activity when all components are combined. The trend component exhibits the strongest correlations, with Kp–SSN at 0.6303 and Ap–SSN at 0.5951, underscoring the dominant role of long-term solar cycles in shaping geomagnetic variations. By contrast, the seasonal correlations are negligible—0.0282 for Kp and 0.0273 for Ap—indicating that short-term periodicities in geomagnetic indices are not strongly aligned with the seasonal variation of sunspot activity. Residual correlations are also minimal, with Kp–SSN at 0.0246 and Ap–SSN at –0.0086, showing little to no relationship between high-frequency fluctuations in solar and geomagnetic activity (Fig. 5). Overall, these findings confirm that the long-term solar trend exerts a significant influence on geomagnetic indices, while seasonal and short-term fluctuations remain largely independent of sunspot variations.

Table 1: Correlation Analysis of Kp and Ap Indices (Average of 3-hour Intervals) with Sunspot Number (SSN).

	Overall	Trend	Seasonal	Residual
Correlation between Kp and SSN	0.1948	0.6303	0.0282	0.0246
Correlation between Ap and SSN	0.1564	0.5951	0.0273	-0.0086

[Source: By the authors (Using Excel &Python)]

To further investigate how solar activity relates to short-term geomagnetic variations, correlations were computed between the Sunspot Number (SSN) and 3-hour interval values of the geomagnetic indices Kp and Ap across four components: overall, trend, seasonal, and residual (Table 2). The overall correlation is relatively strong between Kp 5_15h and SSN, with a value of 0.1946.

Table 2: Correlation Analysis of 3-hour interval values of Kp and Ap with Sunspot Number (SSN).

Correlation	Overall	Trend	Seasonal	Residual
Correlation between Kp1_3h and SSN	0.1302	0.4283	-0.0724	0.0207
Correlation between Kp2_6h and SSN	0.1430	0.4564	-0.0598	0.0173
Correlation between Kp3_9h and SSN	0.1679	0.491	0.0114	0.0195
Correlation between Kp4_12h and SSN	0.1867	0.5198	-0.0788	0.0247
Correlation between Kp5_15h and SSN	0.1946	0.5579	0.018	0.0277
Correlation between Kp6_18h and SSN	0.1750	0.5279	-0.0925	0.0219
Correlation between Kp7_21h and SSN	0.1540	0.4807	-0.0594	0.0167
Correlation between Kp8_24h and SSN	0.1381	0.4457	-0.0176	0.0183
Correlation between Ap1_3h and SSN	0.1050	0.4777	-0.0657	0.0188
Correlation between Ap2_6h and SSN	0.1133	0.5095	0.01	0.0162
Correlation between Ap3_9h and SSN	0.1231	0.5228	0.0718	0.0206
Correlation between Ap4_12h and SSN	0.1311	0.5245	0.013	0.0255
Correlation between Ap5_15h and SSN	0.1451	0.5932	0.0931	0.0308
Correlation between Ap6_18h and SSN	0.1328	0.5635	-0.0015	0.0269
Correlation between Ap7_21h and SSN	0.1190	0.5259	-0.0432	0.0187
Correlation between Ap8_24h and SSN	0.1098	0.4942	-0.0421	0.0186

Source: By the authors (Using Excel & Python)

More pronounced relationships emerge in the trend component, where correlations range from 0.4283 to 0.5579 for Kp and from 0.4777 to 0.5932 for Ap, highlighting the dominant influence of long-term solar activity patterns on geomagnetic indices even at shorter temporal resolutions. Notably, the highest trend correlation occurs during the 12:00–15:00 UT interval for both Kp5_15h and Ap5_15h with SSN. This elevated correlation likely reflects the combined effects of enhanced dayside geomagnetic activity and the persistence of solar cycle-driven responses reinforced by cumulative solar–terrestrial interactions during this time window. By contrast, seasonal correlations are weak—often close to or below zero—suggesting minimal periodic alignment between geomagnetic fluctuations and SSN at 3-hour scales. Residual correlations are negligible across all intervals, indicating that high-frequency variations in geomagnetic indices bear little connection to sunspot activity. An important pattern, however, is that correlations, particularly in the trend component, tend to strengthen with longer averaging intervals for both Kp and Ap, implying that the influence of solar activity becomes clearer when aggregated over time.

4. CONCLUSIONS

This study examined the relationship between solar and geomagnetic activity using time-series decomposition, distribution analysis, and correlation analysis. The decomposition highlights how the linkage between sunspot activity and geomagnetic indices evolves over time: until 1990, Kp and Ap trends show an inverse relationship with SSN, while after 1990 a strong positive association emerges. Seasonal components capture periodic signatures, such as the semi-annual variations in Kp and Ap and the ~11-year solar cycle in SSN. Residuals reveal irregular, short-term disturbances, with Ap displaying sharp spikes tied to transient geomagnetic storms and SSN showing bursts of irregular solar activity.

The spectral and probability distribution analyses reveal distinct temporal and amplitude characteristics. SSN is dominated by low-frequency components, reflecting the long-term solar cycle, whereas Kp and Ap span broader frequency ranges, capturing both long-term cycles and shorter-term variations such as the ~27-day solar rotation. Probability distributions confirm that moderate geomagnetic activity is most frequent, while Ap is more responsive to extreme planetary-scale disturbances compared to Kp.

Correlation analysis offers a quantitative perspective on the solar–geomagnetic relationship across components and timescales. While overall associations are positive but weak, trend components display the strongest correlations, emphasizing the dominant role of long-term solar cycles in driving geomagnetic variability. The highest trend correlations occur during the 12:00–15:00 UT interval for both Kp5_15h and Ap5_15h with SSN, likely reflecting enhanced dayside activity and cumulative solar–terrestrial interactions. Seasonal correlations are weak, underscoring limited solar–geomagnetic periodic alignment, and residual correlations are negligible or slightly negative, pointing to the independence of high-frequency geomagnetic fluctuations from solar activity.

AUTHOR CONTRIBUTIONS

All the authors contributed equally.

CONFLICT OF INTEREST

The authors declare no competing interests with respect to the publication of this manuscript.

ACKNOWLEDGMENTS

We sincerely thank Dr. Anurag Sahay (NIT Patna) and Dr. Bappasona Kar (Panskura Banamali College) for their valuable guidance and insights, which greatly enhanced this study. We are also grateful to Soumen Khatua (NIT Patna) for his constant support and encouragement.

FUNDING

This research received no specific grant from any funding agency in the public, commercial, or not-for-profit sectors.

REFERENCES

[1] L. Svalgaard, Recalibration of Bartels' geomagnetic activity indices Kp and ap to include UT variations, *Journal of Geophysical Research*, **81** (1976) 5182-5188. https://doi.org/10.1029/JA081i028p05182

[2] D. Venkatesan, A.G. Ananth, H. Graumann, S. Pillai, Relationship between solar and geomagnetic activity, Journal of Geophysical Research: *Space Physics*, **96** (1991) 9811-9813. https://doi.org/10.1029/90JA02322

[3] G.K. Rangarajan, T. Lyemori, Time variations of geomagnetic activity indices Kp and Ap: an update, Annales Geophysicae, **15** (1997) 1271-1290. https://doi.org/10.1007/s00585-997-1271-z

[4] G.K. Rangarajan, L.M. Barreto, Use of Kp index of geomagnetic activity in the forecast of solar activity, Earth, *Planets and Space*, **51** (1999) 363-372. https://doi.org/10.1186/BF03352240

[5] Z-G. Yu, V. Anh, R. Eastes, Underlying scaling relationships between solar activity and geomagnetic activity revealed by multifractal analyses, Journal of Geophysical Research, *Space Physics*, **119** (2014) 7577-7586. https://doi.org/10.1002/2014JA019893

[6] N. Urata, G. Duma, F. Freund, Geomagnetic Kp index and earthquakes, Open Journal of Earthquake Research, **7** (2018) 39-52. https://doi.org/10.4236/ojer.2018.71003

[7] A.A. Akyol, O. Arikan, F. Arikan, A machine learning-based detection of earthquake precursors using ionospheric data, *Radio Science*, **55** (2020) 1-21. https://doi.org/10.1029/2019RS006931

[8] P.R. Singh, A.I.S. Farid, A.K. Singh, T.K. Pant, A.A. Aly, Predicting the maximum sunspot number and geomagnetic indices for solar cycle 25, *Astrophysics and Space Science,* **366** (2021) 48. https://doi.org/10.1007/s10509-021-03953-3

[9] E. Echer, L.E.A. Vieira, N.R. Rigozo, M.P. Souza, D.J.R. Nordemann, A study of solar-geomagnetic indices correlation, 7th Int. Congress of the Brazilian Geophysical Society, (2001) cp-217. https://mtcm16.sid.inpe.br/attachment.cgi/sid.inpe.br/marciana/2005/01.24.15.56/doc/SBGF2001-%20Analises.

[10] J. Matzka, C. Stolle, Y. Yamazaki, O. Bronkalla, A. Morschhauser, The geomagnetic Kp index and derived indices of geomagnetic activity, *Space Weather*, **19** (2021) e2020SW002641. https://doi.org/10.1029/2020SW002641

[11] M.A. El-Borie, A.M. El-Taher, A.A. Thabet, S.F. Ibrahim, A.A. Bishara, North–South asymmetry of some solar

parameters during solar cycles 18–24, *Chinese Journal of Physics*, **72** (2021) 1-17. https://doi.org/10.1016/j.cjph.2021.02.007

[12] A. Ozguc, A. Kilcik, V. Yurchyshyn, Temporal and periodic variations of the solar flare index during the last four solar cycles and association with geomagnetic parameters, *Solar Physics*, **297** (2022) 112. https://par.nsf.gov/servlets/purl/10427551

[13] C.I. Uga, S.P. Gautam, E.B. Seba, Cross-correlation analysis of cosmic ray intensity with interplanetary and geomagnetic parameters, *Cosmic Research*, **62** (2024) 34-41. https://doi.org/10.1134/S0010952523600075

[14] D. Samanta, R.K. Dolai, Stochastic modeling of compact binary coalescences for gravitational wave analysis, International Astronomy and Astrophysics Research Journal, **7** (2025) 57-67. https://doi.org/10.9734/iaarj/2025/v7i1116

[15] R.B. Cleveland, STL: A seasonal-trend decomposition procedure based on LOESS, Journal of Official Statistics, 6 (1990) 3-73. https://www.wessa.net/download/stl.pdf

Review of Some Identities Involving Basic Hypergeometric Series

Ghanshyam Pant*

Department of Mathematics, Siddhanath Science Campus, Mahendranagar, Kanchanpur, (T.U.), Nepal

Research Article

ISSN: 3059-9504 (online)
DOI: https://doi.org/10.3126/ajs.v2i1.87770

Article History

Received: October 16, 2025; Revised: November 28 2025; Accepted: November 30, 2025; Published: December 25, 2025

Keywords

Identity, basic hypergeometric series, q- binomial theorem.

***Corresponding Author**

Email: ghanshyam.pant@snsc.tu.edu.np
(GS Pant)

ABSTRACT

In this paper, we review and verify several identities involving basic hypergeometric series including the q- binomial theorem. These identities play a fundamental role in the theory of q-series and may serve as a useful reference for beginners interested in this area of mathematics.

2020 Mathematics Subject Classification: 33D15

1. INTRODUCTION, NOTATION AND DEFINITIONS

In 1812, Gauss [1-5] presented to the Royal Society of Sciences at G$\ddot{o}$ttingen his famous paper, in which he considered the infinite series

$$1+\frac{a.b}{1.c}z+\frac{a(a+1)b(b+1)}{1.2.c(c+1)}z^2+\frac{a(a+1)(a+2)b(b+1)(b+2)}{1.2.3.c(c+1)(c+2)}z^3+\ldots \quad (1.1)$$

as function of *a, b, c, z* where it is assumed that $c \neq 0,-1,-2,-3,\ldots$ .He showed that the series converges absolutely for $|z|<1$ and for |z|=1when Re (c-a-b) > 0. This series is denoted by ${}_2F_1\left[\begin{matrix}a,b;\\c\end{matrix}z\right]$.

$$Thus\ {}_2F_1\left[\begin{matrix}a,b;\\c\end{matrix}z\right]=1+\sum_{n=1}^{\infty}\frac{(a)_n(b)_n z^n}{(c)_n n!}\ for\ c \neq 0,-1,-2,-3,\ldots. \quad (1.2)$$

$$where\ (a)_n=a(a+1)(a+2)\ldots(a+n-1), n \geq 1\ and\ (a)_0=1$$

$If\ a=1, b=c,$ series (1.1) yields thegeometric series

$$1+z+z^2+z^3+\ldots\ ,|z|<1 \quad (1.3)$$

$If\ b=c,$ series (1.1) reduces to binomial theorem

$$1+\frac{a}{1!}z+\frac{a(a+1)}{2!}z^2+\ldots=(1-z)^{-a}, |z|<1. \quad (1.4)$$

Another generalization of Gauss series [2-7] is the generalized hypergeometric series with *r* numerator parameters $a_1,a_2,\ldots,a_r$ and *s* denominator parameters $b_1,b_2,\ldots,b_s$ defined by

$${}_rF_s\left[\begin{matrix}a_1,a_2,\ldots,a_r;\\b_1,b_2,\ldots,b_s\end{matrix}z\right]=\sum_{n=0}^{\infty}\frac{(a_1)_n(a_2)_n\ldots(a_r)_n z^n}{n!\,(b_1)_n(b_2)_n\ldots(b_s)_n} \quad (1.5)$$

in which no denominator parameters $b_1,b_2,\ldots,b_s$ are allowed to be zero or negative integers. Many other mathematicians studied similar series, notably the Swiss L. Euler [8], A. T. Vandermonde [9] Slater [6, 7]. After thirty-three years of Gauss' paper, Heine [10-12] introduced the series

$$1+\frac{(1-q^a)(1-q^b)}{(1-q)(1-q^c)}z+\frac{(1-q^a)(1-q^{a+1})(1-q^b)(1-q^{b+1})}{(1-q)(1-q^2)(1-q^c)(1-q^{c+1})}z^2+\ldots \quad (1.6)$$

$where\ c \neq 0,-1,-2,\ldots$

Series (1.6) converges absolutely for $|z|<1$ when $|q|<1$. Series (1.6) tends to Gauss' series(1.1) as $q \to 1$, due to $\lim_{q\to 1}\frac{1-q^n}{1-q}$

The series (1.6) is called Heine's series or basic hypergeometric series or q-hypergeometric series and is denoted by ${}_2\phi_1\left[\begin{matrix}a,b;\\c\end{matrix}q,z\right]$.

$$Thus,\ {}_2\phi_1\left[\begin{matrix}a,b;\\c\end{matrix}q,z\right]=\sum_{n\,=\,0}^{\infty}\frac{(a;q)_n(b;q)_n}{(q;q)_n(c;q)_n}z^n \quad (1.7)$$

$$where\ (a;q)_n=\begin{cases}1, & n=0\\(1-a)(1-aq)\ldots(1-aq^{n-1}), & n=1,2,3,\ldots\end{cases} \quad (1.8)$$

$is\ q-$shifted factorial.

For brevity,
let $(a_1,a_2,\ldots,a_r;q)_n=(a_1;q)_n(a_2;q)_n\ldots(a_r;q)_n$

The generalized basic hypergeometric [13] series is defined by

$$ {}_r\phi_s\left[\begin{matrix}a_1, a_2, \dots a_r \\ b_1, b_2, \dots b_s\end{matrix}; q, z\right] = \sum_{n=0}^{\infty} \frac{(a_1, a_2, \dots, a_r; q)_n z^n}{(b_1, b_2, \dots, b_s; q)_n} \quad (1.9) $$

$where\ \binom{n}{2} = \frac{n(n-1)}{2}$

The infinite series in (1.9) is absolutely convergent for all values of $z\ if\ r \le s\ and\ for\ r = s+1$, it converges in the region $|z| < 1$.

1.1 Identities frequently used in basic hypergeometric series

In this section we shall discuss about the following identities (1.2.30 - 1.2.40), p.6) [3]. These identities are frequently used in number theory [13] such as partition and mock theta functions. The Notebooks of Ramanujan and his 'Lost' Notebook, containing about 4000 Entries/theorem will continue to be eternal sources of inspiration to the mathematicians of the world. Ramanujan did not provide proofs of maximum such Entries/ theorem. Andrews [14-18], Slater [6, 7] and many other mathematicians gave the proofs of some such Entries/theorem. Anyone who interested in these branches of mathematics, the identities mentioned below are crucial prerequisites for studying such matter. To prove these identities q-factorial relation mentioned in (1.8) is used.

(a) $(a;q)_n = \frac{(a;q)_\infty}{(aq^n;q)_\infty}$ … (2.1)

Proof: $(a;q)_n = (1-a)(1-aq)(1-aq^2)\dots.(1-aq^{n-1})$

$$= \frac{(1-a)(1-aq)(1-aq^2)\dots.(1-aq^{n-1})(1-aq^n)(1-aq^{n+1})}{(1-aq^n)(1-aq^{n+1})\dots.\ to\infty}$$

$$= \frac{(a;q)_\infty}{(aq^n;q)_\infty}$$

(b) $(a^{-1}q^{1-n};q)_n = (a;q)_n(-a^{-1})^n q^{-\binom{n}{2}}$ … (2.2)

Proof:

$$(a^{-1}q^{1-n};q)_n = (1-a^{-1}q^{1-n})(1-a^{-1}q^{1-n}q)(1 - a^{-1}q^{1-n}q^2)\dots(1-a^{-1}q^{1-n}q^{n-1})$$

$$= (1-a^{-1}q^{1-n})(1-a^{-1}q^{2-n})(1 - a^{-1}q^{3-n})\dots(1-a^{-1}q^{-1})(1-a^{-1})$$

$$= \frac{(-1)^n(1-a)(1-aq)\dots(1-aq^{n-1})}{a^n q^{\frac{n(n-1)}{2}}}$$

$$= (a;q)_n(-a^{-1})^n q^{-\binom{n}{2}}$$

$(\boldsymbol{c})$ $(a;q)_{n-k} = \frac{(a;q)_n(-qa^{-1})^k q^{\binom{k}{2}-nk}}{(a^{-1}q^{1-n};q)_k}$ … (2.3)

Proof: $(a;q)_{n-k} = (1-a)(1-aq)(1-aq^2)\dots.(1 - aq^{n-k-2})(1-aq^{n-k-1})$

$$= \frac{(1-a)(1-aq)(1-aq^2)\dots.(1-aq^{n-k-1})(1-aq^{n-k})\dots(1-aq^{n-1})}{(1-aq^{n-k})(1-aq^{n-k+1})\dots(1-aq^{n-1})}$$

$$= \frac{(a;q)_n}{\frac{(-1)^k(1-a^{-1}q^{1-n})(1-a^{-1}q^{2-n})\dots(1-a^{-1}q^{k-n})}{(a^{-1})^k q^{\frac{k(k+1)}{2}-nk}}}$$

$$= \frac{(a;q)_n(-qa^{-1})^k q^{\binom{k}{2}-nk}}{(a^{-1}q^{1-n};q)_k}.$$

$(\mathbf{d})$ $(a;q)_{n+k} = (a;q)_n(aq^n;q)_k$ (2.4)

Proof:

$(a;q)_{n+k} = (1-a)(1-aq)(1-aq^2)\dots(1-aq^n)\dots (1-aq^{n+k-1}) = (a;q)_n(aq^n;q)_k$

$(\mathbf{e})$ $(aq^n;q)_k = \frac{(a;q)_k(aq^k;q)n}{(a;q)n}$ (2.5)

Proof: $(aq^n;q)_k = (1-aq^n)(1-aq^nq)\dots(1-aq^nq^{k-1})$

$$= \frac{(1-a)(1-aq)\dots(1-aq^{n-1})(1-aq^n)(1-aq^nq)\dots(1-aq^nq^{k-1})}{(1-a)(1-aq)\dots(1-aq^{n-1})}$$

$$= \frac{(a;q)_k(aq^k;q)_n}{(a;q)_n}$$

$(\mathbf{f})$ $(aq^k;q)_{n-k} = \frac{(a;q)_n}{(a;q)_k}$ (2.6)

Proof: $(aq^k;q)_{n-k}$

$$= (1-aq^k)(1-aq^kq)\dots(1-aq^kq^{n-k-1})$$

$$= \frac{(1-a)(1-aq)\dots(1-aq^{k-1})(1-aq^k)(1-aq^{k+1})\dots(1-aq^{k+n-k-1})}{(1-a)(1-aq)\dots(1-aq^{k-1})}$$

$$= \frac{(a;q)_n}{(a;q)_k}$$

$(\mathbf{g})$ $(aq^{2k};q)_{n-k} = \frac{(a;q)_n(aq^n;q)_k}{(a;q)_{2k}}$ (2.7)

Proof: $(aq^{2k};q)_{n-k}$

$$= (1-aq^{2k})(1-aq^{2k}q)\dots\left(1 - aq^{2k+n-k-1}\right)$$

$$= \frac{(a;q)_{2k}(1-aq^{2k})(1-aq^{2k}q)\dots(1-aq^nq^{k-1})}{(a;q)_{2k}}$$

$$= \frac{(1-a)(1-aq)\dots(1-aq^{n-1})(1-aq^n)\dots(1-aq^nq^{k-1})}{(a;q)_{2k}}$$

$$= \frac{(a;q)_n(aq^n;q)_k}{(a;q)_{2k}}$$

$(\mathbf{h})$ $(q^{-n};q)_k = \frac{(q;q)_n}{(q;q)_{n-k}}(-1)^k q^{\binom{k}{2}-nk}$ (2.8)

Proof: $(q^{-n};q)_k = (1-q^{-n})(1-q^{-n}q)\dots(1-q^{-n}q^{k-1})$

$$= \frac{(-1)^k(1-q^n)(1-q^{n-1})\dots(1-q^{n-k+1})}{q^{\frac{k(k-1)}{2}-nk}}$$

$$= \frac{(-1)^k(q;q)_{n-k}(1-q^{n-k+1})(1-q^{n-k+2})\dots(1-qq^{n-1})}{q^{\frac{k(k-1)}{2}-nk}(q;q)_{n-k}}$$

$$= \frac{(q;q)_n(-1)^k q^{\binom{k}{2}-nk}}{(q;q)_{n-k}}$$

$(\mathbf{i})$ $(aq^{-n};q)_k = \frac{(a;q)_k(qa^{-1};q)_n q^{-nk}}{(a^{-1}q^{1-k};q)_n}$ (2.9)

Proof: $(aq^{-n};q)_k = \frac{(aq^{-n};q)_\infty}{(aq^{k-n};q)_\infty}$

$$= \frac{(a;q)_\infty}{(a;q)_{-n}}\frac{(a;q)_{k-n}}{(a;q)_\infty} = \frac{(a;q)_{k-n}}{(a;q)_{-n}}$$

$$= \frac{\left(\frac{q}{a};q\right)_n (a;q)_k (aq^k;q)_{-n}}{(-1)^n a^{-n} q^{\frac{n(n+1)}{2}}}$$

$$= \frac{(qa^{-1};q)_n (a;q)_k}{(-1)^n a^{-n} q^{\frac{n(n+1)}{2}}} \times \frac{(-1)^n (aq^k)^{-n} q^{\frac{n(n+1)}{2}}}{\left(\frac{q}{aq^k};q\right)_n}$$

$$= \frac{(a;q)_k (qa^{-1};q)_n q^{-nk}}{(a^{-1}q^{1-k};q)_n}$$

(j) $(a;q)_{2n} = (a;q^2)_n (aq;q^2)_n$ ... (2.10)

Proof: $(a;q)_{2n} = (1-a)(1-aq)(1-aq^2)\dots(1-aq^{2n-1})$

$= (1-a)(1-aq^2)(1-aq^4)\dots(1-aq^{2n-2}) \times (1 - aq)(1-aq^3)(1-aq^5)\dots(1-aq^{2n-1}$

$= (a;q^2)_n (aq;q^2)_n$

(k) $(a^2;q^2)_n = (a;q)_n (-a;q)_n$ ... (2.11)

Proof: $(a^2;q^2)_n = (1-a^2)(1-a^2q^2)\dots(1-a^2q^{2(n-1)})$

$= \{(1-a)(1-aq)\dots(1-aq^{n-1})\} \times \{(1+a)(1+aq)\dots(1-aq^{n-1})\}$

$= (a;q)_n (-a;q)_n$

1.2 The q- binomial theorem

The most fundamental summation formula in the theory of basic hypergeometric series is the q- binomial theorem [3 13]

$${}_1\phi_0[a;-;q,z] = \sum_{n=0}^{\infty} \frac{(a;q)_n}{(q;q)_n} z^n = \frac{(az;q)_\infty}{(z;q)_\infty}, |z|<1, |q|<1 \quad (3.1)$$

Proof: *Let* $f(z) = \frac{(az;q)_\infty}{(z;q)_\infty}$ ... (3.2)

Since $f(z)$ *is an analytic function in* $|z|<1$, *so we have its taylor's expansion in the form*

$$f(z) = \sum_{n=0}^{\infty} A_n z^n \quad \text{... (3.3)}$$

$$f(zq) = \frac{(azq;q)_\infty}{(zq;q)_\infty} = \frac{(1-z)}{(1-az)} \frac{(az;q)_\infty}{(z;q)_\infty}$$

$\Rightarrow (1-az) f(zq) = (1-z) f(z)$

$$\Rightarrow (1-az) \sum_{n=0}^{\infty} A_n z^n q^n = (1-z) \sum_{n=0}^{\infty} A_n z^n \quad (3.4)$$

Equating the coefficients of z^n on both, we get

$A_n q^n - a A_{n-1} q^{n-1} = A_n - A_{n-1}$

$\Rightarrow A_n (1-q^n) = A_{n-1}(1-aq^{n-1})$

$$\Rightarrow A_n = \left(\frac{1-aq^{n-1}}{1-q^n}\right) A_{n-1} \quad (3.5)$$

From (3.5) *we find*

$$A_1 = \frac{1-a}{1-q} A_0, A_2 = \frac{1-aq}{1-q^2} A_1 = \frac{(1-a)(1-aq)}{(1-q)(1-q^2)} A_0$$

Proceeding in this way, we get

$$A_n = \frac{(1-a)(1-aq)\dots(1-aq^{n-1})}{(1-q)(1-q^2)\dots(1-q^n)} A_0 = \frac{(a;q)_n}{(q;q)_n} A_0 \quad (3.6)$$

From (3.3), $f(0) = A_0$ and from (3.2) $f(0) = 1$, *so* $A_0 = 1$

Putting this value in (3.6), we get $A_n = \frac{(a;q)_n}{(q;q)_n}$

Using this value in (3.3), we get

$$f(z) = \sum_{n=0}^{\infty} \frac{(a;q)_n}{(q;q)_n} z^n = \frac{(az;q)_\infty}{(z;q)_\infty}$$

1.3 Some Special unsolved problem [13] obtained by using section (1) and (2)

(i) $(aq^{-n};q)_n = \left(\frac{q}{a};q\right)_n \left(-\frac{a}{q}\right)^n q^{-\binom{n}{2}}$

Proof: $(aq^{-n};q)_n$

$= (1-aq^{-n})(1-aq^{-n}q)\dots(1-aq^{-n}q^{n-2})(1-aq^{-n}q^{n-1})$

$= \left(\frac{q}{a}-1\right)\left(\frac{q^2}{a}-1\right)\dots\left(\frac{q^{n-1}}{a}-1\right)\left(\frac{q^n}{a}-1\right)\frac{a^n}{q^{\frac{n(n+1)}{2}}}$

$= \left(\frac{q}{a};q\right)_n \left(-\frac{a}{q}\right)^n q^{-\binom{n}{2}}.$

(ii) $(aq^{-k-n};q)_n = \frac{(q/a;q)_{n+k}(-a)^n q^{\binom{n}{2}-nk}}{(q/a;q)_k}$

Proof: $(aq^{-k-n};q)_n = (1-aq^{-k-n})(1-aq^{-k-n+1})\dots\times (1-aq^{-k-n+n-2})(1-aq^{-k-n+n-1})$

$$= \frac{(-a)^n \left(1-\frac{q^{k+1}}{a}\right)\left(1-\frac{q^{k+2}}{a}\right)\dots\left(1-\frac{q^{k+n-1}}{a}\right)\left(1-\frac{q^{k+n}}{a}\right)}{q^{kn+\frac{n(n-1)}{2}}}$$

$$= \frac{(q/a;q)_{n+k}}{(q/a;q)_k} \frac{(-a)^n q^{-nk}}{q^{n(n-1)/2}} = \frac{(q/a;q)_{n+k}(-a)^n q^{\binom{n}{2}-nk}}{(q/a;q)_k}$$

(iii) $\frac{\left(qa^{1/2},-qa^{1/2};q\right)_n}{(a^{1/2},-a^{1/2};q)_n} = \frac{1-aq^{2n}}{1-a}$

Proof: $\frac{\left(qa^{1/2},-qa^{1/2};q\right)_n}{(a^{1/2},-a^{1/2};q)_n}$

$= \frac{(1-qa^{1/2})(1-q^2a^{1/2})\dots(1-q^na^{1/2})(1+qa^{1/2})(1+q^2a^{1/2})\dots(1+q^na^{1/2})}{(1-a^{1/2})(1-qa^{1/2})\dots(1-q^{n-1}a^{1/2})(1+a^{1/2})(1+qa^{1/2})\dots(1+q^{n-1}a^{1/2})}$

$= \frac{(1-q^2a)(1-q^4a)\dots\left(1-q^{2(n-1)}a\right)(1-q^{2n}a)}{(1-a)(1-q^2a)\dots(1-q^{2(n-1)}a)}$

$= \frac{1-aq^{2n}}{1-a}$

(iv) $(a;q)_\infty = \left(a^{1/2},-a^{1/2},(aq)^{1/2},-(aq)^{1/2}\right)_\infty$

Proof: $(a;q)_\infty = (1-a)(1-aq)(1-aq^2)(1-aq^3)(1-aq^4)\dots$ *to* ∞

$= \left(1-(a^{1/2})^2\right)\left(1-\{(aq)^{1/2}\}^2\right)\left(1-\{(a^{1/2}q)\}^2\right)\dots$ *to* ∞

$= \{\left(1-a^{1/2}\right)\left(1-a^{1/2}q\right)\dots$ *to*$\infty\}\{\left(1+a^{1/2}\right)\left(1+a^{1/2}q\right)\dots$ *to*$\infty\} \times \{\left(1-(aq)^{1/2}\right)\left(1-(aq)^{1/2}q\right)\dots$ *to*$\infty\}\{\left(1+(aq)^{1/2}\right)\left(1+(aq)^{1/2}q\right)\dots$ *to*$\infty\}$

$= \left(a^{1/2}-a^{1/2}(aq)^{1/2}-(aq)^{1/2}\right)_\infty$

2. CONCLUSION

In the paper, we reviewed some identities of basic hypergeometric series which are essential for entering the higher q- series. Without those identities we can't enter to study the Ramanujan's work. Those identities and q-binomial theorem are proved by using the q-shifted factorial mentioned in (1.8). These identities are necessary but not sufficient for such higher study. Also, in the paper, with the help of those identities, some

unsolved problem of Gasper and Rahman are solved. We hope this paper will help to attract the beginners in this branch of mathematics.

AUTHOR CONTRIBUTION

Whole work was carried by GS Pant.

CONFLIT OF INTEREST

Authors declare no competing interests with respect to the publication of this manuscript.

ACKNOWLEDGEMENT

The authors acknowledge to the reviewers for their valuable comments.

REFERENCES

[1] C.F. Gauss, Disquisitiones generales circa seriem infinitam …, *Commentationes Societatis Regiae Scientiarum Göttingensis Recentiores***,** Vol. II; reprinted in Werke, **3** (1876) 123-162.

[2] E.D. Rainville, Special Functions, *Chelsea Publishing Company Bronx*, New York, (1960) 45-102.

[3] G. Gasper, M. Rahman, Basic Hypergeometric Series, *Cambridge University Press*, New York, (1990) 1-20.

[4] J. Prasad, Certain Results Involving Generalized Modular Identities, *South East Asian Journal of Mathematics and Mathematical Sciences,* **20** (3) (2024) 205-208. https://doi.org/10.56827/SEAJMMS.2024.2003.15

[5] S.P. Singh, A. Rawat, A Note on Heine's Transformation, *South East Asian Journal of Mathematics and Mathematical Sciences* **19** (1) (2023) 73-80. https://doi.org/10.56827/SEAJMMS.2023.1901.7

[6] L.J. Slater, Generalized Hypergeometric Functions, *Cambridge University Press,* (1966) 85-106.

[7] S.N. Singh, S.P. Singh, V. Yadav, Generalization of an Identity of Ramanujan, *Journal of Ramanujan Society of Mathematics and Mathematical Sciences* **7**(1) (2019) 93-100. ISSN (Print): 2319-1023

[8] L. Euler, Introductio in Analysis Infinitorum, *Lausanne*, Vol. I (1748).

[9] A.T. Vandermonde, M*é*moire sur des irrationnelles de diff *é* rens ordres avec une application au cercle, *Mémoires de l'Académie royale des sciences,* (1772) 489-498.

[10] E. Heine, Über die Reihe …, *Journal für die reine und angewandte Mathematik*, **32** (1846), 210–212.

[11] E. Heine, *Untersuchungen über die Reihe …*, Journal für die reine und angewandte Mathematik, **34** (1847) 285 –328.

[12] E. Heine, Handbuch der Kungelfunctionen, *Theorie und Anwendungen*, Vol. I Reimer, Berlin (1878).

[13] G.E. Andrews, Number Theory, *Hindustan Publishing Corporation*, India, (1992) 149-190.

[14] G.E. Andrews, B.C. Berndt, Ramanujan's Lost Notebook, Part I, *Springer New York*, *NY* (1987) 223-256. Doi: 10.1007/0-387-28124-X

[15] G.E. Andrews, B.C. Berndt, Ramanujan's Lost Notebook, Part II, *Springer*, (2009) 1-25. https://doi.org/10.1007/b13290

[16] G.E. Andrews, B.C. Berndt, Ramanujan's Lost Notebook, Part III, *Springer New York*, *NY* (2012) 217-333. https://doi.org/10.1007/978-1-4614-3810-6

[17] G.E. Andrews, B.C. Berndt, Ramanujan's Lost Notebook, Part IV, *Springer New York*, *NY* (2013) 131-148. https://doi.org/10.1007/978-1-4614-4081-9

[18] G.E. Andrews, B.C. Berndt, Ramanujan's Lost Notebook, Part V, *Springer New York*, *NY* (2018) 1-243. https://doi.org/10.1007/978-3-319-77834-1

Mathematical Modeling of Temperature and Rainfall Driven Dengue Transmission in Sudurpashchim Province, Nepal

Yagya Raj Pant[1,*], Nilam Kharel[2], Amrit Bhatta[1], Puja Chaudhary[1]

[1]Department of Mathematics, Siddhanath Science Campus, Kanchanpur, Tribhuvan University, Nepal
[2]Departmant of Mathematics, Mechi Multiple Campus, Jhapa, Tribhuvan University, Nepal

Research Article

ISSN: 3059-9504 (online)
DOI: https://doi.org/10.3126/ajs.v2i1.87772

Article History

Received: October 16, 2025; Revised: December 01, 2025; Accepted: December 06, 2025; Published: December 25, 2025

Keywords

SIR-SI model, basic reproduction number, disease free equilibrium, carrying capacity, transmission rate.

***Corresponding Author**

Email: yrajpantg2000@gmail.com (YR Pant)

ABSTRACT

Dengue disease dynamics highly depends on environmental temperature as its transmitting vectors-*Aedes aegypti* and *Aedes albopictus* mosquitoes are poikilothermal. Temperature influences mosquitoes' key traits, including biting rate, oviposition rate, development rates of aquatic and adult stages, and lifespan. Rainfall in proper amounts, together with suitable temperatures, significantly supports egg hatching and growth of aquatic stage by creating breeding sites. In regions like Nepal, where seasonal variations in temperature and rainfall occur, mosquito population fluctuates seasonally, causing vector-borne diseases like dengue fever to similarly rise and fall. This paper develops a climate-sensitive mathematical model for dengue transmission in Sudurpashchim Province, Nepal, integrating effects of seasonal change in temperature and rainfall on mosquito life traits. We analyze the dengue dynamics model using symbolic and numerical tools to better understand disease patterns. Numerical simulations indicate that increasing mosquito mortality and reducing carrying capacity of environment to limit aquatic phase population are effective strategies for controlling and diminishing dengue outbreaks.

1. INTRODUCTION

Vector-borne diseases such as dengue, Zika, and chikungunya continue to pose significant public health challenges globally, especially in tropical and subtropical regions. Among these, dengue is currently the most threatening vector-borne disease affecting human populations, imposing an estimated yearly infection burden of up to 400 million [1, 2]. Dengue fever is caused by the dengue virus, which exists in four serotypes (DENV1–DENV4), and is transmitted principally by *Aedes aegypti* and, less commonly, *Aedes albopictus* [3]. The transmission cycle follows a "human–mosquito–human" pattern primarily driven by mosquito bites. Dengue transmission is strongly influenced by climatic factors such as temperature and rainfall, which affect mosquito breeding, survival, and biting behavior. Although dengue transmission is mostly seasonal due to weather conditions, *Aedes aegypti* can sustain populations even in dry seasons under suitable temperatures, leading to potential year-round transmission.

Mathematical models have become invaluable tools in studying the transmission dynamics of vector-borne diseases and designing effective intervention strategies. Compartmental models, such as the SEIR–SEI frameworks developed by Esteva and Vargas [4] and Yang and Ferreira [5], form the foundation of vector-borne disease modeling by capturing host–vector interactions and human demography. Subsequent studies have extended these frameworks to incorporate environmental effects, particularly climate variables, to improve realism. For instance, Barsante et al. [6] developed and validated a rainfall driven model of *Aedes aegypti* populations, noting that additional climatic factors such as temperature and humidity should be included for better predictive performance. Johanson et al. [7] analyzed 20 years of data from Puerto Rico to show significant associations between temperature, precipitation, and dengue transmission, while Morin et al. [8] developed a framework to model mosquito growth under climatic influences. Hii et al. [9] used weekly temperature and rainfall data for dengue forecasting. Furthermore, temperature-dependent mosquito traits like development and biting rates have been modeled using the Brière function [10] and quadratic functions [11, 12]. Vaidya and Wang [13] incorporated both seasonal and daily temperature variations in their biologically realistic model.

Motivated by these studies, our work aims to integrate both temperature and rainfall into a mathematical model to capture realistic mosquito population dynamics and dengue transmission patterns. We also focus on accounting for the under-reporting of infections, which remains a significant issue in dengue surveillance. In Nepal, over 90% of dengue cases go unreported due to asymptomatic infections or reporting barriers. In this paper, we formulate a model that incorporates the impacts of summer and rainy seasons on mosquito traits, as well as the phenomenon of under-reported dengue cases. The model is fitted to monthly dengue case data from 2024 in the Sudurpashchim Province of Nepal to estimate key epidemiological parameters and better understand local dengue dynamics.

2. METHODOLOGY

2.1 Data and Tools

We use demographic and epidemiological data, and climate information to formulate and analyze the SIR–SI dengue model with reported and non-reported infections. We manage raw case counts and climatic averages in Microsoft Excel. We perform

symbolic derivations, including the disease-free equilibrium, the basic reproduction number (R_0), and stability conditions, in Mathematica. We run numerical solutions, simulations, and plots in Python to solve the nonlinear differential equations and assess seasonal effects on dengue spread. We obtain monthly dengue case data from the Epidemiology and Disease Control Division (EDCD) of Nepal, demographic information from the 2021 Nepal Census, and climate data (temperature and rainfall) from the Department of Hydrology and Meteorology. These datasets provide the basis for model parameterization.

2.2 Mathematical Model

We formulate the SIR–SI compartmental model by dividing the human population into four compartments: susceptible humans (S_h), reported infectious humans (I_{hr}), non-reported infectious humans (I_{hn}), and recovered humans (R_h). The mosquito population is split into susceptible vectors (S_v) and infected vectors (I_v). We express the dynamics through a system of nonlinear ordinary differential equations, where climate-dependent functions adjust key

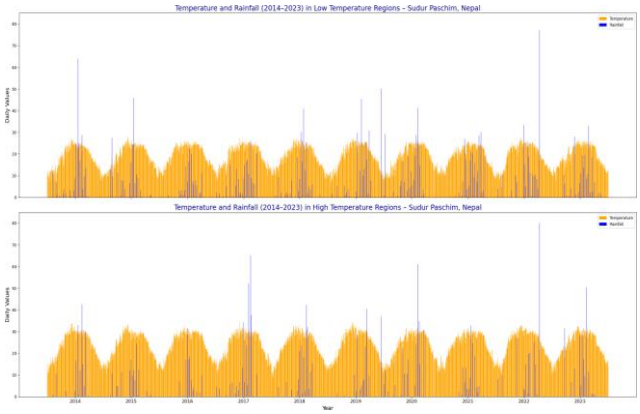

Fig. 1: Periodic pattern of temperature and rainfall in Sudurpashchim.

transmission and growth parameters. The model serves as the main research tool to study unreported infections, determine threshold conditions for disease persistence, and evaluate control strategies. Modeling climatic impacts dengue transmission is highly sensitive to environmental factors such as temperature and rainfall, which directly affect mosquito population dynamics and virus incubation times. To understand the climatic context of Sudurpashchim Province, we observed the pattern made by ten years of weekly meteorological data (2014–2023), specifically weekly average temperatures and total weekly rainfall.

Fig. 1 reveals a clear periodic pattern in both temperature and rainfall, with a one-year cycle. Significant rainfall is concentrated during the monsoon months (June to August), while summer months (April to September) exhibit high temperatures favorable for mosquito development, feeding frequency, and viral replication. This seasonal fluctuation in climatic variables directly motivates our inclusion of periodic effects in the transmission model. In particular, high summer temperatures enhance mosquito biting rate, survival, and viral transmission efficiency while monsoon rainfall increases mosquito breeding sites, thus temporarily boosting the vector carrying capacity.

To further support this, we analyzed the 2022 weekly data of temperature, rainfall, and reported dengue cases in Sudurpashchim.

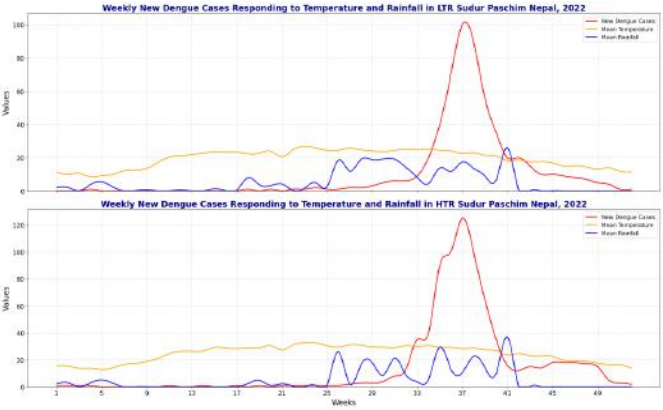

Fig. 2: Dengue trend in 2022 with respect to temperature and rainfall.

As shown in Fig. 2, dengue incidence in 2022 increased sharply starting mid-summer and peaked several weeks after the end of the monsoon season. This lag between rainfall and dengue outbreak is a typical pattern in dengue epidemiology and reflects the life cycle delay between vector proliferation and disease transmission.

These climatic realities of Sudurashchim strongly support the necessity of incorporating seasonal variation in temperature into the vector growth rate r, the transmission rates β_h (from vector to human) and β_v (from human to vector), and the seasonality of rainfall on the carrying capacity K_v in our mathematical model. Thus, we introduce seasonally modulated parameters using scaling factors to better capture the climatic influence on dengue dynamics. Let β_{h0}, β_{v0} and r_0 be baseline values of β_h, β_v and r, respectively, for off-summer season. Now, we define

$$\beta_h = (1+\eta_1)\,\beta_{h0}, \quad \beta_v = (1+\eta_2)\beta_{v0}, r = (1+\eta_3)r_0 \quad (2.1)$$

where η_1, η_2, η_3 = 0 for off-summer time and are some positive constants scales to the rates respectively in average due to warmth in summer. Similarly, we define

$$K_v = (1+\alpha)K_{v0}, \quad (2.2)$$

where K_{v0} denotes off-monsoon carrying capacity (indicating overall space including breeding sites during aquatic stages) and α is additional positive scale to the carrying capacity due to rainfall. Other parameters used in the model are defined as follows. The symbol Λ_h represents the recruitment rate of humans, while μ_h and μ_v denote the natural death rates of humans and vectors, respectively. The parameter γ_h stands for the human recovery rate (Fig. 3). The transmission rate from vector to human is represented by β_h, and the transmission rate from human to vector is denoted by β_v. The symbol θ indicates the proportion of reported infections, r represents the mosquito growth rate, and K_v denotes the carrying capacity for vectors.

Model Equations

$$\frac{dS_h}{dt} = \Lambda_h - \frac{\beta_h I_v}{N_h} S_h - \mu_h S_h \quad (2.3)$$

$$\frac{dI_{hr}}{dt} = \theta \frac{\beta_h I_v}{N_h} S_h - \gamma_h I_{hr} - \mu_h I_{hr} \quad (2.4)$$

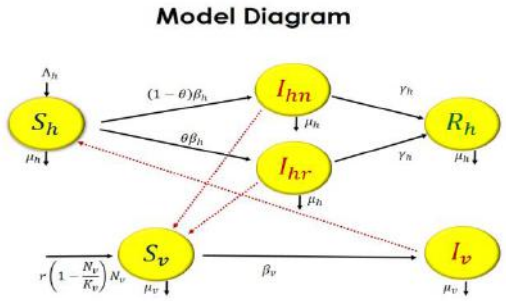

Fig. 3: SIR-SI dengue model with temperature and rainfall impacts.

$$\frac{dI_{hn}}{dt} = (1-\theta)\,\frac{\beta_h I_v}{N_h}\,S_h - \gamma_h I_{hn} - \mu_h I_{hn} \tag{2.5}$$

$$\frac{dR_h}{dt} = \gamma_h(I_{hr} + I_{hn}) - \mu_h R_h \tag{2.6}$$

$$\frac{dS_v}{dt} = r\left(1-\frac{N_v}{K_v}\right)N_v - \frac{\beta_v(I_{hr}+I_{hn})}{N_h}S_v - \mu_v S_v \tag{2.7}$$

$$\frac{dI_v}{dt} = \frac{\beta_v(I_{hr}+I_{hn})}{N_h}S_v - \mu_v I_v \tag{2.8}$$

where $N_h = S_h + I_{hr} + I_{hn} + R_h$ and $N_v = S_v + I_v$.

2.3 Mathematical Analysis

To understand the qualitative behavior of the proposed model, we perform mathematical analysis involving well-posedness, equilibrium analysis, and stability. We use standard techniques from dynamical systems and epidemiological modeling as discussed in [14, 15, 16].

Uniqueness and Existence of Solution

The model equations represent a system of ordinary differential equations (ODEs) with continuously differentiable right-hand sides. By the Picard–Lindelöf theorem [14], there exists a unique solution for given initial conditions in a suitable domain.

Positivity and Boundedness of Solutions

Let all initial values be non-negative. The model ensures that all state variables remain non-negative for all $t > 0$. This can be shown by contradiction: if any variable reaches zero, its derivative is non-negative or bounded below, preventing it from becoming negative. We define the total human and mosquito populations: $N_h(t) = S_h + I_{hr} + I_{hn} + R_h$ and $N_v(t) = S_v + I_v$.

Summing the human equations yields:

$$\frac{dN_h}{dt} = \Lambda_h - \mu_h N_h \Rightarrow N_h(t) \le \frac{\Lambda_h}{\mu_h},$$

which ensures boundedness. Similarly, mosquito population N_v is regulated by logistic growth, bounded above by K_v. Disease-Free Equilibrium (DFE) The disease-free equilibrium (DFE) corresponds to the state where no infection is present in the population, i.e., $I_{hr}^* = I_{hn}^* = R_h^* = I_v^* = 0$. The human susceptible class at DFE satisfies: $\frac{dSh}{dt} = \Lambda_h - \mu_h S_h \Rightarrow S_h^* = \frac{\Lambda_h}{\mu_h}$. For the mosquito population, we consider logistic growth given by:

$$\frac{dN_v}{dt} = rN_v\left(1-\frac{N_v}{K_v}\right) - \mu_v N_v.$$

At DFE, all vectors are susceptible, so $N_v = S_v$. Setting the derivative to zero:

$$0 = rS_v\left(1-\frac{S_v}{K_v}\right) - \mu_v S_v$$

$$\Rightarrow \frac{S_v}{K_v} = 1 - \frac{\mu_v}{r} \Rightarrow S_v^* = K_v\left(1-\frac{\mu_v}{r}\right).$$

This shows that the mosquito population at DFE is strictly less than the carrying capacity, unless $\mu_v \ll r$. This expression is derived from logistic growth dynamics, as supported in [17]. Thus, the disease-free equilibrium is: $E^* = \left(\frac{\Lambda_h}{\mu_h}, 0, 0, 0, K_v\left(1-\frac{\mu_v}{r}\right), 0\right)$.

Basic Reproduction Number (R_0)

We compute R_0 using the next generation matrix (NGM) approach [15]. Take as infected compartments $x = (I_{hr}, I_{hn}, I_v)^\top$. Write the system for these compartments in the form $\frac{dx}{dt} = \mathbf{F}(x) - \mathbf{V}(x)$ where $\mathbf{F}$ contains new infection terms and $\mathbf{V}$ contains transition terms. From the model, the new infection terms are

$$F_1 = \theta\frac{\beta_h I_v}{N_h}S_h, \qquad F_2 = \frac{(1-\theta)\beta_h I_v}{N_h}S_h,$$

$$F_3 = \frac{\beta_v(I_{hr}+I_{hn})}{N_h}S_v$$

and the remaining transition terms are

$$V_1 = (\gamma_h + \mu_h)I_{hr}, \qquad V_2 = (\gamma_h + \mu_h)I_{hn}, \qquad V_3 = \mu_v I_v.$$

We compute the Jacobians F and V of $(F_1, F_2, F_3)^\top$ and $(V_1, V_2, V_3)^\top$ at the E^*. Since at the DFE, $S_h^* = N_h^*$ and $S_v^* = N_v^*$, we obtain

$$F = \begin{pmatrix} 0 & 0 & \frac{\theta\beta_h S_h^*}{N_h^*} \\ 0 & 0 & (1-\theta)\frac{\beta_h S_h^*}{N_h^*} \\ \frac{\beta_v S_v^*}{N_h^*} & \frac{\beta_v S_v^*}{N_h^*} & 0 \end{pmatrix}, V = \begin{pmatrix} \gamma_h+\mu_h & 0 & 0 \\ 0 & \gamma_h+\mu_h & 0 \\ 0 & 0 & \mu_v \end{pmatrix}.$$

The next-generation matrix is $K = FV^{-1}$.
Computing $V^{-1} = \mathrm{diag}((\gamma_h+\mu_h)^{-1}, (\gamma_h+\mu_h)^{-1}, \mu_v^{-1})$, we get

$$K = \begin{pmatrix} 0 & 0 & \frac{\theta\beta_h S_h^*}{N_h^*\mu_v} \\ 0 & 0 & (1-\theta)\frac{\beta_h S_h^*}{N_h^*\mu_v} \\ \frac{\beta_v S_v^*}{N_h^*(\gamma_h+\mu_h)} & \frac{\beta_v S_v^*}{N_h^*(\gamma_h+\mu_h)} & 0 \end{pmatrix}$$

Let $\frac{\theta\beta_h S_h^*}{N_h^*\mu_v} = a$, $(1-\theta)\frac{\beta_h S_h^*}{N_h^*\mu_v} = b$ and $\frac{\beta_v S_v^*}{N_h^*(\gamma_h+\mu_h)} = c$.

Then $K = \begin{pmatrix} 0 & 0 & a \\ 0 & 0 & b \\ c & c & 0 \end{pmatrix}$.

The characteristic polynomial of K can be computed as:

$$\det(K - \lambda I) = -\lambda^3 + \lambda c(a+b) = -\lambda\left(\lambda^2 - c(a+b)\right).$$

Thus, the eigenvalues are $\lambda = 0$ and $\lambda = \pm\sqrt{c(a+b)}$.

The spectral radius is $\rho(K) = \sqrt{c(a+b)}$.

Now, substituting the values of $a+b, c$ and hence using values at DFE, we obtain the formula,

$$R_0 = \rho(FV^{-1}) = \sqrt{\frac{(1+\eta_1)\beta_{h0}(1+\eta_2)\beta_{v0}(1+\alpha)K_{v0}\left(1-\frac{\mu_v}{(1+\eta_3)r_0}\right)}{\mu_v(\gamma_h+\mu_h)N_h^*}}. \quad (2.9)$$

Stability of Disease-Free Equilibrium

On the basis of the theory about the spectral radius of the next-generation matrix [15], we note the following. If $R_0 < 1$, then all eigenvalues of the linearization at E^* have negative real parts and hence E^* is locally asymptotically stable. If $R_0 > 1$, the linearization at E^* has an eigenvalue with positive real part since $R_0 - 1 = \rho(K) - 1 > 0$ gives a real positive root of the characteristic equation, hence E^* is unstable.

3. RESULTS AND DISCUSSION

3.1 Parameter Estimation and Model Calibration

To conduct numerical simulations and reproduce realistic dengue transmission dynamics, model parameters were estimated using a combination of methods:

Calculated Parameters: Demographic parameters such as human recruitment rate (Λ_h) and natural death rate (μ_h) were computed using census data (CBS, 2021) and the average life expectancy in Nepal.

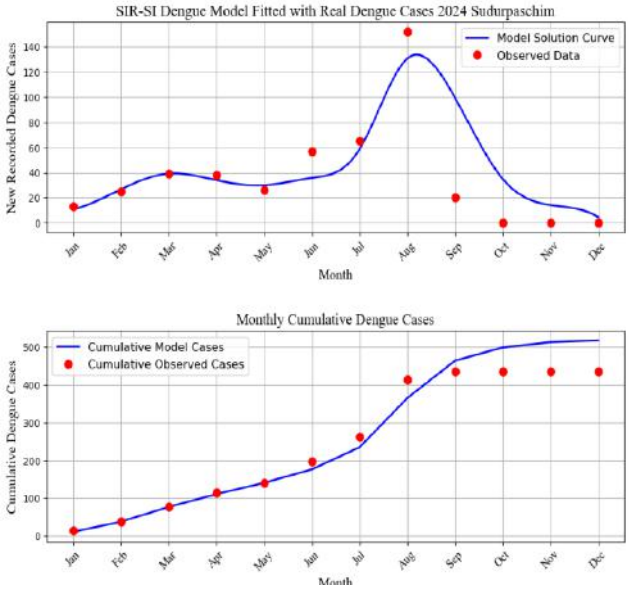

Fig. 4: Fitting the Dengue Model vs Real Time Dengue Data 2024 Sudurpashchim.

Data-Driven Fitting: Monthly new dengue cases of 2024 reported in Sudurpashchim Province was obtained from the Epidemiology and Disease Control Division (EDCD), Nepal. Parameters such as the transmission rate from vector to human (β_h) and human to vector (β_v), reporting proportion (θ), the vector carrying capacity K_v, mosquito death rate (μ_v), mosquito growth rate (r), and human recovery rate (γ_h) were calibrated by minimizing the sum of squared errors between observed and predicted monthly new infections. Here, the initial intervals for values of the fitted parameters during optimization were assumed being based on ranges reported in peer-reviewed literature [4, 18, 19]. Reasonable ranges were selected to reflect the local climatic and epidemiological context of Nepal.

This parameter estimation process ensures the model captures key biological, epidemiological, and environmental factors influencing dengue dynamics in Sudurpahschim.

Table 1: Estimated Parameters: Source and description.

Param - eter	Estimated Value	Source	Parameter	Estimated Value
Λ_h	130	calculated	r	1.4
μ_h	0.00119	calculated	K_v	4976640
β_h	2.79	data fitting	θ	0.11225
β_v	2.77	data fitting	α	2.81
γ_h	2.15827	data fitting	η_1, η_2, η_3	1.5
μ_v	1.80723	data fitting	R_0	1.9499

(Source: Data fitting)

3.2 Sensitivity Analysis

Each of the parameters $\eta_i = \eta, i = 1,2,3$ and α was varied from 75% to 150% of its baseline value. Plots were generated showing the sensitivity of R_0 with respect to key parameters α, γ_h, η and μ_v are presented in Fig. 5 (a). The resulting value of R_0 was computed and heatmap is plotted as shown in Fig. 5 (b).

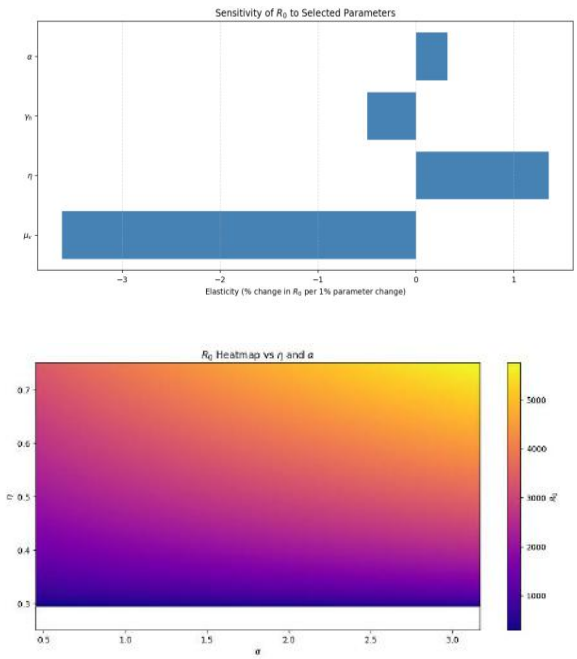

Fig. 5: Sensitivity analysis of the basic reproduction number and heat-map.

These results help to identify which parameters are critical for control strategies (e.g., vector control, sanitation, or public awareness). Sensitivity analysis supports the design of robust, data-informed intervention policies.

Fig. 5 illustrates the sensitivity of dengue outbreak dynamics to key model parameters: mosquito mortality rate (μ_v), initial susceptible

vector population (S_v^0), transmission rates β_h and β_v, and human recovery rate (γ_h). Each subplot reveals how changes in these parameters influence the total number of new dengue cases, peak infection size, and timing of the epidemic peak.

Increment in the mosquito mortality rate μ_v results in a significantly delayed and reduced epidemic peak. Even modest increments in μ_v lead to substantial reductions in disease burden, highlighting the critical role of adult mosquito control (e.g., safe use of insecticides, environmental management). This finding aligns with biological expectations, as higher mosquito death rates limit the infectious lifespan and overall vector population.

Similarly, reduction in the initial susceptible vector population S_v^0—which can be interpreted as lowering the vector carrying capacity via reduced breeding sites (e.g., eliminating stagnant water, waste management)—also results in a notably lower and delayed peak. This supports the effectiveness of pre-monsoon vector source reduction programs in tropical regions like Sudur Pashchim, where vector populations rise with rainfall (Fig.6).

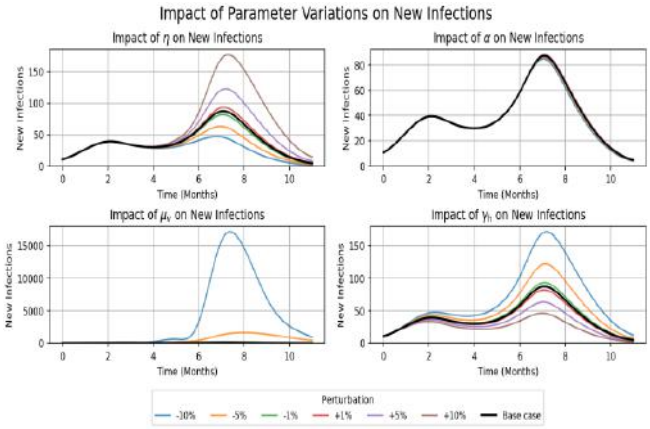

Fig. 6: Impact of some parameters in the peak time and size of infections.

Higher transmission rates β_h and β_v naturally increase the outbreak size and cause earlier peaks, underscoring the importance of reducing human-vector contact. Use of mosquito repellents, protective clothing, and awareness campaigns could help reduce effective transmission. In contrast, increasing the human recovery rate (γ_h) shortens infection duration and dampens the outbreak peak, though this may depend on treatment access and public health response.

4. CONCLUSION AND RECOMMENDATION

Mathematical model for dengue transmission dynamics is constructed, analyzed and fitted with monthly dengue cases of one year reported in Sudur Pashchim province of Nepal. Our model incorporates with the impacts of key climatic factors temperature and rainfall which are periodic in the region. Our model simply includes parameters for average increment in mosquito growth rate, transmission rates, mosquito mortality due to the warm temperature of summer period. Also, the average impact of rainy season over carrying capacity of environment for mosquito population is involved in the model. These parameters make the model more realistic than usual deterministic models employed in other studies in Nepal and better describing the seasonality of dengue in the reasons like Nepal. The small reported proportion and only monthly data availability (not strong) are limitations of our study. If the data were a bit richer (e.g. weekly and well reported) and parameters were time dependent as temperature and rainfall (instead of the impacts in average) the model could do still better.

Based on the findings of our study, we recommend integrated vector management focusing on strategies.

Mosquito mortality increase: Promote safe insecticide use and larvicide treatment to moderately raise μ_v , which simulations show can significantly flatten and delay epidemic peaks.

Source reduction: Reduce S_v^0 by targeting breeding sites before and during monsoon, as this greatly lowers transmission potential.

Transmission reduction: Encourage personal protection measures to reduce β_h and β_v, especially during the summer and post-monsoon months.

Case management: Improve healthcare access and early diagnosis to increase γ_h, reducing infectious periods and secondary transmissions. These interventions, especially when coordinated and seasonally timed, could significantly mitigate dengue burden in Sudurpaschim and similar regions.

AUTHORS CONTRIBUTIONS

YR Pant: Conceptualization, model formulation, analysis, simulation; N Kharel: Conceptualization, model, analysis, simulation; A Bhatta: Mathematical analysis, data collection, data management, typing, simulation; P Chaudhary: Mathematical analysis, data collection, data management, typing, simulation.

ETHICAL ISSUES AND SAFETY

Since we have used only secondary data published/provided by authentic offices with provided proper citations, there is no ethical issues. Our data collection process does not affect public and species.

CONFLICT OF INTEREST

Authors declare that there are no conflicts of interest or competing financial interests to influence the work presented in this paper.

ACKNOWLEDGMENTS

Authors acknowledge Dr. Khagendra Adhikari, Lecturer, Tribhuvan University, Amrit Campus, Kathmandu, for his invaluable guidelines and suggestions.

REFERENCES

[1] S. Bhatt, P.W. Gething, O.J. Brady, J.P. Messina, A.W. Farlow, C.L. Moyes, J.M. Drake, J.S. Brownstein, A.G. Hoen, O. Sankoh, et al., The global distribution and burden of dengue, *Nature*, **496** (7446) 504–507, 2013. doi: 10.1038/nature12060.

[2] World Health Organization, Dengue and severe dengue. https://www.who.int/news-room/fact-sheets/detail/dengue-and-severe-dengue, (2023) Accessed: 2025-06-22.

[3] M.S. Mustafa, V. Rasotgi, S. Jain, V. Gupta, Discovery of fifth serotype of dengue virus (denv-5): A new public health dilemma in dengue control, *Med Journal Armed Forces India*, 2015. Review covers serotypes and vector biology.

[4] L. Esteva, C. Vargas, A model for dengue disease with variable human population, *Journal of mathematical biology*, **38** (3) (1999) 220–240.

[5] H. Yang, M. Macoris, A. Galvani, M. Andraud, A model for the transmission of dengue: development and parameter estimation for Thailand, *Epidemiology and Infection*, **123** (1) (2000) 61–70.

[6] L. Barsante, K. Paixão, K. Laass, R. Cardoso, A. Eiras, J. Acebal, A model to predict the population size of the dengue fever vector based on rainfall data, arXiv preprint arXiv:1409.7942 (2014).

[7] M. Johansson, F. Dominici, G. Glass, Local and global effects of climate on dengue transmission in puerto rico, *PLoS Neglected Tropical Diseases*, **3** (2) (2009) e382.

[8] C.W. Morin, A.C. Comrie, K. Ernst, Meteorologically driven simulations of dengue epidemics in san juan, pr, *PLoS Neglected Tropical Diseases*, **9** (4) (2015) e0004002.

[9] Y.L. Hii, H. Zhu, N. Ng, Forecasting dengue: the importance of rainfall and temperature, *PLoS Neglected Tropical Diseases*, vol. 6, no. 11, p. e1908, 2012.

[10] J.F. Brière, P. Pracros, A.Y. Le Roux, J.S. Pierre, A novel rate model of temperature-dependent development for arthropods, *Environmental Entomology*, **28** (1) (1999) 22–29.

[11] P.E. Parham, E. Michael, Modeling the effects of weather and climate change on malaria transmission*, Environmental Health Perspectives*, **118** (5) (2010) 620–626.

[12] L. Lambrechts, K. Paaijmans, T. Fansiri, Impact of daily temperature fluctuations on dengue virus transmission by aedes aegypti, *Proceedings of the National Academy of Sciences*, **108** (18) (2011) 7460–7465.

[13] N.K. Vaidya, F.B. Wang, Persistence of mosquito vector and dengue: Impact of seasonal and diurnal temperature variations, *Discrete & Continuous Dynamical Systems-B*, 2021.

[14] F. Brauer, C. Castillo-Chavez, Mathematical Models in Population Biology and Epidemiology, volume 40 of Texts in Applied Mathematics. Springer, 2001.

[15] P. Van den Driessche, J. Watmough, Reproduction numbers and sub-threshold endemic equilibria for compartmental models of disease transmission, *Mathematical Biosciences*, **180** (2002) 29–48.

[16] O. Diekmann, H. Heesterbeek, M.G. Roberts, The construction of next-generation matrices for compartmental epidemic models, *Journal of the Royal Society Interface*, **7** (47) (2010) 873– 885.

[17] D.L. Smith, K.E. Battle, S.I. Hay, C.M. Barker, T.W. Scott, F.E. McKenzie, Ross, macdonald, and a theory for the dynamics and control of mosquito transmitted pathogens, *PLoS pathogens*, **8** (4) (2012) e1002588.

[18] G. Chowell, B. Cazelles, H. Broutin, C.V. Munayco, A. Torre, F.E. McKenzie, C. Viboud, Modeling the transmission dynamics of dengue fever: implications for control interventions and vaccination strategies, *Proceedings of the National Academy of Sciences*, **103** (49) (2006) 18195–18200. doi: 10.1073/pnas.0603182103.

[19] C.A. Manore, K.S. Hickmann, S. Xu, H.J. Wearing, J.M. Hyman, Towards an early warning system for forecasting human west nile virus incidence, *PLoS One*, **9** (3) (2014) e92321. doi: 10.1371/journal.pone.0092321.

Mitigating Strategies for Road Accidents in Nepal using IoT, AI and ML

Prakash Datt Bhatt*

Department of Computer Science, Shree Siddhanath Science Campus, Mahendranagar, Kanchanpur, Tribhuvan University, Nepal

Research Article

ISSN: 3059-9504 (online)
DOI: https://doi.org/10.3126/ajs.v2i1.87995

Article History

Received: October 16, 2025; Revised: December 04, 2025; Accepted: December 08, 2025; Published: December 25, 2025

Keywords

IoT, safety road, road accident, smart traffic system, mountain roads.

***Corresponding Author**

Email: prakash.bhatt@snsc.tu.edu.np (PD Bhatt)
Orcid: https://orcid.org/0009-0008-0949-1383

ABSTRACT

Rapid deployment of Internet of Things (IoT) and increasing the number of active IoT devices connected in this network predicts 41billiondevices by 2030, double the number of devices connected now. This prominent technology is being used in every sort of applications, including transportation and traffic management systems. IoT has a significant impact on the safety road as well as accident detection and prevention systems. This paper explores the primary reasons of road accidents in Nepal, how the integration of IoT with AI solutions is embedded into vehicles to monitor and control road accidents, mitigate the number of accidents, and recommend the best IoT-enabled vehicle systems which are more compatible with the roads in mountain and hilly regions like Nepal. Mainly, sentimental analysis to observe the mind-state of the driver and alert the concerned bodies by using cloud-based services is the major concern. Later, using ultrasonic sensor and sensor boards in the sharp turn of the mountain detects another vehicle is arriving from the opposite side or any obstacles is presented nearby and suggests controlling their speed to minimize the accident is another finding. Additionally, face detection and object counting cameras, alcohol detection sensor can also reduce the road accidents by reporting real-time mistakes due to human misbehavior. Finally, the integrated effect of deploying all aforementioned technologies has been computed which seems better than individual's performance. This integrated solution can be proven milestone for reducing the number of accidents in the mountainous road system of Nepal.

1. INTRODUCTION

Nepal being mountainous country, the development of road transportation and road network is in infancy stage. The roads in the mountain region are slippery with sharp turns and difficult to navigate. Also, it has been observed that the roads in the plain region of Nepal are narrower and not managed properly. Moreover, the traffic rules and regulations are not implemented strictly. All these concerns increase the number of road accidents day by day. This is more serious problem than any natural disaster like flood, landslides and earthquake; and more people lost their life than any pandemic like COVID-19. According to police report, it has been found that 12,371 people have lost their life in vehicle accidents across Nepal within five fiscal years and more than two thousand fatalities occurring annually. During this period, 171,098 vehicles were involved in accidents. The statistics of road accidents and their consequences on fatalities and financial loss in the remaining world shows the worst situation. According to data from the World Health Organization (WHO), the global mortality rate caused by road accidents is higher than that caused by fatal diseases such as tuberculosis, diabetes, and kidney-related illnesses. It motivates to carry an extensive study about the reasons behind road accidents and preventing the loss of life and wealth using contemporary technology. Such an immense problem can be solved by integrating Internet of Things (IoT) with vehicle and transportation systems. IoT has been growing rapidly and its integration with artificial integration and machine learning (AI-ML) has fueled its diverse application. As IoT has changed every perspective of human life, safety road system and prevention road accidents can be achieved via smart IoT technology. IoT systems for road safety employ wireless sensor networks, communication modules, and predictive algorithms to detect, alert, and preventing accidents.

The statistical study by Manandhar has found poor road conditions and improper driving skill are the major factors for causing accidents in Nepal [1]. Other reasons can be overloaded vehicles, drunk and drive, weather conditions and technical problems in vehicles. Thus, it is necessary to study these factors extensively and reduce the accident frequency as early as possible. It has been observed that the road accidents can be reduced by maximizing the traffic flow by integrating artificial intelligence with real time response system [2]. In another study, Alehouse et al. [3] have developed a new protocol for vehicular ad-hoc Networks (VANETs) which minimized the frequency of road accidents and reduced the number of lives lost via accidents in Saudi Arabia. The study was conducted using simulation-based methods which revealed that the proposed protocol achieved significantly improved outcomes in comparison to existing approaches. The evaluation was carried out using key performance indicators, namely Message Delivery Ratio, Message Loss Ratio, Average Delay, and Basic Safety Message Rate, all of which demonstrated superior results under the proposed framework. It has been reported that drunk and drive is also the major reason of road-accidents. To address this issue support vector machine (SVM), a machine learning approach, is deployed reducing the number of accidents [4]. This panic situation underscores the necessity of conducting a comprehensive study on the causes of road accidents, ranging from those observed in

developing countries to those in developed and under-developed nations. In this regard, researchers and various governmental bodies have been actively engaged in this issue for a considerable period of time. Furthermore, several governments are emphasizing the development and implementation of smart traffic systems with the objective of strengthening transportation networks and reducing the rate of road accidents. Recently, Senthil et al. [5] proposed a novel framework for vehicle systems which incorporate Artificial Intelligence (AI) with Internet of Things (IoT). Mainly, this framework comprises of three modules namely: *drowsiness alert module*, *speed limitation module*, and *alcohol sensing module*. Additionally, Li-Fi technology is utilized for inter-vehicle communication due to its lower susceptibility to interference, enhanced security, and superior performance in high-density environments such as urban areas.

Table 1: Various IoT and smart technologies for safety roads and impacts.

Ref	Methodology	Technologies Used	Consequences
[2]	Experimental	Arduino board consisting IR sensors, LED lights, and buzzer	Prevent accidents at U-turns by alerting the driver
[6]	Experimental (simulation)	Smartphone sensors (accelerometer, GPS, pressure, microphone), WiFi/3G/4G, cloud	Accident detection and reporting, hospital notification
[11]	Theoreticalwith real-world data analysis	Internet of Vehicles (IoV), Roadside Units (RSUs), cloud computing, Spatio-Temporal Convolutional Long Short-Term Memory (STCLA) deep learning	Real-time accident prediction and prevention
[12]	Experimental (prototype/ simulation)	Mobile traffic sensors, IoT cloud, OpenGTS, MongoDB	Real-time traffic monitoring and alert notification
[13]	Experimental (prototype/ simulation)	Smartphone sensors (Global Positioning System (GPS), accelerometer, gyroscope)	Accident detection and classification using machine learning
[15]	Theoretical/ conceptual	Vehicle-to- Everything (V2X), edge/cloud computing, On-Board Unit (OBU), accelerometer, gyroscope, GPS, camera	Accident detection, notification, data visualization
[15]	Experimental (simulation)	Vehicle-to-Infrastructure (V2I), speed sensors (implied), RMATLAB17 simulator	Alert generation based on speed, accident prevention
[16]	Experimental (prototype)	Accelerometer, ultrasonic, limit switch, GPS, Global System for Mobile Communications (GSM), vibration sensors	Accident detection, notification, automatic braking
[17]	Experimental (prototype)	MQ3 alcohol sensor, SW-420 vibration sensor, camera, GPS, GSM, Deep Learning Convolutional Neural Network (DLCNN)	Alcohol detection, engine lock, accident prediction

Table 2: Terms and abbreviations.

Terms	Abbreviations
AI	Artificial Intelligence
COVID	Corona Virus Disease
DLCNN	Deep Learning Convolutional Neural Network
ECT	Engine Coolant Temperature
ECU	Electronic Control Unit
GPS	Global Positioning System
GSM	Global System for Mobile Communications
IoT	Internet of Things
IoV	Internet of Vehicles
LED	Light Emitting Diode
LiDAR	Light Detection and Ranging
ML	Machine Learning
OBU	On-Board Unit
RSUs	Roadside Units
STCLA	Spatio-Temporal Convolutional Long Short-Term Memory
SVM	Support Vector Machine
TPR	True Positive Rate
V2I	Vehicle-to-Infrastructure
VANETs	Vehicular Ad-hoc Networks

In the context of mountainous roads, a study by Nookala [2] explored a smart road safety and prevention system integrating Artificial Intelligence (AI), the Internet of Things (IoT), and Machine Learning (ML). The proposed system is capable of detecting weather conditions in real time and alerting vehicles to accident-prone scenarios. Moreover, it assists drivers in navigating mountain routes safely by providing real-time information and alerts regarding current road conditions and potential future hazards. Similarly, Bhatti et al., 2019 [6] developed experimental based system using plethora of in-built sensors in vehicle system which are used for accident detection and reporting the incident to nearby hospital so that injured patients got treatment in real-time. Despite of these plenty of literature, there is no any model that that incorporate face detection system for counting people (passengers), detecting alcohol consumption by driver, drowsiness sensor for driver's sleepy state and ultrasonic system for navigating vehicles into single system. That is why this model analyzes the integrated solution to fill the existing research gap. The main objectives of this paper are to analyze the performance of integrated model for safety road system alerting and notifying the traffic police and

concerning entities regarding the same. Summary of literature review is presented in Table 1.

The study is organized into four different sections. State-of-art on contemporary technologies for smart road transportation, and enhancement traffic system for mountain roads; and motivation for this research has been discussed in this section which is followed by methodology and technologies used to improve road system for mitigating accidents and saving the life to large extent. Next section highlights the results and discussion. Finally, the last section incorporates the concluding remarks and future recommendation. The list of acronyms used in this manuscript is depicted in Table 2.

2. METHODOLOGY

A comprehensive review of existing studies indicates that road traffic accidents in Nepal predominantly arise from hazardous mountain terrains, driver-related factors such as alcohol consumption and fatigue during prolonged journeys, and systemic weaknesses within traffic regulation and enforcement. To address these challenges, this paper advocates the integration of advanced smart technologies across multiple levels to strengthen road infrastructure and enhance traffic safety management. The research framework initiates with literature review of various technologies used in road traffic and management system followed by various technologies specially, wireless sensor network and IoT devices, analyzing the performance metrics and finally suggesting the integrated model with better accuracy. The detailed research framework is demonstrated below:

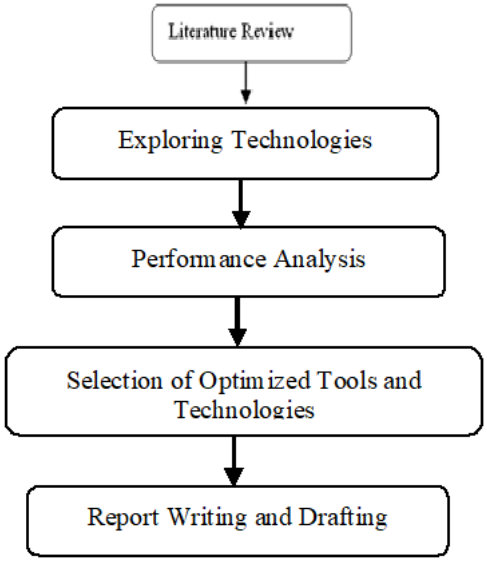

Fig. 1: Research framework for proposed model.

Main technologies and tools that used for the smart transportation and safety road systems are:

Face Detection and Counting Cameras to Enhance Traffic Systems for Vehicle Capacity Management

Face detection and counting technologies are increasingly employed in domains such as biometric authentication, security, pedestrian monitoring, and traffic management. Their integration within vehicles enables real-time monitoring of passenger occupancy and facilitates communication with nearby traffic control systems when overloading occurs, thereby reducing risks associated with excess passenger capacity. Sivaranjini *et al.* [8] proposed the use of the YOLOv9 (You Only Look Once) technique for detecting and counting faces among multiple objects.

Smart Sensors for Safe Driving and Traffic Management Systems

Drunk driving is recognized as a major cause of road accidents in Nepal. The incorporation of alcohol detection sensors that transmit real-time alerts to nearby traffic police can significantly

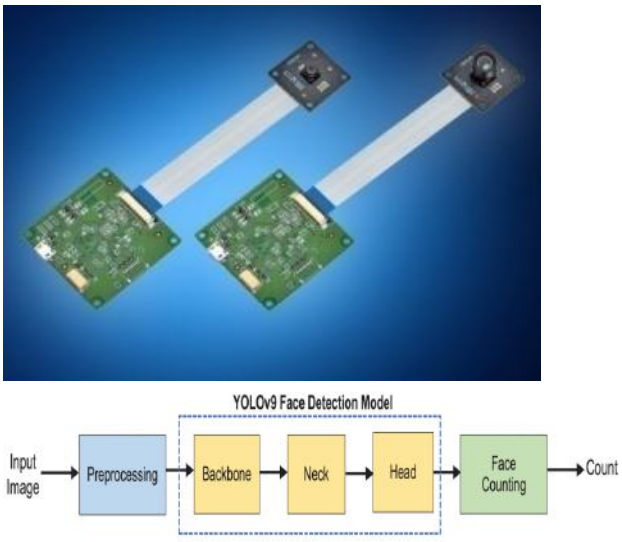

Fig. 2: Face detection camera and YOLOv9 face detection model.

reduce such incidents. Celaya-Padilla *et al.* [4] examined the use of the MQ3 sensor, which, when installed inside the vehicle, collects alcohol concentration data and employs a Support Vector Machine (SVM) classification technique to detect alcohol presence. Recently, Babu *et al.* [7] proposed a multi-sensor framework that combines an eye-blink sensor for drowsiness detection, an MQ3 sensor for alcohol consumption monitoring, and a heart rate sensor for identifying potential cardiac issues in drivers. Integrating these sensor technologies within vehicles enhances safety measures and contributes to the reduction of road accidents.

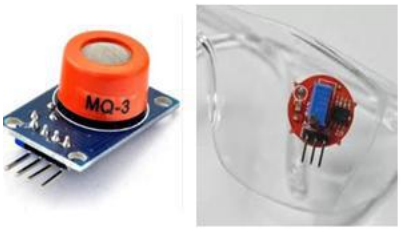

Fig. 3: MQ3 sensor for alcohol detection and Eye-blink sensor for drowsiness detection.

Environmental and Weather Sensing Devices for Navigation

Real-time monitoring of environmental conditions on mountain roads plays a critical role in traffic management and accident prevention. Mountainous routes are particularly challenging due

to sharp curves, slippery surfaces, and unpredictable factors such as humidity, lightning, and atmospheric pressure. An integrated sensing system comprising cameras, temperature sensors, moisture scanners, and

LiDAR can provide comprehensive information on road conditions, including temperature, humidity, visibility, and surface status [10]. Moreover, LiDAR technology can detect oncoming vehicles and issue alerts to drivers, thereby reducing the likelihood of collisions.

Fig. 4: Arduino board with IR sensors, LED, and buzzer to detect obstacles from opposite.

These sensor-based technologies represent a significant advancement toward enhancing road safety and reducing accident rates, particularly in mountainous regions like Nepal. The detail of experiment results, accuracy, and test-train ratio based on secondary data has been illustrated below:

Table 3: Performance analysis of different sensors in road traffic system.

Sensors	Methodology	Accuracy	Remarks
MQ3 sensor [8]	80:20 (ML model)	0.98	Detects alcohol consumption by driver
Face detection sensor [9]	Empirical study	0.98	Counts the passengers inside vehicle and reports to the nearby concerning body
Eye-blink sensor [8]	Experimental study	0.95	Alert the drowsiness of driver (more than 4 seconds)

3. RESULTS AND DISCUSSION

It is important to compute the accuracy of integrated solution in vehicle where all these sensors are included. For this computation fusion rule has been used assuming all three sensors are independent. Let sensitivities (TPR) for these sensors are s_1, s_2, s_3 and specificities (TNR) are t_1, t_2, t_3 respectively, the combined sensitivity can be,

$$Combined\ True\ Positive\ Rate\ (TPR) = 1 - (1 - s_1)(1 - s_2)(1 - s_3) = 99.998\%$$

However, if two of these sensors will be triggered out of three, the combined sensitivity (TPR) will be,

$$P_3 = 0.98 \times 0.98 \times 0.95 = 0.912$$

$$P_2 = (0.98 \times 0.98 \times 0.05) + (0.98 \times 0.02 \times 0.95) + (0.02 \times 0.98 \times 0.95)$$
$$= 0.04802 + 0.01862 + 0.01862 = 0.08526$$
$$\text{TPR (majority)} \approx 0.08526 + 0.912 = \mathbf{0.99726} \ (\approx 99.7\%)$$

Results reveal that the performance (TPR) of the integrated system will be approximately 99.98% when these sensors work independently and 99.7% when two of the sensors will be triggered.

The rapid advancement and deployment of IoT devices across diverse sectors now make it feasible to transform conventional road systems into smart, safety-focused traffic networks. Vehicles equipped with advanced sensor technologies provide significant opportunities for fault detection, navigation, and safe driving, irrespective of road conditions. Furthermore, smart road systems offer benefits to both governmental authorities and the public, enabling efficient traffic monitoring through Wi-Fi–enabled sensor networks and enhancing overall road safety.

As a mountainous country at the early stages of digital development, Nepal faces significant barriers to implementing smart city and smart road initiatives, with the digital divide being a primary constraint. Another critical challenge lies in the system's implementation, as neither transportation companies nor government agencies consistently ensure fair monitoring. Additionally, the presence of bureaucratic corruption further restricts effective deployment. A large portion of existing transportation infrastructure relies on traditional models, making the transition to smart systems is complex and resource-intensive.

4. CONCLUSION

The integration of smart technologies into vehicles and road traffic systems offers a promising pathway to reducing accidents and ensuring sustainable road safety management. Sensors embedded at various levels from drivers' wearable to vehicle components, enable continuous monitoring of driver behavior, passenger load, and mechanical performance, while ultrasonic sensors enhance safety in low-visibility mountain roads. In the context of Nepal's challenging geographical and infrastructural conditions, configuring vehicles with ultrasonic sensors, face detection and passenger-counting systems, and alcohol detection technologies can substantially mitigate accident risks. The adoption of such IoT-enabled solutions not only enhances driver and passenger safety but also strengthens the overall reliability and sustainability of the road transport system. Experimental study in the context of Nepal and evaluating the actual performance of the model is the future recommendation.

AUTHOR CONTRIBUTION

The whole work was carried by PD Bhatt.

DECLARATION OF CONFLICT OF INTEREST

The author declares no known conflicts of interest.

ACKNOWDGMENTS

Authors would like to acknowledge reviewers for their valuable suggestions and Siddhanath Science Campus for research environment.

REFERENCES

[1] R. Manandhar, Determinants of Road Traffic Accidents in Nepal*, The International Research Journal of Management Science,* **7**(12) (2022) 121–130. *doi:10.3126/irjms.v7i1.50632*.

[2] G.R. Nookala Venu, K. Maneesha, K. Anusha, S. Merugu, A. Mohammad, Smart Road Safety and Vehicle Accidents Prevention System for Mountain Road*, International Journal for Innovative Engineering Management and Research*, **11** (6) (2022) 209–214.

[3] A. Aldegheishem, H. Yasmeen, H. Maryam, M.A. Shah, A. Mehmood, N. Alrajeh, H. Song, Smart Road Traffic Accidents Reduction Strategy Based on Intelligent Transportation Systems (TARS), *Sensors*, **18** (7) (2018) 1983. doi:10.3390/s18071983.

[4] J.M. Celaya-Padilla, J.S. Romero-Gonz´alez, C.E. Galvan-Tejada, J.I. Galvan-Tejada, H. Luna-Garc´ıa, J.G. Arceo-Olague, N.K. Gamboa-Rosales, C. Sifuentes-Gallardo, A. Martinez-Torteya, J. I. De la Rosa et al., In-vehicle Alcohol Detection using Low-Cost Sensors and Genetic Algorithms to Aid in the Drinking and Driving Detection, *Sensors*, **21** (22) (2021) 7752. doi:10.3390/s21227752

[5] S.K. Jagatheesaperumal, S.E. Bibri, J. Huang, J. Rajapandian, B. Parthiban, "Artificial Intelligence of Things for Smart Cities: Advanced Solutions for Enhancing Transportation Safety*, Computational Urban Science*, **4** (1) (2024) 10.

[6] F. Bhatti, M. A. Sah, C. Maple, and S. U. Islam, *"A Novel Internet of Things-Enabled Accident Detection and Reporting System for Smart City Environments,"* Sensors, vol. 19, no. 9, p. 2071, 2019. doi:10.3390/s19092071.

[7] T. Babu, R.R. Nair, M. Manjula, V. Manjula, P.C. Shree, Integrating IoT and Sensors for Comprehensive Road Safety: A Systematic Approach to Accident Prevention, in International Conference on Advances and Applications in Artificial Intelligence (ICAAAI 2025). Atlantis Press, 2025, 127–137. doi:10.2991/978-94-6463-738-0_11.

[8] S.P. Narayanan, M.S. Manikandan, L.R. Cenkeramaddi, YOLOv9-Based Human Face Detection and Counting Under Human-Animal Faces, Complex Imaging Environments, and Image Qualities*, IEEE Access*, 13 (2025) 129600-129637. doi: 10.1109/ACCESS.2025.3591247.

[9] S.V., Vasantha, B. Kiranmai, M.A., Hussain, S.S. Hashmi, L., Nelson, L.S. Hariharan, *Face and Object Detection Algorithms for People Counting Applications,* in 2023 2nd International Conference on Automation, Computing and Renewable Systems (ICACRS), pp. 1188-1193, IEEE. doi:10.1109/ICACRS58579.2023.10405114.

[10] V.P. Kumar, K. Chenchireddy, V. Manohar, Smart Road Safety and Vehicle Accident Prevention System for Mountain Roads*, CVR Journal of Science and Technology*, **27** (1) (2025) 80-84.

[11] X. Wei, Enhancing Road Safety in Internet of Vehicles using Deep Learning Approach for Real-Time Accident Prediction and Prevention, *International Journal of Intelligent Networks,* **5** (2024) 212–223. doi:10.1016/j.ijin.2024.05.002.

[12] A. Celesti, A. Galletta, L. Carnevale, M. Fazio, A. Lay-Ekuakille, M. Villari, An IoT Cloud System for Traffic Monitoring and Vehicular Accidents Prevention Based on Mobile Sensor Data Processing, *IEEE Sensors Journal*, **18** (12) (2017) 4795–4802. doi:10.1109/JSEN.2017.2777786.

[13] B.K.M.A. Basit, K.M.B, G.R K. SM, *Road Accident Detection using Machine Learning,*2021 International Conference on System, Computation, Automation and Networking (ICSCAN), Puducherry, India, 2021, pp. 1-5. doi:10.1109/ICSCAN53069.2021.9526546.

[14] K.A. Khaliq, O. Chughtai, A. Shahwani, A. Qayyum, J. Pannek, Road Accidents Detection, Data Collection and Data Analysis using V2X Communication and Edge/Cloud Computing, *Electronics*, **8** (8) (2019) 89.doi:10.3390/electronics8080896.

[15] H. Mohapatra, A.K. Dalai. *IoT based V2I Framework for Accident Prevention.* CSI International Symposium on Artificial Intelligence and Signal Processing, 2022. doi:10.1109/AISP53593.2022.9760623.

[16] S. Barman, M.F.B. Hafiz, N.A. Khan, "*An IoT-Based Smart System for the Detection, Notification and Prevention of Vehicle Accidents,* in 2024 6th International Conference on Electrical Engineering and Information & Communication Technology (ICEEICT), pp. 1169–1174, 2024. doi:10.1109/ICEEICT62016.2024.10534370.

[17] S. Lakshmy, R. Gopan, M. Meenakshi, V. Adithya, M.R. Elizabeth, *Vehicle Accident Detection and Prevention using IoT and Deep Learning,* in 2022 IEEE International Conference on Signal Processing, Informatics, *Communication and Energy Systems (SPICES)*, **1** (2022) 22–27, doi:10.1109/SPICES52834.2022.9774089.

Human–Monkey Conflict and Community Responses in Bheemdatta and Bedkot Municipalities, Kanchanpur, Nepal

Manmati Joshi, Mahadev Bista, Balram Awasthi*

Department of Zoology, Siddhanath Science Campus, Tribhuvan University, Mahandranagar, Nepal

Research Article

ISSN: 3059-9504 (online)
DOI: https://doi.org/10.3126/ajs.v2i1.87998

Article History

Received: October 13, 2025; Revised: December 16, 2025; Accepted: December 20, 2025; Published: December 25, 2025

Keywords

Human–Monkey Conflict, Crop Damage, Community Perception, Mitigation Strategies, Kanchanpur District.

***Corresponding author**

Email: balram.awasthi@snsc.tu.edu.np (BR Awasthi)
Orcid: https://orcid.org/0000-0002-8288-2603

ABSTRACT

Human-monkey conflict is increasing in most parts of Nepal due to rapid land-use change, habitat loss, and expanding human settlements. This study assessed the patterns, drivers, and community responses to HMC in Bheemdatta and Bedkot Municipalities of Kanchanpur District. Data on conflict types, perceived drivers, local mitigation strategies, and community attitudes towards monkeys were collected through household surveys (160 households; 80 per municipality), key informant interviews, and field observations. Most of the respondents reported frequent crop damage, food theft, property destruction, and threats to personal safety. Our results indicated that habitat degradation and food scarcity are the major drivers of HMC. Bedkot, characterized by forest-adjacent farmlands, reported higher crop losses and more frequent encounters, while Bheemdatta experienced predominantly urban-related incidents such as food snatching and household intrusion. Communities primarily relied on reactive measures (stone-throwing, guarding), which were often ineffective. Despite economic losses, cultural and religious values promoted tolerance toward monkeys, although expectations from local authorities varied across municipalities. The present study recommends community-based mitigation, improved land-use planning, and future integration of ecological and spatial data to identify conflict hotspots and guide management strategies.

1. INTRODUCTION

Human–wildlife conflict (HWC) is increasingly recognized as a major conservation and socio-economic challenge worldwide [1], with particularly severe and widespread impacts in South Asia, where rapid human population growth, agricultural expansion, and infrastructure development overlap with wildlife habitats [2]. Contemporary conservation science conceptualizes HWC not merely as a consequence of animal behaviour, but as an emergent property of coupled social–ecological systems, shaped by interactions between wildlife ecology, land-use change, governance structures, and human livelihoods [3, 4]. Within this framework, conflict reflects broader institutional and social dynamics rather than isolated incidents of wildlife damage.

Among various forms of HWC, human–monkey conflict (HMC) has received increasing attention due to the exceptional behavioural adaptability of rhesus macaques (*Macaca mulatta*), their reliance on high-calorie crops and anthropogenic food sources [5,6,7], and their prominent presence in human settlements [8,9]. Rhesus macaques are behavioural generalists capable of rapid learning and innovation, allowing them to exploit with high cognitive flexibility, agricultural fields, household food stores, and waste sites with high efficiency [10, 11]. Such behavioural plasticity creates feedback loops in which human tolerance and food provisioning—intentional or accidental-reinforce macaque habituation and intensify conflict over time [10,11].

In Nepal, rhesus macaques are widely distributed and occupy an important ecological and cultural position [12]. However, they are also among the most problematic wildlife species, frequently raiding crops, stealing household food, and exploiting garbage in peri-urban and rural landscapes. These interactions generate substantial economic losses, social tensions, and negative perceptions among affected communities [13,14]. HMC encompasses a wide range of impacts, including crop and property damage, disturbance to livestock, physical injuries to people, and heightened risks of zoonotic disease transmission [15,16]. Studies consistently identify maize, potatoes, and fruit crops as the most affected agricultural commodities [7]. Beyond agricultural losses, macaques damage household infrastructure and personal belongings, resulting in financial strain and psychological stress [17, 18, 19].

Importantly, the burdens of HMC are not evenly distributed. Women, elderly individuals, and smallholder farmers are disproportionately affected due to gendered divisions of labour, limited mobility, and their primary responsibility for crop guarding and household management [18,19]. This social differentiation positions HMC not only as a conservation issue but also as a concern of environmental justice, where vulnerability is shaped by socio-economic status, age, and gender [20, 21]. Cultural and religious beliefs in Nepal, where monkeys are revered as manifestations of Lord Hanuman, have historically fostered tolerance toward macaques despite recurring losses [22,23]. Cultural norms and spiritual values strongly influence local attitudes, shaping both tolerance thresholds and acceptable management practices [22,24]. However, this tolerance is increasingly eroded by rising economic hardship, health risks, and insufficient institutional support [25,12,19]. In contrast, evidence suggests that awareness of monkey behaviour, combined with education, community engagement, and responsive governance,

can enhance willingness to adopt coexistence-oriented measures [18,23].

Current mitigation measures—ranging from translocation and community-based deterrents like fencing, patrolling, noise-making, and guard animals—are often labor-intensive, costly, and only partially effective [9, 20], while firecrackers, stones, and catapults raise ethical and safety concerns [21, 26]. Previous studies highlight that interventions such as buffer crops, physical barriers, and community-based management can reduce conflict, but their effectiveness depends on local socio-cultural contexts [10, 14, 28]. In addition, fostering positive human attitudes, promoting non-lethal deterrent techniques, and strengthening collaborative management and education initiatives are essential for enhancing coexistence [29].

Despite the growing recognition of these complexities, many conflict-prone areas in Nepal still lack systematic baseline data on conflict drivers, spatial and temporal patterns, socio-economic costs, and community attitudes [18, 26, 28, 30]. This data gap constrains the design of effective, context-specific mitigation strategies and limits evidence-based conservation planning [18,23]. Addressing these gaps is particularly urgent in ecologically sensitive landscapes surrounding protected areas, where conservation objectives intersect directly with local livelihoods [18, 28]. The Far-Western region of Nepal, particularly Kanchanpur District, represents a notable HWC hotspot due to rapid urban expansion, road development, and the proliferation of temple complexes that provide consistent food subsidies and attract macaque populations [15, 31, 32]. Bheemdatta and Bedkot municipalities frequently report crop raiding, property damage, and community distress, yet systematic empirical studies remain scarce (based on local observations). Consequently, existing mitigation efforts often fail to address the intertwined ecological, behavioural, and socio-economic drivers of conflict [12, 22]. Similar human–monkey conflict patterns influenced by local attitudes and mitigation practices occur elsewhere in South Asia [33, 34].

Present study aims to generate an integrated understanding of human–monkey conflict by combining ecological impact assessment with social perception analysis at the municipal scale. Specifically, this study seeks to: (1) identify the primary drivers and impacts of HMC; (2) analyze the types and extent of damage caused by rhesus macaques; (3) examine local perceptions, attitudes, and tolerance levels; and (4) document mitigation strategies employed by communities in Bheemdatta and Bedkot municipalities.

2. METHODOLOGY

2.1 Study area

The study was conducted in Bheemdatta and Bedkot Municipalities of Kanchanpur District, Sudurpashchim Province, Nepal (Fig. 1). The area lies in the Terai region and is characterised by a subtropical climate and a mosaic of agricultural, residential, and forested landscapes.

Bheemdatta Municipality, the primary urban and administrative center of the district, is located between 28°52′–29°08′ N and 80°06′–80°15.5′ E, at elevations ranging from 222.5 m to 1,192 m, and covers an area of 171.34 km² [34]. The municipality encompasses both plains and hilly terrain and supports rural and semi-urban communities with diverse livelihoods and cultural practices. It experiences a tropical to subtropical climate, with temperatures ranging from 6.96 °C to 43 °C and an average annual rainfall of approximately 1,575 mm [35]. Rapid urban expansion and associated land-use changes in recent years have intensified interactions between humans and rhesus macaques.

Bedkot Municipality, established in 2015, lies between 28°34′–28°57′ N and 80°08′–80°15′ E, at elevations ranging from 192 m to 1,401 m, and covers an area of 158.5 km² [35,36]. The municipality includes lowland plains and the foothills of the Siwalik range and is inhabited by a mix of rural and semi-urban communities. It experiences a tropical savannah climate, with mean annual temperatures exceeding 26 °C and annual precipitation ranging from 1,800 to 2,000 mm [36, 37]. Rapid urbanization along the east–west highway, coupled with the expansion of agriculture-based settlements, has intensified human–wildlife interactions, leading to increased crop and property damage while posing challenges for biodiversity conservation.

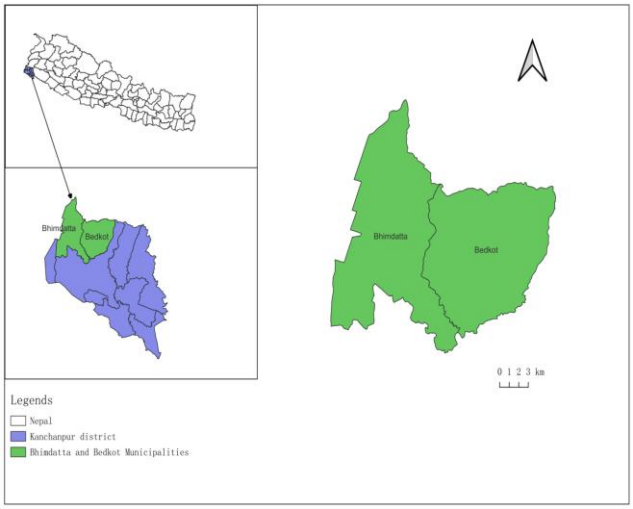

Fig. 1: Map showing Bheemdatta and Bedkot Municipalities, Kanchanpur District.

2.2 Data Collection

This study has used random sampling and mixed-method approaches, including household surveys, key informant interviews, and direct field observations, to obtain robust and representative data on human-monkey conflict in the Bheemdatta and Bedkot Municipalities.

A pre-tested structured questionnaire was administered to 160 randomly selected households (80 for each municipality) across three wards—two in Bheemdatta and one in Bedkot. The survey collected quantitative information on the frequency and intensity of monkey-related damages, causes of conflict, local perceptions, cultural attitudes, and mitigation strategies adopted by the community. Respondents represented diverse age groups, genders, and socio-economic backgrounds. The questionnaire included questions on such topics as types of damage caused by monkeys (including crop, property, physical, and psychological impacts), causes and local perceptions of the conflict, cultural and religious attitudes toward monkeys, and mitigation strategies alongside community-preferred solutions. In addition, in-depth semi-structured interviews were conducted with 16 key informants, including local leaders, experienced farmers, and school teachers, to obtain qualitative insights into historical patterns of human–monkey conflict, community coping mechanisms, and gaps in policy and institutional support. These interviews also helped assess the

effectiveness of existing mitigation strategies and the socio-cultural context of conflict management. Complementing the surveys and interviews, direct field observations were carried out during repeated visits to conflict-prone areas between April and May 2025. Observations focused on documenting locations of frequent monkey encounters, crop raids, property damage, human defensive measures such as fencing, scarecrow deployment, and guarding practices, as well as monkey behavior and movement patterns in relation to human activity. Informed consent was obtained from all participants, ensuring voluntary participation and confidentiality, and the study adhered to ethical research guidelines for human subjects.

2.3 Data analysis

Data from the household survey were first entered, cleaned, and ordered in Microsoft Excel before analysis. Descriptive statistics (frequencies, percentages, and means) were used to describe patterns of human-monkey conflict, damage types, community perceptions, and local response strategies. Results have been visualized with tables and bar charts. All variables were coded and analyzed using descriptive statistics and Pearson's Chi-square tests. Given that both the predictor and outcome variables are categorical in nature, the Pearson's Chi-square test was accordingly used to test associations between demographic factors (gender, age group, education level, and occupation) and respondents' attitudes towards monkeys. No parametric tests (e.g., t-tests, ANOVA) were applied since there were no continuous variables in the dataset that would call for such a test. Statistical significance was set at $p < 0.05$. Additionally, inferential analysis using Chi-square tests in IBM SPSS 20 explored associations between demographic variables (gender, age, education, and occupation) and attitudes toward monkeys, specifically regarding liking monkeys, supporting attacks on monkeys, and supporting harm to monkeys for causing damage [32].

3. RESULTS

3.1 Demographic and Socio-economic Profile of Respondents

Respondents in Bedkot and Bheemdatta Municipalities had different demographic and socio-economic backgrounds (Table 1). In Bedkot, 52.5% of respondents were male, while in Bheemdatta, 52.5% were female. Most people surveyed in Bheemdatta (61.25%) were between 31- 50 years old. In Bedkot, the age groups were more evenly distributed, with 36.84% aged 18–30 and 35% over 50. Agriculture was the main source of income in Bedkot (50%), but in Bheemdatta, more people worked in business (27.5%) and service jobs (13.8%). There were also differences in education: 41.25% of respondents in Bedkot were illiterate, while only 18.75% in Bheemdatta were. In Bheemdatta, 47.5% had completed higher secondary education or above (Table 1).

3.2 Causes of Human–Monkey Conflict

Food scarcity was identified as the primary driver of HMC, with over two-thirds (71.25%) of respondents in both municipalities. Habitat loss also contributed significantly, particularly in Bheemdatta, where deforestation and encroachment intensified conflict. A minority of respondents indicated that both food scarcity and habitat loss influenced HMC, highlighting resource limitation as the main underlying cause (Fig. 2).

Table 1: Demographic profile of respondents.

Variables	Categories	Bedkot (%) (n = 80)	Bheem-datta (%) (n = 80)
Gender	Male	52.50	47.50
	Female	47.50	52.50
Age Group	18–30 years	17.50	25.00
	31–50 years	47.50	61.25
	Above 50 years	35.00	13.75
Occupation	Agriculture/Farming	50.00	38.75
	Business	10.00	27.50
	Service (Govt./Private)	10.00	13.75
	Student	15.00	7.50
	Others (e.g., housewives)	15.00	12.50
Educational Level	Illiterate	41.25	18.75
	Primary (up to Grade 5)	18.75	13.75
	Secondary (6–10)	12.50	20.00
	Higher Secondary & above	27.50	47.50

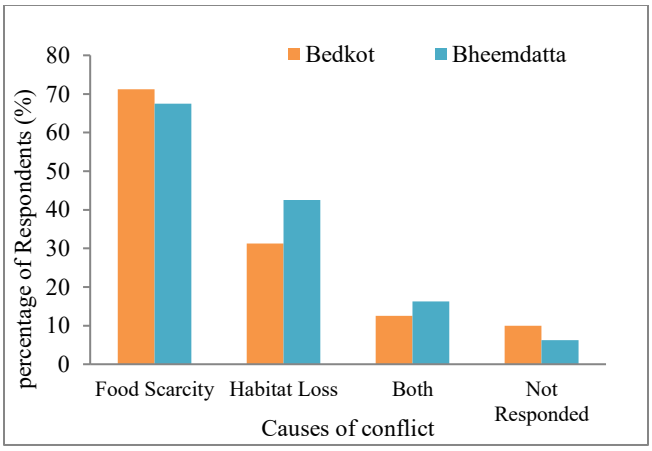

Fig. 2: Comparative causes of human–monkey conflict in Bedkot and Bheemdatta Municipalities (multiple responses allowed).

3.3 Types and Intensity of Damage

The most common effect was crop-destruction, which affected more than three-quarters (77%) of families in both municipalities. In contrast, food snatching was much more common in Bheemdatta (59%) than in Bedkot (34%), indicating closer interactions between humans and monkeys in densely populated areas. Although less common, unintentional injuries, monkey bites, and property destruction were nevertheless serious issues (Fig. 3).

The majority of respondents in Bheemdatta reported medium intensity (53.75%), nearly half (47.5%) of Bedkot respondents reported low impacts, while a larger percentage (15%) claimed severe impacts. These variations imply that, in comparison to Bedkot, conflict in Bheemdatta is both more frequent and more severe (Fig. 4).

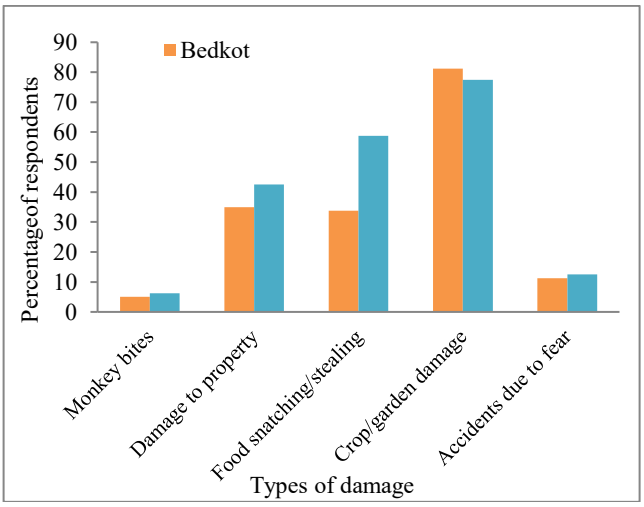

Fig. 3: Monkey-related damages reported by respondents in Bedkot and Bheemdatta Municipalities (Multiple responses allowed).

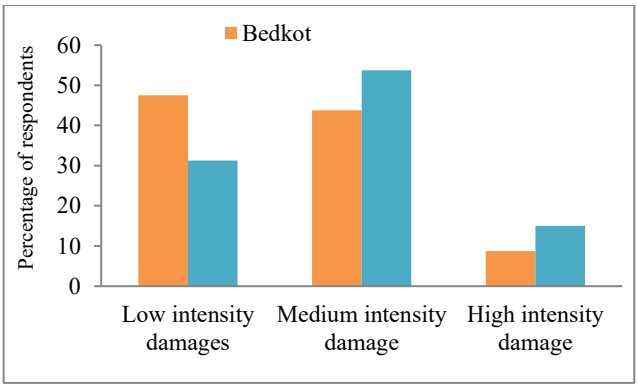

Fig. 4: Intensity caused by monkeys in Bedkot and Bheemdatta Municipalities.

3.4 Psychological Impacts and Community Attitudes

HMC put significant emotional strains on both municipalities. While the majority of responders said monkey-related disruptions were manageable, 15% said they were unbearable, indicating considerable psychological stress. Attitudes toward monkeys reflected this tension, with a slight majority of respondents (55%) disliking them and 45% favoring them. These beliefs are most likely influenced by repeated experiences of crop loss, property damage, and fear (Fig. 5 &6).

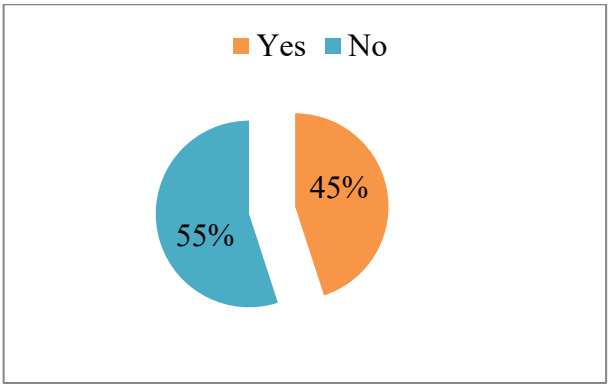

Fig. 5: Distribution of respondents who like or dislike monkeys.

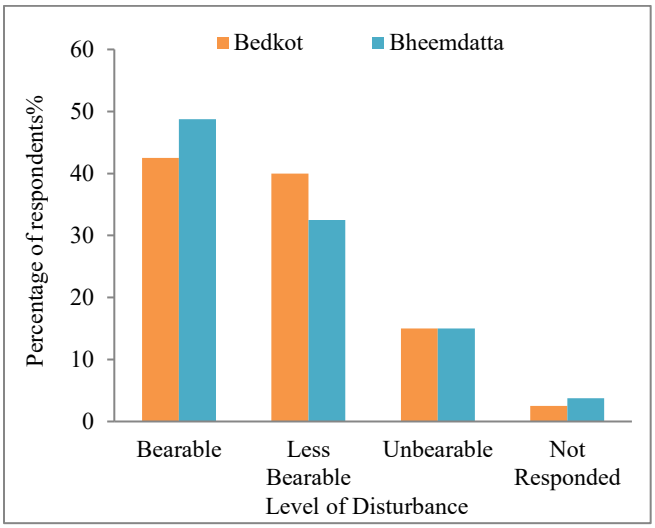

Fig. 6: Mental peace disturbance caused by monkeys in Bedkot and Bheemdatta Municipalities.

Tolerance toward conservation was mixed. Nearly half of respondents expressed continued support for monkey conservation even after damage occurred, though fewer maintained this support if family members were attacked (Table 2). The results revealed no significant associations between gender and any of the three attitude variables: liking monkeys ($p = 0.324$), support for attacking monkeys ($p = 0.493$), or support for harming monkeys due to damage ($p = 0.882$). Similarly, education level showed no significant association with liking monkeys ($p = .968$), support for attacking monkeys ($p = 0.453$), or support for damaging monkeys ($p = 0.356$). Occupation also did not have a significant relationship with any of the attitude variables: liking monkeys ($p = 0.645$), support for attacking monkeys ($p = 0.465$), or support for damaging monkeys ($p = 0.510$). No significant associations were found between age and either liking monkeys ($p = 0.419$) or supporting attacks on monkeys ($p = 0.118$). However, a statistically significant association was found between age and support for harming monkeys due to damage ($\chi^2 = 15.362$, $df = 4$, $p = 0.004$), indicating that attitudes toward this specific issue varied significantly across age groups.

Table 2: Tolerance attitudes toward monkey conservation.

Tolerance attitude	N	Agree	Disagree	Neutral
I support monkey conservation even If a family member is attacked	160	69 (43.12%)	50 (31.25%)	41 (25.25%)
I support monkey conservation even if damage occurred by monkey	160	77 (48.12%)	44 (27.50%)	39 (24.37%)

3.5 Local Mitigation Practices and Expectations

Residents used a variety of locally possible mitigation methods, most notably fear displays, stone-throwing, and the use of sticks. Financial and logistical restrictions made structural barriers less widespread (Fig. 7). Government-led interventions were

overwhelmingly preferred. Respondents ranked fencing and barriers (75% in Bedkot; 36.25% in Bheemdatta) and habitat restoration as priority measures. Interest in scientific approaches like sterilization was low, and compensation or awareness campaigns had little support (Fig. 8). Local governments (Bheemdatta, 58.75%; Bedkot, 56.25%) and farmers were perceived to bear the majority of conflict management responsibilities, with minimal expectation placed on NGOs or the federal government (Fig. 9).

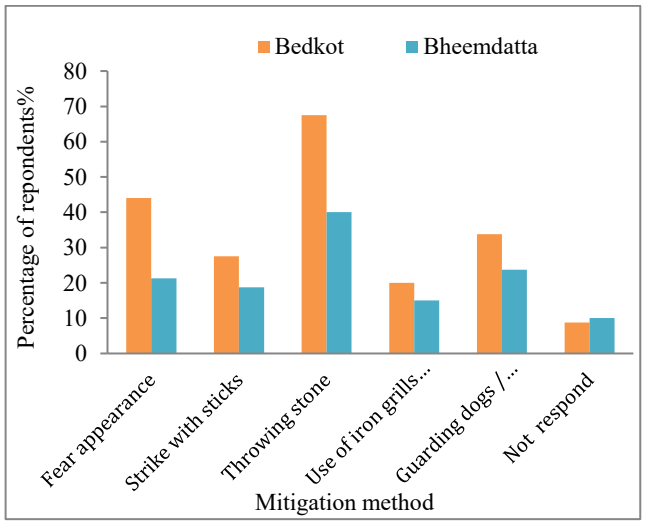

Fig. 7: Mitigation measures against human–monkey conflict in Bedkot and Bheemdatta Municipalities (Multiple responses allowed).

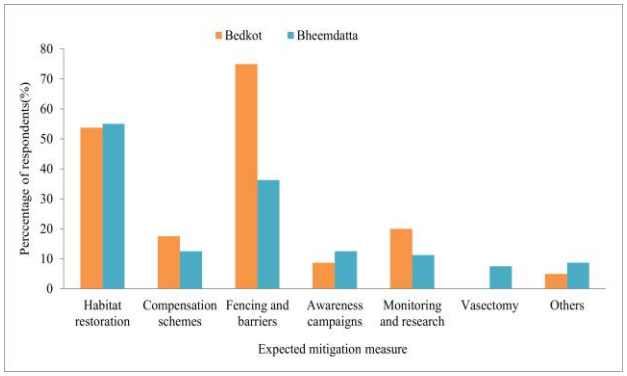

Fig. 8: Suggested Mitigation Measures Expected from Local Government by Respondents in Bedkot and Bheemdatta Municipalities (Multiple Responses Allowed).

3.6 Preferred Management Strategies

Across both municipalities, communities overwhelmingly favored non-lethal management. In Bedkot, translocation (69%) and capture–release (56%) were most supported, while Bheemdatta respondents prioritized translocation (43%) and enclosure-based capture (25%). Only a small minority supported lethal control (6% in Bedkot, 3% in Bheemdatta). These results highlight cultural and ethical values that favor coexistence and humane strategies, while also reflecting openness to innovative, community-based approaches (Fig. 10).

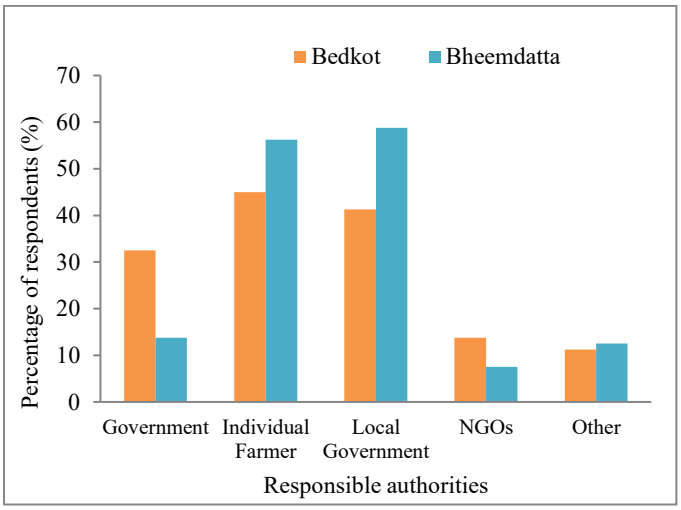

Fig. 9: Perceived responsible parties for managing human–monkey conflict in Bedkot and Bheemdatta Municipalities (Multiple responses allowed).

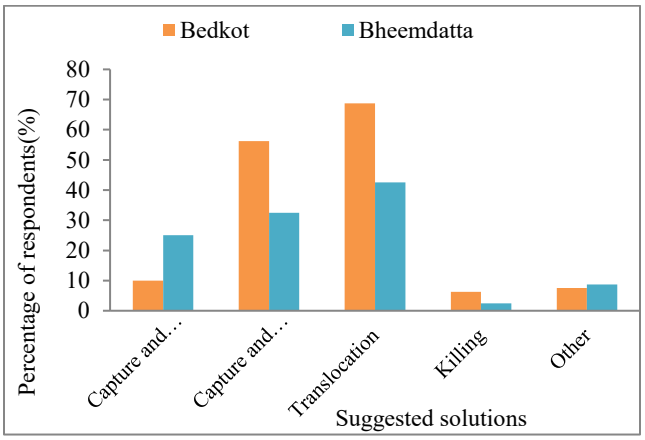

Fig. 10: Perceived problem monkey management strategies in Bedkot and Bheemdatta Municipalities (Multiple responses allowed).

4. DISCUSSION

This study provides an integrated socio-demographic, ecological, and psychological assessment of human–monkey conflict (HMC) in Bedkot and Bheemdatta Municipalities, demonstrating how variations in livelihood dependence, settlement patterns, and resource availability shape both conflict intensity and community responses. Overall, the findings confirm that HMC is not only a material challenge affecting livelihoods, but also a deeply social and emotional issue, underscoring the need for integrated management approaches that address ecological drivers alongside community needs and well-being.

Gender-disaggregated analysis indicates that both men and women face exposure to HMC, albeit in role-specific contexts: men primarily during agricultural activities and women within domestic and peri-household settings [8, 14]. Age structure further revealed heightened vulnerability among elderly populations in Bedkot, likely linked to youth outmigration, reduced physical capacity, and limited access to coping mechanisms [14, 18]. Educational disparities also shaped adaptive capacity; higher literacy levels in Bheemdatta were associated

with greater awareness and openness to alternative mitigation strategies, whereas lower educational attainment in Bedkot constrained uptake of non-traditional approaches. Together, these patterns highlight the importance of age-, gender-, and livelihood-sensitive interventions tailored to local socio-economic contexts. Similar patterns have been observed in other South and Southeast Asian contexts [39, 40, 41]

Respondents consistently reported substantial crop damage, property loss, and time-intensive field guarding. While these impacts clearly undermine household livelihoods, the study did not quantify economic losses in monetary terms. Future valuation of financial costs would provide a more precise estimate of household burden and strengthen the design of compensation mechanisms, insurance schemes, and targeted mitigation investments.

Food scarcity and habitat loss emerged as the primary drivers of HMC across both municipalities, intensifying competition for food and space and aligning with evidence from across South Asia [7, 8, 14]. Higher concern for habitat loss in Bheemdatta reflects rapid urbanization and land-use change, whereas Bedkot's predominantly agrarian landscape—though partially buffered by remaining forest patches—exposes households to frequent crop-raiding risks [12, 27]. However, this study did not incorporate ecological variables such as forest cover, habitat fragmentation, or macaque troop density, which likely influence spatial patterns of conflict. Integrating GIS-based land-use data and ecological indicators in future research would improve hotspot identification and deepen understanding of conflict dynamics.

Crop and garden destruction remained the most pervasive cost of HMC, affecting more than three-quarters of surveyed households, consistent with regional patterns where agriculture is the sector most affected by primate conflict [27, 42]. Food snatching and property damage were more prominent in Bheemdatta, reflecting increased human–monkey encounters in urban and peri-urban environments [43]. Although less frequent, monkey bites and fear-induced accidents highlight under-recognised public health risks [44, 45]. Reports of stress and anxiety—particularly among rural households with limited coping options—demonstrate the cumulative psychological toll of repeated losses.

These patterns reflect broader ecological dynamics: macaques increasingly rely on crops when natural forage is limited [22], while urban expansion accelerates habitat loss and behavioural habituation in Bheemdatta [5]. In Bedkot, remaining forest patches appear to partially buffer conflict, consistent with findings from comparable landscapes in the Western Ghats, India [8]. Together, these variations illustrate how land-use change, settlement proximity, and macaque density interact to shape conflict intensity.

The study reveals a substantial emotional burden associated with HMC, with 15% of respondents reporting unbearable stress [46]. Although many households continued to tolerate disturbances, persistent crop and property losses contributed to increasingly negative perceptions of monkeys. The near-even split between negative (55%) and positive (45%) attitudes reflects ongoing tension between cultural tolerance and lived experiences of harm [47]. Similar patterns have been documented globally, where repeated negative wildlife interactions erode support for conservation initiatives [39, 44].

While most respondents expressed continued support for conservation, this support declined sharply ollowing injuries to family members, underscoring the limits of cultural tolerance in the face of personal harm. Hindu reverence for monkeys remains influential [22, 27, 45], yet livelihood impacts increasingly challenge these norms—a trend widely observed in regions where primates hold religious significance but are perceived as agricultural pests [12, 19, 25]. Notably, most socio-demographic variables were weakly associated with conservation attitudes, suggesting that direct experience of damage outweighs background characteristics in shaping perceptions. Younger and agriculture-dependent respondents tended to express more negative views, even while recognizing monkeys' ecological and cultural importance, highlighting persistent trade-offs between conservation and livelihoods.

Although this study documented commonly used mitigation strategies, their effectiveness was not systematically evaluated. Future research should apply structured ranking or scoring systems to assess efficacy and inform evidence-based community interventions. Despite experiencing significant damage, most respondents favored non-lethal approaches combined with habitat restoration and stakeholder engagement, reflecting Nepal's cultural emphasis on compassion toward wildlife [9, 48, 49]. Households relied predominantly on fear-based deterrents such as shouting, stone-throwing, and using sticks. While these methods provide short-term relief, they may increase habituation or aggression among macaques [8, 50]. Structural interventions were less common, reflecting financial constraints and logistical barriers [50]. Respondents expressed strong expectations of government leadership, prioritizing physical barriers, capture–release, translocation, and habitat restoration—preferences consistent with findings from other South Asian contexts [22, 41, 51].

However, global evidence indicates that translocation often fails due to primates' behavioural adaptability [52]. Consequently, socially acceptable interventions must be complemented by ecological measures such as habitat enrichment, food-source management, and sustained community education to ensure long-term effectiveness [52, 53].

Taken together, these findings demonstrate that HMC in Nepal is a multidimensional challenge shaped by ecological scarcity, land-use change, cultural values, and socio-economic vulnerability. Effective mitigation requires integrated strategies that: (i) restore natural habitats and food resources to reduce crop-raiding pressure; (ii) support cost-effective community defenses while addressing financial barriers; (iii) incorporate psychological well-being into conflict assessments; and (iv) align interventions with cultural values while ensuring ecological effectiveness. Strengthened collaboration among communities, government agencies, and non-governmental organizations will be essential for translating local priorities into durable, culturally sensitive, and ecologically informed solutions.

This study has several limitations. Ecological variables such as forest cover, proximity to habitat edges, food availability, and macaque troop size were not measured, limiting spatial analysis of conflict hotspots. Economic losses were not quantified, constraining assessment of the full socio-economic burden. Additionally, mitigation effectiveness was recorded qualitatively without structured evaluation. Reliance on self-reported data may introduce recall bias and underreporting of sensitive

behaviours. Future research should integrate macaque behavioural ecology with socio-economic surveys, incorporate spatial and longitudinal designs, and evaluate mitigation outcomes over time to strengthen policy relevance and conservation impact.

5. CONCLUSION

Human–monkey conflict is an emerging challenge in Bheemdatta and Bedkot Municipalities, driven by rapid land-use change and shrinking natural habitats. In Bedkot, conflicts are dominated by crop losses and field destruction, while in Bheemdatta, urban interactions—property damage, food theft, and monkey intrusions into homes and markets- are more prevalent. Core drivers, including habitat loss, food scarcity, expanding human settlements, and monkeys' behavioral adaptability, are consistent across both areas. HMC imposes notable psychological burdens, particularly on subsistence farmers and vulnerable populations. Traditional deterrents, such as chasing, firecrackers, and makeshift fencing, are largely reactive and temporary, with limited government support intensifying community frustration. HMC management will require coordinated efforts involving local communities, municipal authorities, and conservation agencies. Future research should incorporate ecological data, economic valuation, and structured evaluation of mitigation strategies to provide a more comprehensive foundation for sustainable, community-based conflict mitigation.

AUTHOR CONTRIBUTIONS

M. Joshi: Conceptualization, Methodology, Field Work, Data Curation, Analysis, Writing – Original Draft, Writing – Review & Editing; M. Bista: Conceptualization, Supervision, Writing- Review & Editing; B. Awasthi: Conceptualization, Methodology, Resources, Analysis, Supervision, Writing-Original Draft, Writing-Review & Editing. All authors contributed to the drafts and gave final approval for publication.

ETHICAL STATEMENT

This research is original and has not been published or submitted elsewhere. Informed consent was obtained from all participants before data collection.

DECLARATION OF CONFLICT OF INTEREST

The authors declare no competing interests.

ACKNOWLEDGEMENT

We are deeply grateful to all who supported this research. We thank the faculty of the Zoology Department, Siddhanath Science Campus, for their guidance. We also gratefully acknowledge the partial financial assistance provided by the University Grants Commission (UGC), Nepal, under Grant No. FRG-80/81-S&T-01. The corresponding author would like to acknowledge the Southeast Asia Biodiversity Research Institute, Chinese Academy of Sciences & Center for Integrative Conservation, Xishuangbanna Tropical Botanical Garden, Mengla, Yunnan 666303, China, and Yunnan International Joint Laboratory of Southeast Asia Biodiversity Conservation & Yunnan Key Laboratory for Conservation of Tropical Rainforests and Asian Elephants, Menglun, Mengla, Yunnan, 666303, China for their collaborative support and contributions to this research. We are also grateful to the local respondents, communities, and authorities for their cooperation and to Miss Jaya Laxmi Jaishi, Mr. Gorakh Bahadur Saud, and Miss Manju Joshi for their invaluable assistance with data collection and field surveys.

REFERENCES

[1] A. Baishya, T.K.S. Rao, A.K. Singh, A. Parmar, Human–wildlife conflict and management with special reference to India, *Annual Research & Review in Biology*, **40** (2025) 133–144. https://doi.org/10.9734/arrb/2025/v40i522461

[2] R. Gopalan, S. Radhakrishna, Moving from coexistence to conflict: A political ecology perspective on human–rhesus macaque conflict in Himachal Pradesh, India, *Human Ecology*, **50** (2022) 463–476 https://doi.org/10.1007/s10745-022-00331-7

[3] S.M. Redpath, J. Young, A. Evely, W.M. Adams, W.J. Sutherland, A. Whitehouse, A. Amar, R.A. Lambert, J.D.C. Linnell, A. Watt, R.J. Gutiérrez, Understanding and managing conservation conflicts, Trends in Ecology & Evolution, **28** (2013) 100–109. https://doi.org/10.1016/j.tree.2012.08.021

[4] N.H. Carter, B.K. Shrestha, J.B. Karki, N.M.B. Pradhan, J. Liu, Coexistence between wildlife and humans at fine spatial scales, *Proceedings of the National Academy of Science of United Stetes of America*, **109** (2012) 15360–15365. https://doi.org/10.1073/pnas.1210490109

[5] W.P.J. Dittus, S. Gunathilake, M. Felder, Assessing public perceptions and solutions to human–monkey conflict from 50 years in Sri Lanka, *Folia Primatologica*, **90** (2019) 89–108. https://doi.org/10.1159/000496025

[6] G.R. Regmi, K.A.-I. Nekaris, K. Kandel, V. Nijman, Crop-raiding macaques: Predictions, patterns and perceptions from Langtang National Park, Nepal, *Endangered Species Research*, **20** (2013) 217–226. https://doi.org/10.3354/esr00502

[7] S. Rai, R. Rai, Monkey menace in Nepal: An analysis and proposed solutions, Journal of Multidisciplinary Sciences, **6** (2024) 26–31. https://doi.org/10.33888/jms.2024.614

[8] A. Sengupta, S. Radhakrishna, Of concern yet? Distribution and conservation status of the bonnet macaque (*Macaca radiata*) in Goa, India, *Primate Conservation*, **27** (2013) 109–114. https://doi.org/10.1896/052.027.0113

[9] A. Treves, R.B. Wallace, L. Naughton-Treves, A. Morales, Co-managing human–wildlife conflicts: A review, *Human Dimensions of Wildlife*, **11** (2006) 383–396. https://doi.org/10.1080/10871200600984265

[10] N.E.C. Priston, M.R. McLennan, Managing humans, managing macaques: Human–macaque conflict in Asia and Africa, in: S. Radhakrishna, M. Huffman, A. Sinha (Eds.), *The Macaque Connection*, Developments in Primatology: Progress and Prospects, vol. 43, Springer, New York, NY, 2013, pp. xxx–xxx. https://doi.org/10.1007/978-1-4614-3967-7_14

[11] A. Sinha, S. Vijayakrishnan, Primates in urban settings, in: M. Bezanson, K.C. MacKinnon, E. Riley, C.J. Campbell, K.A.I. Nekaris, A. Estrada, A.F. Di Fiore, S. Ross, L.E. Jones-Engel, B. Thierry, R.W. Sussman, C. Sanz, J. Loudon, S. Elton, A.

Fuentes (Eds.), *The International Encyclopedia of Primatology*, 2017. https://doi.org/10.1002/9781119179313.wbprim0458

[12] R.C. Adhikari, Study of human and monkey conflict in Dhankuta Municipality, Dhankuta, Province 1, Nepal, Nepalese Journal of Biosciences, **8** (2018) 26–35. https://doi.org/10.3126/njbs.v8i1.51721

[13] R. Saraswat, A. Sinha, S. Radhakrishna, A god becomes a pest? Human–rhesus macaque interactions in Himachal Pradesh, northern India, *European Journal of Wildlife Research*, **61** (2015) 435–443. https://doi.org/10.1007/s10344-015-0913-9

[14] S. Koirala, P.A. Garber, D. Somasundaram, H.B. Katuwal, B. Ren, C. Huang, M. Li, Factors affecting the crop raiding behavior of wild rhesus macaques in Nepal: Implications for wildlife management, *Journal of Environmental Management*, **297** (2021) 113331. https://doi.org/10.1016/j.jenvman.2021.113331

[15] L. Jones-Engel, G.A. Engel, J. Heidrich, M. Chalise, N. Poudel, R. Viscidi, P.A. Barry, J.S. Allan, R. Grant, R. Kyes, Temple monkeys and health implications of commensalism, Kathmandu, Nepal, *Emerging Infectious Diseases*, **12** (2006) 900–906. https://doi.org/10.3201/eid1206.060030

[16] N. Neupane, S. Paudel, R. Sapkota, Y.P. Joshi, Y. Rijal, A. Chalise, Enhancing the resilience of food production systems for food and nutritional security under climate change in Nepal, *Frontiers in Sustainable Food Systems*, **6** (2022) 968998. https://doi.org/10.3389/fsufs.2022.968998

[17] R. Rathi, D. Bhatt, Human–monkey conflict in human dominated landscape of Najibabad forest division, Bijnor, *Indian Journal of Animal Sciences*, **90** (2020) 788–791. https://doi.org/10.56093/ijans.v90i5.104633

[18] B. Pant, H.P. Sharma, B.R. Dahal, S. Regmi, J.L. Belant, Spatio-temporal patterns of human–wildlife conflicts and effectiveness of mitigation in Shuklaphanta National Park, Nepal, *PLOS ONE*, **18** (2023) e0282654. https://doi.org/10.1371/journal.pone.0282654

[19] K. Senthilkumar, P. Mathialagan, C. Manivannan, A case study on conflict between human and monkey at Chengalpet district, Tamil Nadu, *International Journal of Veterinary Sciences and Animal Husbandry*, **9** (2024) 1205–1207. https://doi.org/10.22271/veterinary.2024.v9.i1q.1105

[20] M.V. Ogra, Human–wildlife conflict and gender in protected area borderlands: A case study of costs, perceptions, and vulnerabilities from Uttarakhand (Uttaranchal), India, *Geoforum*, **39** (2008) 1408–1422. https://doi.org/10.1016/j.geoforum.2007.12.004

[21] M. Barua, S.A. Bhagwat, S. Jadhav, The hidden dimensions of human–wildlife conflict: Health impacts, opportunity and transaction costs, *Biological Conservation*, **157** (2013) 309–316. https://doi.org/10.1016/j.biocon.2012.07.014

[22] S. Anand, V.V. Binoy, S. Radhakrishna, The monkey is not always a god: Attitudinal differences toward crop-raiding macaques and why it matters for conflict mitigation, Ambio, **47** (2018) 711–720. https://doi.org/10.1007/s13280-017-1008-5

[23] I. Ganguly, N.S. Chauhan, How perception of local people towards rhesus macaque (*Macaca mulatta*) can influence decision-making of human–macaque conflict mitigation, *Journal of Wildlife and Biodiversity*, **3** (2019) 52–62. https://doi.org/10.22120/jwb.2019.35090

[24] L.R. Baker, O.S. Olubode, A.A. Tanimola, D.L. Garshelis, Role of local culture, religion, and human attitudes in the conservation of sacred populations of a threatened 'pest' species, *Biodiversity and Conservation*, **23** (2014) 1895–1909. https://doi.org/10.1007/s10531-014-0694-6

[25] B. Rijal, Ecological study of rhesus and Assamese macaques and their conflict with humans in Nagarjun Forest, Kathmandu, Nepal (Doctoral dissertation, Central Department of Zoology, Institute of Science and Technology, Tribhuvan University, Kirtipur, Nepal) (2015).

[26] S. Sharma, S. Acharya, Human–rhesus macaque conflict at Pumdivumdi/Tallokodi, Pokhara, West Nepal, *Banko Janakari*, **27** (2017) 46–50. https://doi.org/10.3126/banko.v27i2.21222

[27] K. Aryal, M.K. Chalise, Human–monkey interface in Arkhale and Nayagaun, Gulmi, West Nepal, *Nepalese Journal of Zoology*, **1** (2013) 30–40. Available at: https://www.cdztu.edu.np/njz/index.php/NJZ/article/view/37

[28] B. Shrestha, R.A. Mandal, A.B. Mathema, Depredation of crop caused by monkeys nearby Shivapuri-Nagarjun National Park, Kathmandu, Nepal, *Open Access Journal of Wildlife Conservation*, **5** (2022) 1. https://doi.org/10.23880/oajwx-16000170

[29] B. Awasthi, N.B. Singh, Status of human–wildlife conflict and assessment of crop damage by wild animals in Gaurishankar Conservation Area, Nepal, *Journal of Institute of Science and Technology*, **20** (2015) 107–111. https://doi.org/10.3126/jist.v20i1.13918

[30] K.P. Acharya, P.K. Paudel, P.R. Neupane, M. Köhl, Human–wildlife conflicts in Nepal: Patterns of human fatalities and injuries caused by large mammals, *PLOS ONE*, **11** (2016) e0161717. https://doi.org/10.1371/journal.pone.0161717

[31] G. Joshi, B. Neupane, D. Dahal, S. Shrestha, P. Dhakal, C.M. Jandug, B. Jandug, D. Gautam, Assessment of human–wildlife conflict in Kailali district of Nepal, *Journal of Animal Diversity*, **2** (2020) 24–36. https://doi.org/10.29252/JAD.2020.2.3.5

[32] M. Bhatta, R. Joshi, Analysis of human–wildlife conflict in buffer zone area: A case study of Shuklaphanta National Park, Nepal, *Grassroots Journal of Natural Resources*, **3** (2020) 28–45. https://doi.org/10.33002/nr2581.6853.03033

[33] R.R. Dutta, B. Das, J. Das, K. Kakati, Study on human–monkey conflict in the Nagaon district of Assam: Local mitigation measures, *Journal of Bioresources*, **12** (2024) 57–62. https://doi.org/10.5281/zenodo.14800585

[34] T.R. Joshi, M.P. Awasthi, J. Joshi, R.R. Pant, H.S. Bist, G.S. Thagunna, Perception-based assessment of the water supply system in Bhimdatta Municipality, Sudurpashchim Province, Nepal, *Journal of Engineering Technology and Planning*, **5** (2024) 114–131. https://doi.org/10.3126/joetp.v5i1.69730

[35] K. Dahal, K.P. Timalsina, Dimensions of land use change and implications in spatial planning of emerging town Bedkot Municipality, Kanchanpur District, Nepal, *Geographical Journal of Nepal*, **13** (2020) 185–200. https://doi.org/10.3126/gjn.v13i0.28158

[36] ENPHO, SFD report: Bedkot Municipality, Nepal, Environment and Public Health Organization, 2022. https://www.susana.org/_resources/documents/default/3-5064-7-1662632757.pdf

[37] S. Hamal, R. Bist, B. Pant, B. Adhikari, Water quality index and human health risk assessment for heavy metals in groundwater of Bedkot Municipality, Kanchanpur, Nepal: A cross-sectional study, *EQA - International Journal of Environmental Quality*, **69** (2025) 73–86. https://doi.org/10.6092/issn.2281-4485/21769

[38] A.M.N.S. Poornima, W.M.L.S. Weerasekara, M. Vinobaba, K.A.N.K. Karunarathna, Community-level awareness and attitudes towards human–monkey conflict in Polonnaruwa district, Sri Lanka, *Primates*, **63** (2022) 261–270. https://doi.org/10.1007/s10329-022-00985-3

[39] E.P. Riley, The human–macaque interface: Conservation implications of current and future overlap and conflict in Lore Lindu National Park, Sulawesi, Indonesia, *American Anthropologist*, **109** (2007) 473–484. https://doi.org/10.1525/aa.2007.109.3.473

[40] C.M. Hill, A.D. Webber, Perceptions of nonhuman primates in human–wildlife conflict scenarios, *American Journal of Primatology*, **72** (2010) 919–924. https://doi.org/10.1002/ajp.20845

[41] M. Barua, S.A. Bhagwat, S. Jadhav, The hidden dimensions of human–wildlife conflict: Health impacts, opportunity and transaction costs, *Biological Conservation*, **157** (2013) 309–316. https://doi.org/10.1016/j.biocon.2012.07.014

[42] A. Fuentes, M. Southern, K.G. Suaryana, Monkey forests and human landscapes: Is extensive sympatry sustainable for Homo sapiens and Macaca fascicularis on Bali? In J.D. Paterson & J. Wallis (Eds.), Commensalism and conflict: The human-primate interface (pp. 168–196), Norman: American Society of Primatologists, 2005.

[43] J.C.M. Sha, M.D. Gumert, B.P. Lee, L. Jones-Engel, S. Chan, A. Fuentes, Macaque–human interactions and the societal perceptions of macaques in Singapore, *American Journal of Primatology*, **71** (2009) 825–839. https://doi.org/10.1002/ajp.20710

[44] C.M. Hill, F. Osborn, A.J. Plumptre, Human-wildlife conflict: Identifying the problem and possible solutions (Vol. 1), Albertine Rift Technical Report Series, Wildlife Conservation Society, 2002.

[45] S. Radhakrishna, M.A. Huffman, A. Sinha, *The Macaque Connection: Cooperation and Conflict between Humans and Macaques*, Springer, New York, NY, 2013. https://doi.org/10.1007/978-1-4614-3967-7

[46] Z. Zhang, X. Dong, Z. Liu, N. Liu, Social status predicts physiological and behavioral responses to chronic stress in rhesus monkeys, *iScience*, **27** (2024) 110073. https://doi.org/10.1016/j.isci.2024.110073

[47] P.C. Lee, N.E. Priston, Human attitudes to primates: Perceptions of pests, conflict and consequences for primate conservation, in: *Commensalism and Conflict: The Human–Primate Interface*, 2005. https://doi.org/10.1002/047001539X.ch1

[48] P.A. Pebsworth, R. Gawde, M. Bardi, B.V. Vijayan, S. Radhakrishna, To kill or not to kill? factors related to people's support of lethal and non-lethal strategies for managing monkeys in India, Human Dimensions of Wildlife, **26** (2021) 541–558. https://doi.org/10.1080/10871209.2020.1856453

[49] Y. Liu, Living in the Animal/Human Borderland: Human-Macaque Relationships in Chitwan, Nepal (Master's thesis, San Diego State University) (2022).

[50] S. Malaivijitnond, Y. Hamada, Current situation and status of long-tailed macaques (*Macaca fascicularis*) in Thailand, *Tropical Natural History*, **8** (2008) 185–204. https://doi.org/10.58837/tnh.8.2.102975

[51] R. Rudran, S.C. de Mel, A. Sumanapala, R.K. De Mel, K.K.T.I. Mahindarathna, An ethnoprimatological approach to mitigating Sri Lanka's human-monkey conflicts, *Primate Conservation*, **35** (2021) 1–10.

[52] M. Franquesa-Soler, J.F. Aristizabal, E. Andresen, I.V. del Burgo, A. Shedden-González, E. Rodríguez-Luna, Long-term assessment of the translocation of an endangered primate into an agroforestry system, *Endangered Species Research*, **48** (2022) 235–246. https://doi.org/10.3354/esr01195

[53] E.A. Williamson, K.H. Farmer, J. Sherman, Applying best practice to feasibility assessment and strategic planning for great ape translocation: A case study of Grauer's gorilla (Gorilla beringei graueri), *Biological Conservation*, **292** (2024) 110521. https://doi.org/10.1016/j.biocon.2024.110521